PONTIFICIA UNIVERSIDAD CATOLICA DE CHILE
SCHOOL OF ENGINEERING

CRUSTAL PALEO-STRESS AND PERMEABILITY IN A STRIKE-SLIP SETTING: INSIGHTS FROM THE SOUTHERN VOLCANIC ZONE (38-39°), CHILE.

PAMELA VIVIANA PÉREZ FLORES

Thesis submitted to the Office of Graduate Studies in partial fulfillment of the requirements for the Degree of Doctor in Engineering Sciences

Advisor:
JOSÉ CEMBRANO.

Santiago de Chile, May, 2017

PONTIFICIA UNIVERSIDAD CATOLICA DE CHILE
SCHOOL OF ENGINEERING

CRUSTAL PALEO-STRESS AND PERMEABILITY IN A STRIKE-SLIP SETTING: INSIGHTS FROM THE SOUTHERN VOLCANIC ZONE (38-39°S), CHILE.

PAMELA VIVIANA PÉREZ FLORES

Members of the Committee:
JOSÉ CEMBRANO
DANIEL HURTADO
GLORIA ARANCIBIA
ANDRÉS VELOSO
ANDREA BROGI
CRISTIÁN VIAL

Thesis submitted to the Office of Graduate Studies in partial fulfillment of the requirements for the Degree of Doctor in Engineering Sciences

Santiago de Chile, 2017

Gratefully to Raul Pérez and Helia Flores

ACKNOWLEDGEMENTS

This thesis is the result of the enthusiasm, generosity and effort of many people and institutions. The *Pontificia Universidad Católica de Chile* funded my first semester scholarship. The *Comisión Nacional de Ciencia y Tecnología* (CONICYT) granted me a scholarship (*Beca doctorado nacional*-21120519) and funded my tuition fees, operational expenses and a 10-month internship at the University College London. The *Centro de Excelencia en Geotermia de Los Andes* (CEGA) FONDAP/CONICYT Project 15090013 funded my field trips, chemical analyses, and attendance to international meetings.

I deeply thank my advisor José Cembrano; his concepts, enthusiasm, and patience were the basis of this thesis from the beginning to the end. He introduced to me to the geological structural world and the enjoyment of little things. I thank José for inviting me to be part of the Geoscience UC project together with Gloria Arancibia, Gonzalo Yañez and Isabel Santibañez. Thanks to Mariel Castillo for her company and advice.

Professor Andrés Veloso made a significant contribution to development and conclusion of the subjects of this work. Pablo Sanchez was a fundamental friend and research partner during long field trips and discussions.

Special thanks to Tom Mitchell for his advice and care during my internship at the University College London. His patience during the laboratory experiments and development of Chapter 4 were fundamental. Phil Meredith's suggestions, ideas, discussions, and reviews were essential for the improvement of Chapter 4 and during the experimental work.

None of this work would have been possible without the help of key colleagues during the field work and data processing: Daniele Tardani, Felipe Astudillo, Martin Lizama, Pablo Iturrieta, Nicolas Pérez-Estay, Juan Ignacio Sanchez, Tomás Roquer y Juan Fernando Rubilar. Intense and productive discussions were fundamental to conclude this thesis, thanks to Rodrigo Gomila, Gerd Sielfeld and Felipe Aron for their time and great ideas.

I am very grateful at the thorough comments of the external reviewer Andrea Brogi; his suggestions improved the goal and internal consistency of this work.

Finally, thanks to my parents Raul and Helia; their love and support have been fundamental for my growth and allowed me to do what I like and enjoy it. My brother showed me what Geology is and took my hand from the beginning and is still there.

TABLE OF CONTENTS

ACKNOWLEDGEMENTS ii

TABLE OF CONTENTS iii

LIST OF FIGURES vii

LIST OF TABLES xiii

ABSTRACT xiv

RESUMEN xv

1 THESIS SUMMARY

1.1 Organization of the thesis 1

1.2 Introduction 1

1.3 Hypothesis 8

1.4 Research question and aims 8

1.5 Methodology 8

1.5.1 Fault slip inversion 12

1.6 Results 14

1.7 Concluding remarks 17

1.8 Future work 21

1.9 Publication and abstract resulting from this research 22

1.9.1 Publications 22

1.9.2 Conference abstracts 22

1.10 Publication and abstract resulting from side-projects 23

1.10.1 Publications 23

1.10.2 Conference abstracts 24

2 TECTONICS, MAGMATISM, AND PALEO-FLUID DISTRIBUTION IN A STRIKE-SLIP SETTING: INSIGHTS FROM THE NORTHERN TERMINATION OF THE LIQUIÑE-OFQUI FAULT SYSTEM, CHILE

2.1 Introduction 27

2.2 Geological background 31

2.2.1 Structural setting 31

2.2.2 Geometry and spatial distribution of dikes and eruptive centers. 33

2.3 Methodology 34

2.3.1 Field and laboratory structural geology 34

2.3.2 Fault-slip data inversion 36

2.3.3 Determination of strain field 36

2.3.4 Determination of stress field 37

2.4 Results 38

2.4.1 Architecture and geometry of fault fracture networks in the study area. 38

2.4.2 Kinematics and dynamics of fault-fracture networks 44

2.5 Discussion 49

2.5.1 Deformation partitioning at the Southern Volcanic Zone 49

2.5.2 Magmatic and hydrothermal fluid migration 52

2.6 Conclusions 55

2.7 Acknowledgments 58

3 FRACTURE NETWORK, FLUID PATHWAYS AND PALEOSTRESS AT THE TOLHUACA GEOTHERMAL FIELD 59

3.1 Introduction 59

3.2 Geological and tectonic framework 61

3.2.1 Tolhuaca geothermal system 64

3.3 Methodology 67

3.3.1 Structural data collection and sampling 67

3.3.2 Paleomagnetic measurement 68

3.3.3 Structural data analysis 69

3.4 Results 69

3.4.1 Demagnetization patterns and RM vectors (Table 2). 70

3.4.2 Structural elements on Tol-1 borehole (see details in appendix SM4 and Table 3). 75

3.4.3 Strain field 78

3.4.4 Stress field 78

3.5 Discussion 79

3.5.1 Magnetic reorientation 79

3.5.2 Re-oriented structural elements and the regional tectonic setting 80

3.6 Conclusions 83

3.7 Acknowledgements 84

4 THE EFFECT OF OFFSET ON FRACTURE PERMEABILITY. INSIGHT OF THE ANDEAN SOUTHERN VOLCANIC ZONE, CHILE.

4.1 Introduction 85

4.2 Fault-fracture network architecture and geo-fluid flow within the SVZ. 87

4.3 Materials and Methods 91

4.3.1 Sample materials 91

4.3.2 Permeameter and permeability measurement methodology 92

4.3.3 Experimental protocol 93

4.4 Results 95

4.4.1 Permeability of intact and macro-fractured SVZ rocks. 95

4.4.2 Permeability of macro-fractured SVZ rocks as a function of fracture offset. 97

4.4.3 Permeability of macro-fractured Seljadalur basalt as a function of fracture offset and gouge. 98

4.4.4 Fracture trace analysis 101

4.5 Discussion 105

4.6 Conclusions 111

Acknowledgements 112

5 REFERENCES 113

6 A P P E N D I X 124

LIST OF FIGURES

Figure 1-1. Plane view cartoons show the extreme cases from no-partitioned (a) to partitioned deformation (b) imposed by oblique convergence (Fossen et al., 1994; Teyssier et al., 1995; Teyssier and Tikoff, 1998). (c) Relation among angle of relative plate motion (α), orientation of minimum and maximum instantaneous shortening axis for transpression/transtension (θ) and degree of strike-slip partitioning. This graphic shows two examples: no strike-slip partitioning at New Zealand (α = 29°) and strike-slip partitioned at San Andreas fault system (α = 5°) (Teyssier et al., 1995). 3

Figure 1-2. Cartoon showing the ideal orientation of crack networks surrounding planar faults in a strike-slip, extensional and compressional tectonic regime (Faulkner and Armitage, 2013). The bottom shows the likely orientation and relative magnitude of the principal axes of the permeability tensor for each tectonic regime (Faulkner and Armitage, 2013). σ_1, σ_2, σ_3 are the principal stress axes and k_v, k_{hmin}, k_{Hmax} are the vertical, horizontal maximum and minimum permeability, respectively. 4

Figure 1-3. Cartoon showing the elements of a fault zone architecture: fault core, damage zone and their related fracture frequency and permeability (e.g. Faulkner et al., 2010; Ganerød et al., 2008). 5

Figure 1-4. (a) Southern Volcanic Zone relief map showing the location and extent of the LOFS (black lines), ATF (red lines) and the study area location. Convergence velocity vector after Angermann et al. (1999) (b) Google Earth image showing the principal fault zones: LOFS (black lines) and ATF (red lines) and their special relationship with hot springs and volcanoes (Cembrano and Lara, 2009; Pérez-Flores et al., 2016; Sánchez et al., 2013; Sielfeld et al., 2016). 7

Figure 1-5. These photographs show an example of structural elements from structural sites at outcrop scale: (a) Fault zone with 2 m width fault core, (b) Right lateral fault plane with horizontal striae and calcite slickenfibers, (c) zeolite tensional veins with euhedral zeolite crystals perpendicular to veins wall (d) hydrothermal breccia veins consist of zeolite vein clasts in a gouge matrix. Clasts come from the original massive vein to the right. 10

Figure 1-6. Structural elements identified in Tol-1 drill core mapping. (a) Iron-oxide veins crosscut and displaced by hybrid fault filled with calcite. (b) Calcite vein with hydrothermal breccia. (c) Zeolite vein and (d) Striated fault plane. 11

Figure 1-7. Criteria for the sense of displacement on fault surface in brittle rocks. (a) Terminology for description of elementary secondary fractures in a simple shear context. (b) Striation due to a ploughing element (asperity ploughing), (c) crystallization on the lee side of asperities (d) Main types of criteria based on repetitive secondary fractures (redrawn from Petit, 1987). 11

Figure 1-8. (a) Scheme shows the fault-slip data used for the strain and stress analysis (Veloso et al., 2015). The diagram (b) and lower-hemisphere, equal area stereographic projection (c) show the fault plane perpendicular to a common plane (movement plane) that contain kinematic axes, slip direction and fault pole, with P and T axes forming angles of 45° with both the slip direction, the fault pole (P) and the pole of movement plane (Marrett and Allmendinger, 1990). 12

Figure 1-9. Stereograms show σ_1 axes and σ_3 axes sub-solutions, the φ value represented by color coded (from 0 to 1) and the plunge of stress axes denoted by length of the tails of tadpole symbols (Yamaji, 2000). 14

Figure 1-10. Effective σ_1 (σ_1 minus hydrostatic pressure) at different depths for each stress field regime (Zang et al., 2012). Dashed lines show the depth at which each stress regime reaches a maximum effective principal stress of 40 MPa. 20

Figure 1-11. Block diagram showing the main geologic features of the NNE-, NE- and NW-striking structural domains along with their local stress field, inferred fluid migration paths, potential storage regions and depth limit for advective/convective flow. 21

Figure 2-1. (a) Composite Digital Elevation Model and 1:1.000.000 geological map of the Southern Andes Volcanic Zone (SVZ) (Perez-Flores et al., 2013). Regional map showing the location and extent of the LOFS (black lines), ATF (red lines) and main Holocene volcanoes (red triangles). Previously published focal mechanisms of crustal earthquakes are shown for the LOFS (Black) and ATF (Red) (Barrientos and Acevedo-Aránguiz, 1992; Lange et al., 2008; Legrand et al., 2011). A selection of GPS vectors are showing (Lin et al., 2013; Wang et al., 2007) (b) Digital Elevation Model showing the principal fault systems in southernmost Chile: LOFS (black line) and ATF (red line). Convergence velocity vector after Angermann et al. (1999). Subduction zone earthquakes (blue stars), ATF earthquakes (red stars) and LOFS earthquakes (black stars) are shown as well as their respective focal mechanisms (redrawn after Cifuentes, 1989; Haberland et al., 2006; Moreno et al., 2011). The coseismic shortening and extension axes calculated for 1960 earthquake are showing (Plafker and Savage, 1970). 30

Figure 2-2. Digital Elevation Models showing the preferential orientation of flank cones (red circles) and volcanic vents (blue lines) (Bertin, 2010; Bouvet de Maisonneuve et al., 2012; Maurice, 2012; Sielfeld, 2008) of the (a) Callaqui, (b) Lonquimay and Tolhuaca, (c) Llaima volcanoes. 34

Figure 2-3. Geological-structural map of the Southern Volcanic Zone of the Andes, between 37°30'S and 39°S (see location at Fig. 2-1b) showing the northern termination of the LOFS and the NW-striking faults belonging to ATF (red lines). The white squares show areas of detailed structural mapping sites. 35

Figure 2-4. (a) Google Earth image showing the Lolco, Ralco and Troyo structural sites. Panels b to c show examples of different structural elements seen in the field and under the microscope. (b) East-striking, shallowly-dipping, sinistral fault (N85°W/45°S rake:20°W); (c) N10E-striking, steeply dipping, dextral fault with zeolite slickenfibers.....41

Figure 2-5. See location in Fig. 2-4a. (a) Dilatational jog between NNE and NE-striking dextral faults hosting bladed-like calcite; (b) Oriented thin section perpendicular to the fault plane and parallel to striae showing calcite microstructure. Note that a sigmoidal piece of the wall rock is detached at the dilational site; (c) N60°E-striking fault with subhorizontal striae and dextral strike-slip kinematics; (d) Oriented thin section photo-mosaic showing calcite slickenfibers sheets with sharp contact surfaces and a transitional texture from a brittle shear zone in the host rock contact (da) to blocky crystal types following the slip direction. (db) Extension fractures (N70ºE) locally cut some clasts of the wall-rock. 42

Figure 2-6. (a) Satellite image showing major faults (black lines), lineaments (dotted line), vein orientation (cyan line) and hot springs (blue symbol) at Las Mentas and La Poza structural sites. Las Mentas structural site: (b) strongly foliated (N05W/81W) rock deformed band (N20E/70W) crosscut by ENE-striking veins. (c) Oriented thin section from the deformed band consists of andesitic rock with preferentially oriented, undeformed plagioclase crystals forming sigmoidal S-C fabrics that indicate dextral displacement. 43

Figure 2-7. (a) Google Earth image showing the major faults (black lines) and lineaments (dotted line) at the Las Raices and Las Animas structural sites. Las Animas structural site: (b) Photograph and related line-drawing of one NW-striking fault showing a volcanic interlayered sequence of andesite and hornblende andesite forming a gentle anticline fold near the fault core, which corresponds to a fault-propagated fold. The fault core consists of a foliated gouge with Ca-rich zeolite veins cut by small reverse faults (c). Las Raices structural site: (d) Photograph SSW view showing

NE-striking normal-dextral slip fault and NE-striking dike cut by ENE-striking tensional zeolite veins (e). 45

Figure 2-8. (a) Lower hemisphere, equal-area projection showing the orientation of measured fault planes and their associated displacement vector (striae); (b) Stress field solutions as given by the MIM method applied to the study area. Results of these analyses show that the lower hemisphere stereonet (σ1 and σ3 to the left and right side, respectively, Fig. 1-14b)) calculated by using Multiple Inverse Method (MIM) (Yamaji, 2000), the color represents the φ-value from purple to red (0-1, respectively). (b) φ-histogram graphic shows a bi-modal distribution of the best-possible fit between real and modeled data. (c) Stress field solutions from MIM, σ1 (blue triangle) and σ3 (red star) with red and green line for φ=0.9 and 0.38 respectively. (d) Graphic showing the angular misfit for each solution. 46

Figure 2-9. Lower hemisphere, equal-area projections showing gathered fault-slip data and results of strain and stress analyses, at each structural site. (a) mesoscopic fault-slip data; (b) orientation of T (red dots), P (blue dots) and B (black) axes (e.g Marrett and Allmendinger, 1990). (c) orientation of calculated stress axes (σ1 and σ3) MIM (Yamaji, 2000). (d) Density diagram of the poles-to-veins together with the orientation of σ1 (triangle), σ2 (circle) and σ3 (star) principal stress axes shown in (c).....48

Figure 2-10. Transpressional strain partitioned model (e.g Fossen et al., 1994; Teyssier et al., 1995) applied to the study area (a) non-partitioned, (b) completely partitioned and (c) partially partitioned strain; showing shortening-trending axis (P).....50

Figure 2-11. Schematic diagram showing oblique convergence at 38°S and the strain partitioning analysis with the orientation of maximum shortening axes proposed for the forearc, and σ1 direction calculated for the intra-arc region and the local stress field calculated for each structural site (R: Ralco, L: Lolco, T: Troyo, LP: La Poza, LM: Las Mentas, LR: Las Raices, LA: Las Animas). Details in Table 1. 53

Figure 2-12. Schematic block diagram illustrating the geometrical arrangement and kinematics of faults and other structural elements at the northern termination of the LOFS (black lines) together with the main traces of the ATF (red lines). The cartoon shows the local stress field solutions and the veins main orientation at each structural site (R: Ralco, L: Lolco, T: Troyo, LP: La Poza, LM: Las Mentas, LR: Las Raices, LA: Las Animas).....56

Figure 3-1. (a) Composite Digital Elevation Model (DEM) and 1:1.000.000 geological map of the Southern Andes Volcanic Zone (Pérez-Flores et al., 2016; Sánchez et al., 2013) shows the study area (white square). Regional map showing the location and extent of the LOFS (black lines), ATF (red lines) and main Holocene volcanoes (red triangles). (b). Detailed map of the study area (white square on Fig. 3-1a) showing the main faults and lineaments of the LOFS and ATF (e.g. Biobío Aluminé Fault System), which are spatially and genetically associated with the Tolhuaca and the Lonquimay volcanoes, clusters of minor eruptive centers, hot springs and shallow seismicity (Barrientos and Acevedo-Aránguiz, 1992; Lange et al., 2008; Legrand et al., 2011). The white star shows the location of drill hole Tol-1, drilled by GeoGlobal Energy Chile (GGE Chile). 63

Figure 3-2. Geological map at 1:100.000 scale (Suárez and Emparan, 1997) showing the Tolhuaca and Lonquimay volcanoes. The LOFS (black line) has been interpreted to form a dilatational jog geometry genetically associated with Lonquimay volcano and clusters of flank vents (red asterisk) (Pérez-Flores et al., 2016; Rosenau et al., 2006). Flank vents, fissures (red line) and fumarole areas (blue asterisk) are aligned in a NW trend (red dashed line) at the NW-flank of the Tolhuaca volcano, where the Tolhuaca Geothermal System (TGS) is located. See the legend in Fig. 3-1.....64

Figure 3-3. Tol-1 coherent segment core of andesite (a) shows a vein and the spatially associated sample (white lines) used for paleomagnetic analysis. (b) Vertical view of the axis´ core containing a fault plane with slickenlines; (c) side view of Tol-1 core including banded vein filled with quartz and zeolite. 66

Figure 3-4. Cartoon showing the sampling and structural measurement methodology. (a) For each coherent segment (or adjacent core pieces) containing structural elements, a reference line was drawn. (b) The spatial orientation of each structural element includes: (1) true dip (α_s) and relative strike (β_s, with respect to the reference line), (2) displacement direction, (3) thickness in mm (ε), (4) mineral infill and (5) orientation – measured as a rake angle (ρ) – of the striae, slickenline and mineral fiber. (c) A standard paleomagnetic mini-coring oriented by their true plunge (α) and relative trend (β, with respect to the arbitrary reference line) was measured for each coherent segment. 68

Figure 3-5. Results of progressive thermal demagnetization of representative samples, from 32 m (a) and 992 m (b) depth, displayed by partial demagnetization graphic (left wards) and vector end point diagrams (right wards) (Zijderveld, 1967). For Zijderveld diagrams, each data point represents the projection of the magnetization vector for individual demagnetization steps onto the horizontal (red circle solid symbols) and vertical (blue square open symbols) plane. Numbers adjacent to data points indicate the demagnetization step (leftwards). Sample number, sample depth and NRM intensity are shown at the top of each diagram. Data shown in core coordinates. 73

Figure 3-6. (a) General lithological and alteration zones logging of the borehole Tol-1 (modified from Sanchez-Alfaro et al., 2016) (see supplementary figure SM4). (b) Temperature (°C) (red line) and temperature gradient (blue line) vs. depth profile for the Tol-1 (Sanchez-Alfaro et al., 2016). (c) Blocking temperatures vs. depth for each specimen. Blocking temperatures showed for key minerals as a reference: goethite (Gth), pyrrhotite monoclinic (Po-M) and hexagonal (Po-H), hematite (Hem) and magnetite (Mag) with variation of titanium composition until titanomagnetite containing 60 mol% Ti (TM60) (Whitney and Evans, 2010). (d) Inclination of remanent magnetization vectors, (e) faults and veins striking and (f) dipping variation through the depth of Tol-1 borehole..... 74

Figure 3-7. Lower hemisphere, equal-area projection shows wide orientation range for veins throughout Tol-1 core: (a) poles veins (b) petals each 10°. 77

Figure 3-8. (a) Fault-slip data mapped on the borehole Tol-1. (b) Lower hemisphere, equal-area projection showing the calculated strain axes (using Faultkin 7.4). P- and T-axes of each fault (blue and red dot, respectively) with their mean vectors (blue and red circle) and error ellipse (dashed line). 78

Figure 3-9. (a) Stress field solutions as given by the MIM applied to the fault-slip data. Results show σ_1 (rightwards) and σ_3 (leftwards) axes plotted on a lower hemisphere equal-area projection; the color represents the φ-value from purple - red (0-1, respectively). (b) φ-histogram graphic shows a unimodal distribution with maximum value at φ =0.4. (c) Lower hemisphere, equal-area projection shows stress field best solution, vertical σ_1-axis (83/74) (red triangle) and horizontal σ_3-axis (184/3) (blue star); fault-slip data colors represent the misfit value. (d) Misfit value histogram between real and modeled striae calculated by MIM. 79

Figure 3-10. Schematic block diagram illustrating the proposed tectonic setting of Tolhuaca-Lonquimay volcanoes (looking south). The model shows the spatial distribution of flank-vents (dark grey), fumaroles (blue flames), stratovolcanoes and faults, which are kinematically compatible with regional stress field (biggest unfilled arrows) (Lavenu and Cembrano, 1999; Pérez-Flores et al., 2016), previous calculated local stress field (unfilled arrows) (Pérez-Flores et al., 2016) and stress field solution (filled arrows) at the Tol-1 core location. 83

Figure 4-1. Schematic view of strike-slip fault and a secondary normal-dextral fault showing the slip directions (black arrows), maximum and minimum permeability within the fault plane ($Kpmax$ and $Kpmin$, respectively; blue arrows) stress field and kinematically associated extension fractures. Also, are showed the stress field orientation and permeability tensors (Faulkner and Armitage, 2013). 86

Figure 4-2. Geological-structural map of the Chilean Southern Volcanic Zone, between 37°30′S and 39°S, showing the northern termination of the LOFS, the NW-striking faults belonging to ATF (red lines) (Pérez-Flores et al., 2016) and rock samples location (white star): (1) crystalline tuff, (2) andesitic dike, (3) altered andesite and (4) granodiorite. 88

Figure 4-3. (a) Altered andesite crosscut by fractures and zeolite veins. (b) NE-striking fault zone-hosted andesitic dike, zeolite-calcite veins, and hydrothermal breccia. (c) NE-striking fault crosscut altered andesite. (d) Fault plane detail shows rough surface along the slip direction. 90

Figure 4-4. Cylindrical samples (38 mm in diameter) and thin section images (cross polarized light) of the five lithologies used in this study: (a) crystalline tuff, (b) andesite dike, (c) altered andesite, (d) granodiorite, and (e) Seljadalur basalt. 92

Figure 4-5. Schematic diagram of the permeameter used for all measurements (after Nara et al., 2011; Wang et al., 2016). 94

Figure 4-6. (a) Modified Brazil disk apparatus for producing macro-fractured samples, (b) macro-fractured sample of granodiorite, and (c) plan view of macro-fractured sample of crystalline tuff. 95

Figure 4-7. Schematic diagram illustrating the methodology used to prepare macro-fractured samples with controlled offsets. (a) Original mated macro-fractured sample; (b) and (c) show, respectively, a schematic and photograph of the mated sample with the offset dimension (L_{off}) ground off opposing sample halves; and (d) shows the final, unmated sample with a controlled offset produced by aligning the end faces of the ground halves. 95

Figure 4-8. Permeability of intact samples of crystalline tuff, andesitic dike, altered andesite and granodiorite at an effective pressure of 5 MPa, and of macro-fractured but mated samples as a function of increasing effective pressure up to 60 MPa.....96

Figure 4-9. Change in permeability of SVZ rocks samples with increasing fracture offset and effective pressure of: (a) crystalline tuff, (b) andesite dike, (c) altered andesite and (d) granodiorite. Insets show the permeability on a linear scale (axis to the right). 98

Figure 4-10. Change in permeability of Seljadalur basalt with increasing fracture offset. Inset shows the permeability on a linear scale (axis to the right). 99

Figure 4-11. Effect of the presence and thickness of gouge (0, 0.3, 0.6 and 1.0 mm) on the permeability of mated (zero offset) and un-mated (offsets from 0.25 to 3.0 mm) samples of SB with as a function of increasing effective pressure. 101

Figure 4-12. Examples of fracture traces from sectioned rock samples to show the fracture roughness parallel to the fluid flow direction. Both vertical and horizontal axes are on the same scale. 102

Figure 4-13. Fourier power spectral density P(k) as a function of the spatial frequency for fracture traces of each lithology. 103

Figure 4-14. Schematic diagram illustrating the fracture aperture calculation method: (a) Mated traces of fracture, (b) opposite traces displaced by the offset distance, L_{off}, (c) displaced traces separated by the minimum amount required to remove any overlap (red arrow). The mean aperture ($\bar{a}$) is then the arithmetic mean of all a_x. 104

Figure 4-15. Mean aperture ($\bar{a}$) with increasing offset, calculated for several fracture traces of each lithology. 105

Figure 4-16. Graphics show the cubic aperture of the fracture traces with increase L_{off} (blue dot) and permeability of the un-mated macro-fractured sample with increase L_{off} (black square) for each lithology. 108

Figure 4-17. Mated macro-fractured samples permeability under 5 MPa effective pressure in relation with the average of roughness index *H* for each lithology. (b) The increment of permeability between unmated macro-fractured sample (L_{off} = 0) and unmated macro-fractured sample with L_{off} = 0.25 mm in relation with the average of roughness index *H* for each lithology. The bars show the roughness standard deviation. 108

Figure 4-18. Permeability measurements with increasing offset and re-ground re-mated macro-fractured sample for increasing effective pressure (5 to 60 MPa) of basalt sample. 109

Figure 4-19. Permeability of intact (circle) sample, mated macro-fractured samples (triangle for 5 MPa and white square 60 MPa) and the highest value measured on unmated macro-fractured samples (black square) for each lithology from the SVZ. These permeability values are in context of a range of permeabilities for consolidated rocks, fault rock, seismogenic permeability (SP) estimated from migrating microseismicity of reservoirs in shallow crust, permeability bulk (k) for the Ohaaki-Broadlands & Wairakei geothermal systems, and the minimum permeability limits for the development of fluid convection (under hot/cold hydrostatic condition) and the condition for development of forced overpressures in areas of strong fluid release (Rowland and Sibson, 2004 and references therein). 111

LIST OF TABLES

Table 1. The table summarized the detail mapping at each structural site. The information displays are the host rock age from closer data of Suárez and Emparan (1997), main structural element with their texture and minerals, strain, and stress axes solutions. 39

Table 2. Paleomagnetic sampling information and thermal demagnetization results showing: N, steps number; T. min/T. max, temperature (°C) minimum and maximum; MAD, maximum angular deviation; declination/inclination in sample coordinate and RM vectors in geographic coordinate used by fault and veins reorientation. 71

Table 3. Geological-structural mapping summary. 76

Table 4. Table of sample material properties. 92

Table 5. Properties of the fracture traces for each lithology, showing the mean pre-factor, $\bar{C}$, the mean roughness exponent, $\bar{H}$, and their errors 103

ABSTRACT

This study addresses the interplay between strain/stress fields and geofluid migration in the Southern Andean Volcanic Zone (SVZ). The SVZ coexists with the margin-parallel Liquiñe-Ofqui Fault System (LOFS) and with NW-striking Andean Transverse Faults (ATF). To tackle the role of different fault-fracture systems on deformation distribution and magma/fluid transport, was mapped the geometry and kinematics of faults, veins, and dikes at various scales.

Fault-slip data analysis allows to calculate stress and strain fields from the full study area data base (regional scale) and fault zones representative of each fault system and a drill core from Tolhuaca volcano (local scale). Regional scale strain analysis shows kinematically heterogeneous faulting. Stress field analysis at regional scale indicates a strike-slip dominated transpressional regime with N64E-trending σ1 and N30W-trending σ3. Deformation is further partitioned within the arc through NNE-striking dextral-reverse faults, NE-striking dextral-normal faults, and NW-striking sinistral-reverse faults with normal slip activation. The regional tectonic regime controls the geometry of NE-striking dikes and volcanic centers. NE-striking faults record local stress axes that are clockwise rotated with respect to the regional stress field and locally with tensional stress field (Tolhuaca volcano). NNE- and NE-striking faults are favorably oriented for reactivation under the regional stress field and show poorly-developed damage zones. Conversely, sinistral-reverse NW-striking fault systems, misoriented under the regional stress field, show multiple fault cores, wider damage zones, dense veins networks. This fault zone records a NS-trending tension axis that would be activated under fluid overpressure. The experimental permeability measurement in representative rock units from the SVZ shows that the intact granodiorite sample has two orders of magnitude highest permeability (10^{-18} m^2) than intact volcanic rocks (10^{-20} m^2). This could favor the existence of a fractured fluid reservoir in intrusive rocks, which is the main lithology that composes the basement south of 38°S. Permeability increase with the fault activation from $4x10^{-20}$ m^2 to $8x10^{-14}$ m^2 in crystalline tuff and from $1x10^{-18}$ to $3x10^{-14}$ in granodiorite. Conversely, permeability decreases with the effective pressure increment and macro-fractures maintenance the permeability under high effective pressure (60 MPa).

RESUMEN

Esta tesis explora el control de los campos de deformación/esfuerzo en la migración de geofluidos en Zona Volcánica Sur (ZVS) de los Andes. La ZVS coexiste con los sistemas de falla Liquiñe-Ofqui (SFLO) y con las Fallas Transversales a los Andes (FTA). Para abordar el rol de los diferentes sistemas de fallas y fracturas en la distribución de la deformación y el transporte de geofluidos, se mapeó la geometría y cinemática de fallas, vetas, y diques a varias escalas. El análisis de datos de fallas permitió calcular el campo de esfuerzo y deformación a escala regional y local. A escala regional se registra una deformación con fallamiento heterogéneo, mientras que el campo de esfuerzo muestra un régimen de transpresional con σ_1 orientado N64E y $\sigma 3$ N30W. La deformación es particionada dentro del arco en fallas de orientación NNE dextral y dextral-inversas, NE dextral-normal, y NW sinistral-inversas con reactivaciones de cinemática normal. El campo de esfuerzo regional controla la geometría de diques y centros volcánicos. Las zonas de fallas NE registran un campo de esfuerzo local tensional (volcán Tolhuaca) rotado en dirección horaria con respecto a campo de esfuerzo regional. Fallas NNE y NE están favorablemente orientadas para la reactivación bajo el campo de esfuerzo regional y muestran zonas de daño poco desarrolladas. Por el contrario, fallas NW sinistral-inversas se encuentran mal orientadas para la reactivación bajo el campo de esfuerzo regional. Estas fallas presentan múltiples núcleos de fallas, amplias zonas de daño y densas redes de vetas, desarrolladas bajo tensión NS las que podrían haber sido activas bajo sobrepresión de fluido. Medidas experimentales de permeabilidad en muestras representativas de la ZVS registran que roca intrusiva (granodiorita) intacta tiene una permeabilidad dos órdenes de magnitud más alta (10^{-18} m^2) que las rocas volcánicas (andesita y toba cristalina) (10^{-20} m^2). Esto podría favorecer la existencia de reservorios fracturados de fluidos hidrotermales en rocas intrusivas, la litología principal del basamento al sur de los 38°S. La permeabilidad aumenta con el deslizamiento de fallas desde $4x10^{-20}$ m^2 a $8x10^{-14}$ m^2 en tobas cristalinas y desde $1x10^{-18}$ a $3x10^{-14}$ en granodiorita. La permeabilidad, en macro-fracturas, decrece con el aumento de la presión confinante (profundidad) mientras que el desplazamiento de las fracturas permite mantener una alta permeabilidad (10^{-14}) a alta presión efectiva (60 MPa).

1 THESIS SUMMARY

1.1 Organization of the thesis

This thesis is organized into four, self-contained chapters. Chapter 1 presents a general view of this work including theoretical and geological background, a statement of the scientific problem, hypothesis, goals, the methodology applied, main results and general conclusions. Chapter 2 is a paper published in Tectonophysics an International Scientific Indexing (ISI) journal with 5-year impact of 3.13. This chapter documents the role of stress field variations at local scale on paleo-fluid/magma distribution for different fault-fracture orientations at the northern termination of LOFS (38°-39°S). I provide a comprehensive and integrated view of the interplay between regional/local stress field orientation and fault-fracture meshes in an intra-arc transpressional setting. Chapter 3 is a paper published in Journal Structural Geology an ISI journal with 5-year impact of 2.6. This chapter tackles the tectonics and geofluid entailment at local scale within the northern termination of the LOFS, in a drill core from the Tolhuaca Geothermal System. I contribute to a local structural model for the Lonquimay and Tolhuaca volcanoes and its connection with the geofluid distribution. Chapter 4 is a manuscript submitted to Journal Structural Geology. This chapter provides quantitative results for the permeability of representative lithologies from the SVZ. This chapter shows the permeability variation in mated macro-fractured samples, unmated macro-fractured samples, and micro-fractured samples with increasing effective pressure. I provide an overview of the hydraulic proprieties of SVZ rocks behavior at depth.

1.2 Introduction

The style of regional-scale deformation at the plate boundary zone is primarily controlled by the magnitude and angle of the relative plate motion vector (Fig. 1-1) (e.g. Fossen et al., 1994; Teyssier et al., 1995; Tikoff and Greene, 1997). Large convergence angles ($20° < \alpha < 90°$) favor a pure-shear-dominated transpressional regime with no strike-slip partitioning as is observed at Australian-Pacific plate boundary in New Zealand (Fig. 1-1a) (e.g. Jarrard, 1986; Mccaffrey, 1992; Teyssier et al., 1995). In contrast, low convergence angle ($\alpha<20°$) favors a strike-slip partitioned system, as in the case of wrench-dominated transpressional regime at the Pacific–North America plate boundary of the western US, where the San

Andreas Fault takes up most of the simple shear component (Fig. 1-1b) (e.g. Teyssier et al., 1995; Teyssier and Tikoff, 1998). Fig. 1-1c shows the kinematic analysis of the quantitative relation among the angle of plate motion (α), instantaneous shortening axes (S_3), and strike-slip partitioning (Teyssier et al., 1995). This angular relationship is modified by the presence of magmatic arcs that cause a thermal weakness within the intra-arc zone, which promotes an intra-arc fault system (Blanquat et al., 1998). The degree of deformation partitioning commands the dominant tectonic regime within the overriding plate. The tectonic regime controls the geometry and orientation fault-fracture network as well as the direction of the maximum permeability (Faulkner and Armitage, 2013; Sibson, 1996, 1985) (Fig. 1-2). In this context, the paleo-stress field, paleo-strain field, tectonic regime, paleo-fluid pathway and fluid condition during mineral precipitation can be recorded within a fault zone (Fig. 1-3) by fault-slip data and texture and geometry of veins, faults and hybrid faults at different scales (Fig. 1-4) (Bons et al., 2012). Thus, field observation and structural element analysis allow me to understand the architecture of permeability within a fault system (e.g. Connolly and Cosgrove, 1999; Wibberley and Shimamoto, 2003).

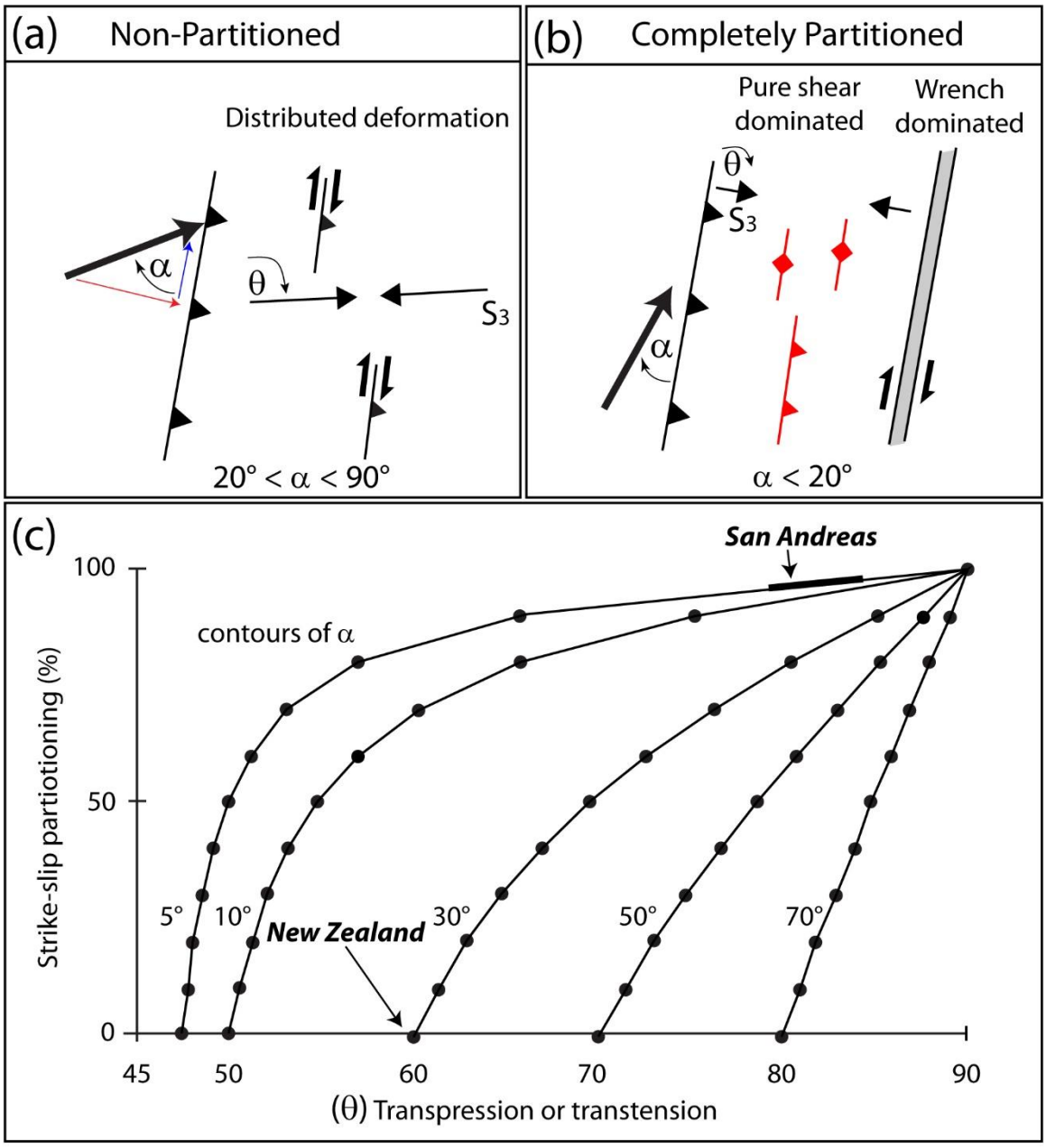

Figure 1-1. Plane view cartoons show the extreme cases from no-partitioned (a) to partitioned deformation (b) imposed by oblique convergence (Fossen et al., 1994; Teyssier et al., 1995; Teyssier and Tikoff, 1998). (c) Relation among angle of relative plate motion (α), orientation of minimum and maximum instantaneous shortening axis for transpression/transtension (θ) and degree of strike-slip partitioning. This graphic shows two examples: no strike-slip partitioning at New Zealand (α = 29°) and strike-slip partitioned at San Andreas fault system (α = 5°) (Teyssier et al., 1995).

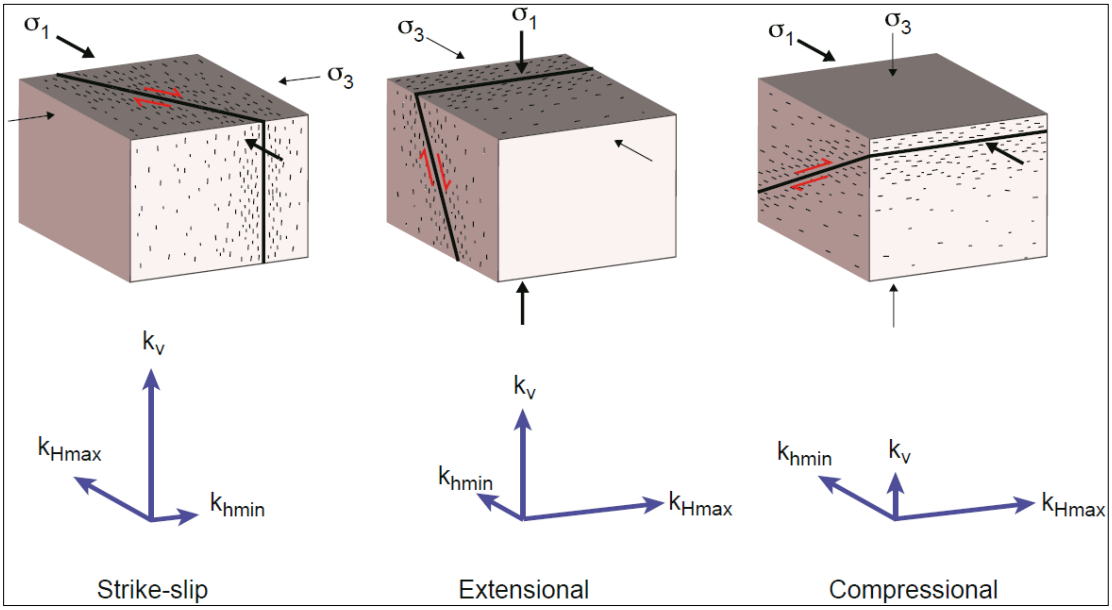

Figure 1-2. Cartoon showing the ideal orientation of crack networks surrounding planar faults in a strike-slip, extensional and compressional tectonic regime (Faulkner and Armitage, 2013). The bottom shows the likely orientation and relative magnitude of the principal axes of the permeability tensor for each tectonic regime (Faulkner and Armitage, 2013). σ_1, σ_2, σ_3 are the principal stress axes and k_v, k_{hmin}, k_{Hmax} are the vertical, horizontal maximum and minimum permeability, respectively.

Fractured zones within the upper crust are a potential high permeability pathway for geofluids (magma and hydrothermal fluid) migration. These fractured zones are spatially restricted to fault zones, especially into the damage zone (Fig. 1-3) (e.g. Caine et al., 1996; Faulkner et al., 2010; Ganerød et al., 2008).

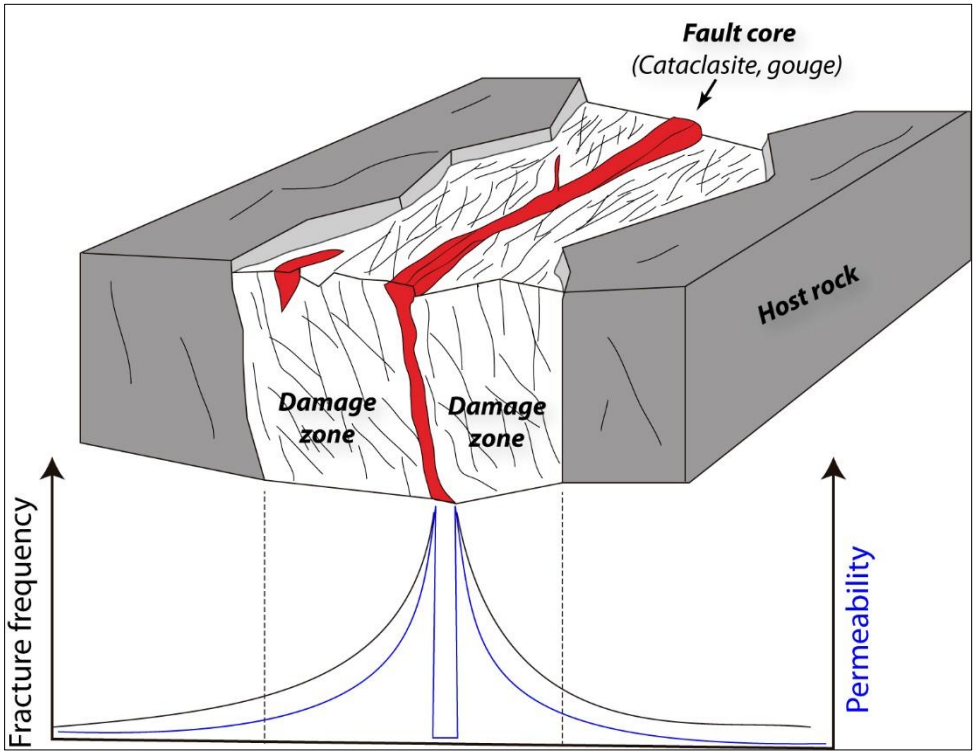

Figure 1-3. Cartoon showing the elements of a fault zone architecture: fault core, damage zone and their related fracture frequency and permeability (e.g. Faulkner et al., 2010; Ganerød et al., 2008).

Laboratory experiments show that micro-fractured crystalline rocks exhibit a permeability around three orders of magnitude higher than that of intact rocks on Etnean and Seljadur basalts (Benson et al., 2006b; Nara et al., 2011; Nasseri et al., 2009; Vinciguerra et al., 2005) and granite (Benson et al., 2006b; Pratt et al., 1977). Similarly, macro-fractures increase permeability of crystalline rocks around four orders of magnitude compared with intact rock (Nara et al., 2011).

The combination of field and experimental studies result in a strong analysis tool that can be used to understand the geological processes involved in the architecture development of fault zones. This gives us an overview to understand how fault zones have served as geofluid pathways.

The case of study of this work is located at the Chilean Southern Volcanic Zone (SVZ) (Fig. 1-4a). The SVZ (33°S-46°S) located in the southern Andes is a continuous volcanic arc segment 1400 km long, NS oriented. This segment include > 70 Pleistocene and Holocene composite stratovolcanoes and large volcanic fields, and at least 9 caldera complexes, as

well as hundreds of minor eruptive centers (Stern et al., 2007). The tectonic setting of the SVZ is characterized by the oblique convergence between the Nazca and South America plates, in addition to thermal weakening are the main driving mechanisms for the onset of the trench-parallel, intra-arc Liquiñe-Ofqui Fault System (LOFS). The LOFS crops out from the area around the Callaqui volcano until about 1200 km south near the Golfo de Penas area (Fig. 1-4a) (Beck, 1988; Blanquat et al., 1998; Cembrano et al., 2000, 1996). The LOFS shows complex crosscutting relationship with several NW-striking Andean Transvers Faults (ATF), which partially control the occurrence, spatial distribution, and geometry of major stratovolcanoes (Fig. 1-4a) (Cembrano and Lara, 2009; Lara et al., 2008; Melnick et al., 2006a; Sielfeld et al., 2016). Present-day activity of LOFS accommodates ca. 6.5 mm/yr of the margin-parallel component of oblique convergence leading to northward motion of the forearc, as recorded by GPS (Wang et al., 2007) and widespread crustal seismicity. Numerical models show that the LOFS accommodates dextral-reverse slip between 1 and 7 mm/yr during the interseismic period of subduction cycle; the ATF accommodate a maximum sinistral-reverse slip of 1.4 mm/yr (Stanton-Yonge et al., 2016). During the subduction cycle, the coseismic phase, the LOFS and ATF switch their kinematics: the LOFS becomes sinistral and the ATF normal-dextral (Stanton-Yonge et al., 2016). Both LOFS and ATF record shallow (<25 km) seismic activity (Haberland et al., 2006; Lange et al., 2008).

The study area is located at the northern termination of the LOFS between the Callaqui and Llaima volcanoes (Fig. 1-4b). The LOFS is defined by a series of major dextral NNE-striking master faults and dextral-normal NE-striking secondary faults. This spatial arrangement forms duplex and horsetail geometries (Fig. 1-4b). The ATF presents in this area is the sinistral, NW-striking Biobío-Alumine Fault System (BAFS) (Fig. 1-4a) (Melnick et al., 2006a; Muñoz et al., 1988; Rosenau et al., 2006). The BAFS, at regional scale, is represented by a rectilinear, NW-trending valley filled with Quaternary glacio-fluvial deposits. In the northern part of the study area, the LOFS master faults displace the BAFS in a dextral sense. At local scale, the LOFS and ATF have a complex crosscutting relationship, which are kinematically compatible as conjugate faults (Fig. 1-4b) (Rosenau et al., 2006).

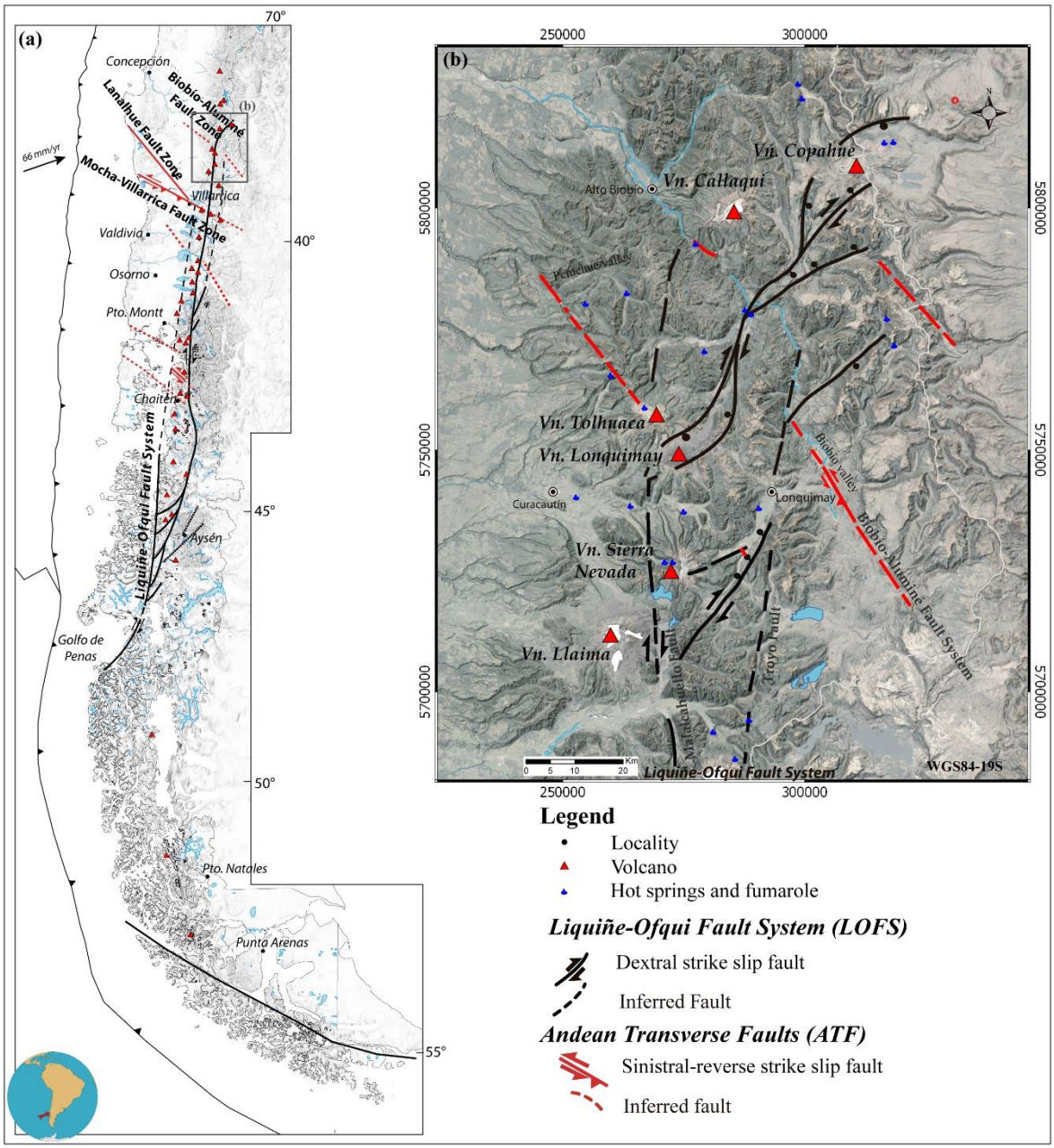

Figure 1-4. (a) Southern Volcanic Zone relief map showing the location and extent of the LOFS (black lines), ATF (red lines) and the study area location. Convergence velocity vector after Angermann et al. (1999) (b) Google Earth image showing the principal fault zones: LOFS (black lines) and ATF (red lines) and their special relationship with hot springs and volcanoes (Cembrano and Lara, 2009; Pérez-Flores et al., 2016; Sánchez et al., 2013; Sielfeld et al., 2016).

1.3 Hypothesis

The fault systems role in mineral precipitation and fluid flow depend on its geometry, kinematic and orientation with respect to the stress field orientation ($\sigma_1 \geq \sigma_2 \geq \sigma_3$). Thus, with a regional stress field with σ_1 NE-trending the NE-striking fractures are favorable to open and to promote the vertical fluid migration under hydrostatic pressure. While in the NNE-striking faults the dilatational jogs could be the pathway for fluid migration. The NW-striking faults are misoriented for reactivation/opening with respect to the regional stress field. These faults could allow the horizontal fluid flow under overpressure condition.

1.4 Research question and aims

The main goal of this thesis is to better understand the interplay between tectonic strain/stress fields and fluid migration in the upper crust, using the Southern Andean Volcanic Zone (SVZ) as a case study. The question arises as how deformation imposed by oblique convergence between the Nazca and South America plates is distributed along and across the overriding plate, and how the resulting geometry controls the hydrothermal and magmatic fluid migration (chapters 2 and 3). This study presents the first permeability measurements conducted on the main rock units of the SVZ, by simulating, in the laboratory, the fault-zone pressure conditions at different depths (chapter 4). Previous studies have attempted to answer some of these questions (Arancibia et al., 1999; Cembrano and Lara, 2009; Lavenu and Cembrano, 1999; Rosenau et al., 2006; Sánchez et al., 2013; Sielfeld et al., 2015; Tardani et al., 2016). However, most of these studies are focused at a regional scale and do not address the local variation within a fault zone, neither the quantitative permeability fluctuation in fractured rocks from the Southern Volcanic Zone.

1.5 Methodology

The methodology used to tackle the aims of this thesis includes fieldwork and laboratory experiments. The strategy used to unravel the fault architecture at the northern termination of the LOFS was defined using a combination of photo-interpretation on digital elevation models/Quickbird images (from Google Earth Pro), previous works (Melnick et al., 2006b; Rosenau et al., 2006; Suárez and Emparan, 1997; Thiele et al., 1987) and field studies both at the regional (1:50.000) and local (1:100) scales. The regional scale encompasses the area

from Callaqui to Llaima volcanoes (ca. 100 x 70 km) within the intra-arc zone of the SVZ (Fig. 1-4b). The local scale includes mapping at the outcrop and drill core mapping. The drill core (Tol-1) was available from the Tolhuaca Geothermal Field exploration phase located in the NW flank of the Tolhuaca volcano (Fig. 1-4b). The structural mapping at the outcrop (Fig. 1-5a) and drill core (Fig. 1-6) scales recorded the following: faults, veins, hybrid faults and hydrothermal breccia (Fig. 1-5 and 6). Collected structural data include description, measurement and logging of the geometry, sense of displacement, texture, mineralogy, and crosscutting relationship at the outcrop to thin section scales (from meters to micron scales). The sense of movement is defined by minor structures on the fault planes such as secondary fractures, mineral crystallization and tension cracks, among others (Fig. 1-6) (e.g. Petit, 1987).

Kinematic analysis of faults from the Tol-1 drill core required the paleomagnetic reorientation (see details in Chapter 3). The paleomagnetic analysis was conducted during a one month long internship contract between the GeoGlobal Energy LLC company and the Geoscience group of the Pontificia Universidad Católica de Chile that took place at the Petrofabrics and Paleomagnetics Laboratory of the University of Hawaii at Manoa (SOEST-HIGP) in 2013 (see details in Chapter 3).

Fault-slip data allows the calculation of the strain and stress fields at regional and local scales using the free software Multiple Inverse Method (MIM) (Yamaji, 2000) and Faultkin (Marrett and Allmendinger, 1990), respectively (see details in Chapter 2 and Chapter 3).

Permeability variations between an intact and fractured rock were recorded in laboratory experiments, simulating a rock located within and surrounded by a fault zone (Chapter 4). The experiments were completed during a 10-month long internship supported by CONICYT at the Rock and Ice Physics Laboratory, University College London, United Kingdom in 2014-2015. The experiments consisted of permeability measurements of representative lithologies from the intra-arc SVZ. The rock samples measured for each lithology consisted of intact rocks, micro-fractured rocks, macro-fractured rocks, and macro-fractured rocks with a series of offsets (see details in Chapter 4). In the following section I will describe the basic methodologies not detailed in the article chapters.

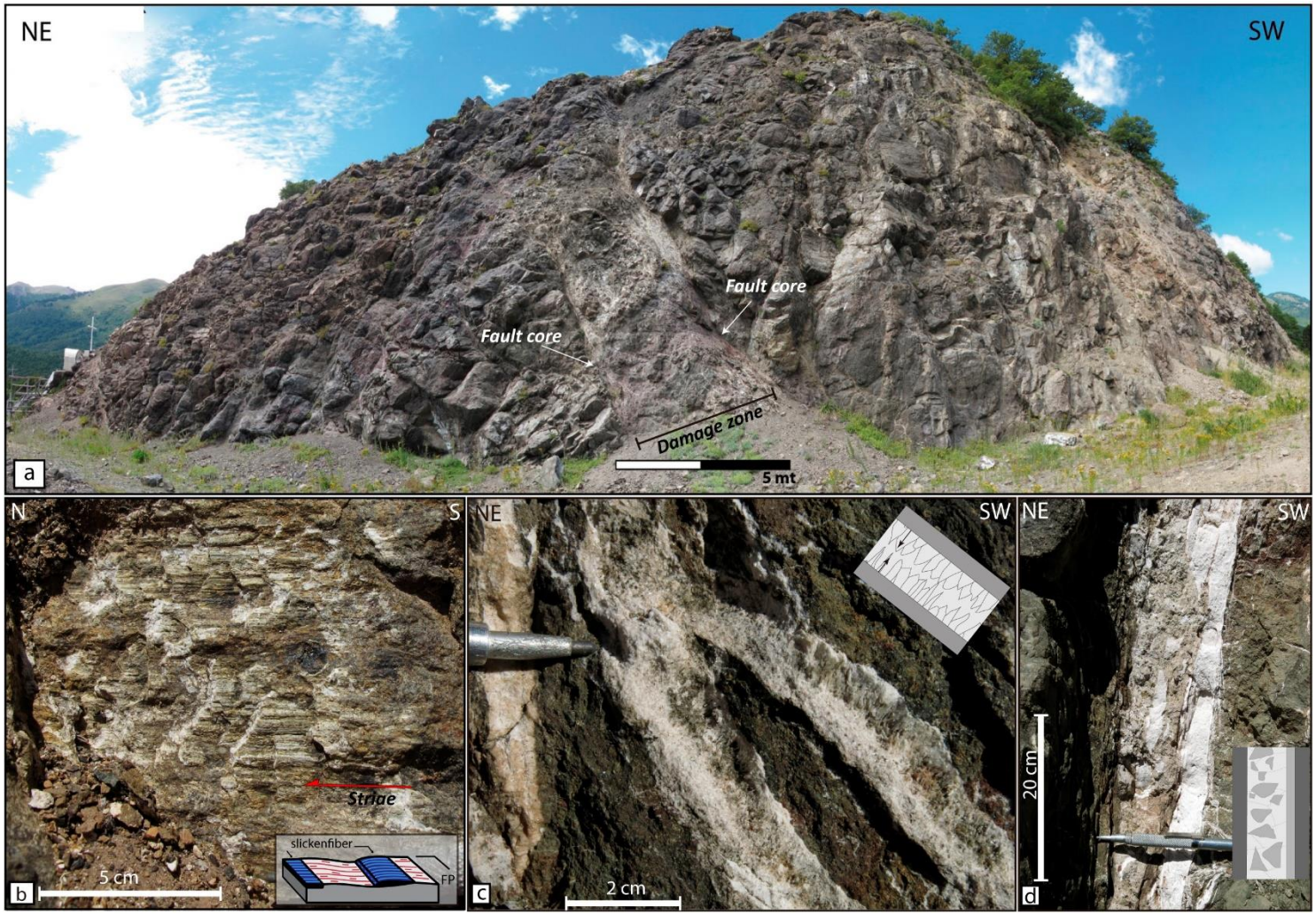

Figure 1-5. These photographs show an example of structural elements from structural sites at outcrop scale: (a) Fault zone with 2 m width fault core, (b) Right lateral fault plane with horizontal striae and calcite slickenfibers, (c) zeolite tensional veins with euhedral zeolite crystals perpendicular to veins wall (d) hydrothermal breccia veins consist of zeolite vein clasts in a gouge matrix. Clasts come from the original massive vein to the right.

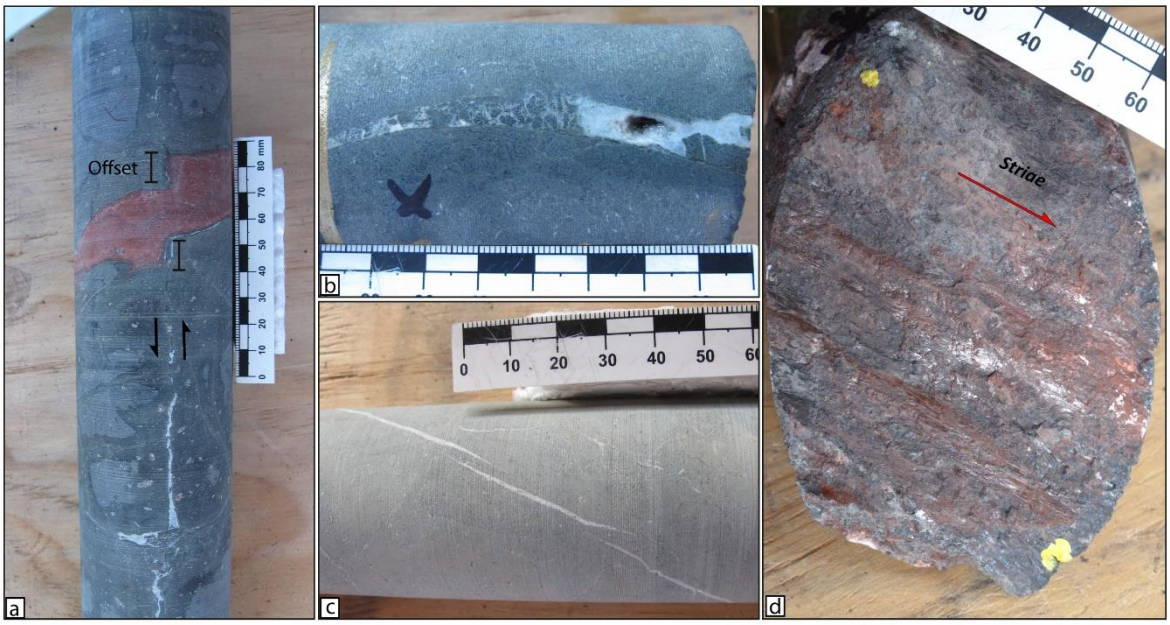

Figure 1-6. Structural elements identified in Tol-1 drill core mapping. (a) Iron-oxide veins crosscut and displaced by hybrid fault filled with calcite. (b) Calcite vein with hydrothermal breccia. (c) Zeolite vein and (d) Striated fault plane.

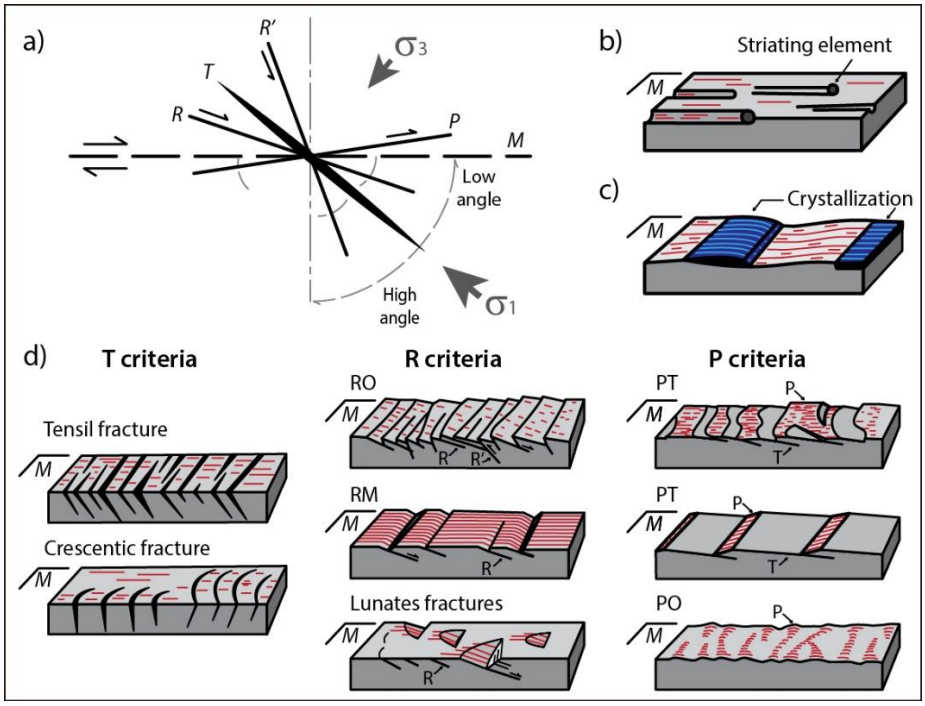

Figure 1-7. Criteria for the sense of displacement on fault surface in brittle rocks. (a) Terminology for description of elementary secondary fractures in a simple shear context. (b) Striation due to a ploughing element (asperity ploughing), (c) crystallization on the lee side of asperities (d) Main types of criteria based on repetitive secondary fractures (redrawn from Petit, 1987).

1.5.1 Fault slip inversion

The necessary fault-slip data to calculate strain and stress field include: fault plane geometry (strike and dip), slip direction (rake), displacement sense, local bedding orientation, average displacement and fault surface area (Fig. 1-8a) (Marrett and Allmendinger, 1990). The graphical reconstruction of fault-slip data allows to calculate the principal incremental shortening (P) and extension (T) axes. Each pair of axes lies in the movement plane containing the slip vector and the normal vector (fault pole) to the fault plane, and make angles of 45° with T and P vectors (Fig 8b and 8c). The kinematic axes of fault are a graphic representation convenient for geometric analysis (Marrett and Allmendinger, 1990). The main, or representative, orientations of both P and T axes for a given fault population are calculated if the data represents a uniform deformation field (spatially and temporally). In this case, the main P-and T-axes are calculated if these are clustered following a statistical Bingham distribution. Non-clustered P- and/or T-axes, indicate that the fault data population is the result of kinematically heterogeneous faulting, represented by girdle or multi-modal patterns of shortening and/or extension axes. Kinematic heterogeneity can arise from several causes, such as triaxial deformation, anisotropy reactivation, strain compatibility constraints and/or polyphasic deformations (Marrett and Allmendinger, 1990).

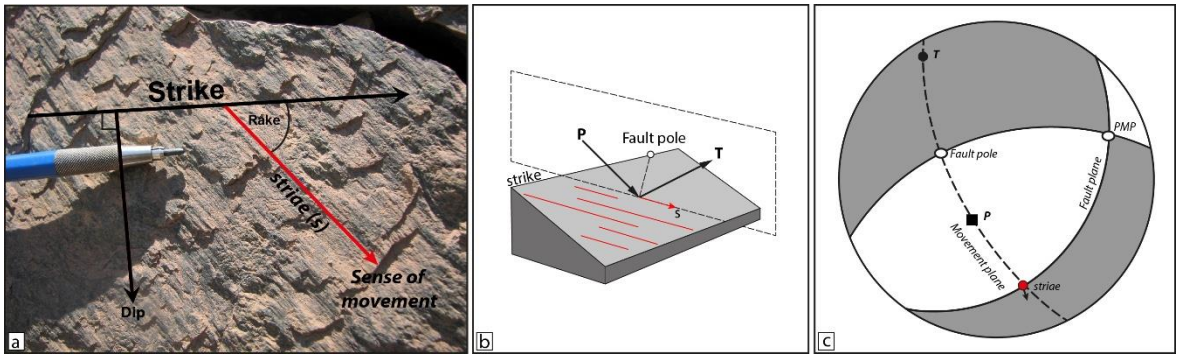

Figure 1-8. (a) Scheme shows the fault-slip data used for the strain and stress analysis (Veloso et al., 2015). The diagram (b) and lower-hemisphere, equal area stereographic projection (c) show the fault plane perpendicular to a common plane (movement plane) that contain kinematic axes, slip direction and fault pole, with P and T axes forming angles of 45° with both the slip direction, the fault pole (P) and the pole of movement plane (Marrett and Allmendinger, 1990).

Stress analysis is based on a geometrical criterion being a modification of the classic inverse technique of Angelier (1984). The method can calculate and sort the orientation of the principal stress axes derived from a heterogeneous fault-slip data set by generating a combinatorial (Eq. 1) number of groups containing each *k*-number of fault-slip data elements extracted from the whole data set (Yamaji et al., 2005). Then it applies Angelier's (1984) inverse technique to these randomly generated subsets.

$$C = \frac{N!}{k!(N-k)!} \quad \text{(Eq. 1)}$$

The orientations of the calculated stress axes for each generated group of k-number fault-slip data are plotted onto separate stereograms: one for σ_1 axes and another for σ_3 axes sub-solutions (Fig. 1-9) (Otsubo et al., 2006; Yamaji, 2000). Each sub-solution is represented as a tadpole indicating the orientation of one of the principal axis with an attached 'tail' pointing towards the orientation of the complementary principal axis (*i.e.*, σ_1's tadpole points toward the orientation of σ_3 and vice versa) (Fig. 1-9). This symbol is, additionally, color-coded per the calculated stress ratio ($\varphi = (\sigma_2-\sigma_3)/(\sigma_1-\sigma_3)$). Thus, groups of tadpoles with similar colors and similar orientations of their tails indicate a compatible stress field solution (Fig. 1-9) (Federico et al., 2010; Otsubo et al., 2006; Veloso et al., 2015, 2009; Yamaji, 2000). The distribution of φ-values is therefore used to establish a φ-value range for the principal stress axes solution. In the case where φ-histograms show a bimodal distribution, it is calculated one field stress solution for each range of representative φ-values. Thus, for the field stress obtained, the misfit angle or difference between observed and theoretical slip direction obtained from an assumed stress state is calculated. The stress axes orientation solution is calibrated by choosing the solution with the largest number of activated faults with misfit angles of less than 30°. Thus, the tectonic regime is defined by the principal stress axes orientation as extensional, compressional or strike-slip (Ritz, 1994). The strike-slip regime could be either transpressional or transtensional regimen depending of stress ratio value (φ). A $\varphi > 0.55$ represent transtensional tectonic regime, $\varphi < 0.45$ represent transpressional tectonic regime and $0.45 < \varphi < 0.55$ represent a simple shear dominated strike-slip tectonic regime (see detailed discussion about φ-value interpretation at Bellier and Zoback, 1995; Siame and Bellier, 2005).

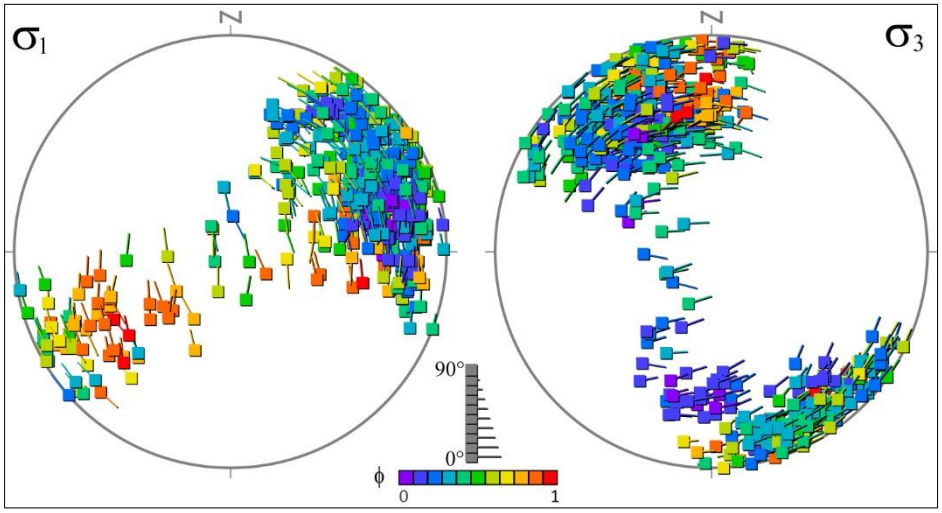

Figure 1-9. Stereograms show σ_1 axes and σ_3 axes sub-solutions, the φ value represented by color coded (from 0 to 1) and the plunge of stress axes denoted by length of the tails of tadpole symbols (Yamaji, 2000).

1.6 Results

The architecture of northern termination of the LOFS consists of three fault sets (Chapter 2, Fig. 1-12). (1) NNE-striking subvertical master faults (first order), (2) NE-striking, steeply-dipping splay faults (second order) and (3) ENE to EW-striking, steeply to moderately dipping local faults (third order). This fault system cuts and displaces the NW-striking faults (ATF) at regional scale. At local scale, NW-striking faults are kinematically compatible with the LOFS.

First-order faults, tens of km-long, are represented by two subparallel faults: Malalcahuello and Troyo faults, as well as by four synthetic NNE-striking faults in the northern area (Chapter 2, Fig. 1-12). These faults record right lateral strike-slip and dextral reverse oblique-slip at different fault planes. The NE-striking faults are m- to km-long and mainly splay off from master faults or locally connect them. They consist of m-scale single fault cores with asymmetric fault zones recording dextral-normal slip and dextral slip that locally cut and connect some of the NNE-striking master faults. The third-order faults-fractures consist of cm-scale, sinistral-reverse faults spatially and genetically connected with the second order faults. The NW-striking faults record sinistral reverse and normal slip on the same fault planes. These fault zones are formed by thick damage zones and multiple fault

cores that host thicker and more pervasive NW-striking veins and hydrothermal breccia bodies than the LOFS (Chapter 3, Figs. 12; 16, Las Animas structural site)

The entire fault-slip data analysis allows to define the strain and stress field at regional scale. The strain analysis shows that individual (single fault datum) P and T axes are widely distributed, without forming well-defined clusters. This suggests that the analyzed fault-slip data population carries kinematically heterogeneous information about the faulting mechanism and evolution of the intra-arc zone. The regional stress analysis shows two stress field solutions with bimodal φ-histogram distribution with modes at 0.4-0.5 and at 0.9 (Chapter 2, Fig. 1-17). The best solution records a transpressional strike-slip stress field (φ = 0.38) with N64E-trending subhorizontal σ_1 axis and a N30W-trending subhorizontal σ_3 (Chapter 2, Fig. 1-17). The secondary solution reveals a transtensional strike-slip field (φ = 0.9) has an EW-trending subhorizontal σ_1 and NS-trending subhorizontal σ_3 axes (Chapter 2, Fig. 1-17). The heterogeneous fault population is evaluated by integrating the results of kinematic and dynamic fault-slip analyses from each fault zones orientation. Thus, the NNE-striking faults reveal a homogeneous deformation with NW-trending stretching and NE-trending shortening with plane- to flattening-strain ellipsoid. Similarly, stress axes solution shows a strike-slip tectonic regime (φ=~0.50) with a subhorizontal NE-trending σ_1 and NW-trending σ_3 axes. The NE-striking faults show a preferential clustering of T-axes on a NNW-trending direction and a wide distribution of P-axes with plane-strain ellipsoid. This kinematically heterogeneous faulting could be attributed to strain compatibility (Marrett and Allmendinger, 1990) between two fault sets, with slip parallel to fault intersection (Las Raices structural site, Chapter 2, Fig. 1-16). The stress analysis indicates a transpressional regime (φ =0.20) with an ENE-trending σ_1 and subhorizontal NNW-trending σ_3. The local stress field analysis at the Tolhuaca Geothermal Field drill core (Tol-1) shows a tensional regime with horizontal, NS-striking σ_1 and vertical σ_3 axes, which is representative for the Tolhuaca and Lonquimay volcanic complex (Chapter 3. Fig. 3-2).

The ATF, represented by Las Animas structural site (Chapter 2, Fig. 1-16), shows a widely-scattered distribution of both P- and T-axes, suggesting a polyphasic deformation and/or a pre-existing anisotropy reactivation. Similarly, stress analysis shows two distinctive stress axes solutions. The obtained strike-slip and tensional local stress fields share a common

subhorizontal, N-trending σ_3 axes, but the minimum and intermediate stresses switch position, defining one strong solution with a subhorizontal, ESE-trending σ_1 in a strike-slip regime (φ =0.6), and a secondary solution with a moderately plunging, WSW-trending σ_1 in a transtensional regime (φ =0.9).

The transpressional strike-slip regime (N60E-striking σ_1 and N30W-striking σ_3 axes) recorded in the intra-arc domain favors vertical magma/hydrothermal fluid migration (e.g. Brogi, 2011; Faulkner and Armitage, 2013; Sibson, 1994). The regional σ_1 orientation is parallel to volcanic feeder dikes (Lonquimay, Llaima and Callaqui volcanoes), NE-elongation of stratovolcanoes and the NE- tending flanks vents alignment (Chapter 2, Fig. 1-11). The paleo-fluid distribution at the first order fault zones occur within a main fault plane forming slickenfibers, cm- to mm-width, NE-striking veins genetically associated with multiple reactivations and cm-long, dilatational jogs formed between NNE- and NE- striking faults. The second order faults host metric dikes, which are cut by cm- to mm-width, ENE-striking tensional, zeolite veins genetically associated with second order faults. The NE-striking fault zone where the Tolhuaca and Lonquimay volcanic complex is emplaced documents the magma pathway role of these structures recorded by the NE-alignment of volcanic vents and volcanic fissures (Chapter 3, Fig. 3-2). The third order structures of the LOFS are mainly represented by EW-striking tensional veins filled with zeolite and calcite, hybrid faults and hydrothermal breccia at the outcrop scale, which are compatible with the local stress field produced by second order faults. The NW-striking faults are genetically associated with massive mineral precipitation, recorded by wide zone of hydrothermal breccia and dense zeolite-calcite veins network. Despite the fact that these NW-striking faults are kinematically compatible with the stress field, they have an unfavorable orientation for faulting and therefore, are likely to require high fluid-pore pressure to rupture (e.g. Sibson, 2004). The NW-striking faults are not only suitable for magma and/or hydrothermal migration but also for transient fluid storage.

The architecture of the northern termination of LOFS promotes the vertical hydrothermal/magma migration through faults and fractures primarily of NE-striking and secondary of ENE-striking, whereas the massive mineral precipitation and fluid/magma storage occur within NW-striking fault zones.

The lithologies that host these fault zones exhibit permeability between 10^{-20} to 10^{-18} m^2, where the crystalline tuff and granodiorite record the lowest and highest values, respectively. In the mated macro-fractured samples, permeability increases between 4 to 6 orders of magnitude with respect to intact sample under 5 MPa of effective pressure (confining pressure less fluid pressure). The macro-fractured samples permeability decrease quickly with increasing effective pressure, especially in the andesitic dike lithology. In the case of micro-fractured samples, permeability increases between 2 to 4 orders of magnitude with respect to intact samples, which remains at highest effective pressure 60 MPa. The unmated macro-fractured samples (with offset) increase the permeability around 1 order of magnitude with respect to mated macro-fractured samples (without offset) under 5 MPa effective pressure. This permeability difference increases between 2 and 3 orders of magnitude under high effective pressure 60 MPa, which reveals that the offset (fault-slip) help to remains the fracture open at depth. The unmated macro-fractured samples permeability show oscillations with increasing offset. This permeability oscillations are different for each lithology and have a close correlation with the fracture roughness (see details in the Chapter 4).

1.7 Concluding remarks

A complete analysis of the structural elements and rock permeability of the intra-arc domain of the northern termination of the LOFS between 38°S and 39°S was performed. These analyses record the control that the regional and local stress fields exert on magma/fluid transport and arrest (Chapter 2 and 3), supported by the permeability potential of fractured rocks from SVZ (Chapter 4). The main conclusions of this thesis are summarized as follows:

1- Deformation driven by oblique convergence is partially partitioned into each morphotectonic domain: subduction zone, forearc and intra-arc. At intra-arc domain, the tectonic regime corresponds to a strike-slip-dominated transpression (Fig. 2-10).

2- The regional stress field at the intra-arc region is the result of two independent and homogeneous stress fields. The prevailing stress field solution corresponds to a transpressional stress regime with a subhorizontal, N64E-trending σ_1 axis and a subhorizontal, N30W-trending, σ_3 axis. The second stress field is a transtensional stress regime with a subhorizontal, N88E-trending σ_1 axis and a subhorizontal N05W-trending σ_3 axis (Fig. 2-8).

3- Deformation is also further partitioned within the intra-arc domain by faults with NNE-, NE-, ENE- and NW-strikes. Features of these faults are (Fig. 2-11):

   a. The NNE-striking faults show either right lateral strike-slip or dextral-reverse displacement, accommodating part of the trench-parallel and trench-orthogonal shortening components.

   b. The NE-striking fault zones are mostly hybrid faults with dextral-normal displacements. The associated local stress regime is clockwise-rotated with respect to the regional solution, thus favoring the emplacement of ENE-striking veins and dikes. At the intersection between NE- and NNE-striking faults, the stress regime is nearly compressive. Locally, the tensional stress field at the Tolhuaca area can be explained as a switch between σ_1 and σ_2 main stress axes as driven by local extension at the Lonquimay releasing bend structure within the LOFS and/or locally low lithospheric pressure at the Tol-1 core depth (1020 m).

   c. The NW-striking faults document two different kinematic and dynamic behaviors. One of them is compatible with the regional stress field and accommodates the orthogonal to the trench-shortening component. The second stress field solution is decoupled from the prevailing regional stress field and has a stronger long-term deformation imprint at the outcrop scale.

4- The NNE-striking master faults constitutes a localized fluid/magma pathway, which focus the emplacement of syntectonic dike intrusions and the distribution of arrested paleo-fluids mainly at dilational jogs. The NE-striking fault-fractures host dikes and volcanic vents at kilometric scale, according with tensional fractures activated by the regional stress field. These structural elements constitute pathways for magma and hydrothermal fluid migration. The local stress field variation has a strong control on the vein systems and dikes orientation at outcrop scale (Fig. 1-11).

5- ATF fault zones may constitute a large hydrothermal fluid reservoir with wide fault zones and a strongly developed fault-fracture network spatially associated with mineral precipitation (Fig. 1-11).

6- The basement intrusive rock is a good lithology for hydrothermal fluid storage with the highest permeability for intact rock (10^{-18}). At the damage zones, small (mm) fault-slip can increase the permeability up to 6 orders of magnitude, which decreases around 1 km depth. The micro-fractures remain open with high permeability at depth. Crystalline tuff and andesitic dike may constitute hydrothermal fluid barriers recording the lowest permeability for intact rock (10^{-20}).

7- Field observations and structural analysis support a strong interplay between stress field, fault-fracture orientation and magma/paleofluid distribution. The fault-fracture networks favorably oriented for reactivation with respect to the regional stress field constitute well-defined vertical pathways for magma/fluid transport through the lithosphere (Fig. 1-11). These structures define restricted damage zones and local hydrothermal veins systems. Conversely, fault-fracture systems misoriented with respect to the regional stress field exhibit larger damage zones and widely distributed hydrothermal veins and breccia veins. These, combined with a permeable lithology layer, might act as efficient reservoir for magma and/or hydrothermal fluids (Fig. 1-11).

8- Permeability experiments document that mated macro-fractures can maintain convective/advective flow regime ($k \geq 10^{-16}$ m^2), typical of active geothermal systems, up to a critical effective pressure, varying for each lithology (Fig. 4-8). In the case of granodiorite, the convective/advective flow is kept up to P_{eff} = 40 MPa, beyond which fault slip is required to maintain it. The World Stress Map Database (Zang et al., 2012) allows calculating the approximate effective pressure for any given depth under different stress field regimes (Fig. 1-10). Thus, σ_1 minus the hydrostatic pressure at any given depth corresponds to effective σ_1 (σ'_1) for each stress regime, which in turn is the effective pressure used in the laboratory. The calculated depth for the convective/advective limit at P_{eff} = 40 MPa, varies depending on the stress regimes: 800 m for reverse, 1600 m for strike-slip and 2400 m for normal stress regime (Fig. 1-10). These results, schematically represented in Fig. 1-11, indicate the most suitable structural domains to promote advective/convective

flow within a fault system as a function of the predominant local stress field and spatially associated rock units.

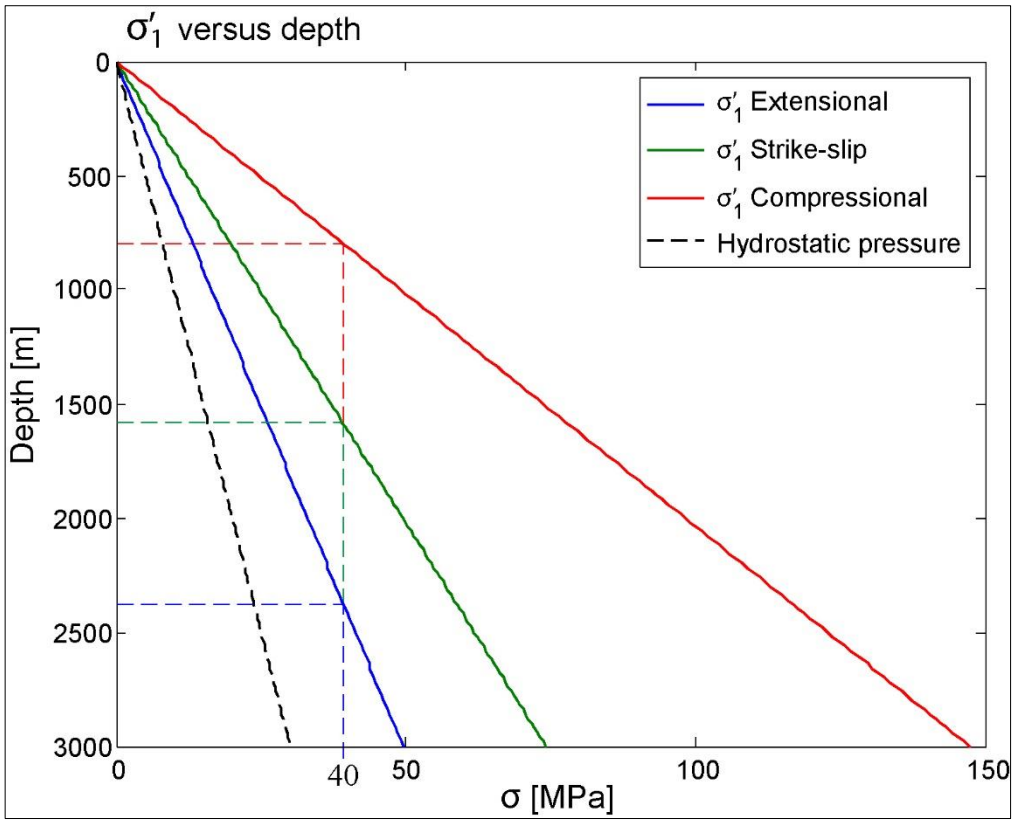

Figure 1-10. Effective σ_1 (σ_1 minus hydrostatic pressure) at different depths for each stress field regime (Zang et al., 2012). Dashed lines show the depth at which each stress regime reaches a maximum effective principal stress of 40 MPa.

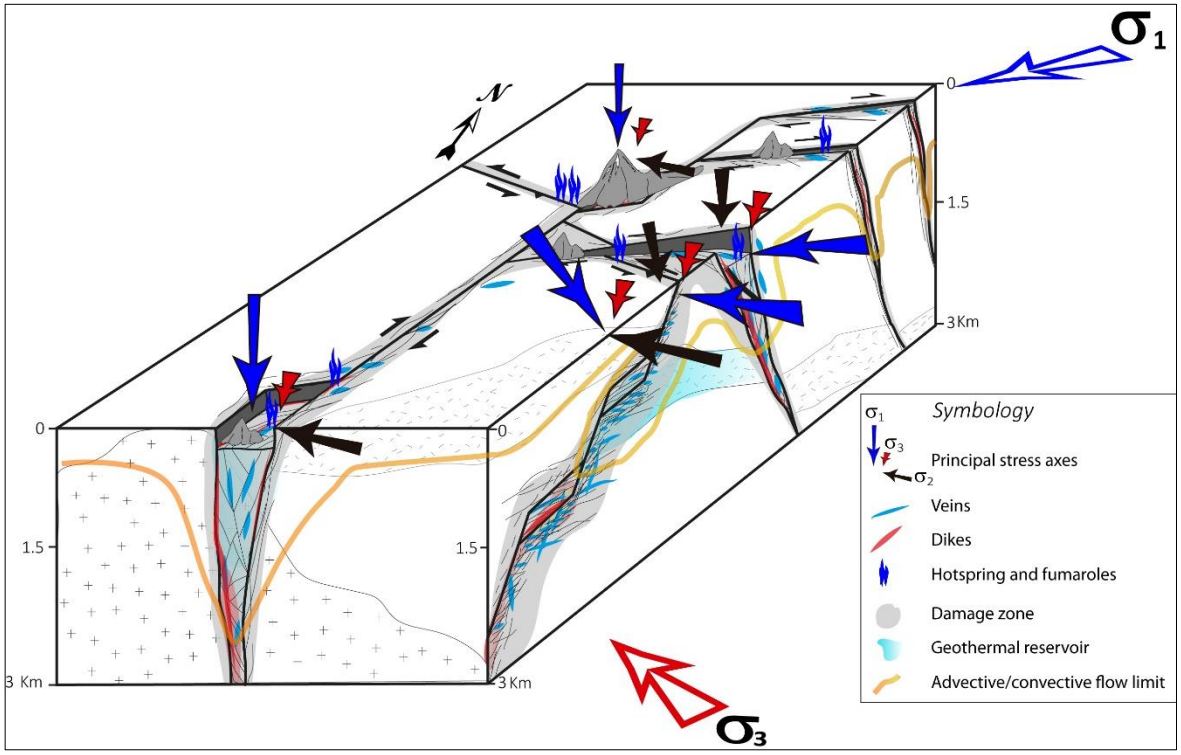

Figure 1-11. Block diagram showing the main geologic features of the NNE-, NE- and NW-striking structural domains along with their local stress field, inferred fluid migration paths, potential storage regions and depth limit for advective/convective flow.

1.8 Future work

The results of this thesis provide a geological-structural model that can help constraining hydrothermal fluid/magma pathways and storage areas. These results, supported by permeability experimental data, may provide key boundary conditions to generate numerical simulations yielding an improved 3D permeability model for the northern termination of the LOFS. This 3D model could also be tested through geophysical experiments to improve the knowledge of fault geometry at depth. Finally, an important pending issue is to better constrain the timing of deformation by obtaining new absolute ages of rock units such as Mio-Pliocene dikes and hydrothermal synkinematic minerals (e.g. calcite and zeolite veins and slickenfibers).

1.9 Publication and abstract resulting from this research

1.9.1 Publications

Pérez-Flores, P., Cembrano, J., Sánchez-Alfaro, P., Veloso, A., Arancibia, G., Roquer, T., 2016: Tectonics, magmatism and paleo-fluid distribution in a strike-slip setting: Insights from the northern termination of the Liquiñe-Ofqui fault System, Chile, Tectonophysics (2016), doi:10.1016/j.tecto.2016.05.016. **Chapter 2.**

Pérez-Flores, P., Veloso, E., Cembrano, J., Sánchez-Alfaro, P., Lizama, M., Arancibia, G., 2017. Fracture network, fluid pathways and paleostress at the Tolhuaca geothermal field. J. Struct. Geol. 96. doi:10.1016/j.jsg.2017.01.009. **Chapter 3**.

Pérez-Flores, P., Wang, G., Mitchell, T. M., Meredith, P. G., Nara, Y., Sarkar, V., Cembrano, J. The effect of offset on fracture permeability of rocks from the Andean Southern Volcanic Zone, Chile. Submitted to Journal Structural Geology. **Chapter 4.**

1.9.2 Conference abstracts

Pérez-Flores, P. and Cembrano, J. Paleo-esfuerzo y permeabilidad cortical en un sistema de falla de rumbo: registro en la terminación norte del Sistema de Falla Liquiñe-Ofqui. Simposio de Tectónica Sudamericano, 2016, Santiago, Chile.

Perez-Flores, P., Cembrano, J., Sánchez-Alfaro, P. Local Stress fields and paleo-fluid distribution within a transtensional duplex: An example from the northern termination of the Liquiñe-Ofqui Fault System. 2015. Tectonic Session Group (TSG), European Geosciences Union, Edinburgh, United Kingdom.

Pérez-Flores, P. Sarkarc, V., Mitchell, T., Meredith, PG & Nara, Y. Effect of offset on fracture permeability in basalt. 2014. Low Permeability Meeting. Permeability workshop. Paris, France.

Perez-Flores, P., Cembrano, J., Sanchez-Alfaro, P. Local Stress fields and paleo-fluid distribution within a transtensional duplex: An example from the northern termination of the Liquiñe-Ofqui Fault System. 2014. AGU fall Meeting San Francisco, EE.UU.

Perez-Flores P, Eugenio E Veloso, Cembrano P., Sánchez P., 2013. Paleomagnetic Reorientation of Structural Elements in Drill Cores: an example from Tolhuaca Geothermal Field. AGU fall Meeting, San Francisco, EE.UU.

Perez-Flores P, Sánchez P, Sielfeld G., Cembrano P. 2013. Tectonics, magmatism and fluid flow in a transtensional strike-slip setting: The northern termination of the dextral strike-slip Liquiñe-Ofqui fault System, Chile. AGU Meeting of Americas, Mexico.

Perez-Flores P., Marquardt M., Cembrano, J., Perez A. 2012. Modelo geológico-estructural de un depósito IOCG en el Segmento El Salado, Sistema de Falla de Atacama: Mina Filipina. XII Congreso Geológico de Chile, Antofagasta, Chile.

Perez-Flores P., Sánchez P., Arancibia G., Cembrano J., Veloso E., Lohmar S., Stimac J., Reich M., Rubilar J. 2012. Sampling and detailed structural mapping of veins, fault-veins and faults from Tolhuaca Geothermal System, Southern Chile. XII Congreso Geológico de Chile, Antofagasta, Chile.

1.10 Publication and abstract resulting from side-projects

1.10.1 Publications

Mitchell, T. M., Cembrano, J., Fujita, K., Hoshino, K., Faulkner, D. R., **Pérez-Flores, P**., Arancibia, G., Rempe, M., Gomila, R., (in press). Fluid inclusion evidence of co-seismic fluid Flow induced by Dynamic rupture. AGU Books

Sanchez-Alfaro, P., Reich, M., Arancibia, G., **Pérez-Flores, P**., Cembrano, J., Driesner, T., Lizama, M., Rowland, J., Morata, D., Heinrich, C., C.A., Tardani, D., Campos, E., 2016. Physical, chemical and mineralogical evolution of the Tolhuaca geothermal system, southern Andes, Chile: Insights into the interplay between hydrothermal alteration and brittle

deformation. J. Volcanol. Geotherm. Res. 324, 88–104. doi: 10.1016/j.jvolgeores. 2016.05.009.

Tardani, D., Reich, M., Roulleau, E., Takahata, N., Sano, Y., **Pérez-Flores, P**., Sánchez, P., Cembrano, J., Arancibia, G., 2016. Exploring the structural controls on helium, nitrogen and carbon isotope signatures in hydrothermal fluids along an intra-arc fault system. Geochim. Cosmochim. Acta. doi:http://dx.doi.org/10.1016/j.gca.2016.04.031

Sanchez-Alfaro, P., Reich, M., Driesner, T., Cembrano, J., Arancibia, G., **Pérez-Flores, P**., Heinrich, C., Rowland, J., Tardani, D., Lange, D., Campos, E., 2016. The optimal windows for seismically-enhanced gold precipitation in the epithermal environment, Ore Geology Reviews, doi: 10.1016/j.oregeorev.2016.06.005

Sánchez, P., **Pérez-Flores, P**., Arancibia, G., Cembrano, J., Reich, M., 2013. Crustal deformation effects on the chemical evolution of geothermal systems: the intra-arc Liquiñe–Ofqui fault system, Southern Andes, International Geology Review, DOI:10.1080/00206814.2013.

1.10.2 Conference abstracts

Del Valle, F., Marquardt, C., **Pérez-Flores, P**., Gomila, R., Aron, F., Estay, N. P.; Cembrano, J., Yáñez, G., Lira, E. Neotectónica de la Falla Laguna Verde y su potencial sismogénico, Región de Valparaíso, Chile. 2016. Simposio de Tectónica Sudamericano, Santiago, Chile.

Meulle-Stef, M., **Pérez-Flores, P**., Tassara, A. Régimen de esfuerzo y modelo estructural para el complejo volcánico Nevados de Chillán, Chile. 2016. Simposio de Tectónica Sudamericano, Santiago, Chile.

Sanchez-Alfaro, P., **Pérez-Flores, P**., Tardani, D., Reich, M., Arancibia, G., Cembrano, J. Crustal Deformation Effects on the Chemical Evolution of Geothermal Systems: Case

Studies from Southern Andes. World Geothermal Congress, April 19-24 2015, Melbourne Australia.

Roquer, T., Terrón, E., **Perez-Flores, P**., Arancibia, G., Cembrano, J. Fault Zone Architecture and Mineralogy: Implications in Fluid Flow and Permeability in Crustal Scale Fault Zones in the Southern Andes. 2014. AGU fall Meeting San Francisco, EE.UU.

Fujita, K., Mitchell, T. M., Cembrano, J., Hoshino, K., **Perez-Flores, P**., Faulkner, D., Arancibia, G., Gomila, R., Rempe, M. Fluid inclusion evidence of post-seismic fluid flow induced by dynamic rupture. 2014. Abstract T23E-2644. AGU fall Meeting San Francisco, EE.UU.

Sanchez-Alfaro, P., Driesner T., Heinrich C., Reich M., **Perez-Flores P.**, Arancibia G., Cembrano J., Campos, E., Lohmar, S. Fluid evolution in an Andean geothermal system: coupling fluid inclusions thermometry, LA-ICP-MS and geochemical modeling. 2014. Pan-American Current Research on Fluid Inclusions (PACROFI-XII), Denver, USA, June 2–5.

Sánchez P., **Pérez-Flores P**, Reich M., Arancibia G., Cembrano J., Campos E., 2013. The influence of fault-fracture network activity on fluid geochemistry and mineral precipitation at the Tolhuaca geothermal system, southern Chile. Goldschmidt, Florence, Italy.

Sánchez P., **Pérez-Flores P**., Reich M., Arancibia G., Cembrano J. 2013. The interplay between fault-fracture networks activity, fluid flow and mineralization in the Andes: A case study in the Tolhuaca geothermal system, southern Chile. AGU Meeting of Americas, Mexico.

Cembrano, J., **Pérez-Flores P.**, Sánchez, P., Sielfeld, G. 2013. Tectonics, magmatism, and fluid flow in a transtensional strike-slip setting: The northern termination of the Liquiñe-Ofqui fault System, Chile. AGU fall Meeting San Francisco, EE.UU.

Tardani, D., Sanchez, P., **Pérez-Flores**, **P**., Reich, M., Tassi, F., Capaccioni, B., Chiodini, G., Vaselli, O. 2013, Geochemistry of geothermal fluids in the active Liquiñe-Ofqui Fault System (Southern Andes Volcanic Zone, Chile). IAVCEI 2013 Scientific Assembly.

Fujita, K., Mitchell, T. M., Cembrano, J., Hoshino, K., **Perez-Flores**, P., Faulkner, D., Arancibia, G., Gomila, R., Rempe, M. Fluid inclusion evidence of post-seismic fluid flow induced by dynamic rupture. AGU fall Meeting San Francisco, EE.UU.

Reich M, Arancibia G., **Perez-Flores P**., Sánchez P., Cembrano, J., Silke L., Stimac J. 2012. The Feedback active tectonics, fluid flow and mineralization in an Andean geothermal reservoir a case study from the Tolhuaca system, southern Chile. AGU fall Meeting, San Francisco, EE.UU.

2 TECTONICS, MAGMATISM, AND PALEO-FLUID DISTRIBUTION IN A STRIKE-SLIP SETTING: INSIGHTS FROM THE NORTHERN TERMINATION OF THE LIQUIÑE-OFQUI FAULT SYSTEM, CHILE

2.1 Introduction

Bulk transpressional deformation is expected at continental margins where oblique convergence dominates (e.g. Dewey et al., 1998; Fossen and Tikoff, 1998; Sanderson and Marchini, 1984). Kinematic models show that transpressional deformation resulting from oblique convergence is accommodated by distinctive structural styles along and across the overriding plate (Dewey et al., 1998; Federico et al., 2010; Fitch, 1972; Veloso et al., 2015). Strain in transpressional regimes can be partitioned into strike-slip and shortening components, depending mostly on the angle between the plate motion vector and the trench (convergence angle, α) and on the thermal constraints (Blanquat et al., 1998; e.g. Fossen et al., 1994; Teyssier et al., 1995; Tikoff and Greene, 1997). Large convergence angles ($20° < \alpha < 90°$) favor a pure-shear-dominated transpression with no strike-slip partitioning as is observed at Australian-Pacific plate boundary in New Zealand (e.g. Jarrard, 1986; Mccaffrey, 1992; Teyssier et al., 1995). In contrast, a low convergence angle ($\alpha \leq 20°$) favors a strike-slip partitioned system, as in the case of wrench-dominated transpression at the Pacific–North America plate boundary of the western US, where the San Andreas Fault takes up most of the simple shear component (Teyssier et al., 1995; e.g. Teyssier and Tikoff, 1998). The requirement of low angle of plate convergence is not applicable to magmatic arcs, where thermally weak intra-arc shear zones can accommodate a significant part of the bulk transpressional deformation by developing a trench-parallel fault system (Blanquat et al., 1998). Such intra-arc fault systems help to enhance crustal permeability as they host fault-fracture networks suitable for geothermal reservoirs, hydrothermal mineralization and/or volcanic activity (e.g. Caine et al., 1996; Cox, 1999; Micklethwaite and Cox, 2004; Rowland and Sibson, 2004; Sibson, 1994). During fault rupture, propagation of individual faults may develop an associated damage zone where discontinuous fracturing, dilatant sites and minor shear dominate and provide suitable places for storage of fluid-related materials (Connolly and Cosgrove, 1999; Sibson, 1996; Zhang et al., 2008). As such, faults-fracture

systems are potential fluid pathways in the crust, which is otherwise relatively impermeable (e.g. Connolly and Cosgrove, 1999; Faulkner et al., 2010).

Numerical models, mechanical experiments and field observations reveal that damage zones enhance rock permeability acting as a conduits for hydrothermal fluid flow and magma migration (Cox, 1999; Curewitz and Karson, 1997; Gudmundsson et al., 2001; Mitchell and Faulkner, 2012; Sheldon and Micklethwaite, 2007; Zhang et al., 2008). In hydrothermal systems, episodic mineral precipitation seals both the intrinsic permeability related to the primary rock porosity as well as that related to fracture networks (Cox, 2010). Therefore, repeated reactivation of the fault-fracture network is required to maintain the permeability within the fracture controlled hydrothermal systems. Moreover, reactivation of pre-existing fault and opening of extension fracture networks or hybrid extensional–shear fractures (permeability regeneration) depends mainly on depth, rock mechanical properties, pore fluid pressure and the orientation of faults with respect to the maximum principal stress axis (Cox, 2010; Faulkner and Armitage, 2013; Moeck et al., 2009; Sibson, 2004, 2003, 1996).

Distinctive mineral textures observed on a variety of structural elements such as slickenfibers on fault surfaces, veins, and fault-veins, suggest a direct link between these and the episodic fault reactivation or seismic cycle (e.g. Power and Tullis, 1989; Uysal et al., 2011). For example, dilational implosion breccia exhibiting evidences of hybrid (dilatant and shear deformation) are thought to represent co-seismic dilatancy and hydraulic connection with an ancient geothermal reservoir (Caine et al., 2010; Kolb et al., 2005; Melosh et al., 2014; Micklethwaite and Cox, 2004). Other specific mineral textures, such as lattice bladed or jigsaw calcite and silica, are thought to result from precipitation by boiling processes, indicating quick depressurization caused by space-opening (Moncada et al., 2012; Sibson et al., 1975; Uysal et al., 2011). Moreover, slickenfibers, a distinctive feature of fault-veins, are interpreted as episodic mineral growth at relatively low strain rate during the interseismic period (e.g. Power and Tullis, 1989) and/or as a fossil evidence of repeated microearthquakes (Fagereng et al., 2011).

Because magma also uses fault-fracture meshes as preferential conduits to migrate through the crust, the spatial distribution of intrusive bodies, dike swarms and volcanic centers record the regional and local stress fields (Acocella and Funiciello, 2006; Karaoğlu et al., 2014;

Nakamura, 1977). Extension fractures develop perpendicular to the minimum principal stress axis (σ_3). Within fault-fracture meshes, the high permeability direction is developed parallel to the intermediate principal stress axis (σ_2), which is commonly parallel to fault-fracture intersections and orthogonal to fault slip vectors (Sibson, 1996).

Thus, the question arises as to how deformation partitioning across the overriding plate controls the hydrothermal and magmatic fluid migration pathways. A complete geological and structural record present in the Southern Volcanic Zone (SVZ) provides an excellent natural laboratory to unravel the interactions between stress field variations within strike-slip settings, hydrothermal fluid permeability and magmatic emplacement (Fig. 2-1). The SVZ exposes a regional fault system parallel to the Andean belt, the Liquiñe-Ofqui Fault System (LOFS), and several Andean Transverse Faults (ATF) (called arc-oblique fault system by Sanchez et al, 2013). These structures have different geometry, kinematics and complex cross-cutting relationships (Cembrano and Lara, 2009; Chernicoff et al., 2002; Lara et al., 2006; Melnick et al., 2006a; Sánchez et al., 2013). In this study, it is analyzed the role of stress field variations at local scale on paleo-fluid/magma distribution at different fault-fracture orientations at the northern termination of Liquiñe-Ofqui fault system. This chapter provide a comprehensive and integrated view of the interplay between regional/local stress field orientation and fault-fracture meshes in an intra-arc transpressional setting.

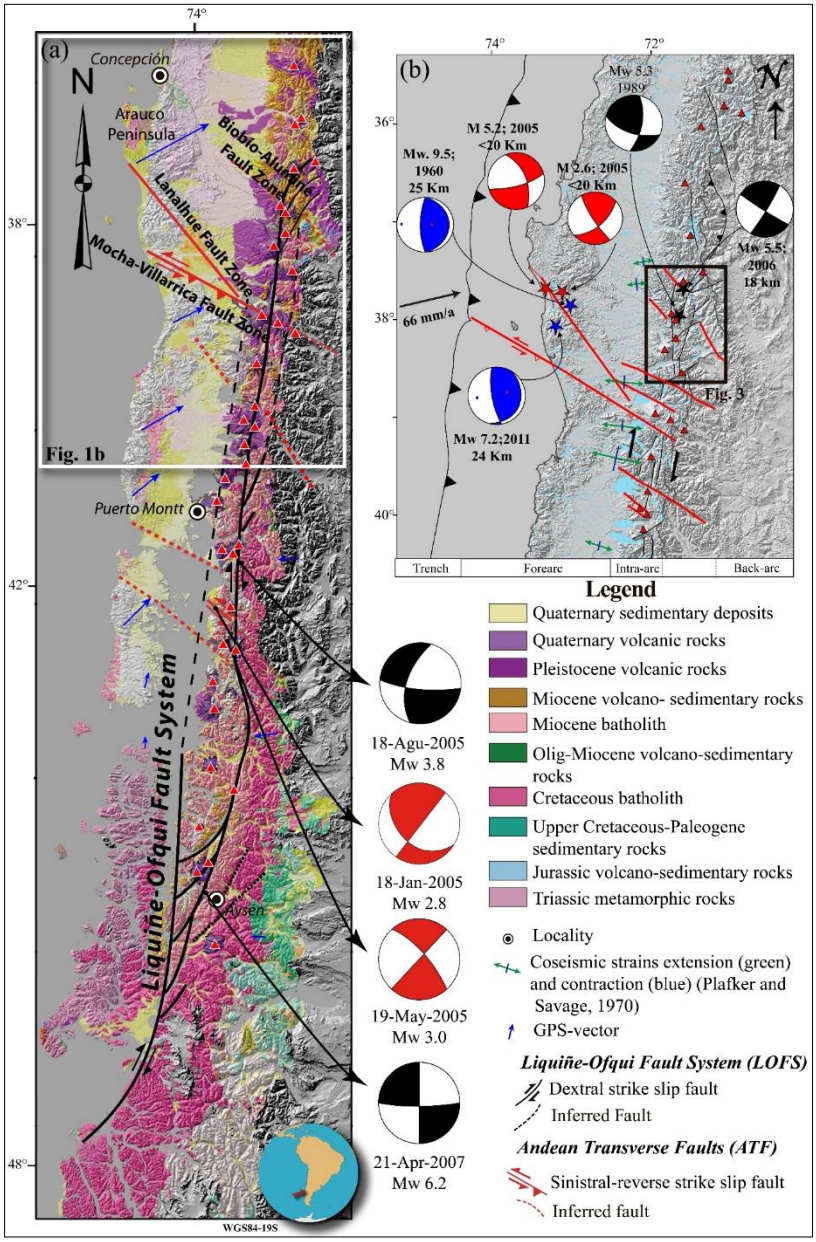

Figure 2-1. (a) Composite Digital Elevation Model and 1:1.000.000 geological map of the Southern Andes Volcanic Zone (SVZ) (Perez-Flores et al., 2013). Regional map showing the location and extent of the LOFS (black lines), ATF (red lines) and main Holocene volcanoes (red triangles). Previously published focal mechanisms of crustal earthquakes are shown for the LOFS (Black) and ATF (Red) (Barrientos and Acevedo-Aránguiz, 1992; Lange et al., 2008; Legrand et al., 2011). A selection of GPS vectors are showing (Lin et al., 2013; Wang et al., 2007) (b) Digital Elevation Model showing the principal fault systems in southernmost Chile: LOFS (black line) and ATF (red line). Convergence velocity vector after Angermann et al. (1999). Subduction zone earthquakes (blue stars), ATF earthquakes (red stars) and LOFS earthquakes (black stars) are shown as well as their respective focal mechanisms (redrawn after Cifuentes, 1989; Haberland et al., 2006; Moreno et al., 2011). The coseismic shortening and extension axes calculated for 1960 earthquake are showing (Plafker and Savage, 1970).

2.2 Geological background

2.2.1 Structural setting

Oblique convergence between the Nazca and South America plates is the driving mechanism for the stress distribution and deformation pattern imposed on the overriding plate (Beck, 1988; Cembrano et al., 2000, 1996). For the southernmost part of South America, the convergence angle (α) ranges between 64º and 70º over the last 10 Ma (Fig. 2-1b) (e.g. Pardo-Casas and Molnar, 1987; Cande and Leslie, 1986). GPS data indicates that present-day convergence velocity of the Nazca oceanic plate is about 66 mm/year, with a subduction angle of ca. 20° (Angermann et al., 1999).

Part of the deformation imposed by oblique plate motion is accommodated by the intra-arc Liquiñe-Ofqui Fault System (LOFS) (Fig. 2-1) (e.g. Arancibia et al., 1999; Cembrano and Herve, 1993; Cembrano and Lara, 2009; Lavenu and Cembrano, 1999). As a result of the subduction process, the forearc and intra-arc zones document changes on the degree of deformation partitioning, along and across the Southern Andes (Arancibia et al., 1999; Lavenu and Cembrano, 1999; Rosenau et al., 2006).

The LOFS is a 1200 km-long intra-arc strike-slip fault system, which is defined by a series of major NNE-striking right-lateral strike-slip faults associated with NE-striking normal-dextral faults that splay off NNE-striking faults. This spatial arrangement forms duplex and horsetail geometries at both ends of the fault system (Fig. 2-1) (Cembrano and Lara, 2009; Rosenau et al., 2006). The LOFS partially controls the occurrence, spatial distribution and geometry of major stratovolcanoes (Cembrano and Lara, 2009; Lara et al., 2008; Melnick et al., 2006a; Sielfeld et al., 2016) (Fig. 2-1). The LOFS records right-lateral ductile deformation between 6 and 3 Ma (Cembrano et al., 2000) that is crosscut by dextral brittle deformation since 1.6 Ma (Lavenu and Cembrano, 1999). Present-day activity of this fault system would absorb about 6.5 mm/yr. of northward motion of the forearc, as recorded by GPS (Wang et al., 2007) and widespread crustal seismicity (Fig. 2-1). Shallow (<25 km) seismic activity (Haberland et al., 2006; Lange et al., 2008) is present throughout the LOFS. At the southern termination of LOFS (Aysén Fjord) a seismic swarm occurred in April 2007 together with a Mw 6.2 earthquake at 12 km of depth, with a right-lateral focal mechanism at a NS-striking fault plane (Fig. 2-1a) (Legrand et al., 2011). Similarly, at the northern

termination of LOFS, in December 2006 a Mw. 5.5 earthquake at 18 km depth was recorded south of Callaqui volcano (Fig. 2-1b). The focal mechanism of this event (http://www.globalctm.org) can be attributable to right lateral NNE-striking fault slip or left lateral NW-striking fault slip, both faults are present in the area. At Lonquimay volcano (Fig. 2-1b), a Mw. 5.3 earthquake at 15 km of depth was recorded after two months of a flank cone eruption. The focal mechanism of this event is a right-lateral oblique slip in a NNE-striking fault (Barrientos and Acevedo-Aránguiz, 1992; Dziewonski et al., 1990). These events are compatible with ENE-shortening and NNW-extension.

The ATF is formed by a series of discrete NW-striking faults inherited from pre-Andean geological processes (Fig. 2-1a) (e.g. Radic, 2010). At the scale of the Andean Orogen, the faults that conform the ATF are spatially and genetically associated with the occurrence of several ore deposits (e.g. El Pescado, Cerro Guachi and Chuquicamata mines) (e.g. Chernicoff et al., 2002), Cenozoic basins (e.g. Radic, 2010) and the segmentation of subduction earthquakes (Melnick et al., 2009). Furthermore, transverse faults are linked with Quaternary volcanism in the Central and Southern Andes (Fig. 2-1) (Acocella and Funiciello, 2006; Cembrano and Lara, 2009; Cembrano and Moreno, 1994; Lara et al., 2006, 2004; Sánchez et al., 2013; Tibaldi et al., 2005). Remote sensing, field observations and geophysical evidence (such as Vp/Vs tomography, magnetic anomalies, gravimetry and shallow seismicity) suggest that the faults of the ATF are deep-seated lithospheric-scale structural elements (Sánchez et al., 2013; Yáñez et al., 1998). The ATF partially control the past and present-day fluid flow, volcanic activity and shallow seismic activity (Haberland et al., 2006; Lara et al., 2006, 2004; Sánchez et al., 2013; Tardani et al., 2016). One of ATF (Pichilemu fault), recorded permanent extensional coseismic deformation in forearc after the Maule subduction earthquake (*Mw* 8.8) in central Chile (35°S), including the *Mw* 6.9 and *Mw* 7.0 events at depths between 16 and 20 km WSW-trending extension axis (Aron et al., 2013). The Lanalhue fault (Fig. 2-1a), another transverse fault, recorded interseismic transpressional deformation of the forearc (38°S) including a M_L 5.2 at 12 km depth with a left-lateral focal mechanism (Fig. 2-1b) (Haberland et al., 2006). Within the study area, the expression of these series of faults is the so-called Biobio-Alumine Fault System (BAFS)

(Fig. 2-1) (Melnick et al., 2006a; Muñoz et al., 1988) which is represented by a rectilinear, NW-trending valley filled with Quaternary fluvial deposits.

2.2.2 Geometry and spatial distribution of dikes and eruptive centers.

At the northern termination of LOFS (Fig. 2-1b), flank vents and dikes are aligned along N60E-trending orientations (e.g. Cembrano and Lara, 2009; López-Escobar et al., 1995). Associated eruptive products range from andesite to basalt, similar to the composition of dikes that locally feed eruptive vents (Sielfeld et al., 2016). Most of such flank vents are Holocene or younger (historical). At Callaqui volcano, flank vents ages are constrained from late-Pleistocene to Holocene and dikes ages are bracketed between 146±30 ka and 77±28 ka (^{40}Ar-^{39}Ar, basaltic groundmass) (Sielfeld et al., 2016). At Lonquimay volcano, there was a recent flank vent eruption on December 25th, 1988 (Navidad vent) (Fig 2b). At Llaima volcano, flank cones record three eruptions at 2008, 1957 and ~1850 (Bouvet de Maisonneuve et al., 2012).. These young volcanic centers have been used to unravel the geometry and kinematics of underlying feeder fractures (e.g. Corazzato and Tibaldi, 2006; Nakamura, 1977; Van Wyk De Vries and Merle, 1998).

Morphological analysis of flank vents on several volcanoes at the SVZ shows the spatial distribution of their feeder fractures. For example, at Callaqui volcano, this analysis reveals a preferential NE-trending alignment of feeder fractures, consistent with the spatial distribution of spatially associated dyke systems. The dikes and flank vent distribution constitute the architecture of the NE-elongation of Callaqui volcano (Fig. 2-2a) (Sielfeld et al., 2016). Similarly, at Lonquimay and Llaima volcanoes, the distribution of flank vents suggests that feeder fractures have the same preferential orientation (N60E) (Fig. 2-2b) (Bertin, 2010; Bouvet de Maisonneuve et al., 2012).

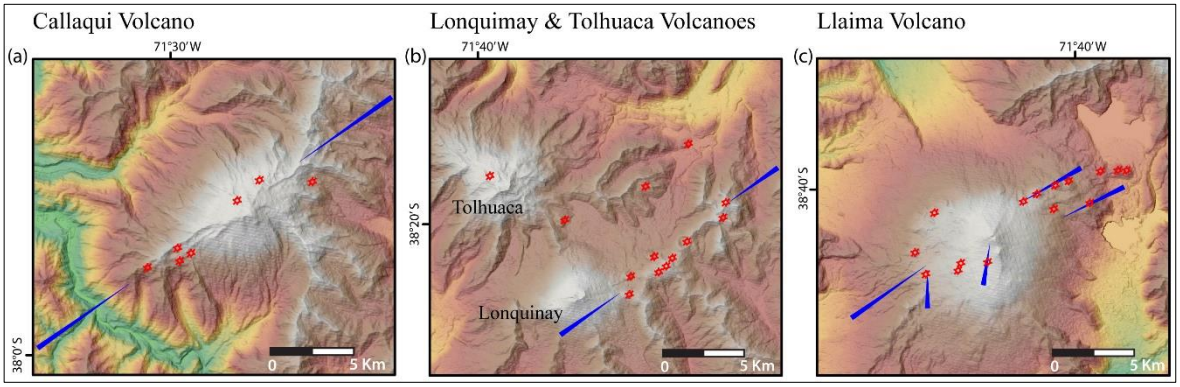

Figure 2-2. Digital Elevation Models showing the preferential orientation of flank cones (red circles) and volcanic vents (blue lines) (Bertin, 2010; Bouvet de Maisonneuve et al., 2012; Maurice, 2012; Sielfeld, 2008) of the (a) Callaqui, (b) Lonquimay and Tolhuaca, (c) Llaima volcanoes.

2.3 Methodology

2.3.1 Field and laboratory structural geology

The study area is located between the Callaqui and Llaima volcanoes encompassing a region of about 150 km by 80 km in the main Andean Cordillera of southern Chile (Fig. 2-1b and Fig 12). The major structural domains documented in this work were defined based on a combination of photointerpretation on digital elevation models and quickbird images (from Google Earth), previous work (Melnick et al., 2006b; Rosenau et al., 2006; Suárez and Emparan, 1997; Thiele et al., 1987) and the field study from regional (1:50.000) to local (1:500) scales. Three representative areas were selected for detailed structural mapping to characterize the geometry, kinematics, and timing of deformation on structural domains of the LOFS and ATF as present in the study area (Fig. 2-3). Within these areas, I defined seven key structural sites, which are representative of LOFS and ATF fault zones; La Poza, Las Mentas, Ralco, Lolco, Las Raices, Las Animas structural sites (Table 1) (Figs. 2-3, 2-4a,2-5a, 2-6a). Collected structural data include description, measurement and logging of the geometry, kinematics, texture, mineralogy, and crosscutting relationship of different structural elements (i.e. fault-veins, veins, hydrothermal breccia). When kinematics or mineralogy was not clear at the outcrop scale, was performed microstructural analysis using optical microscope. When mineral identification at hand and optical microscope scale was not possible, was used X-ray diffraction (XRD) and scanning electron microscope (SEM). XRD analyses were performed at the Laboratorio de Cristalografía of the Universidad de

Chile using a Bruker D8 Advance X-Ray Diffractometer (radiation Cu Kα=1.5406Å), equipped with a Cu X-Ray tube (operating at 40kV/30mA), Ni filter, sample spinner and a solid-state detector (Lineal LynxEye). The resulting diffractograms were interpreted with the software package Match! by CrystalViewer, and compared with Panalytical-ICSD (Inorganic Crystal Structure Database) database. SEM analyses were performed in the University College London laboratory using a Jeol JSM-6480LV high-performance, Variable Pressure Analytical Scanning Electron Microscope with a high resolution of 3.0nm, along with EDS (Energy Dispersive System) and EBSD (Electron Backscatter Diffraction) using the Oxford Link system.

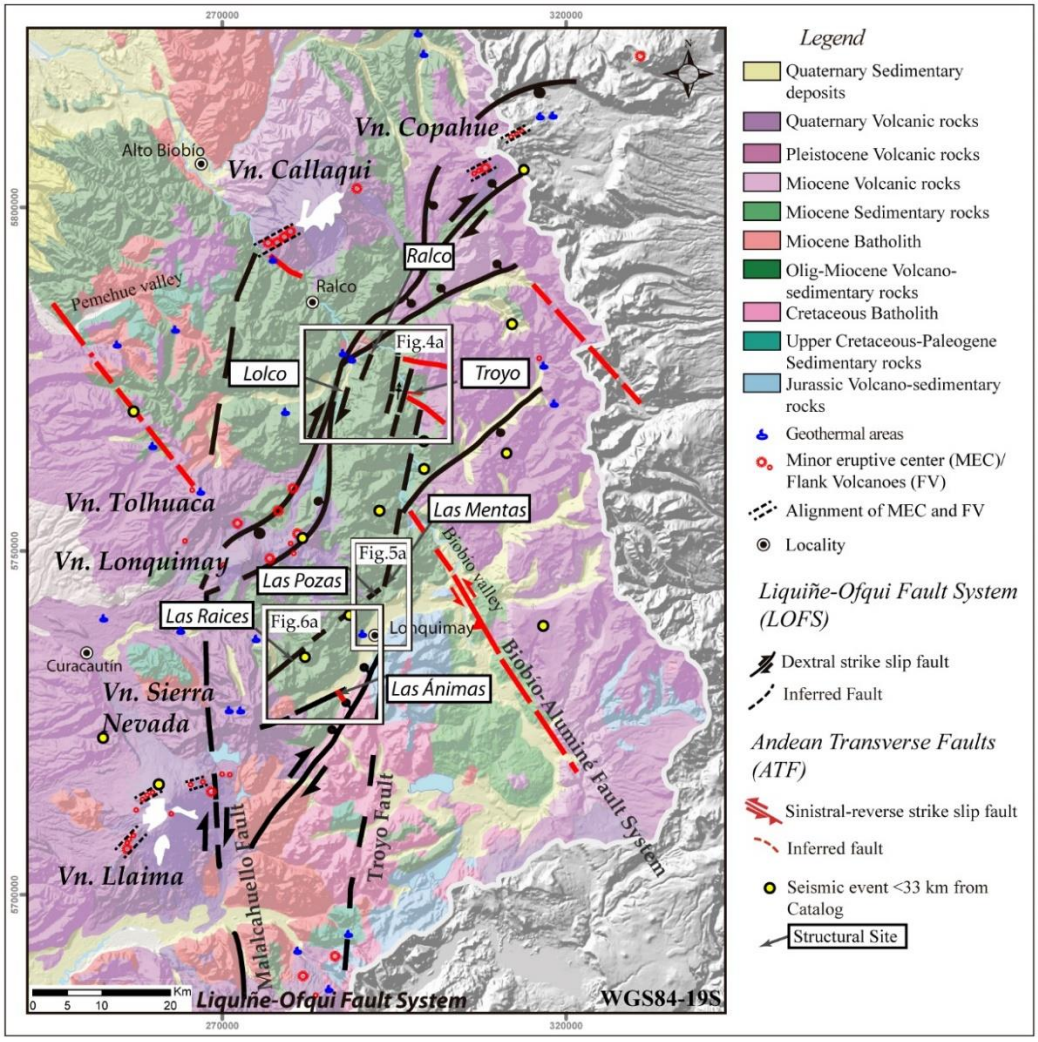

Figure 2-3. Geological-structural map of the Southern Volcanic Zone of the Andes, between 37°30'S and 39°S (see location at Fig. 2-1b) showing the northern termination of the LOFS and the NW-striking faults belonging to ATF (red lines). The white squares show areas of detailed structural mapping sites.

2.3.2 Fault-slip data inversion

Collected structural data collected was analyzed from regional and local scales. The inversion of complete fault-slip data collected within the study area define the regional scale (Fig. 2-3), whereas for local scale, the inversion is the result of fault-slip data of each structural site: Ralco, Lolco, Troyo, Las Mentas, Las Pozas, Las Raices and Las Animas (Fig. 2-3). Two different software were used to determine the strain and stress axes, Faultkin 7.4.1 and Multiple Inversion Method (MIM).

2.3.3 Determination of strain field

The software Faultkin 7.4.1 (Allmendinger et al., 2012; Marrett and Allmendinger, 1990) is a graphical and numerical technique that allows qualitative and quantitative kinematic analysis of fault-slip data by calculating the orientations of the maximum shortening (P) and the maximum stretching (T) axes associated with each individual fault plane. P- and T-axes are an integrated and alternative representation of the orientation and kinematics of a fault, since calculus of both axes requires knowledge of the orientation of the (fault) plane and of the displacement vector resolved on such (fault) plane (slickenline) (Marrett and Allmendinger, 1990). For a single fault-slip datum, the orientation of the P- and T-axes lies in the movement plane – defined by the maximum shear vector (striae) and the fault pole vector – at 45° to the pole vector (Marrett and Allmendinger, 1990). The main, or representative, orientations of both P and T axes for a given fault population are calculated assuming the data represents a uniform deformation field (spatially and temporally). In this case, the main P-and T-axes are calculated assuming that these are clustered following a statistical Bingham distribution. However, non-clustered P- and/or T-axes, indicate that the fault data population is the result of kinematically heterogeneous faulting, represented by girdle or multi-modal patterns of shortening and/or extension axes. Kinematic heterogeneity can arise from several causes, such as triaxial deformation, anisotropy reactivation, strain compatibility constraints and/or polyphasic deformations (Marrett and Allmendinger, 1990). Because P and T axes are related to the orientation of the principal incremental strain axes, it is possible to measure the shape of the strain ellipsoid by using the ratio, $R=(E_2-E_3)/(E_1-E_3)$, where E_1, E_2 and E_3 are the eigenvalues of the Bingham moment tensor obtained for each clustered T, B, and P axis respectively. R values equal to 1.00, 0.50 and 0.00 indicate

ideal flattening, plane-strain and constrictional ellipsoids, respectively. In a general sense, and as pointed by Diraison et al., (2000), values between 0.00 and 0.35 indicate a constrictional type, whilst values between 0.35 and 0.65 indicate a plane strain type. Values in the range of 1.00 - 0.65 indicate a flattening type strain ellipsoid.

2.3.4 Determination of stress field

The "Multiple Inverse Method" (MIM) is based on a geometrical criterion (Yamaji, 2000), being a modification of the classic inverse technique of Angelier (1984). The method can calculate and sorting the orientation of the principal stress axes derived from a heterogeneous fault-slip data set by generating a combinatorial number of groups containing each *k*-number of fault-slip data elements extracted from the whole data set (Yamaji et al., 2005). Then it applies Angelier's (1984) inverse technique to these randomly generated subsets. Finally, the orientations of the calculated stress axes for each generated group of k-number fault-slip data are plotted onto separate stereograms: one for σ_1 axes and another for σ_3 axes sub-solutions (Otsubo et al., 2006; Yamaji, 2000). Each sub-solution is represented as a tadpole indicating the orientation of one of the principal axis with an attached 'tail' pointing towards the orientation of the complementary principal axis (*i.e.*, σ_1's tadpole points toward the orientation of σ_3 and vice versa). This symbol is, additionally, color-coded according to the calculated stress ratio ($\varphi = (\sigma_2-\sigma_3)/(\sigma_1-\sigma_3)$; φ=1-stress shape ellipsoid (R)). Thus, groups of tadpoles with similar colors and similar orientations of their tails indicate a compatible stress field solution (Federico et al., 2010; Otsubo et al., 2006; Veloso et al., 2015, 2009; Yamaji, 2000). The distribution of φ-values is therefore used to establish a φ-value range for the principal stress axes solution. In the case where φ-histograms show a bimodal distribution, it is calculated one field stress solution for each range of representative φ-values. Thus, for the field stress obtained, the misfit angle or difference between observed and theoretical slip direction obtained from an assumed stress state is calculated. The stress axes orientation solution is calibrated by choosing the solution with a bigger number of activated faults with misfit angles of less than 30°. Thus, the tectonic regime is defined by the principal stress axes orientation as extensional, compressional or strike-slip (Ritz, 1994). The strike-slip regime could be either transpressional or transtensional regimen depending of stress ratio

value (φ). A φ > 0.55 represent transtensional tectonic regime, φ < 0.45 represent transpressional tectonic regime and 0.45 < φ < 0.55 represent a simple shear dominated strike-slip tectonic regime (see detailed discussion about φ-value interpretation at Bellier and Zoback, 1995; Siame and Bellier, 2005).

2.4 Results

2.4.1 Architecture and geometry of fault fracture networks in the study area.

Based on the detailed mapping at each structural site, the main features of structural elements are summarized in Table 1. Structural elements described in the study area are hosted by volcanic and sedimentary rocks belonging to the Cura-Mallin Formation, dated between 19 and 12 Ma (K-Ar ages on whole-rock and plagioclase from andesite) (Suárez and Emparan, 1997).

The northern termination of the LOFS consists of three fault sets (Fig. 2-3). (1) NNE-striking subvertical master faults (first order), (2) NE-striking, steeply-dipping splay faults (second order) and (3) ENE to EW-striking, steeply to moderately dipping local faults (third order). First-order faults are tens of km-long, which are represented by two subparallel faults: Malalcahuello and Troyo Faults as well as by four synthetic NNE-striking faults in the northern area (Fig. 2-4a). A series of aligned scarps and valleys mark the Malalcahuello Fault, mostly covered by Holocene volcanic rocks derived from the Llaima, Lonquimay, Tolhuaca and Callaqui volcanoes. A NE-trending alignment volcanic vents and fissure record transfer zone at the Lonquimay volcano. This transfer zone appears to connect the Malalcahuello fault with Lolco fault (Fig. 2-3). Lolco fault is a right-lateral strike slip fault, which splays off northward into two NE-striking faults forming one typical horsetail geometry (Fig. 2-3). At Lolco structural site (Fig. 2-4a) several cm-scale thick, right-lateral strike-slip faults exhibit zeolite slickenfibers (Fig. 2-4c). This fault zone cuts andesite and tuff belonging to the Cura-Mallin Fm. (12,0±1.6, K-Ar) (appendix SM1b).

Table 1. The table summarized the detail mapping at each structural site. The information displays are the host rock age from closer data of Suárez and Emparan (1997), main structural element with their texture and minerals, strain, and stress axes solutions.

Host rock	*Age (Ma)*	*Structural element*	*Principal orientation*	*Mineralogy and texture*	*Strain solution*				*Stress solution*			
					P	*T*	*R*	*Strain ellipsoid*	ϕ	$\sigma 1$	$\sigma 3$	*Tectonic regime*
Andesite. Cura-Mallin Formation	13.1±0.7 K-Ar Whole rock	Dextral faults	NNE	Several centimetric faults with zeolite slickenfibers.	066/24	157/2	0.48	Plane-strain	0.40	066/21	335/02	Strike-slip
		Veins and Hydrothermal breccia	NE	0.1-2.0 cm-thick, laumontite, fault-veins.								
Shale and sandstone. Cura-Mallin Formation	19.1±2.8 K-Ar Whole rock	Dextral faults	NNE	Several, 0.2-1.0 cm-thick faults with calcite slickenfibers.	237/57	329/01	0.27	Constrictional	0.50	041/43	138/07	Strike-slip
		Normal fault	NE	Gauge fault core, 2 cm thick and 1 m offset.								
		Veins	NE	Sintaxial calcite, with high dip variability, usually parallel to shale lamination								
		Hydrothermal breccia	NNE-NE intersection	Mosaic breccia texture with bladed-like calcite.								
Andesite. Cura-Mallin Formation	14.1±1.6 K-Ar Whole rock	Dextral faults	NS	Decametric, 20 cm thick and zeolite slickenfibers.	167/61	311/25	0.56	Plain strain	0.70	211/23	312/25	Strike-slip transtensional
		Sinistral faults	WNW	50 cm thick fault core with zeolite slickenfibers displaying Riedel-type shears fractures locally exhibiting hydrothermal breccia lenses.								
		Veins	NE	0.2-1.0 cm-thick zeolite veins form dextral duplex.								
Andesite. Cura-Mallin Formation	11.9±0.8 K-Ar Whole rock	Dextral deformed band	NNE	50 cm thick foliated band and S-C fabric.	208/75	332/9	0.74	Flattening	0.40	067/31	327/16	Strike-slip
		Dextral-reverse faults	NS	10 cm gouge core fault								
		Veins	NE	0.3-5 cm thick zeolite veins locally forming crackle breccia.								
		Sinistral-reverse faults	EW	Several centimetric fault with calcite slickenfibers								
		Veins	ENE to ESE	0.3-2.0 cm thick calcite filled with locally breccia lenses								
Andesite. Cura-Mallin Formation.	11.9±0.8 K-Ar Whole rock	Dextral faults	NNE	Several 0.1-1.0 cm gouge thick fault cores.	243/02	153/0	0.46	Plane strain	0.20	059/05	326/46	Strike-slip transpressional
		Dextral-normal faults	NE	Decametric fault with 15-30 thick fault core, consist of gouge and fault breccia.								
Andesite.	19.9±1.4 K-Ar Whole rock	Dextral -reverse faults	NNE	Several 0.5-2.0 cm thick faults with calcite slickenfibers.	261/02	352/19	0.56	Plane strain	0.20	078/32	346/03	Strike-slip transpressional
		Normal-dextral faults	NE-ENE	Decametric faults between 10 to 50 cm thick fault core with laumontite and stilbite veins and less calcite, locally form hydrothermal breccia lenses.								
		Andesitic dikes	NE-ENE	20 to 50 cm wide hosted throughout NE-ENE faults.								
		Veins	ENE	Sintaxial stilbite veins 0.5-3.0 cm thick								
Interlayer of andesite and hornblende andesite.	-	Sinistral-reverse faults with reactivation of normal faults	NW	Foliated fault cores between 30-50 cm wide. Asymmetric damage zone stronger at hanging wall. 1 m normal offset of marker layer and 0.2-1.0 cm reverse offsets inside of core fault, forming a gentle fault propagated anticline fold.	-	-	-	-	0.90	227/45	356/32	Strike-slip transtensional
Cura-Mallin Formation		Hydrothermal breccias bodies	NW-NE intersection	Tabular bodies between 4-6 m wide which have transition from veins stockwork, crackle breccias and hydrothermal breccia consist of rounded clasts (10-30 cm diameter) with zeolite-calcite matrix.	-	-	-	-	0.60	110/19	011/22	Strike-slip
		Veins and hydrothermal breccias	NW-EW	0.2-15.0 cm wide, banded veins consist of stilbite edge and hydrothermal breccia center with laumontite matrix and locally calcite. 0.2-2 cm wide, stilbite veins.								

A synthetic fault zone is recorded at Ralco structural site (Fig. 2-4a). Here, faults and veins are mostly randomly oriented and locally parallel to shale (host rock) lamination. Locally, dilatational jogs are formed at linking zones between NNE- and NE-striking faults (Fig. 2-5a). Syntaxial bladed-like calcite crystals of about 1 cm in size fill these dilatational jogs (Fig. 2-5b). From outcrop to micro scales, NE-striking laumontite-, calcite-filled veins and hybrid faults relate both spatially and genetically to master faults (appendix SM1b1 and c2). Fig. 2-5c shows a hybrid fault on a thin section from a N45°E/80°W oriented, right-lateral strike-slip fault. This section shows a calcite slickenfiber with several parallel sheets with sharp contact surfaces (Fig. 2-5d) and a transitional texture from a brittle shear zone in the host rock contact (Fig. 2-5db) to blocky crystals following the slip direction. The thin section also shows a couple of calcite extension veins (N70°E) genetically and kinematically related to master faults (Fig. 2-5ba). Two synthetic NNE-faults are documented at Troyo structural site and vicinity (Fig. 2-4a). One is a right-lateral fault-slip with 10 cm thick of gouge fault core that crosscuts an EW-striking (Fig. 2-4b) fault and is spatially and kinematically related to NE-striking veins and hydrothermal breccia at Troyo structural site. The second fault, further east, is a dextral-reverse oblique fault-slip gently dipping (50°E) with 20 cm thick gouge core (appendix SM1d). A rectilinear NS-striking valley is the morphological expression of Troyo Fault Zone. Along this valley, at Las Mentas structural site (Fig. 2-6a), NNE-striking master faults locally host a synkinematic strongly deformed andesitic dike (Fig. 2-5b). A thin section made in this deformed rock record a dextral slip documented by sigmoidal S-C fabrics (Fig. 2-6c). NE-striking veins (Fig 2-6c) crosscut this deformed band and NE-striking second order faults (Table 1).

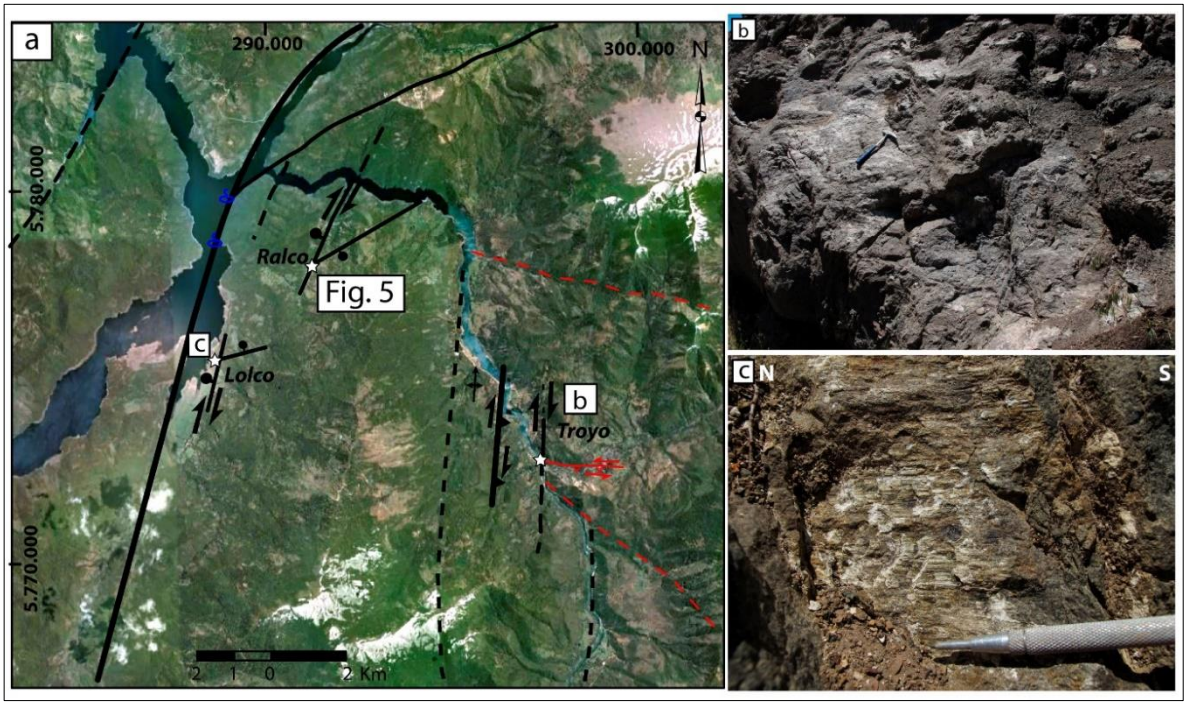

Figure 2-4. (a) Google Earth image showing the Lolco, Ralco and Troyo structural sites. Panels b to c show examples of different structural elements seen in the field and under the microscope. (b) East-striking, shallowly-dipping, sinistral fault (N85°W/45°S rake:20°W); (c) N10E-striking, steeply dipping, dextral fault with zeolite slickenfibers.

Second order faults are NE-striking normal-dextral oblique slip and right lateral strike-slip faults that locally connect and cut some of the master and synthetic NNE-striking faults (e.g. Las Raices and La Poza structural site, Fig. 2-3). At regional scale, these fault-fracture networks host volcanic vents and dikes. Las Raices structural site is a representative outcrop of second order faults (Fig. 2-7). Here, NE-striking dextral-normal oblique faults consist of 10 to 50 cm thick-banded fault core formed by laumontite and stilbite veins and hydrothermal breccia (appendix SM2b, b1 and b2) (Las Raices structural site, Table 1). These crosscut NNE-striking dextral-reverse oblique slip faults with calcite slickenfibers. The NE-striking fault damage zone is rather asymmetric (Fig. 2-7d and appendix SM2b), being more penetrative in the hanging wall than in the footwall. These fault-fracture networks host syntectonic N65E-striking dikes (Fig. 2-7d) which are cut by N70-80E-striking, syntaxial, stilbite veins (Fig. 2-7e, appendix SM2b and Table 1).

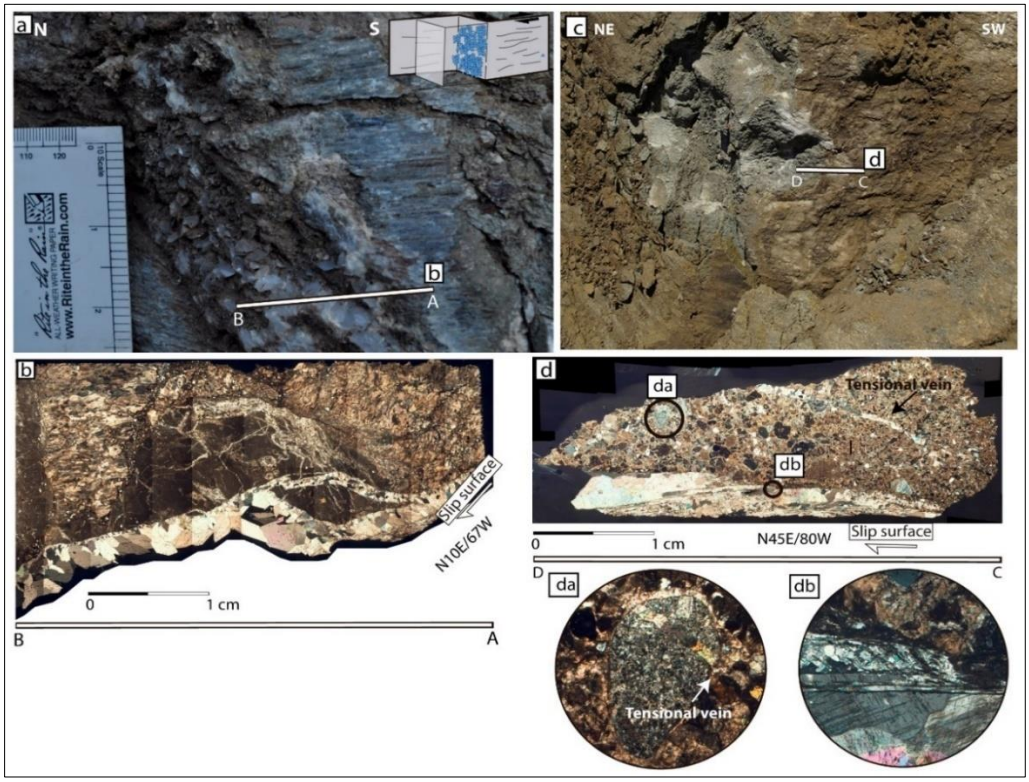

Figure 2-5. See location in Fig. 2-4a. (a) Dilatational jog between NNE and NE-striking dextral faults hosting bladed-like calcite; (b) Oriented thin section perpendicular to the fault plane and parallel to striae showing calcite microstructure. Note that a sigmoidal piece of the wall rock is detached at the dilational site; (c) N60°E-striking fault with subhorizontal striae and dextral strike-slip kinematics; (d) Oriented thin section photo-mosaic showing calcite slickenfibers sheets with sharp contact surfaces and a transitional texture from a brittle shear zone in the host rock contact (da) to blocky crystal types following the slip direction. (db) Extension fractures (N70ºE) locally cut some clasts of the wall-rock.

The third-order faults-fractures consist of cm-scale, sinistral-reverse faults locally exhibiting calcite slickenfibers and ENE- to WNW-striking veins and hydrothermal breccias. One of this vein system is well recorded at outcrop scale at Las Mentas structural site, consisting of one ENE-WNW/70-45°S striking vein system filled with euhedral calcite grains ranging between 0.3-2.0 cm in diameter. These hybrid faults and vein networks are commonly present at second order outcrop faults.

Despite being a well-marked lineament in the study area, the Biobio-Alumine Fault System, records no obvious outcrops. Nevertheless, along stretches of the Biobío river valley, there are well-exposed decametric triangular facets and outcrop-scale normal faults developed on fluvial deposits indicating neotectonic activity. The master faults of the LOFS locally cut and displace those of the BAFS at regional scale (Fig. 2-3).

Numerous hot springs located at the NW flank of the Tolhuaca volcano also define a NW-trending alignment with hydrothermal alteration (Fig. 2-3). Las Animas structural site is a representative outcrop of NW-striking faults belonging to ATF (Fig. 2-7a). Here, a ca. 60 m wide, NW-striking fault zone is well exposed, consisting of two subparallel NW-striking faults with thickness of 30-50 m and two well-exposed 2-6 m thick faults with breccia and hydrothermal breccia fault cores (appendix SM2c, c1 and c2).

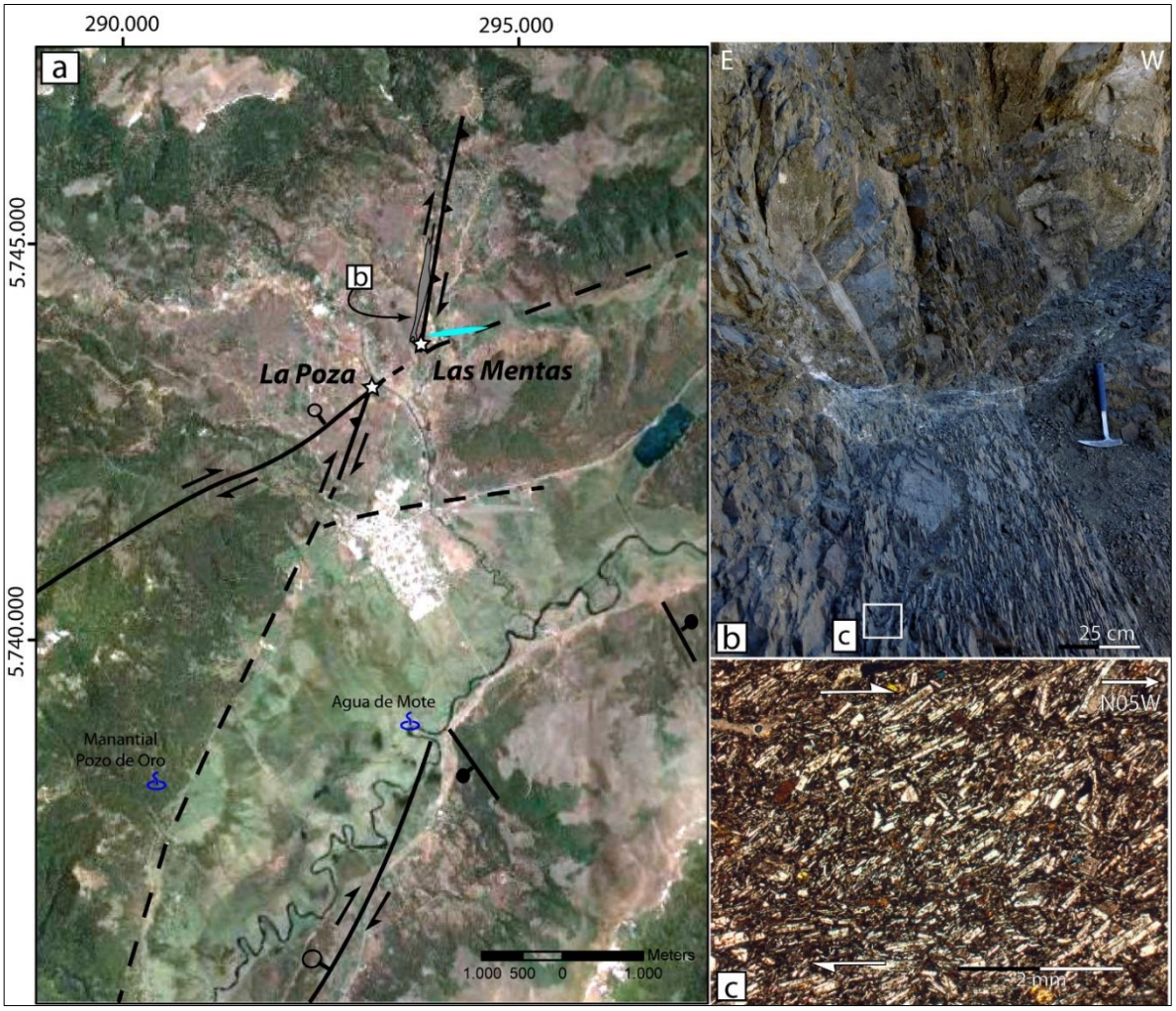

Figure 2-6. (a) Satellite image showing major faults (black lines), lineaments (dotted line), vein orientation (cyan line) and hot springs (blue symbol) at Las Mentas and La Poza structural sites. Las Mentas structural site: (b) strongly foliated (N05W/81W) rock deformed band (N20E/70W) crosscut by ENE-striking veins. (c) Oriented thin section from the deformed band consists of andesitic rock with preferentially oriented, undeformed plagioclase crystals forming sigmoidal S-C fabrics that indicate dextral displacement.

One N50W-striking fault (Fig. 2-7) exhibits a foliated, 50 cm thick core with zeolite veins. NW-striking reverse faults crosscut and displace the zeolite veins (Fig. 2-7c). Here, an

asymmetrical hanging wall damage zone developed, showing a significant hydrothermal alteration expressed as a denser occurrence of sub-vertical stilbite filled veins and laumontite/stilbite rich matrix hydrothermal breccias (Fig. 2-7b) (Las Animas site, Table 1). A gentle, fault-propagated fold near the fault core confirms a reverse movement (Fig. 2-7b). The fault breccia consists of zeolite-filled vein-breccia that locally develops stockworks and lenticular, clast-supported zeolite hydrothermal breccia bodies with sub-rounded host-rock clasts ranging from 10 to 30 cm in diameter (appendix SM2c, c1 and c2).

2.4.2 Kinematics and dynamics of fault-fracture networks

2.4.2.1 Regional fault slip analysis

Regional kinematic and dynamic parameters result from applying inversion procedures, seeking strain and stress fields representative of the entire fault population (n=190) collected from 7 structural sites (appendix, SM3) and vicinities (Fig. 2-8a). The regional strain analysis shows that individual (single fault datum) P and T axes are widely distributed, without forming well-defined clusters. This suggests that the analyzed fault-slip data population carries kinematically heterogeneous information about the faulting mechanism and evolution of the intra-arc zone. Following this, the strain analysis would not be representative without an arbitrary data selection (Angelier, 1984; Federico et al., 2010; Marrett and Allmendinger, 1990; Veloso et al., 2015; Yamaji, 2000). I analyze the fault-slip data by structural sites to differentiate local-scale homogeneous strain fields recorded within the regionally heterogeneous fault-data set, as shown further along in the text.

Regional stress analysis shows a bimodal φ-histogram distribution with modes at 0.4-0.5 and at 0.9 (Fig. 2-8d). However, clustering of stress axes solutions has associated φ-values of 0.38 and 0.90. The transpressional strike-slip stress field associated with a φ-value of 0.38 yields a N64E-trending subhorizontal σ_1 axis and a N30W-trending subhorizontal σ_3 (Fig. 2-8c). The transtensional strike-slip field associated with a φ value of 0.9 has an EW-trending subhorizontal σ_1 axis and NS-trending subhorizontal σ_3 (Fig 2-8c, 2-8e).

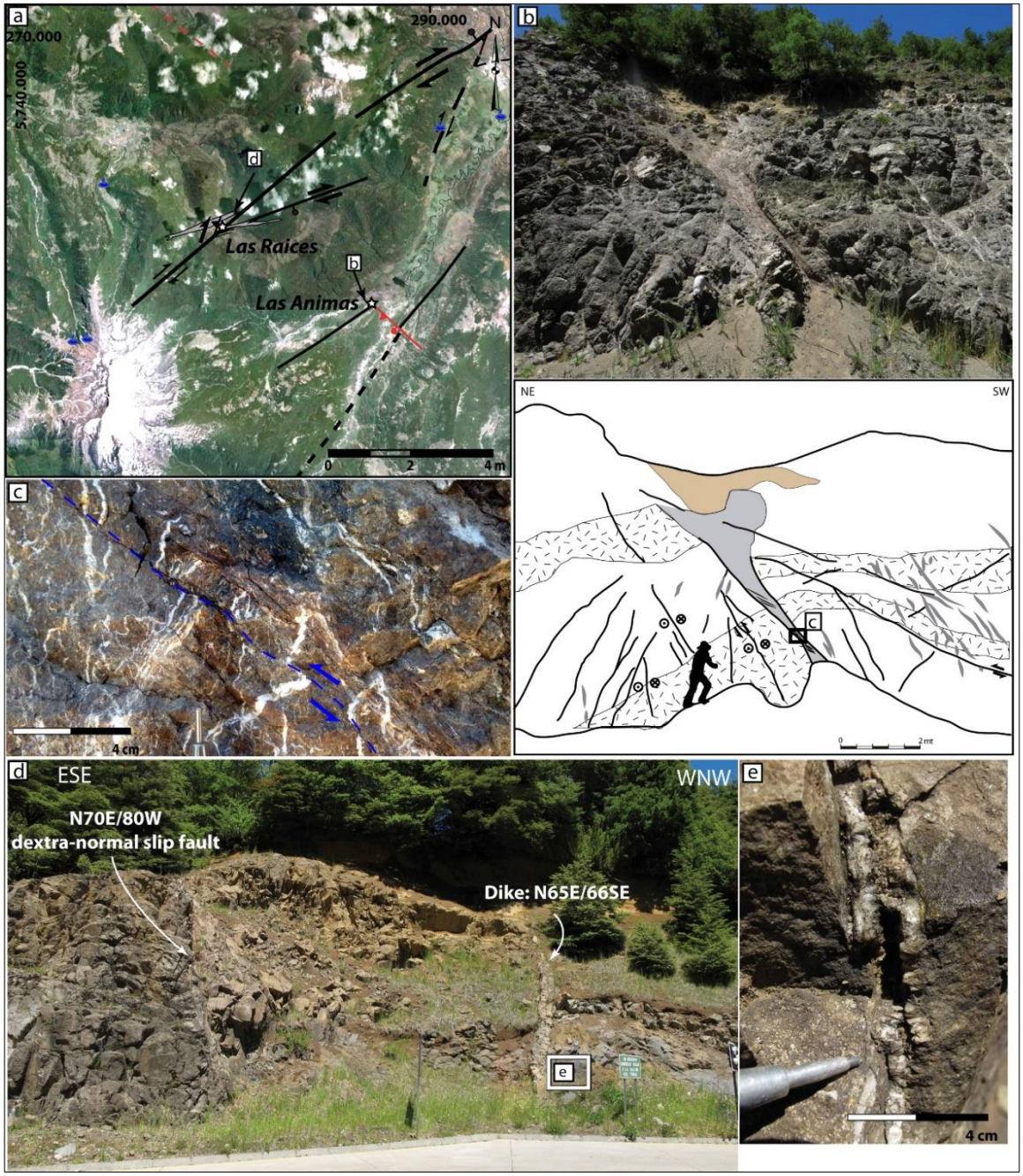

Figure 2-7. (a) Google Earth image showing the major faults (black lines) and lineaments (dotted line) at the Las Raices and Las Animas structural sites. Las Animas structural site: (b) Photograph and related line-drawing of one NW-striking fault showing a volcanic interlayered sequence of andesite and hornblende andesite forming a gentle anticline fold near the fault core, which corresponds to a fault-propagated fold. The fault core consists of a foliated gouge with Ca-rich zeolite veins cut by small reverse faults (c). Las Raices structural site: (d) Photograph SSW view showing NE-striking normal-dextral slip fault and NE-striking dike cut by ENE-striking tensional zeolite veins (e).

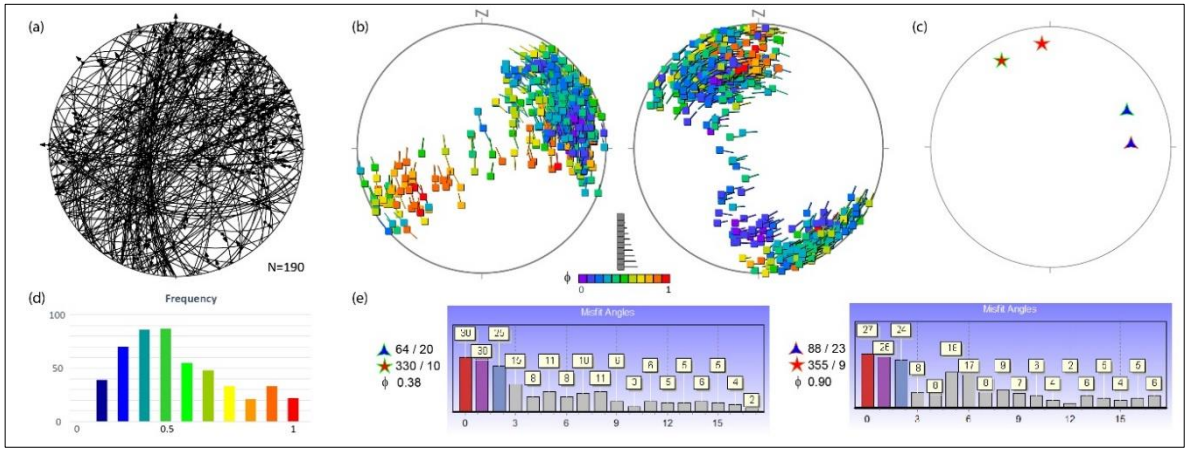

Figure 2-8. (a) Lower hemisphere, equal-area projection showing the orientation of measured fault planes and their associated displacement vector (striae); (b) Stress field solutions as given by the MIM method applied to the study area. Results of these analyses show that the lower hemisphere stereonet (σ1 and σ3 to the left and right side, respectively, Fig. 1-14b)) calculated by using Multiple Inverse Method (MIM) (Yamaji, 2000), the color represents the φ-value from purple to red (0-1, respectively). (b) φ-histogram graphic shows a bi-modal distribution of the best-possible fit between real and modeled data. (c) Stress field solutions from MIM, σ1 (blue triangle) and σ3 (red star) with red and green line for φ=0.9 and 0.38 respectively. (d) Graphic showing the angular misfit for each solution.

2.4.2.2 Local fault-slip analysis

A summary of the strain and stress field results of fault-slip data at each structural site is shown in Fig. 2-9 and in Table 1.

The NNE-striking fault zones show a homogenous deformation with well-defined clusters of P- and T- axes (Lolco and Troyo structural sites). The principal strain axes solution indicates NW-trending stretching and NE-trending shortening with plane- to flattening-strain ellipsoid. At Ralco structural site, fault-slip data recorded the reactivation of shale lamination, showing a wide distribution of P- and T-axes. The stress axes solution shows a strike-slip tectonic regime (φ=~0.50) with a subhorizontal NE-trending σ_1 and NW-trending σ_3 axes. The orientation of strain and stress axes solutions shows a good agreement for these NNE-striking set of faults.

The second order NE-trending faults, well represented at Las Raices structural site (Fig. 2-9 and Table 1); show a preferential clustering of T-axes on a NNW-trending direction and a wide distribution of P-axes with plane-strain ellipsoid. This kinematically heterogeneous faulting could be attributed to strain compatibility (Marrett and Allmendinger, 1990) between two fault sets, with slip parallel to fault intersection (Las Raices structural site, Fig.

2-9). The stress analysis indicates a transpressional regime (φ =0.20) with an ENE-trending σ_1 and a subhorizontal NNW-trending σ_3. The minimum principal stress axis, σ_3, changes plunge to nearly sub-vertical (compressional tectonic regime) at the intersection with the LOFS master faults (La Poza structural site, Fig. 2-9).

Fault-slip data analysis from Las Animas structural site shows a widely-scattered distribution of both P- and T-axes, suggesting a polyphasic deformation and/or a pre-existing anisotropy reactivation. Similarly, dynamic analysis of the same ATF data with the aid of the MIM shows two distinctive stress axes solutions. The obtained strike-slip and tensional local stress fields share a common subhorizontal, N-trending σ_3 axes, but the minimum and intermediate stresses switch position, defining one strong solution with a subhorizontal, ESE-trending σ_1 in a strike-slip regime (φ =0.6), and a secondary solution with a moderately plunging, WSW-trending σ_1 in a transtensional regime (φ =0.9).

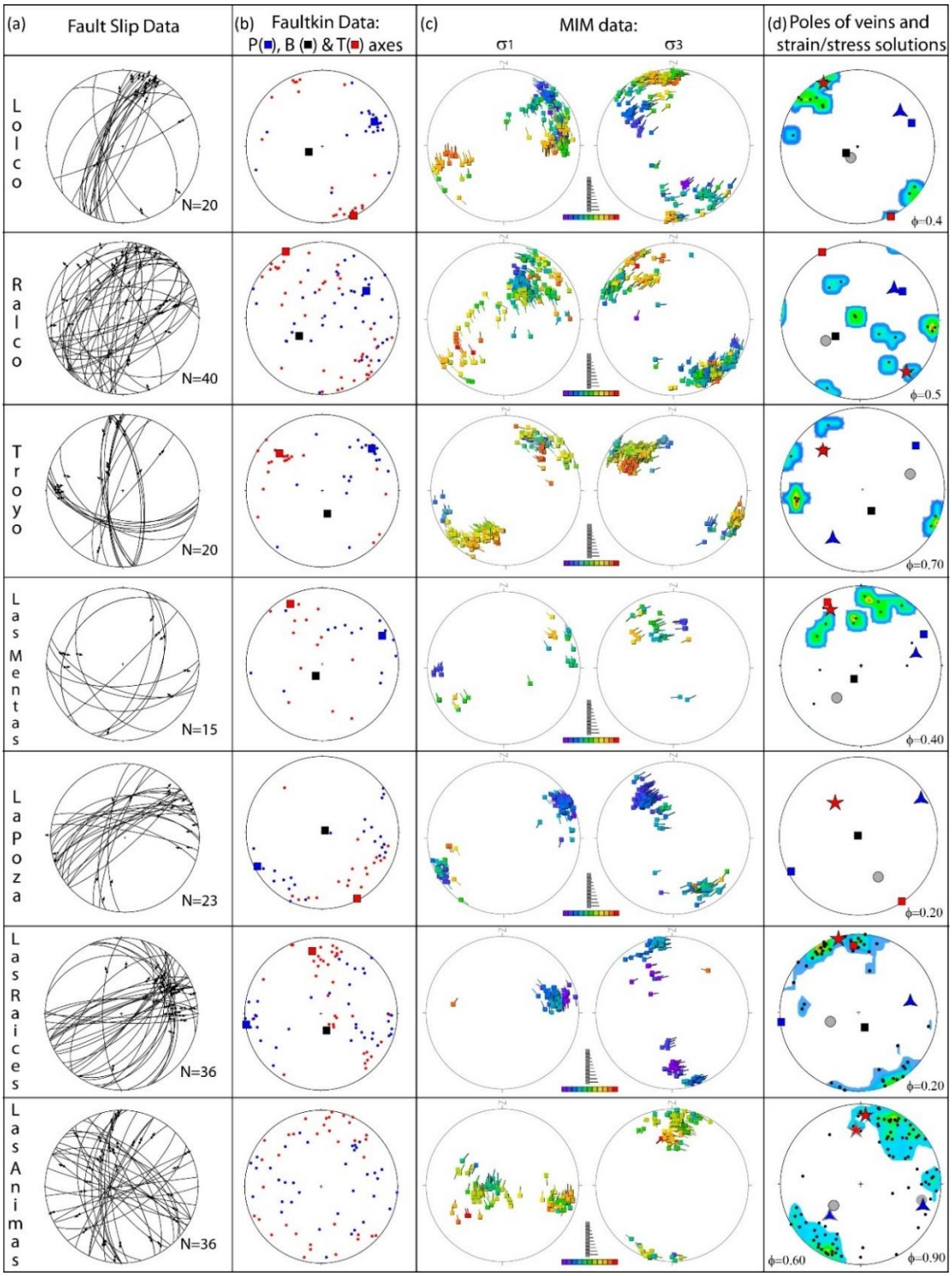

Figure 2-9. Lower hemisphere, equal-area projections showing gathered fault-slip data and results of strain and stress analyses, at each structural site. (a) mesoscopic fault-slip data; (b) orientation of T (red dots), P (blue dots) and B (black) axes (e.g Marrett and Allmendinger, 1990). (c) orientation of calculated stress axes (σ1 and σ3) MIM (Yamaji, 2000). (d) Density diagram of the poles-to-veins together with the orientation of σ1 (triangle), σ2 (circle) and σ3 (star) principal stress axes shown in (c).

2.5 Discussion

2.5.1 Deformation partitioning at the Southern Volcanic Zone

Deformation partitioning arising from oblique convergence can be analyzed by using a geometrical relationship between the angle of relative plate motion and the trench (convergence angle α=70°; Fig. 2-10) and the orientation of maximum strain axes in the forearc and intra-arc domains (Teyssier et al., 1995). This geometrical analysis uses the kinematic model of strike-slip partitioning developed by Teyssier et al (1995). This model is based on two end-members: strike-slip non-partitioned and completely partitioned. Based in this model, the non-partitioned deformation indicates a fixed orientation of the maximum shortening axis (i.e. P-axis) of N88°E, which is evenly distributed throughout the forearc and intra-arc domains (Fig. 2-10a). Conversely, in the case of a completely partitioned transpression, P-axis ought to trend N100°E in the forearc and N55°E in the in the intra-arc structural domain of the LOFS (Fig. 2-10b). Based on these two end-members and the kinematic/dynamic analyses shown before, I postulate a partial strain partitioning for the study area (Fig. 2-10c) with P-axes preferentially oriented N88º-100ºE in the forearc domain and N55°-88ºE in the intra-arc domain. The strain and stress field results, from fault slip data in the intra-arc domain, provide the tectonic context to compare the nature of strike-slip partitioning with the geometrical model depicted on Fig. 2-10. As a first approximation, the average orientation of T-and P gives the orientation of the regional-scale strain axes-axes obtained for the entire fault-slip data population. Although results show a good agreement with field observations at a local scale, the dispersion of both P- and T-axes obtained for the entire fault-slip data at the LOFS (intra-arc) domain is very high, preventing the calculation of a geologically representative average value. Another possibility is to use the stress field as a proxy for the strain field. Thus, the orientation of the σ_1-axis would be parallel to that of the minimum horizontal strain axis (S_3 or P) of the incremental strain ellipsoid. This implicitly assumes that the orientation of both stress and incremental strain axes has remained coaxial through the faults history – i.e. since at least from the Late Miocene- in the study area.

The N64°E orientation of the maximum principal stress axis (σ_1) obtained for the intra-arc is consistent with a partially partitioned deformation (Fig. 2-10c). In this case, the maximum

shortening direction within the forearc is likely to lie close to an EW-trend (N88°E<P<N100°E). This orientation is favorable for the development (or reactivation) of NW-striking discontinuities as, most probably, sinistral-reverse faults. Such geometry and kinematics are compatible with seismic activity and the kinematics proposed at a regional-scale (Glodny et al., 2008; Melnick et al., 2009) for the Mesozoic to recent history of the NW-striking Lanalhue Fault (Fig. 2-10), a fault of the ATF running through both the intra-arc and the forearc region.

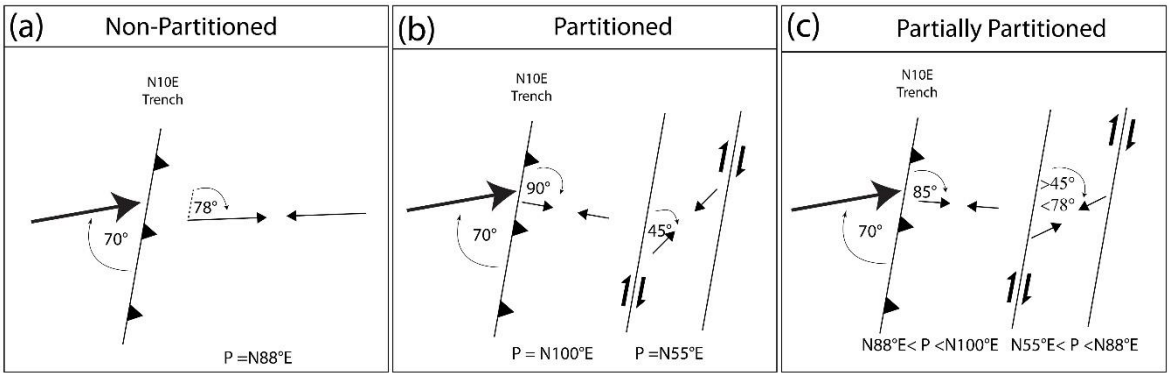

Figure 2-10. Transpressional strain partitioned model (e.g Fossen et al., 1994; Teyssier et al., 1995) applied to the study area (a) non-partitioned, (b) completely partitioned and (c) partially partitioned strain; showing shortening-trending axis (P).

The stress axes orientation and stress ratio (φ =0.20) obtained from the entire fault-slip data (Fig. 2-8) indicates that the intra-arc is dominated by strike-slip transpression compatible with plane to flattening strain at each structural site. Moreover, results from the dynamic and kinematics analysis indicate that deformation is even further partitioned within the intra-arc itself. The main evidence for this is the difference between the local stress fields calculated at each structural site and the regional stress field calculated for the entire intra-arc zone. Fig. 2-11 shows the regional and local stress fields and the main structural elements identified within the intra-arc, presenting different scales of deformation. Within the intra-arc, there are NNE-striking faults recording right lateral strike-slip and other oblique-reverse right lateral strike-slip (Fig. 2-11). This is an evidence that intra-arc domain is accommodating simple shear deformation. The principal stress axes for the second order faults are slightly oblique with respect to the regional stress field and show plunge variations at structural sites where fault intersections are present (La Poza structural site, Fig. 2-9, 2-11, Table 1). Similarly, variation of local stress axes orientation within a fault systems

recorded by fault-slip data or earthquake focal mechanism has been documented at the Atacama Fault System (Veloso et al., 2015), South Island, New Zealand (Herman et al., 2014), Alhama de Murcia fault (Martínez-Díaz, 2002) and Maghreb region (Ousadou et al., 2014) among others.

Fault-slip data analysis of the LOFS structural elements yielded homogeneous orientations of the strain axes, suggesting that deformation occurred as a continuous deformation phase. In contrast, fault-slip data analysis of the ATF yielded heterogeneous orientations of the strain axes, suggesting that at least two deformation phases acted upon these structural elements. Accordingly, the MIM analysis shows two stress field solutions: one strike-slip (φ=0.6) and one transtensional tectonic regime (φ=0.9) (Fig. 2-8). Field observations at Las Animas structural site (Fig. 2-7b and 2-7c) document both stress field solutions, where one conspicuous NW-striking fault shows evidence of both normal-slip offset and of sinistral-reverse slip. The strike-slip local stress field solution (φ=0.6) had a similar orientation to that of the theoretical maximum shortening axis previously discussed for fore-arc deformation (Fig. 2-11). These results record a deformation partitioning pattern within the intra-arc, accommodating part of the shortening perpendicular to the trench by sinistral-reverse NW-striking faults. The orientation of a second transtensional strike-slip stress field solution (φ=0.90) is decoupled from the regional stress field and is consistent with the observed normal faulting and vertical veins networks present at the outcrop scale. This deformation pattern is similar to that obtained from focal mechanism analysis of the NW-striking Pichilemu fault during its reactivation after the Maule earthquake in the forearc domain (Aron et al., 2014, 2013). Furthermore, a similar maximum stretching axis orientation of this solution was modeled for the co-seismic deformation during the 1960 Valdivia earthquake (Moreno et al., 2009; Plafker and Savage, 1970).

The geometry formed by right-lateral strike-slip NNE-striking master fault and dextral-reverse synthetic faults with NE-striking normal-dextral and NW-striking sinistral-reverse faults is compatible with the geometry shown in strike-slip analog model (σ_1=45°) (González et al., 2012). Nevertheless, this model records a fault system mainly composed of reverse-dextral faults accommodating the shortening imposed by oblique subduction. Fault-slip data shows a strike-slip dominated fault system probably because the analog model does not

include the subduction zone and forearc region, which accommodate most of the shortening component. Another important factor to consider is the thermal weakness present at the intra-arc region, not considered in the analog model.

2.5.2 Magmatic and hydrothermal fluid migration

The integration of strain and stress analysis of fault-fracture networks with the microstructural analyses of minerals from different structural elements allows constraining the tectonic and mechanical conditions operating during migration and crystallization of hydrothermal fluids and magmas (e.g. Bons et al., 2012). The transpressional strike-slip regime recorded in the intra-arc domain favors vertical magma/hydrothermal fluid migration (e.g. Brogi, 2011; Faulkner and Armitage, 2013; Sibson, 1994). The orientation of the regional stress field (N60E-striking σ_1 and N30W-striking σ_3 axes) seems to control the NE-striking orientation of volcanic feeder dikes observed at, for example, the Lonquimay, Llaima and Callaqui volcanoes. This is also recorded by the NE-elongation of stratovolcanoes and flanks vents NE-trending alignment (Fig. 2-2).

The NNE-to-NS-striking master faults of the LOFS record a strike-slip tectonic regime with similar orientation to that of the regional stress field. The NE-striking veins of this system are parallel to the orientation of σ_1 and perpendicular to σ_3 (Fig. 2-11). This fault-vein network reveals multiple reactivation events and coeval mineral precipitation at centimeter-scale (slickenfibers). Dilational jogs, which are likely to serve as efficient fluid conduits, are preferentially located at the intersection between NNE- and NE-striking faults (Fig. 2-4, Lolco and Ralco). Bladed-like texture of calcite aggregates sealing those dilational jogs suggests that fault activity triggered mineral precipitation by transient changes in the pore fluid pressure (Sibson, 1987; Weatherley and Henley, 2013).

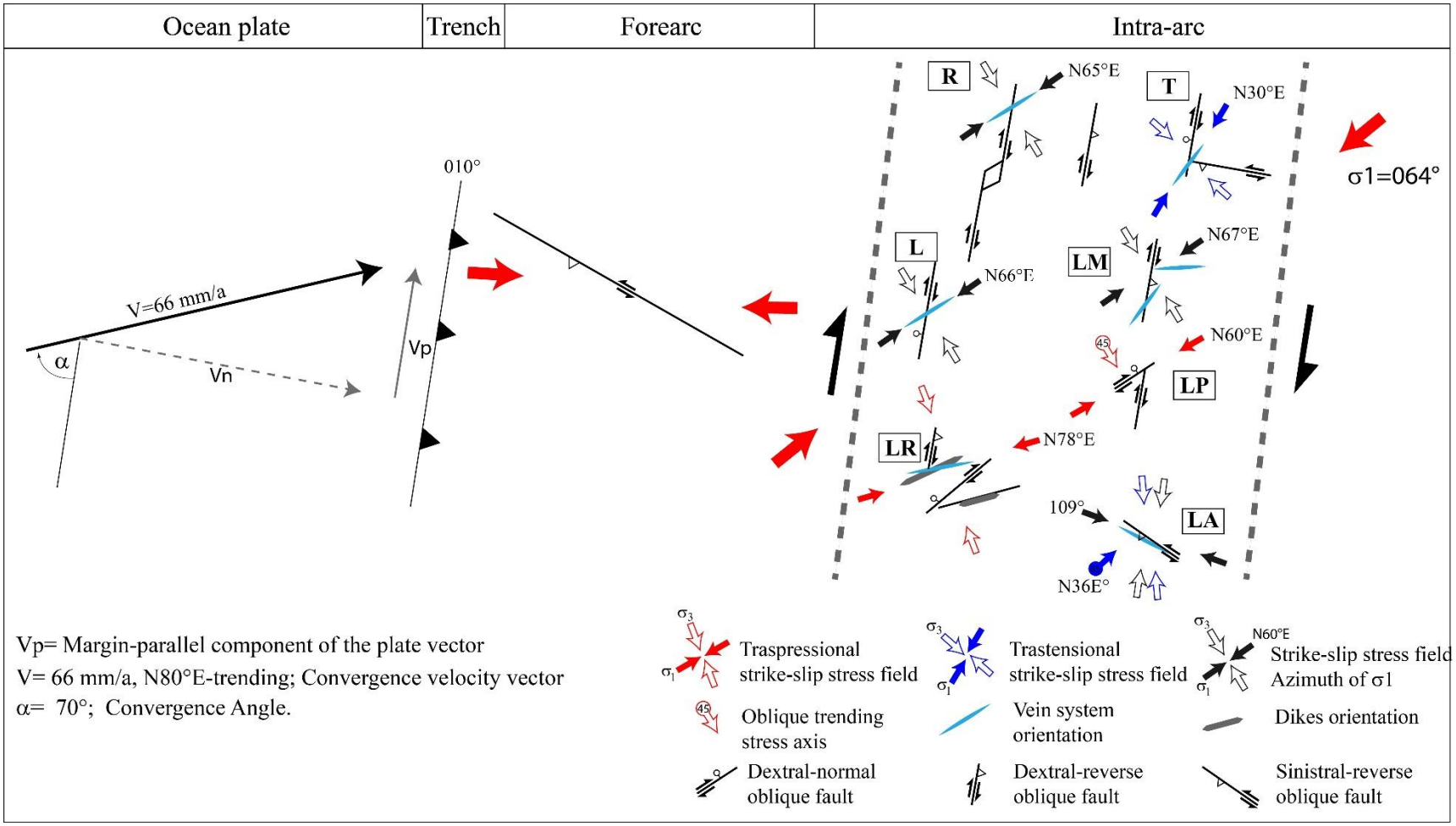

Figure 2-11. Schematic diagram showing oblique convergence at 38°S and the strain partitioning analysis with the orientation of maximum shortening axes proposed for the forearc, and σ1 direction calculated for the intra-arc region and the local stress field calculated for each structural site (R: Ralco, L: Lolco, T: Troyo, LP: La Poza, LM: Las Mentas, LR: Las Raices, LA: Las Animas). Details in Table 1.

The second order faults of the LOFS are spatially and genetically associated with ENE-striking veins compatible with the orientation of the calculated local stress field (Figs. 2-9 and Fig. 2-11; Las Raices structural site). Dikes preferentially intrude NE-striking decametric faults, which are reused by ENE-NE-striking tensional veins filled with zeolite and hydrothermal breccia lenses. Magma intrusion and superimposed hydrothermal activity record the favorable orientation of NE-ENE-striking faults and fractures to vertical magma/fluid transport at different times and depth. The third order structures of the LOFS are mainly represented by EW-striking tensional veins filled with zeolite and calcite, hybrid veins and hydrothermal breccias at the outcrop scale, which are compatible with the local stress field produced by second order faults (Figs. 2-9, 2-10, Las Mentas).

The ATF faults are composed of a thick damage zone and multiple fault cores and host thicker and more pervasive NW-striking veins and breccia bodies than the LOFS (Table 1; Figs. 2-9; 2-10, Las Animas structural site). Despite the fact that these NW-striking faults are kinematically compatible with the stress field, they have an unfavorable orientation for faulting and therefore, are likely to require high fluid-pore pressure to rupture (e.g. Sibson, 2004). Overpressure conditions are likely to form breccia bodies and stockworks at meter-scale and to produce large pore fluid pressure fluctuations. Therefore, structural elements related to the ATF faults are not only suitable for magma and/or hydrothermal migration but also for transient fluid storage.

Minerals precipitated within fault-fractures network are mainly zeolite (stilbite and laumontite) and locally calcite. The hydrothermal activity temperature recorded by laumontite + stilbite assemblage indicates crystallization temperatures at 110-170ºC (Liou et al., 1987). The different minerals do not reveal, at regional scale, a preferential distribution, or a clear spatial association with a particular structural element. Evidence recorded at the NW-striking discontinuities reflects the higher volume of mineral precipitation and associated larger damage zone. Similar mineralogy has been recognized at shallow depths (≤ 500 m) in active hydrothermal systems from the Southern Andes Volcanic Zone, such as Tolhuaca and Copahue Geothermal Fields (Mas et al., 2005; Mas, 2005; Melosh et al., 2012, 2010). These active systems are also spatially related to both the LOFS

and the ATF faults, suggesting that they might be the present-day active analogs of the structural sites analyzed.

Thus, results show the complexity in the spatial distribution of stress fields within strike-slip systems and their role in the geometrical distribution of fluid flow, part of which may account for the reactivation of inherited faults or strain incompatibilities at fault intersections. This work suggests that the structural elements, and the systems that they define, record a long-lived deformation coeval with magma/fluid migration within the crust, from early magmatic stages to late hydrothermal mineral precipitation (veins) that used, essentially, the same discontinuities over time and space.

2.6 Conclusions

A complete analysis of structural elements at the intra-arc domain of the LOFS and ATF between 38°S and 39°S reveals the mechanism of control that the regional and local stress fields exert on magma/fluid transport and arrest (Fig. 2-12). Conclusions are summarized as follows:

1- Deformation driven by oblique convergence is partially partitioned into each morphotectonic domain: subduction zone, forearc and intra-arc. At intra-arc domain, the tectonic regime corresponds to a strike-slip-dominated transpression.

2- The regional stress field at the intra-arc region is the result of two independent and homogeneous stress fields. The prevailing stress field solution corresponds to a transpressional stress regime with a subhorizontal, N64°E-trending σ_1 axis and a subhorizontal, N30°W-trending, σ_3 axis. The second identified stress field solution is a transtensional stress regime with a subhorizontal, N88°E-trending σ_1 axis and a subhorizontal N05°W-trending σ_3 axis.

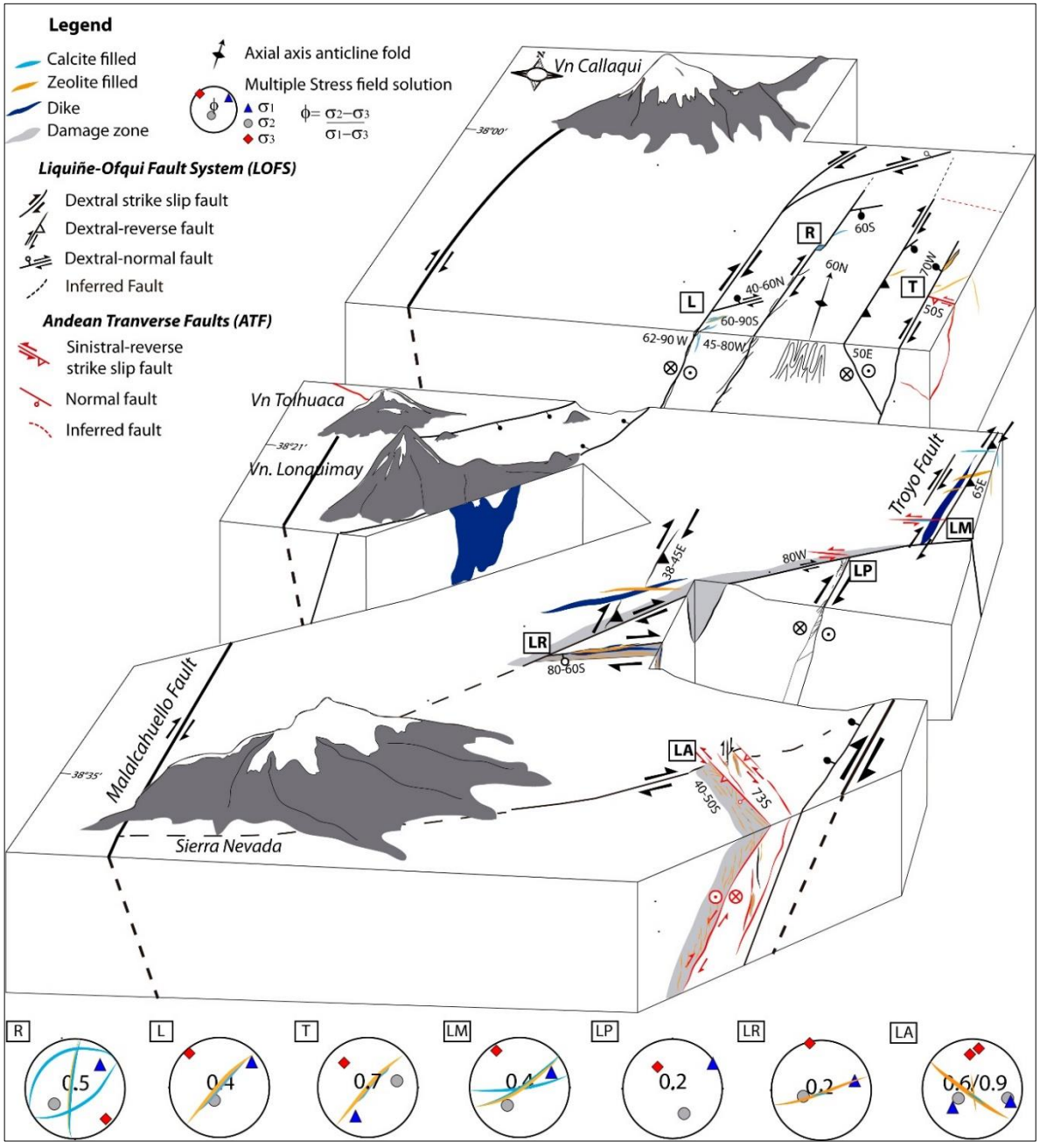

Figure 2-12. Schematic block diagram illustrating the geometrical arrangement and kinematics of faults and other structural elements at the northern termination of the LOFS (black lines) together with the main traces of the ATF (red lines). The cartoon shows the local stress field solutions and the veins main orientation at each structural site (R: Ralco, L: Lolco, T: Troyo, LP: La Poza, LM: Las Mentas, LR: Las Raices, LA: Las Animas).

3- Deformation is also further partitioned within the intra-arc domain by faults with NNE-, NE-, ENE- and NW-strikes. Features of these faults are:
    a. The NNE-striking faults show either right lateral strike-slip and dextral-reverse displacement, accommodating part of the trench-parallel and trench-orthogonal shortening components.
    b. The NE-striking faults are mostly hybrid faults with dextral-normal displacements. The associated transpressional local stress regime is clockwise-rotated with respect to the regional solution, thus favoring the emplacement of ENE-striking veins and dikes. At the intersection between NE- and NNE-striking faults, the stress regime is nearly compressive.
    c. The NW-striking faults document two different kinematic and dynamic behaviors. One of them is compatible with the regional stress field and accommodates the orthogonal to the trench-shortening component. The second stress field solution is decoupled from the prevailing regional stress field and has a stronger long-term deformation imprint at the outcrop scale.
4- The LOFS constitutes a localized fluid/magma pathway, where NNE-striking master faults focus the emplacement of syntectonic dike intrusions and the distribution of arrested paleo-fluids mainly at dilational jogs. The NE-striking fault-fractures host dikes and volcanic vents at kilometric scale, according with tensional fractures activated by the regional stress field. These structural elements constitute pathways for magma and hydrothermal fluid migration. The local stress field variation has a strong control on the vein systems and dikes orientation at outcrop scale.
5- ATF may constitute a large hydrothermal fluid reservoir with wide fault zones and a strongly developed fault-fracture network spatially associated with mineral precipitation.
6- The observations support a strong interplay between stress field, fault-fracture orientation and magma/paleofluid distribution. The fault-fracture network favorably oriented for reactivation with respect to the regional stress field constitute well-defined vertical pathways for magma/fluid transport through the lithosphere. These structures define restricted damage zones and thin veins systems. Conversely, fault-

fracture systems misoriented with respect to the regional stress field might act as efficient reservoir for magma and fluid under high fluid pressures.

2.7 Acknowledgments

I am grateful to Julie Rowland, Diego Morata, Martin Reich, and Gerd Sielfeld for fruitful discussions on the interplay among tectonics, volcanism, and hydrothermal fluid flow over the last years. Thanks to the generous help of Martin Lizama, Felipe Astudillo and Juan Ignacio Sanchez, during and after fieldwork. I sincerely thank Associated Editor Rob Govers and reviewers Elena Druguet and Ozgur Karaoglu for their constructive comments on this manuscript. I also thank Tom Mitchell for hosting PPF at the UCL Rock Preparation Laboratory and Jim Davy for his help with thin sections preparation and SEM analysis. Thanks, are also due to my colleagues Daniele Tardani, Rodrigo Gomila, Pablo Iturrieta, Ashley Stanton-Yonge and Felipe Aron. This paper is a contribution to the Andean Geothermal Center of Excellence (CEGA) FONDAP/CONICYT Project 15090013. Perez-Flores's PhD studies are funded by CONICYT-Beca Doctorado Nacional 21120519. Sanchez, P acknowledges support given by Millennium Science Initiative grant NC130065.

3 FRACTURE NETWORK, FLUID PATHWAYS AND PALEOSTRESS AT THE TOLHUACA GEOTHERMAL FIELD

3.1 Introduction

Tectonic activity in areas of intense heat flux, controls the dynamics of deformation, fluid-flow ascent and heat transfer (e.g. Barnhoorn et al., 2010; Nakamura, 1977; Sibson, 1996). These processes lead to the generation of structural elements (fault, veins, and joints), which are arranged as a complex fracture network. These structural elements are important pathway for the migration, ascent and/or emplacement of deep-seated fluids in hydrothermal systems because primary permeability and porosity is continuously sealed by hydrothermal mineralization (Bons et al., 2012; Rowland and Sibson, 2004; Zhang et al., 2008). Examining the nature, spatial distribution, and geometry of such fracture network can help to unravel the fundamental geological processes operating on both ancient and active geothermal systems (e.g. Brogi, 2008; Curewitz and Karson, 1997; Rowland et al., 2012).

Surface structural mapping of fault-fracture networks in active geothermal systems helps understanding the overall geometry and preferential orientation of fluid pathways– and eventually the nature of heat transfer – yet these are only proxies of the actual conditions operating at depth (Nukman and Moeck, 2013). Subsurface information can be collected using geophysical methods or by means of coring and drilling. Structural elements contained on recovered whole rock drilling pieces can then be spatially oriented with respect to the core axis, providing valuable inclination-only data about the general and downhole distribution of geological elements (e.g. Dobson et al., 2003; Ganerød et al., 2008; Moncada et al., 2012). However, random rotations of the rock pieces about the axis of the core prevent direct measurements of azimuthal data. Then, it becomes necessary to re-orient recovered rock pieces into the geographic coordinate system, to further re-orient measured structural elements. Re-orientation techniques are varied (e.g. MacLeod et al., 1994; Ureel et al., 2013; Virgil et al., 2015) and include the following: (1) drawing of a reference line as drill-bits are recovered; (2) plaster pieces on bottom to mark the spatial position of a certain piece or section of the core; (3) geophysical imaging of the drilled hole, and (4) paleomagnetic re-orientation (e.g. Didenko, 1996; Virgil et al., 2015; Zhang et al., 2007). Paleomagnetic core re-orientation has been successfully used in hydrocarbon exploration projects defining

fracture orientations confirmed by borehole image logging, mostly in sedimentary rocks (e.g. Alstine and Butterworth, 2002; Hailwood and Ding, 1995).

The Tolhuaca geothermal field (TGF, Melosh et al., 2010) is located on a tectonically active area of the southern Andean Volcanic Zone (Fig. 3-1a), south of the Callaqui-Copahue-Mandolegüe (CCM) first-order transfer zone (Fig. 3-1a). The CCM is a ENE-striking transitional zone regarding the nature of the rock basement, volcanism, and intra-arc tectonics (Fig. 3-1a) (e.g. Cembrano and Lara, 2009; Glodny et al., 2007; Melnick et al., 2006a). The regional to local-scale fracture network in and around of the TGF is spatially associated with both the Liquiñe-Ofqui Fault System and the Andean Transverse Faults (ATF) (Cembrano and Lara, 2009; Melnick et al., 2006a; Sanchez-Alfaro et al., 2016) (Fig. 3-1a). The LOFS includes a series of tens to hundred-kilometers long, subvertical NNE-striking master faults, NE-striking secondary faults and third order ENE-to-EW-striking faults, all cropping out from the area around the Callaqui volcano for about 1200 km south to the Golfo de Penas area (e.g. Cembrano et al., 2000; Lange et al., 2008; Veloso et al., 2009). The LOFS records a transpressional tectonic regime with a predominant dextral strike-slip deformation pattern (e.g. Lavenu and Cembrano, 1999; Pérez-Flores et al., 2016; Rosenau et al., 2006). This system is spatially and genetically associated with major stratovolcanoes (e.g. Copahue, Callaqui, Llaima, Lonquimay, Tolhuaca) and with shallow seismic activity (< 25 km depth) (Fig. 3-1b) (Barrientos and Acevedo-Aránguiz, 1992; Lange et al., 2008; Legrand et al., 2011). The ATF includes a series of NW-striking structural elements – most probably inherited from a pre-Andean architecture (e.g. Radic, 2010) – with sinistral-reverse kinematics and local normal-slip re-activation (Pérez-Flores et al., 2016). These faults accommodate deformation driven by oblique convergence between Nazca and South America plates, with different kinematics depending of the preferential orientation of the fault-fracture network (Pérez-Flores et al., 2016). The transpressional regional tectonic regime, characterized by N65°E-trending σ_1 favors dextral/oblique displacement along NNE-striking faults, NE-ENE-striking extensional fractures and hybrid faults, and sinistral-reverse NW-striking faults (Lavenu and Cembrano, 1999; Pérez-Flores et al., 2016). Strain partitioning at these different tectonic domains control the chemistry of the volcanic products, the geometric and spatial arrangement of volcanic centers, as well as the

hydrothermal activity in the intra-arc zone (Lara et al., 2006; Pérez-Flores et al., 2016; Radic, 2010; Sánchez et al., 2013; Sepúlveda et al., 2005; Sielfeld et al., 2016; Tardani et al., 2016).

Although these major faults have been widely recognized in the field at various scales, there is no published information on the subsurface distribution and orientation of structural elements in and around the TGF (Lohmar et al., 2012; Melosh et al., 2012, 2010). In this contribution, it is report new structural data collected from a vertical non-oriented, ca. 1080 m deep, borehole drilled in the NW flank of the Tolhuaca volcano (Tol-1). GeoGlobal Energy LLC kindly provided the Tol-1 drill core sampled during an exploration campaign held in 2012. I analyze standard mini-cores from the Tol-1 core using paleomagnetic techniques allowing the isolation of characteristic remanent magnetic vectors, thus providing a tool for the re-orientation of the drilled core. The orientation and characteristics of the local strain and stress fields of the TGF were then estimated with re-oriented fault-slip data.

3.2 Geological and tectonic framework

The Tolhuaca volcano is located at the intersection of the northern termination of the LOFS and a NW-striking fault of the ATF (Fig. 3-1a). Major structural elements present around of the volcanic edifice are spatially related to one of these faults, which could have provided a long-lived potential pathway for the ascent of deep-seated fluids (Pérez-Flores et al., 2016; Sanchez-Alfaro et al., 2016). Tolhuaca is a stratovolcano, which erupted both lava and pyroclastic flows, rising ca. 900 m above its basement – mostly Oligo-Miocene volcano-sedimentary rocks and Miocene granitic rocks of the Patagonian Batholith (Fig. 3-2) (Suárez and Emparan, 1997). Basaltic and basaltic-andesitic lava and pyroclastic flows, interbedded with andesite and dacite lava flows dominate the eruptive products (Lohmar et al., 2012; Melosh et al., 2012), which built up the volcanic edifice from at least ca. 290 ka (Ar-Ar method, Polanco et al., 2014). On the NW flank of Tolhuaca volcano two events of NW-striking fissural volcanism are dated to 160 ± 30 and 60 ± 30 ka (Ar-Ar method, Polanco et al., 2014), while the unglaciated NW-fissure and cone confirm volcanic activity after the last glaciation (<24.000 yr. B.P.) (Hulton et al., 2002; Kaplan et al., 2008; McCulloch et al., 2000). Nevertheless Tolhuaca volcano has no record of historical eruptions (Lohmar et al., 2012; Suárez and Emparan, 1997; Thiele et al., 1987). At the NW-fissure location, there are

several high-sulfur springs and fumaroles aligned on a NW-trending direction (e.g. Heuser, 1997; Melosh et al., 2010) suggesting the existence of one NW-striking fault that promotes the hydrothermal and magma ascent. Geochemical studies suggest the existence of a geothermal reservoir in this area with an estimated temperature of about 220º-300ºC (Melosh et al., 2010). These series of high-sulfur springs and fumaroles define the Tolhuaca Geothermal System (Fig. 3-2) (TGS; Melosh et al., 2010). The Lonquimay volcano, located 8 km to the south east of Tolhuaca volcano (Fig. 3-2), is an andesitic-basaltic stratovolcano built during the Upper-Pleistocene (mainly ca 100 ka; Polanco et al., 2014). The NE-flank of Lonquimay volcano consists of more than ten Holocene, NE-trending aligned, monogenetic cones (Polanco et al., 2014) with the last activity on the eruption of the Navidad cone in 1989. The radiometric ages record synchronous activity between the Lonquimay and Tolhuaca volcanoes (Polanco et al., 2014), using NE- and NW-striking fracture networks, respectively.

Regional to local-scale geometrical arrangements of faults, veins, and other structural elements of the LOFS develop in between two major NS-to-NNE-striking master faults linked by several NE-striking splays (Fig. 3-1b) (Melnick et al., 2006a; Pérez-Flores et al., 2016; Rosenau et al., 2006). At the northernmost end of the LOFS (near the Tolhuaca, Callaqui and Lonquimay volcanoes) a series of *en echelon* NE-striking faults define a horse-tail geometry termination where a series of bends in the trace of these faults result in local dilatational jogs (e.g. Cembrano and Lara, 2009; Pérez-Flores et al., 2016; Rosenau et al., 2006). The Biobío-Aluminé Fault System is a blind sinistral-reverse fault which belongs to the ATF and is spatially associated with a linear NW-trending valley where it is possible to observe discrete fault outcrops (Melnick et al., 2006a; Muñoz et al., 1988). The dextral strike-slip LOFS crosscuts and displaces the Biobío-Aluminé Fault System.

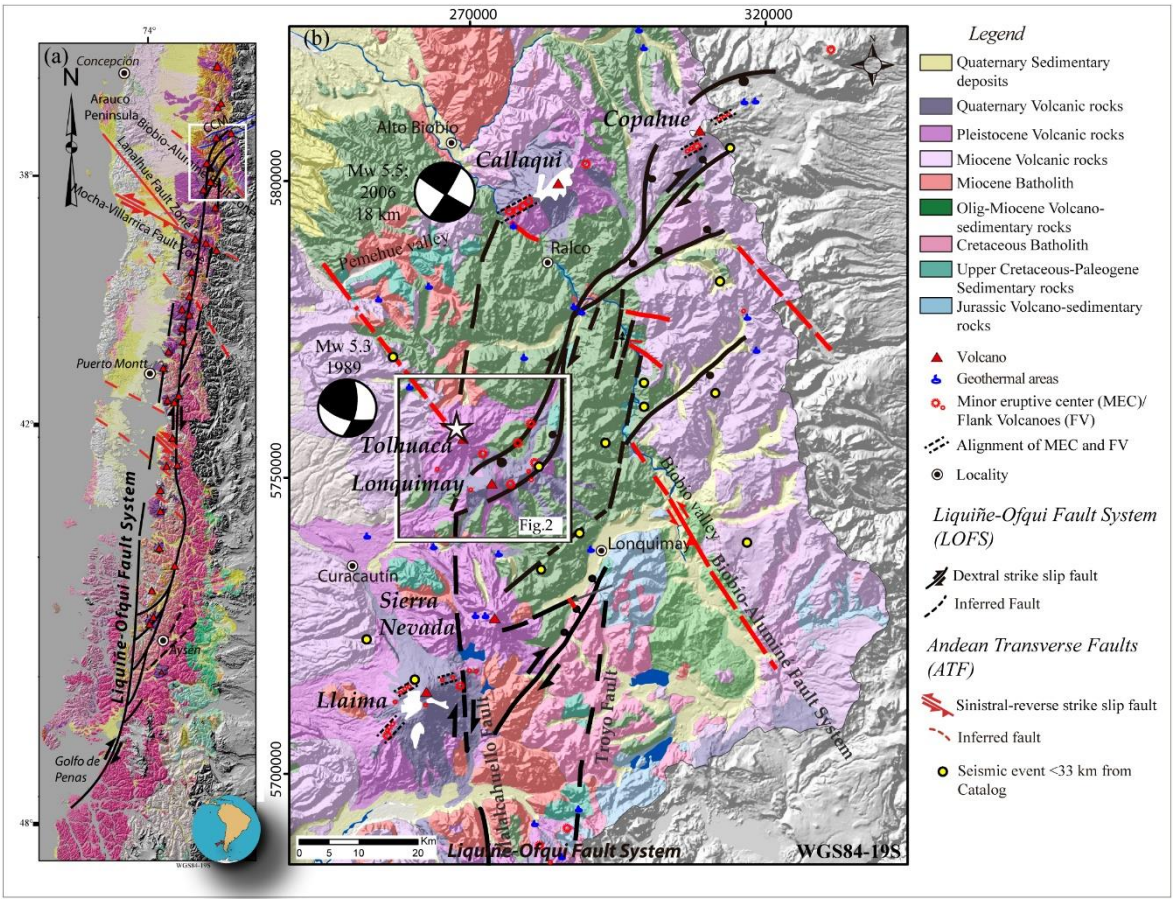

Figure 3-1. (a) Composite Digital Elevation Model (DEM) and 1:1.000.000 geological map of the Southern Andes Volcanic Zone (Pérez-Flores et al., 2016; Sánchez et al., 2013) shows the study area (white square). Regional map showing the location and extent of the LOFS (black lines), ATF (red lines) and main Holocene volcanoes (red triangles). (b). Detailed map of the study area (white square on Fig. 3-1a) showing the main faults and lineaments of the LOFS and ATF (e.g. Biobío Aluminé Fault System), which are spatially and genetically associated with the Tolhuaca and the Lonquimay volcanoes, clusters of minor eruptive centers, hot springs and shallow seismicity (Barrientos and Acevedo-Aránguiz, 1992; Lange et al., 2008; Legrand et al., 2011). The white star shows the location of drill hole Tol-1, drilled by GeoGlobal Energy Chile (GGE Chile).

The Tolhuaca volcano is located on a NNE-striking master fault of the LOFS, close to a releasing bend defined by NE-striking faults at the Lonquimay volcano location. The extensional nature of the underlying NE-striking faults is documented by NE-aligned flank vents and a NE-striking fissure vent, both located at the NE-flank of the Lonquimay volcano (Fig. 3-2) (Pérez-Flores et al., 2016; Rosenau et al., 2006).

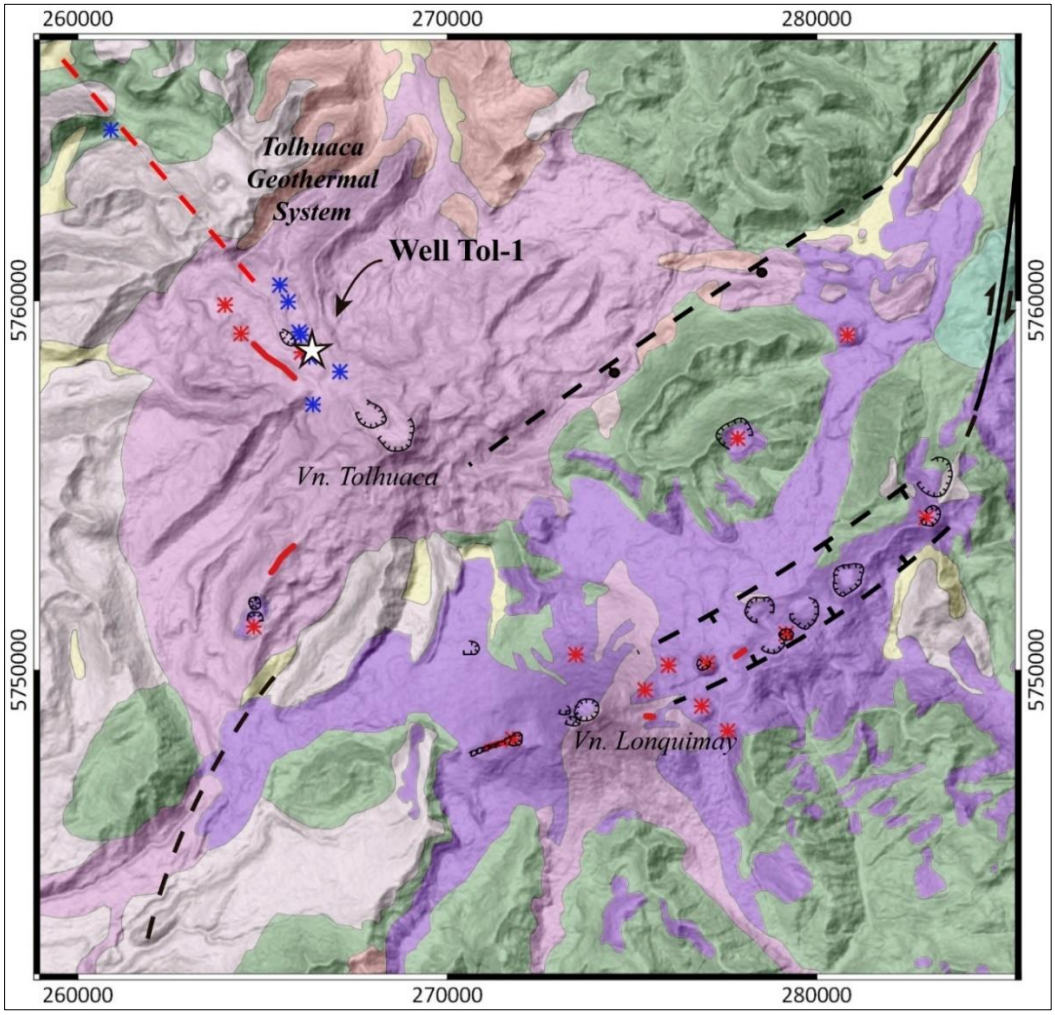

Figure 3-2. Geological map at 1:100.000 scale (Suárez and Emparan, 1997) showing the Tolhuaca and Lonquimay volcanoes. The LOFS (black line) has been interpreted to form a dilatational jog geometry genetically associated with Lonquimay volcano and clusters of flank vents (red asterisk) (Pérez-Flores et al., 2016; Rosenau et al., 2006). Flank vents, fissures (red line) and fumarole areas (blue asterisk) are aligned in a NW trend (red dashed line) at the NW-flank of the Tolhuaca volcano, where the Tolhuaca Geothermal System (TGS) is located. See the legend in Fig. 3-1.

3.2.1 Tolhuaca geothermal system

Geothermal exploration campaigns including surface mapping, fluid geochemistry analyses, resistivity measurements and borehole logging have revealed the existence of a high enthalpy reservoir in the area (Lohmar et al., 2012; Melosh et al., 2010). Two slim holes (Tol-1 and Tol-2) and two larger diameter wells (Tol-3 and Tol-4) were drilled vertically down to 2117 m below surface. Tol-1 is the only one performed by diamond core drilling, with whole-rock recovery allowing for a detailed mineralogical and geometric analysis of

faults, veins, and fractures. Temperature logging and analyses conducted on fluid sampling confirm the presence of a geothermal reservoir at ca. 1.5 km depth, at liquid-saturated conditions with temperatures up to 300°C and a strong meteoric water component (Melosh et al., 2012). The main reservoir is overlain by a steam heated aquifer at shallow depths that reaches up to 160 °C of temperature (Melosh et al., 2012, 2010).

The Tol-1 borehole (Fig. 3-2) was cored through a thick pile of volcano-clastic deposits of mostly basaltic andesite composition. Predominant rock units correspond to lava flows and related breccia, volcanoclastic sediments, and minor tuff layers (see supplementary figure SM1). Hyaloclastites and pillow breccia occur at different levels in the Tol-1 core, indicating eruptions in contact with glacial ice and/or water (Lohmar et al., 2012) . A series of faults, joints, veins, and hydrothermal breccia are present all along the core (Fig. 3-3).

The alteration intensity is variable through the core, even at thin-section scale; the groundmass alteration is stronger than the phenocrysts. The following three main alteration zones are identified along the Tol-1 core: (1) shallow (< 300 m depth) argillic characterized by clay minerals (smectite, interlayered chlorite-smectite), iron oxides and stilbite; (2) intermediate (300-670 m depth) sub-propylitic dominated by occurrence of interlayered chlorite-smectite and illite; and (3) deep (670-1073 m depth) propylitic alteration zones characterized by the occurrence of epidote and chlorite (Lizama et al., 2015; Sanchez-Alfaro et al., 2016). Mineralogy of argillic alteration records a temperature < 200 °C (Lizama et al., 2015; Sanchez-Alfaro et al., 2016), while propylitic alteration forms in a broad range temperature between 200 to 350 °C (Reyes, 1990; Sanchez-Alfaro et al., 2016; Stimac et al., 2015). Mineralogical and geochemical studies (Lizama et al., 2015; Sanchez-Alfaro et al., 2016) of the TGS suggest that the system evolution is controlled by the interaction of mineralogical, hydrological and structural process segmented in depth, which affect the mechanical and hydrological properties of host-rock (Sanchez-Alfaro et al., 2016). In that sense, the clay-rich alteration zone (argillic zone) modifies the host-rock mechanical properties, promoting the generation/activation of shear faults and inhibiting highly permeable extensional fracturing (Sanchez-Alfaro et al., 2016). In contrast, in the deep up flow zone the less pervasive formation of clay mineral assemblages has allowed retention of

rock strength and dilatant behavior during slip, sustaining high permeability conditions (Sanchez-Alfaro et al., 2016).

Figure 3-3. Tol-1 coherent segment core of andesite (a) shows a vein and the spatially associated sample (white lines) used for paleomagnetic analysis. (b) Vertical view of the axis´ core containing a fault plane with slickenlines; (c) side view of Tol-1 core including banded vein filled with quartz and zeolite.

Sanchez-Alfaro et al, (2016) recognized four veins mineral paragenetic stages in the Tol-1 borehole. The paragenetic stages are present throughout Tol-1 with mineralogical variations. The earliest stage (S1) consists of a sequence of iron oxides (hematite), bands of amorphous silica and/or chalcedony and late pyrite with minor chalcopyrite. Clay mineral assemblages including smectite, minor interlayered chlorite-smectite, stilbite and epidote at depth dominate the stage S2, whereas calcite with lattice-bladed texture and quartz with various textures (euhedral, plumose, and microcrystalline) represent the stage S3. The S4

stage consists of microcrystalline quartz, amorphous silica phases and locally calcite, at deep propylitic zone by the occurrence of wairikite and late prehnite.

3.3 Methodology

3.3.1 Structural data collection and sampling

I measured a total of one hundred cm- and mm-scale structural elements – including faults, hybrid faults, veins, and breccia– recovered from the Tol-1 drill core (Fig. 3-3), taking as a reference frame the core axis and an arbitrary line drawn on the surface of the each recovered piece (Fig. 3-4). I drew an arbitrary reference line as perpendicular as possible to all structural elements present on the piece (or a coherent and adjacent series of them). Structural elements were only measured on pieces/sets of pieces longer than 40 cm, avoiding any possible rotation about an axis different from the axis of the core of the piece and therefore of the associated structural elements. The structural data collected include (Fig. 3-4): (1) the spatial orientation of a given structural element taken as a true dip (α_s) and relative strike (β_s, with respect to the reference line); (2) sense of movement (e.g. Doblas, 1998; Petit, 1987), (3) thickness in mm (ε), (4) mineral infill and (5) slickenfiber, striae and/or slickenline orientation (measured as a rake angle, ρ) (Fig. 3-4b, see mapping details at supplementary figure SM1).

I collected two hundred standard paleomagnetic mini-cores (20 mm diameter and length), oriented by using their true inclination (α) and relative declination (β, with respect to the arbitrary reference line) (see supplementary figure SM1; Fig. 3-4c). The mini-cores were collected in segments where the structural data was measured and sampled.

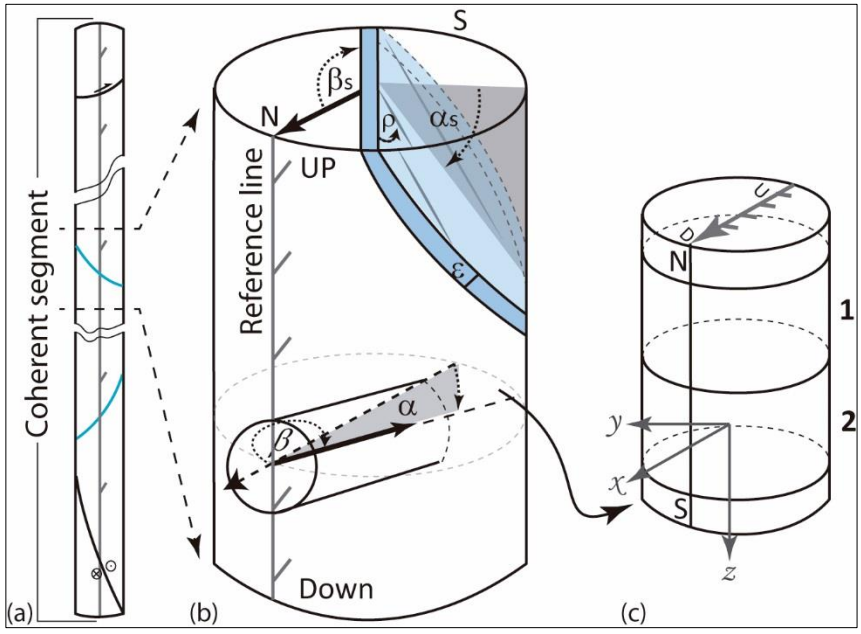

Figure 3-4. Cartoon showing the sampling and structural measurement methodology. (a) For each coherent segment (or adjacent core pieces) containing structural elements, a reference line was drawn. (b) The spatial orientation of each structural element includes: (1) true dip (α_s) and relative strike (β_s, with respect to the reference line), (2) displacement direction, (3) thickness in mm (ε), (4) mineral infill and (5) orientation – measured as a rake angle (ρ) – of the striae, slickenline and mineral fiber. (c) A standard paleomagnetic mini-coring oriented by their true plunge (α) and relative trend (β, with respect to the arbitrary reference line) was measured for each coherent segment.

3.3.2 Paleomagnetic measurement

I demagnetized all mini-cores (Fig. 3-4c) by means of incremental temperature technique at the Petrofabrics and Paleomagnetics Laboratory of the University of Hawai´i at Manoa (SOEST-HIGP) using a MMTD-80 thermal demagnetizer. The demagnetization incremental steps were 50ºC from room temperature up to 600º-700ºC. It is measured orientation and intensity of magnetic remanent (RM) vectors, at each step for all specimens, using the JR-5 Spinner Magnetometer. It is used the "principal component analysis" of Kirschvink (Kirschvink, 1980) with the aid of Tauxe (1998)´s PMagPy routines for the orientation of ChRM vectors from the demagnetization paths of each specimen. ChRM vectors with MAD (maximum angular deviation) values larger than 15º are ill-defined and therefore rejected for further analyses (e.g. Butler, 1998).

It is rotated each individual ChRM vector declination about a vertically oriented axis to fit to a determined reference frame. The reference frame corresponds to the orientation of

the Geocentric Axial Dipole (GAD) model (000°, -57.7°) (Butler, 1998) calculated for the Tolhuaca area (38.29°S and 71.67°W). It is worth noticing that this reference frame assumes that no rotation affected the Tol-1 site since, at least, the age of the deepest drilled lava flow (i.e. < 1 My Lohmar et al, 2012). The fitting procedure of NRM vectors declination data to the reference frame provided the rotational declination angle for each individual (set of) piece. It is rotated piece by piece, and hence the measured structural data using the rotational declination angle.

3.3.3 Structural data analysis

It is determined the orientation of strain and stress fields from the kinematic and dynamic analysis of the re-oriented fault-slip data. The average orientation of the P (shortening) and T (stretching) axes (e.g. Marrett and Allmendinger, 1990) calculated for each fault allows to estimate the orientation of the strain field. These axes restrict on space the orientation of both shortening and stretching quadrants. It is estimated the orientation of the principal stress axes through the "Multiple Inverse Method" (e.g. Yamaji, 2000) using the stress regimes defined by Ritz (1994) as tensional, compressional or strike-slip. The method estimates a best-fit stress tensor for each of all possible subpopulations drawn from the entire structural data. Best-fit tensor solutions are then plotted on separate stereonets – one for σ_1 and other for σ_3 – using a color-coded symbol according to its stress ratio ($\varphi=\sigma_2-\sigma_3/\sigma_1-\sigma_3$) and with an attached tail pointing towards the orientation of the complementary axis (i.e. tail on σ_1 points towards σ_3). Common stress field solutions are seen as clusters of sub-solutions with similar colors and with their tails pointing towards a common orientation (e.g. Otsubo et al., 2006; Yamaji, 2000). Thus, for the obtained stress field, the difference between observed and theoretical slip direction obtained corresponds to the misfit angle. The solution with more activated faults with misfit angles less than 30° is the stress axes orientation solution.

3.4 Results

Fig. 3-6 shows the general lithologies and alteration zones identified along of Tol-1 core (Fig. 3-6a) and temperature/gradient (°C) profile measured (Fig. 3-6b). This information contextualizes into the Tol-1 core geology the paleomagnetic and structural results.

3.4.1 Demagnetization patterns and RM vectors (Table 2).

Natural remanent magnetization (NRM) intensities (prior to thermal demagnetization) are variable, ranging from 10.6 to 34.9x10^3 mA/m. Thermal demagnetization vector patterns are stable with incremental demagnetization steps going towards the origin on a nearly linear trajectory from the beginning to the end of the core (Figs. 3-5a, 3-5b). The fractional thermal remanent demagnetization (Fig. 3-5) allows calculating the blocking temperatures of magnetic signal carrying on minerals of each mini-core along the Tol-1 core (Fig. 3-6c). The bulk of demagnetization occurs in the range 400° to 675°C (Fig. 3-6c), suggesting the presence of magnetite, with varying Ti-content, as the principal remanence carrier. Magnetization left after demagnetization at >645ºC suggest minor amounts of hematite (Fig. 3-6c).

NRM vectors record inclinations mainly between -80° to -50° (Fig. 3-6d) yet eight samples yielded positive inclinations. The local normal polarity field inclination, defined by GAD model, is -58°. Samples yielding normal polarity inclinations are, within statistical error, close to the theoretical GAD inclination (-57.7 ± 20°). (e.g. Butler, 1998; Tauxe, 1998) for the Tol-1 borehole latitude. The inclinations of NRM vectors recorded along to the Tol-1 core are mainly normal polarity. I did not find any continuous break from normal (- inclination) to reverse (+ inclination) polarity, but instead peaks on where sudden and short polarity changes occur. Scattered reverse polarity specimens could record polarity excursions or errors due to incorrect up/down assessment in the core segments. The origin of these reverse polarities need to be tested so that I decide to reject these samples and its associated structural data.

Table 2. Paleomagnetic sampling information and thermal demagnetization results showing: N, steps number; T. min/T. max, temperature (°C) minimum and maximum; MAD, maximum angular deviation; declination/inclination in sample coordinate and RM vectors in geographic coordinate used by fault and veins reorientation.

Sampling information							*Demagnetization*						*RM vector (Geo. Coord.)*	
Sample	*Lithology*	*Aleteration*	*Trend*	*Hade*	*Plunge*	*Depth*	*N*	*T. min*	*T. max*	*MAD*	*Declination*	*Inclination*	*Declination*	*Inclination*
P63A2	Andesite flow interior	Unalterated	183	88	3	22	7	100	500	2.4	36	20	239	-49
P65A2	Amygdaloidal andesite. Flow Breccia	Unalterated	184	91	-1	33	11	100	600	3.7	22	-22	322	-59
P66B2	Amygdaloidal andesite. Flow Breccia	Argillic	191	88	3	37	10	100	575	3.8	29	15	249	-56
P64B1	Amygdaloidal andesite. Flow Breccia	Argillic	184	90	1	43	10	100	575	3.2	11	25	206	-63
P1B1	Andesite flow interior	Argillic	179	81	9	81	8	200	550	4.5	336	21	142	-52
P1B2	Andesite flow interior		179	82	8	81	5	200	450	2.5	341	29	153	-48
P2C1	Andesite flow interior	Argillic	194	87	3	96	8	300	575	6.6	333	-10	89	-62
P2C2	Andesite flow interior		194	87	3	96	9	200	575	4	336	18	147	-59
P3A2	Andesite flow interior	Argillic	183	89	2	97	11	0	575	3.9	157	17	238	63
P3B1	Andesite flow interior		183	90	0	97	7	200	525	8.9	153	21	233	57
P4B1	Andesite flow interior	Argillic	200	89	1	99	6	350	550	1.5	335	18	148	-59
P5A2	Andesite flow interior	Argillic	185	89	1	103	11	0	550	4.5	329	-4	89	-58
P6A2	Amygdaloidal andesite. Flow interior	Argillic	187	89	2	128	13	0	625	2	24	23	229	-56
P7A2	Amygdaloidal andesite. Flow interior	Argillic	186	89	2	129	12	0	600	2.7	209	20	132	56
P8A2	Amygdaloidal andesite. Flow interior	Argillic	175	91	-1	145	11	200	675	2.3	14	11	229	-74
P9B2	Andesite flow breccia	Sub-propylitic	187	87	3	161	14	0	650	3	34	-6	284	-56
P10A2	Andesite flow interior	Argillic	233	91	-1	180	11	200	625	1.9	23	-16	0	-62
P11A2	Andesite flow interior	Argillic	188	88	3	181	9	200	575	2.8	12	35	204	-51
P12B2	Andesite flow interior	Argillic	182	90	0	193	7	300	600	2.6	322	-17	65	-49
P13A2	Andesite flow interior	Argillic	176	90	0	199	10	100	575	3.3	334	16	119	-59
P14A2	Andesite flow interior	Argillic	227	88	2	198	8	100	525	3.3	329	-9	124	-58
P15A2	Andesite-basaltic, flow interior	Argillic	173	90	0	241	9	200	575	2.3	13	-25	327	-62
P16A2	Andesite-basaltic, flow interior	Argillic	183	91	-1	271	7	200	525	3.8	17	25	217	-61
P17A2	Andesite-basaltic, flow interior	Sub-propylitic	193	87	3	275	6	100	450	3.5	179	38	195	55
P18A2	Andesite-basaltic, flow interior	Sub-propylitic	198	86	4	292	8	300	575	6.3	2	-31	15	-63
P19A1	Andesite-basaltic, Breccia	Sub-propylitic	172	91	-1	298	-	-	-	-	-	-	-	-
P20B1	Andesite flow interior	Sub-propylitic	184	89	1	376	9	200	575	5.6	39	13	252	-49
P21B1	Andesite flow breccia	Sub-propylitic	179	93	-3	394	13	200	675	5.4	17	46	195	-44
P22B1	Andesite flow breccia	Sub-propylitic	180	89	1	411	11	0	575	6.3	351	38	168	-50
P23B2	Andesite flow breccia	Sub-propylitic	194	89	2	410	10	0	550	8	344	29	168	-56
P24A2	Andesite flow breccia	Sub-propylitic	179	92	-2	413	13	200	675	4.5	327	29	132	-49
P25A2	Andesite flow breccia	Sub-propylitic	172	90	0	415	9	350	625	1.8	318	-1	81	-48
P26A2	Andesite flow breccia	Sub-propylitic	178	85	6	418	11	200	625	4.1	28	21	223	-52
P27A2	Volcanoclastic andesite, Tuff	Sub-propylitic	184	89	2	428	12	300	675	5.3	353	1	116	-83
P28B1	Andesite flow interior	Sub-propylitic	181	88	2	447	13	0	625	3.9	348	-31	22	-59
P29B1	Andesite-basaltic, flow interior	Sub-propylitic	188	87	4	463	15	0	675	1.7	17	-17	318	-69
P30B1	Andesite-basaltic, flow interior	Sub-propylitic	183	89	2	470	9	200	575	3	338	4	108	-66
P31A2	Andesite-basaltic, flow interior	Sub-propylitic	177	95	-5	489	8	300	575	3.4	340	-17	41	-61
P32A2	Andesite-basaltic, flow interior	Sub-propylitic	189	90	1	489	7	350	575	3	336	-17	63	-62
P33B1	Andesite flow interior	Sub-propylitic	182	91	-1	561	10	100	575	3.1	9	11	224	-76
P34A1	Andesite flow breccia	Sub-propylitic	173	87	4	566	11	200	625	5.6	14	11	216	-70
P35B	Andesite flow breccia	Sub-propylitic	177	87	3	567	13	200	675	4.3	7	24	191	-63
P36B	Pillow Breccia and Hyaloclastite Andesite	Sub-propylitic	169	90	0	579	11	200	625	2.1	15	11	223	-71
P37B1	Andesite flow interior	Sub-propylitic	180	88	3	597	12	100	625	3.5	340	8	119	-67
P38B1	Andesite flow interior	Sub-propylitic	186	88	2	607	9	200	575	2.4	5	-14	342	-77
P39B1	Volcanoclastic andesite, Tuff	Sub-propylitic	178	92	-2	631	10	100	575	4.8	353	-13	25	-74

Table 2. Continuation.

Sampling information							*Demagnetization*						*RM vector (Geo. Coord.)*	
Sample	*Lithology*	*Aleteration*	*Trend*	*Hade*	*Plunge*	*Depth*	*N*	*T. min*	*T. max*	*MAD*	*Declination*	*Inclination*	*Declination*	*Inclination*
P40B1	Volcanoclastic andesite, Tuff	Sub-propylitic	185	88	2	660	8	0	500	9.2	4	-24	355	-68
P41B1	Volcanoclastic andesite, Tuff	Sub-propylitic	181	88	2	697	9	100	550	4.6	172	19	204	71
P42B1	Volcanoclastic andesite, Tuff	Sub-propylitic	181	93	-3	713	12	0	600	4.1	343	0	82	-73
P43B1	Volcanoclastic andesite, Tuff	Propylitic	181	90	0	768	10	200	600	6.3	14	15	223	-69
P44B	Volcanoclastic andesite, Tuff	Propylitic	181	90	0	806	8	200	550	4.3	350	-22	23	-66
P45B1	Volcanoclastic andesite	Propylitic	180	89	1	824	9	200	575	5.7	19	19	222	-63
P46B	Volcanoclastic andesite	Propylitic	184	91	-1	830	9	200	575	4.2	18	18	229	-65
P47B	Volcanoclastic andesite	Propylitic	180	91	-1	866	10	100	575	3.1	10	6	242	-79
P48B	Volcanoclastic andesite	Propylitic	182	92	-2	901	5	200	600	4.4	355	-3	47	-83
P49B	Andesite flow interior	Propylitic	181	89	2	920	10	100	575	5.5	353	15	158	-73
P50B1	Andesite flow interior	Propylitic	181	89	1	928	6	400	600	5.3	21	15	232	-64
P51B1	Andesite flow interior	Propylitic	179	90	0	948	11	100	600	10.4	183	-7	21	83
P52B1	Andesite flow interior	Propylitic	194	89	2	955	13	0	625	8	341	-4	97	-71
P53B1	Andesite flow interior	Propylitic	177	90	0	961	11	0	575	9.2	1	1	219	-89
P54B	Andesite flow interior	Propylitic	193	89	2	975	11	0	575	10	357	-4	64	-86
P55B1	Andesite flow interior	Propylitic	181	91	-1	976	10	100	575	12.2	360	4	172	-87
P56B1	Andesite flow interior	Propylitic	178	89	2	992	12	0	600	2.9	359	11	173	-78
P57B	Andesite flow interior	Propylitic	177	89	2	994	14	0	650	5.6	191	-3	66	78
P58B1	Andesite flow interior, breccia	Propylitic	184	93	-3	1002	8	450	650	5.7	349	-19	31	-66
P59A	Pillow Breccia and Hyaloclastite Andesite	Propylitic	179	89	2	1038	13	200	675	6	13	27	202	-59
P60B	Pillow Breccia and Hyaloclastite Andesite	Propylitic	172	90	0	1042	4	525	600	3.8	107	8	254	16
P61B	Andesite flow interior, breccia	Propylitic	183	89	2	1071	14	100	675	8.1	12	-4	280	-78
P62A1	Andesite flow interior, breccia	Propylitic	193	90	0	1085	13	0	625	9.5	9	3	265	-81

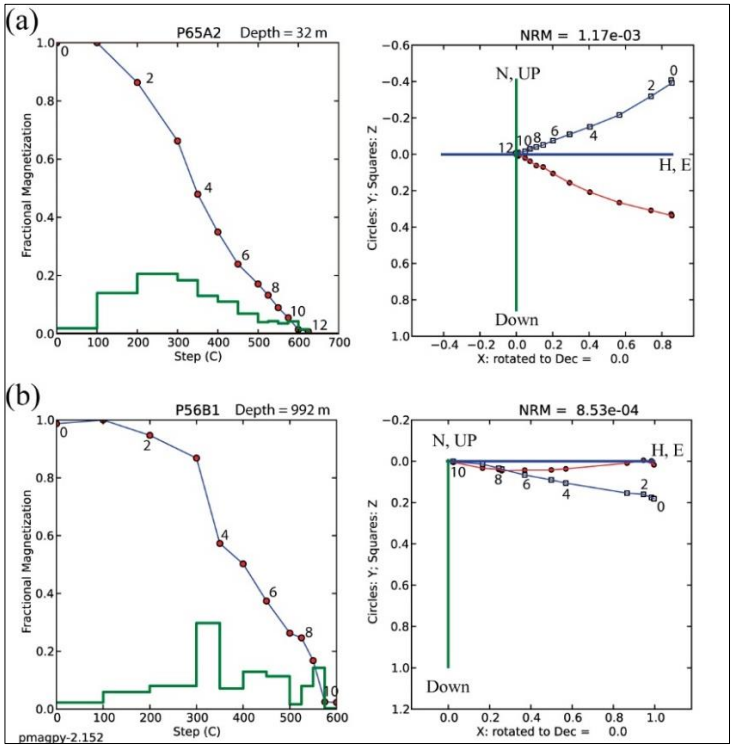

Figure 3-5. Results of progressive thermal demagnetization of representative samples, from 32 m (a) and 992 m (b) depth, displayed by partial demagnetization graphic (left wards) and vector end point diagrams (right wards) (Zijderveld, 1967). For Zijderveld diagrams, each data point represents the projection of the magnetization vector for individual demagnetization steps onto the horizontal (red circle solid symbols) and vertical (blue square open symbols) plane. Numbers adjacent to data points indicate the demagnetization step (leftwards). Sample number, sample depth and NRM intensity are shown at the top of each diagram. Data shown in core coordinates.

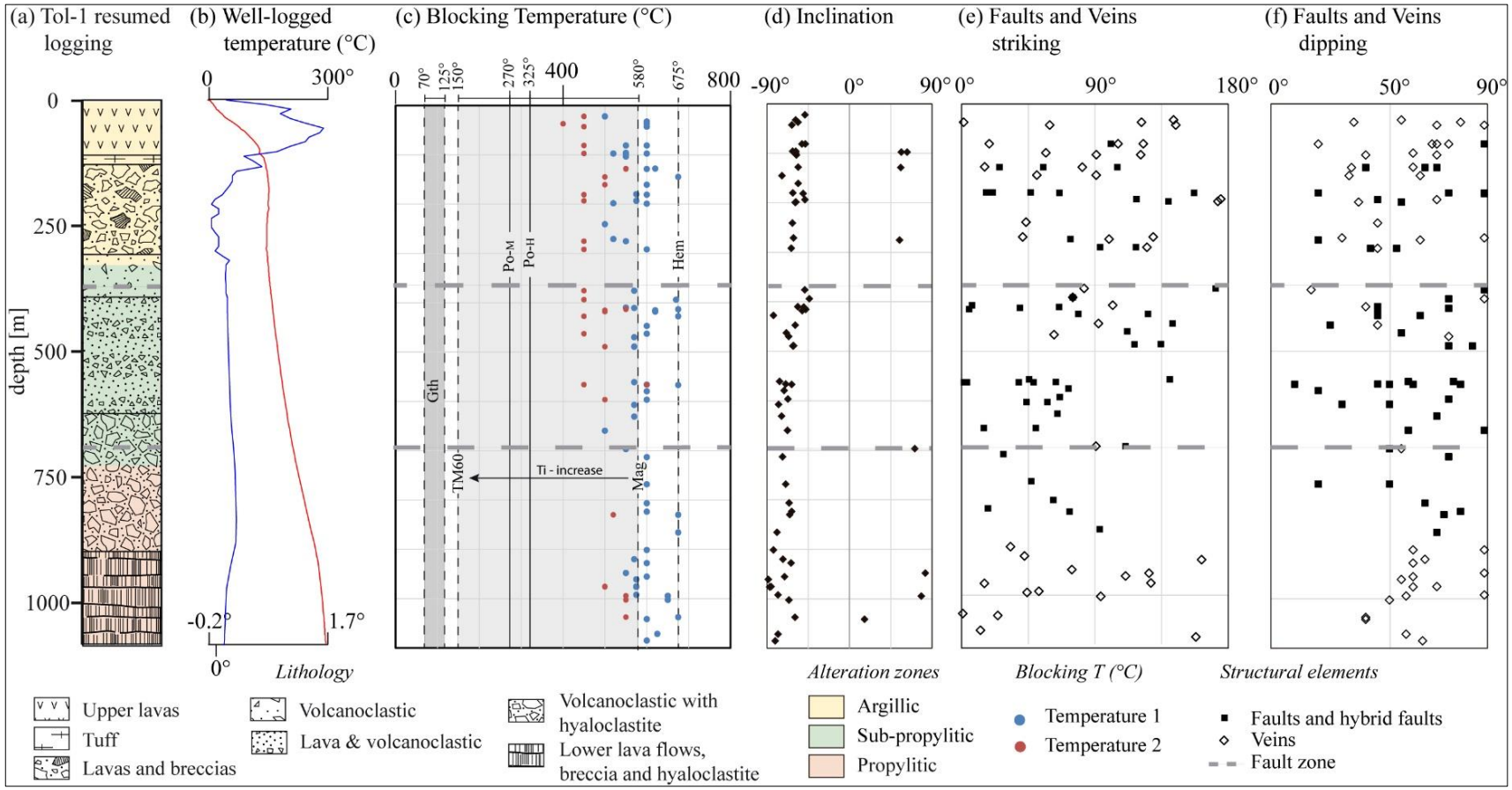

Figure 3-6. (a) General lithological and alteration zones logging of the borehole Tol-1 (modified from Sanchez-Alfaro et al., 2016) (see supplementary figure SM4). (b) Temperature (°C) (red line) and temperature gradient (blue line) vs. depth profile for the Tol-1 (Sanchez-Alfaro et al., 2016). (c) Blocking temperatures vs. depth for each specimen. Blocking temperatures showed for key minerals as a reference: goethite (Gth), pyrrhotite monoclinic (Po-M) and hexagonal (Po-H), hematite (Hem) and magnetite (Mag) with variation of titanium composition until titanomagnetite containing 60 mol% Ti (TM60) (Whitney and Evans, 2010). (d) Inclination of remanent magnetization vectors, (e) faults and veins striking and (f) dipping variation through the depth of Tol-1 borehole.

3.4.2 Structural elements on Tol-1 borehole (see details in appendix SM4 and Table 3).

Detailed mapping of the Tol-1 borehole identifies 93 mesoscopic-scale veins and faults (supplementary figure SM4). Reoriented structures show a slight NE- and NW-striking preferential orientation. I recognized two major fault zones at 310 m and 660 m (with 50 cm and 40 cm of gouge, respectively); their precise orientation was not possible to obtain because of their irregular boundary. These fault zones are spatially associated with alteration zones boundaries (Fig. 3-6a). The reoriented structural elements show a wide distribution of strike and dip throughout the core (Fig. 3-6d, 3-6e). I recognized three zones with contrasting faults and veins patterns (strike and dip) and hydrothermal alteration mineral assemblages. There is a shallow (above 450 m depth) zone, where faults and veins are filled with one or more of the following minerals: Fe-oxides, calcite, quartz, silica, chalcedony, zeolite and chlorite/smectite. Mineral assemblages indicate an argillic alteration type. Breccia textures are typically found at the bottom of this structural-mineralogical zone. Faults and veins in the shallow zone display a wide range of strikes and dips. Faults and hybrid faults filled with calcite, quartz, chalcedony, chlorite/smectite and less common Fe-oxide, zeolite, silica, and magnetite dominate the intermediate (400-700 m) zone, indicating a propylitic alteration type. Faults orientation predominantly are NNE-ENE-striking and >50° dipping. Finally, veins filled with epidote, calcite, zeolite, prehnite, quartz, pyrite, and less common chalcedony and chlorite/smectite dominate the deep zone (>700 m); indicating a propylitic alteration type. Similar to the veins and hybrid faults observed up-hole, here, these structural elements are predominantly NNE-ENE-striking and >50° dipping. Veins show a preferential striking EW to ENE (Fig. 3-7), with thicknesses that vary throughout the core between 1 to 20 mm.

Table 3. Geological-structural mapping summary.

Lithology	*Alteration*	*Strike*	*Dip*	*Rake*	*Type*	*Sense*	*Fe-ox*	*Cal*	*Zeo*	*Prh*	*Silica*	*Chal*	*Qz*	*Chl/sme*	*Mag*	*Py*	*Ep*	*Width (mm)*	*Depth*
Amygdaloidal andesite. Flow Breccia	Unalterated	143	55	-	V		x											5	33
Amygdaloidal andesite. Flow Breccia	Argillic	1	80	-	V		x	x			x	x						7	37
Amygdaloidal andesite. Flow Breccia	Argillic	121	35	-	V		x											5	37
Amygdaloidal andesite. Flow Breccia	Argillic	240	90	-	V		x											6	43
Amygdaloidal andesite. Flow Breccia	Argillic	145	70	-	V		x											4	43
Andesite flow interior	Argillic	298	75	30	F	NL	x	x										0.5	81
Andesite flow interior	Argillic	303	70	-	V		x	x										0.5	81
Andesite flow interior	Argillic	303	68	-	V		x	x										0.5	81
Andesite flow interior	Argillic	199	75	-	V		x	x										4	81
Andesite flow interior	Argillic	286	20	-	V		x											0.5	81
Andesite flow breccia	Argillic	57	60	-	V		x	x	x		x	x				x		5	99
Andesite flow breccia	Argillic	91	70	-	V		x	x	x		x					x		10	103
Andesite flow breccia	Argillic	121	40	-	V		x											6	103
Amygdaloidal andesite. Flow interior	Argillic	16	60	-	V		x											3	128
Amygdaloidal andesite. Flow interior	Argillic	274	20	133	F	TL	x	x										1	129
Amygdaloidal andesite. Flow interior	Argillic	352	50	130	F	NR	x	x										4	129
Amygdaloidal andesite. Flow interior	Argillic	262	34	-	V		x											6	129
Amygdaloidal andesite. Flow interior	Argillic	74	65	62	F	-	x	x										2	129
Amygdaloidal andesite. Flow interior	Argillic	91	63	-	V		x	x										12	145
Amygdaloidal andesite. Flow interior	Argillic	51	33	-	V		x											1	145
Andesite flow interior	Argillic	320	80	110	F	NR	x	x										1	180
Andesite flow interior	Argillic	197	73	110	F	NR	x	x										1	180
Andesite flow interior	Argillic	47	70	55	F	-	x	x										1	180
Andesite flow interior	Argillic	201	75	63	F	NR	x	x										0.5	181
Andesite flow interior	Argillic	246	85	108	F	-	x	x	x									0.5	181
Andesite flow interior	Argillic	157	58	90	F	NR	x	x										2	193
Andesite flow interior	Argillic	355	70	-	V		x											3	193
Andesite flow interior	Argillic	298	77	54	F	NL	x	x				x						1	198
Andesite flow interior	Argillic	173	37	-	V		x	x										1	198
Andesite-basaltic, flow interior	Argillic	44	45	-	V			x				x						1	241
Andesite-basaltic, flow interior	Argillic	221	90	-	V			x					x					2	271
Andesite-basaltic, flow interior	Argillic	309	30	-	V		x											25	271
Andesite-basaltic, flow interior	Argillic	280	63	-	V		x	x			x	x	x					10	275
Andesite-basaltic, flow interior	Argillic	206	45	105	F	-	x	x						x				2	275
Andesite-basaltic, flow interior	Sub-propylitic	305	45	-	V		x	x					x					15	292
Andesite-basaltic, flow interior	Sub-propylitic	105	60	45	F	NL	x							x				1	292
Andesite-basaltic, flow interior	Sub-propylitic	235	10	140	F	-	x							x				5	292
Andesite flow interior	Sub-propylitic	101	80	120	F	-		x										1	376
Andesite flow interior	Sub-propylitic	83	17	-	F													0	376
Andesite flow breccia	Sub-propylitic	75	50	32	F	NR		x										1	394
Andesite flow breccia	Sub-propylitic	75	90	-	V		x	x				x	x					50	394
Andesite flow breccia	Sub-propylitic	282	40	-	V		x	x				x	x		x			4	410
Andesite flow breccia	Sub-propylitic	7	20	67	F	NL	x	x				x	x	x				1	410
Andesite flow breccia	Sub-propylitic	66	75	20	F	TR		x										2	413
Andesite flow breccia	Sub-propylitic	40	50	40	F	-												2	415
Andesite flow breccia	Sub-propylitic	5	30	90	F	TL		x										1	418
Volcanoclastic andesite, Tuff	Sub-propylitic	126	70	65	F	NL												0	428
Volcanoclastic andesite, Tuff	Sub-propylitic	259	90	165	F	NR												0	428
Andesite flow interior	Sub-propylitic	92	45	-	V						x		x	x				5	447
Andesite flow interior	Sub-propylitic	322	58	70	F	-		x										1	447
Andesite-basaltic, flow interior	Sub-propylitic	292	50	80	F	NL	x	x										1	463
Andesite-basaltic, flow interior	Sub-propylitic	242	75	-	V		x	x	x			x	x	x				15	470
Andesite-basaltic, flow interior	Sub-propylitic	315	25	90	F	TL		x						x				1	489
Andesite-basaltic, flow interior	Sub-propylitic	117	55	65	F	-	x											1	489
Andesite flow interior	Sub-propylitic	321	45	105	F	TL	x	x					x	x				1	561
Andesite flow interior	Sub-propylitic	226	75	160	F	-		x										1	561

Table 3. Continuation.

Lithology	Alteration	Strike	Dip	Rake	Type	Sense	Fe-ox	Cal	Zeo	Prh	Silica	Chal	Qz	Chl/sme	Mag	Py	Ep	Width (mm)	Depth
Andesite flow breccia	Sub-propylitic	244	45	128	F	NR		x										1	566
Andesite flow breccia	Sub-propylitic	184	45	167	F	-		x										2	567
Andesite flow breccia	Sub-propylitic	2	45	70	F	NL												1	567
Andesite flow breccia	Sub-propylitic	39	63	10	F	TR												1	567
Andesite flow breccia	Sub-propylitic	229	75	170	F	TL												2	567
Pillow Breccia and Hyaloclastite Andesite	Sub-propylitic	252	53	130	F	-	x	x	x			x	x	x		x		1	579
Andesite flow interior	Sub-propylitic	66	42	100	F	NR		x										1	597
Andesite flow interior	Sub-propylitic	58	90	5	F	TR	x	x					x	x				5	607
Andesite flow interior	Sub-propylitic	44	20	100	F	-	x											2	607
Volcanoclastic andesite, Tuff	Sub-propylitic	65	55	15	F	-												1	631
Volcanoclastic andesite, Tuff	Sub-propylitic	195	75	45	F	-		x										1	660
Volcanoclastic andesite, Tuff	Sub-propylitic	50	90	40	F	NL												1	660
Volcanoclastic andesite, Tuff	Sub-propylitic	291	20	150	F	NR		x										1	697
Volcanoclastic andesite, Tuff	Sub-propylitic	271	55	-	V			x										6	697
Volcanoclastic andesite, Tuff	Sub-propylitic	28	90	65	F	TR		x								x	x	3	713
Volcanoclastic andesite, Tuff	Propylitic	47	90	45	F	TR		x	x				x	x		x	x	5	768
Volcanoclastic andesite, Tuff	Propylitic	47	45	100	F	NR												1	768
Volcanoclastic andesite, Tuff	Propylitic	62	40	105	F	-		x										5	806
Volcanoclastic andesite	Propylitic	18	70	140	F	NR		x								x		1	824
Volcanoclastic andesite	Propylitic	73	65	90	F	NR		x					x					3	830
Volcanoclastic andesite	Propylitic	273	90	85	F	-		x					x				x	15	866
Volcanoclastic andesite	Propylitic	33	90	-	V			x									x	5	901
Volcanoclastic andesite	Propylitic	213	60	-	V			x					x	x		x	x	4	901
Andesite flow interior	Propylitic	43	65	-	V			x									x	1	920
Andesite flow interior	Propylitic	162	60	-	V			x									x	1	928
Andesite flow interior	Propylitic	254	90	-	V				x	x		x				x	x	1	948
Andesite flow interior	Propylitic	307	60	-	V								x				x	3	955
Andesite flow interior	Propylitic	111	55	-	V			x					x					4	961
Andesite flow interior	Propylitic	308	70	-	V			x	x	x		x	x	x			x	6	975
Andesite flow interior	Propylitic	195	60	-	V			x					x				x	2	976
Andesite flow interior	Propylitic	232	90	-	V				x	x		x	x			x		5	992
Andesite flow interior	Propylitic	224	57	-	V								x					6	994
Andesite flow interior, breccia	Propylitic	94	50	-	V				x				x					1.5	1002
Pillow Breccia and Hyaloclastite Andesite	Propylitic	1	40	-	V				x				x					20	1038
Pillow Breccia and Hyaloclastite Andesite	Propylitic	24	40	-	V			x					x					5	1042
Andesite flow interior, breccia	Propylitic	193	57	-	V			x	x			x	x	x			x	5	1071
Andesite flow interior, breccia	Propylitic	158	64	-	V			x					x			x	x	22	1085

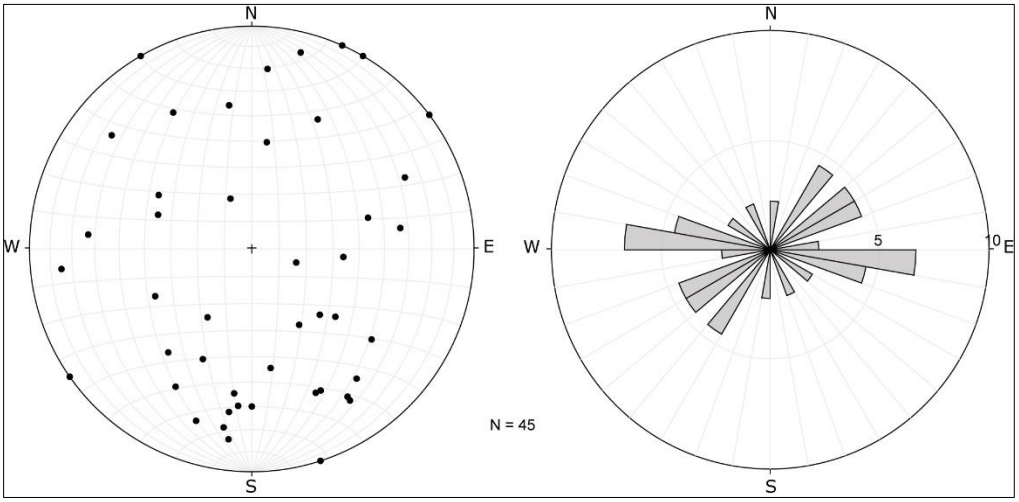

Figure 3-7. Lower hemisphere, equal-area projection shows wide orientation range for veins throughout Tol-1 core: (a) poles veins (b) petals each 10°.

3.4.3 Strain field

Fault-slip data inversion (Fig. 3-8a) yielded a widely-scattered distribution for both P- and T-axes clusters (Fig. 3-8b). P-axes are roughly distributed along a major girdle on an EW direction whereas T-axes are scattered about N and S orientations (Fig. 3-8b). The mean shortening vector is oriented 352º/38º (95 per cent confidence cone, α_{95} > 20°) and the stretching vector is 177º/78º (α_{95} = 19°).

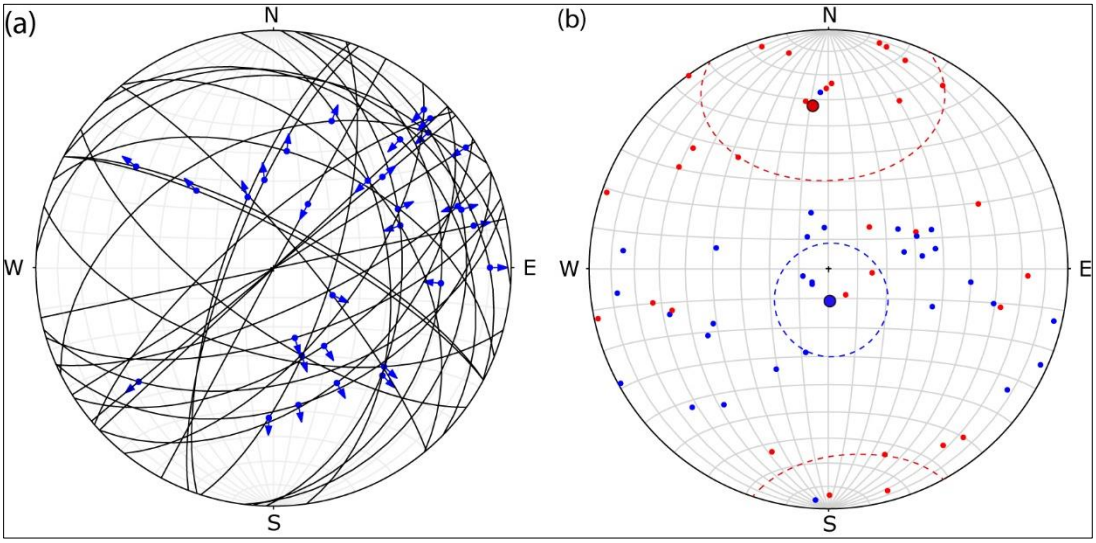

Figure 3-8. (a) Fault-slip data mapped on the borehole Tol-1. (b) Lower hemisphere, equal-area projection showing the calculated strain axes (using Faultkin 7.4). P- and T-axes of each fault (blue and red dot, respectively) with their mean vectors (blue and red circle) and error ellipse (dashed line).

3.4.4 Stress field

Dynamic analysis shows a well-defined orientation for both clusters of σ_1 and σ_3 axes (Fig. 3-9a), with a normal-like distribution of φ values (maximum value φ=0.4) (Fig. 3-9c). This analysis indicates a tensional tectonic regime with vertical σ_1 (083º/74º) and N-trending subhorizontal σ_3 (184°/03°) (Fig. 3-9b). The angular misfit (Fig. 3-9d) indicates that nearly all the analyzed faults respond to a common stress field.

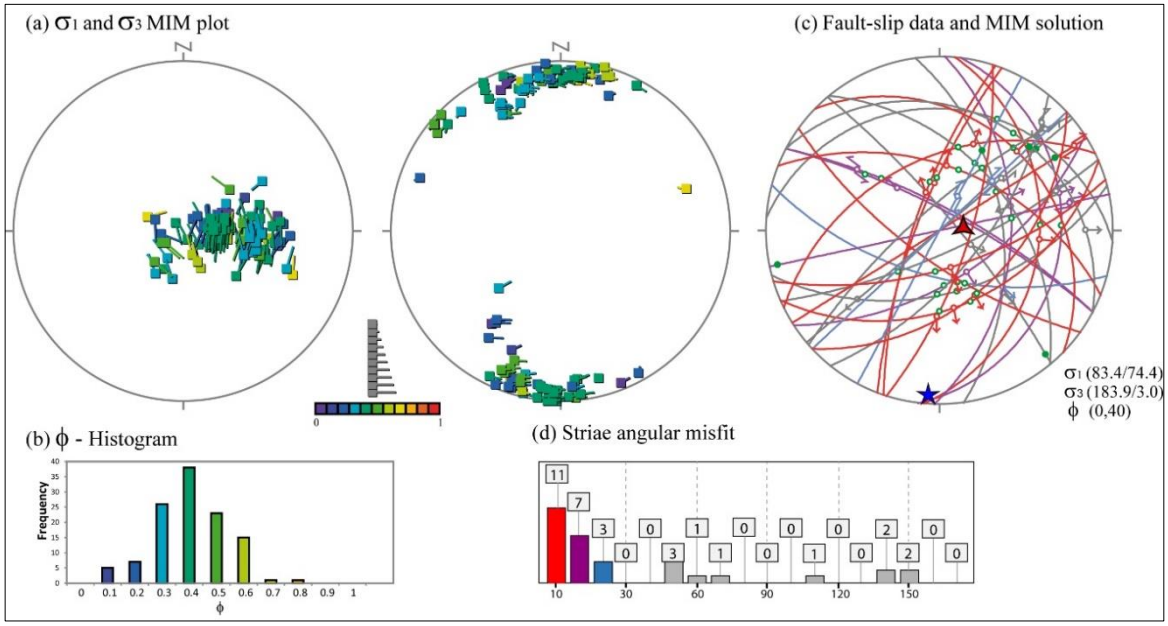

Figure 3-9. (a) Stress field solutions as given by the MIM applied to the fault-slip data. Results show σ_1 (rightwards) and σ_3 (leftwards) axes plotted on a lower hemisphere equal-area projection; the color represents the φ-value from purple - red (0-1, respectively). (b) φ-histogram graphic shows a unimodal distribution with maximum value at φ =0.4. (c) Lower hemisphere, equal-area projection shows stress field best solution, vertical σ_1-axis (83/74) (red triangle) and horizontal σ_3-axis (184/3) (blue star); fault-slip data colors represent the misfit value. (d) Misfit value histogram between real and modeled striae calculated by MIM.

3.5 Discussion

3.5.1 Magnetic reorientation

Deformation genetically associated with LOFS and ATF mostly records *in situ* tectonic blocks rotations (Cembrano et al., 1992; Hernandez-Moreno et al., 2016, 2014). Paleomagnetic evidence (Hernandez-Moreno et al., 2016, 2014) shows that tectonic blocks next to the LOFS (measured on Mio-Pliocene rocks) record mainly N-ward translation without a significant rotation. However, sub-circular blocks undergo great rotation. I assumed that the tectonic block containing the Tol-1 core has no significant rotation. Hence, I use the GAD reference frame to restore the different pieces and structural elements. GAD has associated a paleo-secular variation error of ± 20°, which is considered in the stress field orientation result.

Thermal step-wise demagnetization suggests that magnetite and hematite mineral phases are the main carriers of the remanent magnetic signal (Fig. 3-6c). I recognized blocking temperatures in the range of (400° to 600°C) which most probably depict a variable titanium

content in magnetite from TM60 to TM100 (Dunlop and Ozdemir, 2000; Winklhofer et al., 1997) (Fig. 3-6c). Well-defined ChRMs in mostly all piece of the Tol-1 core allowed to re-orient most veins and faults. Inclinations of ChRM vectors downcore (Fig. 3-6d) record normal polarity.

Although there are no available absolute ages for the whole Tol-1 rock sequence, the oldest rock units of Tolhuaca and Lonquimay volcanoes are 290 ky old (Ar-Ar whole rock method, Polanco et al., 2014) and 700-400 ky (Moreno et al., 2012) respectively. This is consistent with one of the oldest volcanic units dated in the southern volcanic zone corresponding to 600 ± 70 Ka, at the base of Villarrica volcano, (Ar-Ar whole rock method, Moreno and Clavero, 2006). These stratigraphic ages constraints combined with the magnetic normal polarity documented in this work along the Tol-1 core, suggest that the natural magnetization identified in the Tol-1 core rock sequence was acquired at some time during Brunhes polarity chron (0 -780 ka) (Suganuma et al., 2015).

Re-orienting the original structures hosted by sedimentary rocks implies making more critical assumptions than for volcanic rocks because sedimentary rocks do not necessarily hold their primary magnetization (Parés et al., 2008; Zhang et al., 2007). Nevertheless, volcanic rocks can undergo magnetic overprinting. The Tolhuaca volcanic sequence has excellent lithological and magnetic conditions for paleomagnetic core-reorientation, especially because they are young volcanic rocks not affected by Mio-Pleistocene locally tectonic rotations (Hernandez-Moreno et al., 2016, 2014). The hydrothermal alteration recognized along the core is characteristic of a temperature lower than 350° C while the blocking temperature of magnetic mineralogy is between 400° and 600° C. These temperature difference and the single demagnetization patterns support that the titano-magnetite minerals carry the primary magnetization.

3.5.2 Re-oriented structural elements and the regional tectonic setting

At regional scale the northern termination of Liquiñe-Ofqui Fault System records a transpressional tectonic regime with a N65E-trending σ_1 axis and a N30W-trendig σ_3 axis (Fig. 3-10) (e.g. Cembrano et al., 2000; Lavenu and Cembrano, 1999; Pérez-Flores et al., 2016). This regional tectonic regime results from the local stress/strain field variations within the fault zone which depends, among other things, on specific fault orientations

(Pérez-Flores et al., 2016). In this context, fault-slip data records a strain field where the orientation of both P- and T-axes shows a wide-ranging distribution. Multi-modal patterns of P- and T-axes reveal a kinematically heterogeneous faulting, which is probably produced by anisotropy reactivation and/or multiple deformation (Marrett and Allmendinger, 1990). The local deformation can reactivate pre-existing anisotropies that are not ideally oriented for accommodating deformation. This reactivation can be promoted by high fluid pressure in the geothermal system (Barnhoorn et al., 2010; Cox, 2010; Sibson, 2012, 1985). High fluid pressure is likely to have occurred in the TGS, as indicated by numerical simulations and the mineralogical observations (Sanchez-Alfaro et al., 2016).

On the contrary, calculated stress fields yielded clear σ_1- and σ_3-axes clusters that indicate a local tensional tectonic regime with vertical compression (σ_1) and NS-tension (σ_3), which is compatible with a transtensional regional stress field solution independently documented from field work in the area (Pérez-Flores et al., 2016). Southeast of Lonquimay volcano, Perez-Flores et al. (2016), identified similar minimum stress axis orientation (σ_3) under a bulk transpressional local stress field within a NE-striking fault (Fig. 3-10). At both locations, local stress field orientations are kinematically compatible with ENE- to EW-striking tensional fractures. Focal mechanisms of shallow (< 25 km) earthquakes located within the NE-striking releasing bend (LOFS) at Lonquimay volcano (Fig. 3-10) (Barrientos and Acevedo-Aránguiz, 1992; Dziewonski et al., 1990) and the NE-striking fault below the Callaqui volcano (http://www.globalctm.org/CMTsearch.html) (Fig. 3-1b) are consistent with NS maximum extension and EW shortening. Focal mechanisms, ENE-trending flank-vents alignment and the Lonquimay ENE-striking volcanic fissure (Pérez-Flores et al., 2016; Rosenau et al., 2006) are consistent with the NS maximum extension recorded at the Tolhuaca volcano (Fig. 3-10). Similarly, focal mechanisms of the Aysén seismic swarm (2007) located at the southern termination of LOFS identified NE-striking normal and NS-striking right-lateral strike-slip faults coeval with magma/fluid activity (e.g. Legrand et al., 2011; Russo et al., 2011), which support the tensional stress field result and the extensional deformation at the NE- and ENE-striking faults spatially associated with NS-striking faults (LOFS).

Under this local stress field, both NE- and NW-striking discontinuities can be activated, developing complex fault-vein networks and promoting magma/fluid ascent, conducive to synchronous volcanic activity within NE-striking and NW-striking fissure at Lonquimay and Tolhuaca volcanoes, respectively.

Vein networks display two slightly distinctive orientations: EW- and NE-striking. The EW-striking veins are kinematically compatible with the calculated local stress field and with the third-order structures described at regional scale (Pérez-Flores et al., 2016). The NE-striking veins are kinematically compatible with the regional stress field, volcanoes elongation, alignment of flank-vents and dikes orientation (e.g. Bouvet de Maisonneuve et al., 2012; Pérez-Flores et al., 2016; Sielfeld et al., 2016).

Strike and dip distribution of faults and veins throughout the Tol-1 core (Fig. 3-6d and 3-6e) shows that within the upper argillic alteration zone (< 400 m), these are randomly oriented with variable dipping angles (20° to 90°). Below the clay-cap (sub-propylitic zone, > 300 m), I identified a weakly-defined NNE-ENE-striking arrangement of veins and faults, down to the borehole bottom. The deeper zone (> 700 m) mostly records steeply-dipping > 50° veins and faults. These results suggest that the control of the local and regional stress field on veins and faults orientation strongly faints at shallow depth, with reduced vertical stress (σ_1) and lithostatic pressure. Although a tensional tectonic regime promotes steeply-dipping vein-networks (e.g. Faulkner and Armitage, 2013; Sibson, 1996), these results show that the vertical faults and veins best observed below to 700 m deep (Fig. 3-6e).

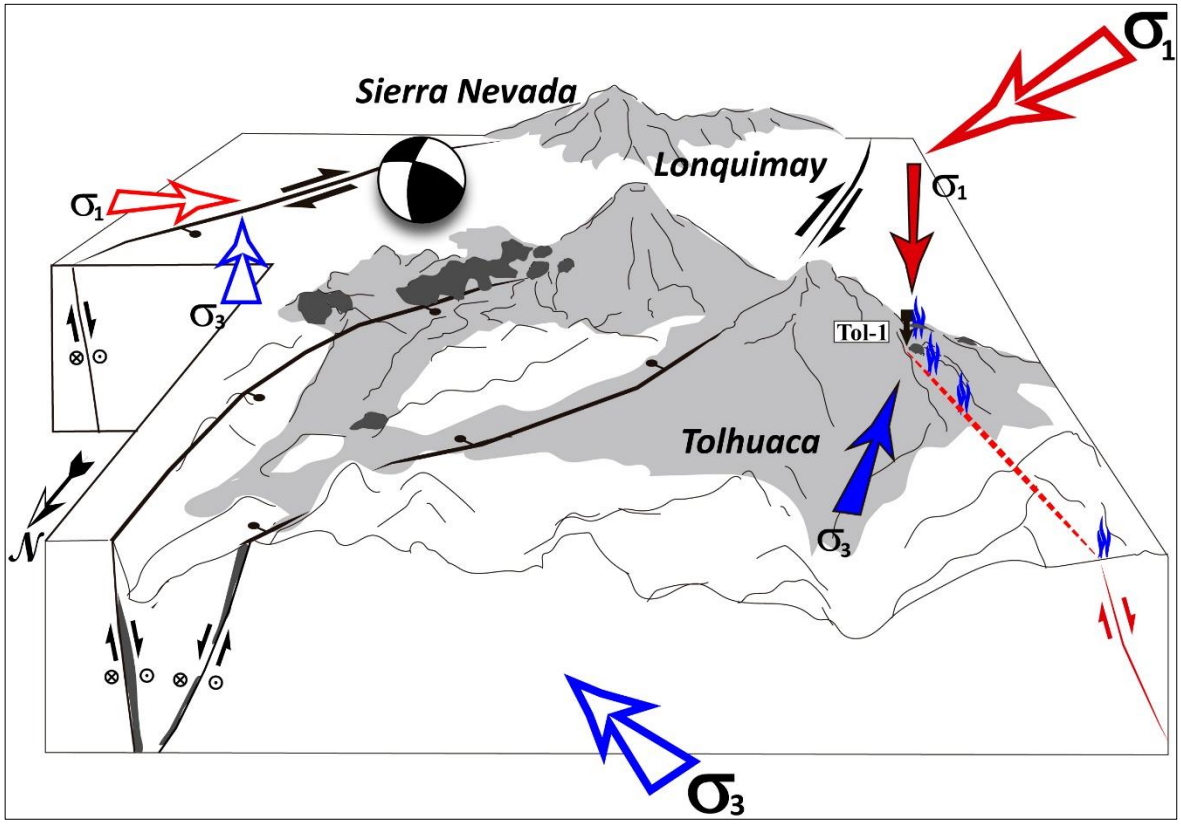

Figure 3-10. Schematic block diagram illustrating the proposed tectonic setting of Tolhuaca-Lonquimay volcanoes (looking south). The model shows the spatial distribution of flank-vents (dark grey), fumaroles (blue flames), stratovolcanoes and faults, which are kinematically compatible with regional stress field (biggest unfilled arrows) (Lavenu and Cembrano, 1999; Pérez-Flores et al., 2016), previous calculated local stress field (unfilled arrows) (Pérez-Flores et al., 2016) and stress field solution (filled arrows) at the Tol-1 core location.

3.6 Conclusions

i. This work is the first successful attempt to reorient a core with paleomagnetic methodology in the Chilean southern volcanic zone and proved to be an efficient and cost-effective technique for re-orient veins and fault to geographical coordinates throughout non-oriented drill cores.

ii. The heterogeneous deformation documented by strain analysis of the fault population probably occurred by anisotropy reactivation of pre-existing discontinuities promoted by high fluid pressure within the geothermal system, under a tensional local stress field with NS-trending tension and EW-compression axes.

iii. The prevailing transpressional regional stress field within the intra-arc zone, with NE-trending σ_1 and NW-trending σ_3, is locally accommodated at the NE-striking

fault zones with clearly defined N- to NNW-trending tension and E- to ENE-trending compression axes. The tensional local stress field at the Tolhuaca area can be explained as a switch between σ_1 and σ_2 main stress axes as driven by local extension at the Lonquimay releasing bend structure within the LOFS and/or locally low lithospheric pressure at the Tol-1 core depth (1020 m).

iv. The vertically oriented σ_1 and horizontally N-trending σ_3 axes are kinematically compatible with ENE- and WNW-striking hybrid faults and EW-striking extensional veins. This tectonic environment can promote a synchronous volcanism or hydrothermal activity along either NE and/or NW volcanic vent fissures.

v. The N-trending σ_3 axis is compatible with earthquake focal mechanisms available for the area showing consistency of the long- and short-term intra-arc tectonics.

vi. These results attest that the tensional local stress field at the Tolhuaca Geothermal System has week control on the spatial distribution of veins orientations above 700 m deep which increase below 700 m.

3.7 Acknowledgements

CONICYT-FONDAP Project Andean Geothermal Centre of Excellence 15090013 (CEGA) is funding this research. Perez-Flores's PhD studies are funded by CONICYT — Beca Doctorado Nacional 21120519 and Sanchez-Alfaro acknowledges support given by Millennium Science Initiative grant NC130065. I thank MRP-Chile Ltd. and former GGE Ltd., S. Iriarte, S. Lohmar, G. Melosh, J. Stimac and A. Colvin for providing access to Tolhuaca and for the information and samples used in this study. I sincerely thank Associated Editor Ian Alsop and reviewers Fabio Speranza and Anita Di Chiara, they provided very useful comments and criticism that helped to improve the manuscript. Thanks to Herrera, E. for laboratory runs and Rubilar, J. for his help in the field work. Thanks to P. Iturrieta for his important help with the data analysis and R. Gomila for his helpful revision of the manuscript.

4 THE EFFECT OF OFFSET ON FRACTURE PERMEABILITY. INSIGHT OF THE ANDEAN SOUTHERN VOLCANIC ZONE, CHILE.

4.1 Introduction

Understanding the influence of fractures on the hydraulic properties of rocks is key to many fundamental and applied areas of geoscience, such as deformation and faulting (Barton et al., 1995; Evans et al., 1997), geophysical hazards (e.g. Scholz and Gupta, 2000), geothermal energy recovery (e.g. Meixner et al., 2016; Rowland and Sibson, 2004), genesis of ore deposits (e.g Cox, 1999; Micklethwaite et al., 2010) and subsurface storage of oils and gas (e.g. Gudmundsson et al., 2012, 2010). In crystalline rocks, geo-fluids are primarily stored within and migrate through fault-fracture networks at all scales (Cox, 2007; Curewitz and Karson, 1997; Uehara and Shimamoto, 2004; Walker et al., 2013; Zhang and Tullis, 1998). Since fractures serve as the main pathways for fluid flow, any change in fracture properties will result in a concomitant change in rock hydraulic properties. Therefore, it is essential to quantify how fractures affect rock permeability, and this process's variability in elevated pressure at depth.

Fault zones accommodate more displacement in their cores, while developing a variety of surrounding damage zones geometries defined by fractures at all scales, from micro-fractures to macro-fractures (Kim et al., 2004; Mitchell and Faulkner, 2009). Permeability in damage zones is enhanced in by the hydraulic properties of the fault-fracture network (Caine et al., 2010, 1996; Faulkner et al., 2010; Mitchell and Faulkner, 2012; Sibson, 1996), where macro-fractures dominate permeability at lower effective pressure (shallow depth), but are closed more easily at higher pressure so that the microfracture matrix becomes more dominant (Mitchell and Faulkner, 2012; Nara et al., 2011; Wang et al., 2016). However, most of the above studies only considered perfectly mated fractures, whereas the majority of faults found in nature are rough and unmated (Bistacchi et al., 2011; Candela et al., 2012, 2009; Griffith et al., 2010; Sagy et al., 2007). Under these circumstances, the fluid flow direction is controlled by the global stress field orientation, where the maximum permeability is parallel to the σ_2 axis (Fig. 4-1) (Faulkner and Armitage, 2013; Rowland and Sibson, 2004; Sibson, 1996). Within a fault plane the minimum permeability direction is parallel to the slip direction and perpendicular to σ_2 axis (Fig.4-1). In this context, fault slip

induces dilation/opening controlled by the fault roughness (Fig. 4-1), thus allowing the formation of the flow channeling phenomenon , increasing permeability by concentration of fluid flow through connected shear fractures even under high confining pressure (Min et al., 2004; Nishiyama et al., 2014; Olsson and Barton, 2001; Olsson and Brown, 1993; Raven and Gale, 1985; Walsh and Grosenbaugh, 1979; Watanabe et al., 2008). Permeability increases rapidly during initial shear displacement, but then changes more gradually or reaches steady-state with increasing shear displacement (Esaki et al., 1999) where gouge production reduces permeability by several orders of magnitude respect to the unfilled fracture (Faulkner and Rutter, 1998; Mohanty and Hsiung, 2011; Nara et al., 2013; Wang et al., 2016). Furthermore, dilational jogs and extension fractures at the tips of individual faults and/or fault intersections provide locations where stress concentrates, which leads to fault reactivation and re-opening, so that they also become the most common locations for hydrothermal outflow (Curewitz and Karson, 1997; Rowland and Sibson, 2004; Zhang et al., 2008).

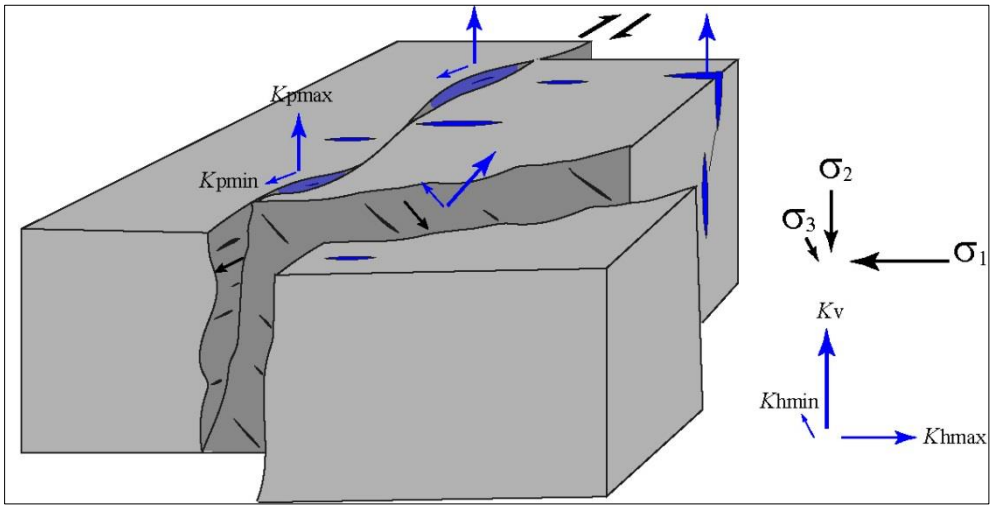

Figure 4-1. Schematic view of strike-slip fault and a secondary normal-dextral fault showing the slip directions (black arrows), maximum and minimum permeability within the fault plane (K_{pmax} and K_{pmin}, respectively; blue arrows) stress field and kinematically associated extension fractures. Also, are showed the stress field orientation and permeability tensors (Faulkner and Armitage, 2013).

In this study, we focus on basement rocks from the Andean Southern Volcanic Zone (SVZ) (Fig. 4-2), which forms part of the Chilean volcanic arc. The Chilean SVZ represents one of the largest undeveloped geothermal provinces in the world, with an estimated potential of ~

16,000 MW (Aravena et al., 2016; Lahsen et al., 2015a, 2015b; Sanchez-Alfaro et al., 2016). In recent years there has been a significant progress in unravelling the architecture and tectonic behavior of intra-arc fault systems in the SVZ, as well as their role in controlling migration and storage of magma and hydrothermal fluid, from a geometric and kinematic perspective (e.g. Arancibia et al., 1999; Cembrano et al., 1996; Cembrano and Lara, 2009; Lara et al., 2006, 2008; Legrand et al., 2011; Pérez-Flores et al., 2016; Rosenau et al., 2006; Sánchez et al., 2013; Sielfeld et al., 2016; Tardani et al., 2016). However, we still have no quantitative knowledge of how slip and displacement of the fault-fracture networks may influence permeability in SVZ rocks.

Therefore, in order to improve the understanding of fracture control on permeability variation along depth, we measured the permeability of rock samples from the main basement lithologies of this volcanic province. These lithologies are the host rock of the fault systems, volcanoes, and hydrothermal activity. To compare these permeabilities, we also measured a baseline value on samples of Seljadalur basalt, a lithology that has been extensively studied previously and whose hydraulic characteristics are well-constrained (Eccles et al., 2005; Nara et al., 2013, 2011; Vinciguerra et al., 2005; Wang et al., 2016). In the present study, we analyze on how permeability varies with increasing effective pressure in (i) intact samples, (ii) samples with mated macro-fractures, and (iii) samples with unmated macro-fractures where we varied the amount of fracture offset (and, hence, also the fracture aperture).

4.2 Fault-fracture network architecture and geo-fluid flow within the SVZ.

The deformation imposed by oblique convergence between the Nazca and South America plates (Fig. 4-2a) is partitioned through the overriding plate within the trench, fore-arc, intra-arc, and back-arc zones. The intra-arc zone accommodates transpressional strike-slip-dominated deformation, from regional to local-scale, by a series of fault-fracture networks, which belong to both the intra-arc Liquiñe-Ofqui Fault System (LOFS) and the Andean Transverse Faults (ATF) (Fig. 4-2a) (Cembrano and Lara, 2009; Melnick et al., 2006a; Pérez-Flores et al., 2016). The LOFS includes a series of kilometric, subvertical NNE-striking master faults, subvertical NE-striking secondary faults and third order ENE-to-EW-striking faults, all cropping out from the area around Callaqui volcano to ~1200 km south in

the Golfo de Penas area (Fig. 4-2a) (e.g. Cembrano et al., 2000; Lange et al., 2008; Veloso et al., 2009).

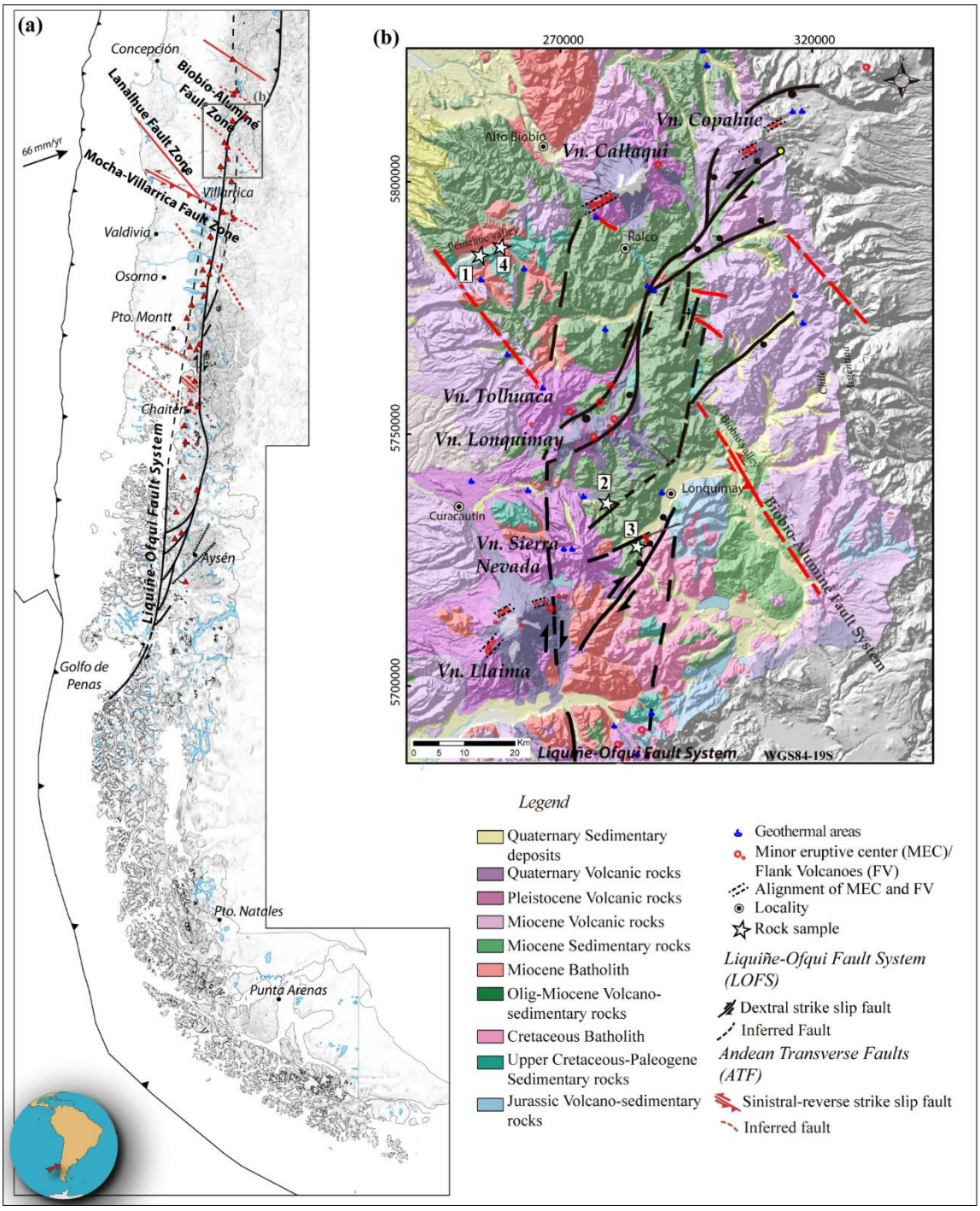

Figure 4-2. Geological-structural map of the Chilean Southern Volcanic Zone, between 37°30′S and 39°S, showing the northern termination of the LOFS, the NW-striking faults belonging to ATF (red lines) (Pérez-Flores et al., 2016) and rock samples location (white star): (1) crystalline tuff, (2) andesitic dike, (3) altered andesite and (4) granodiorite.

The study area from which all our SVF sample material was collected is located between 38° and 39°S (Fig. 4-2b). Here, deformation is distributed within the intra-arc fault-fracture networks belonging to the LOFS and ATF (Pérez-Flores et al., 2016). These faults crosscut mainly volcano-sedimentary rocks belonging to the Cura-Mallin Formation (19 – 12 Ma; K-Ar ages on whole rock and plagioclase from andesite) and the Vizcacha-Cumilao Formation (Upper Cretaceous-Paleogene), and intrusive rocks from Upper Jurassic to Miocene age (Suárez and Emparan, 1997), which are predominant south of the 39°S (Llaima volcano).

The LOFS records a transpressional tectonic regime with N60E-trending σ_1 and N30E-trending σ_3, while displaying a predominant dextral to dextral-reverse slip within the NNE-striking faults, dextral-normal within the NE- ENE-striking faults and NE-striking extensional fractures (e.g. Lavenu and Cembrano, 1999; Pérez-Flores et al., 2016; Rosenau et al., 2006). The ATF includes a series of NW-striking faults, most likely inherited from a pre-Andean architecture (e.g. Radic, 2010), with sinistral-reverse kinematics and local normal-slip re-activation (Pérez-Flores et al., 2016). These fault systems are spatially and genetically associated with major stratovolcanoes (e.g. Callaqui, Llaima, Lonquimay, Tolhuaca), hot springs and with shallow earthquakes (Fig. 4-2) (Barrientos and Acevedo-Aránguiz, 1992; Lange et al., 2008; Legrand et al., 2011). The NE- ENE-striking fault fracture networks are favorably oriented with respect to the regional stress field for their aperture (parallel to σ_1), promoting extensional/hybrid fracturing and vertical magma/hydrothermal fluid migration (Cembrano and Lara, 2009; Pérez-Flores et al., 2016; Sielfeld et al., 2016). Moreover, fault planes consist of rough surface, commonly with multiple steps and slickenfibers (Fig. 4-3a; 4-3b). These fault-fracture networks record a long history of magma and hydrothermal fluid pathways, as revealed by veins (Fig. 4-3c), dikes (Fig. 4-3d) and hydrothermal breccia emplaced within these fault zones (Cembrano and Lara, 2009; Lara et al., 2008; Pérez-Flores et al., 2016; Sielfeld et al., 2016). Conversely, the NW-striking fault fracture networks are misoriented with respect to the regional stress field, favoring magma residence and hydrothermal fluid storage (Pérez-Flores et al., 2016; Sánchez et al., 2013). The interseismic slip rate of the LOFS, calculated from boundary element models is between 1 and 7 mm/yr, whereas a maximum slip calculated for NW-striking faults is 1.4 mm/yr (Stanton-Yonge et al., 2016). This tectonic context provides

suitable conditions for both storage and migration of geo-fluids, allowed by the interaction of these fault-fracture networks (Pérez-Flores et al., 2016; Roquer et al., 2017; Sánchez et al., 2013).

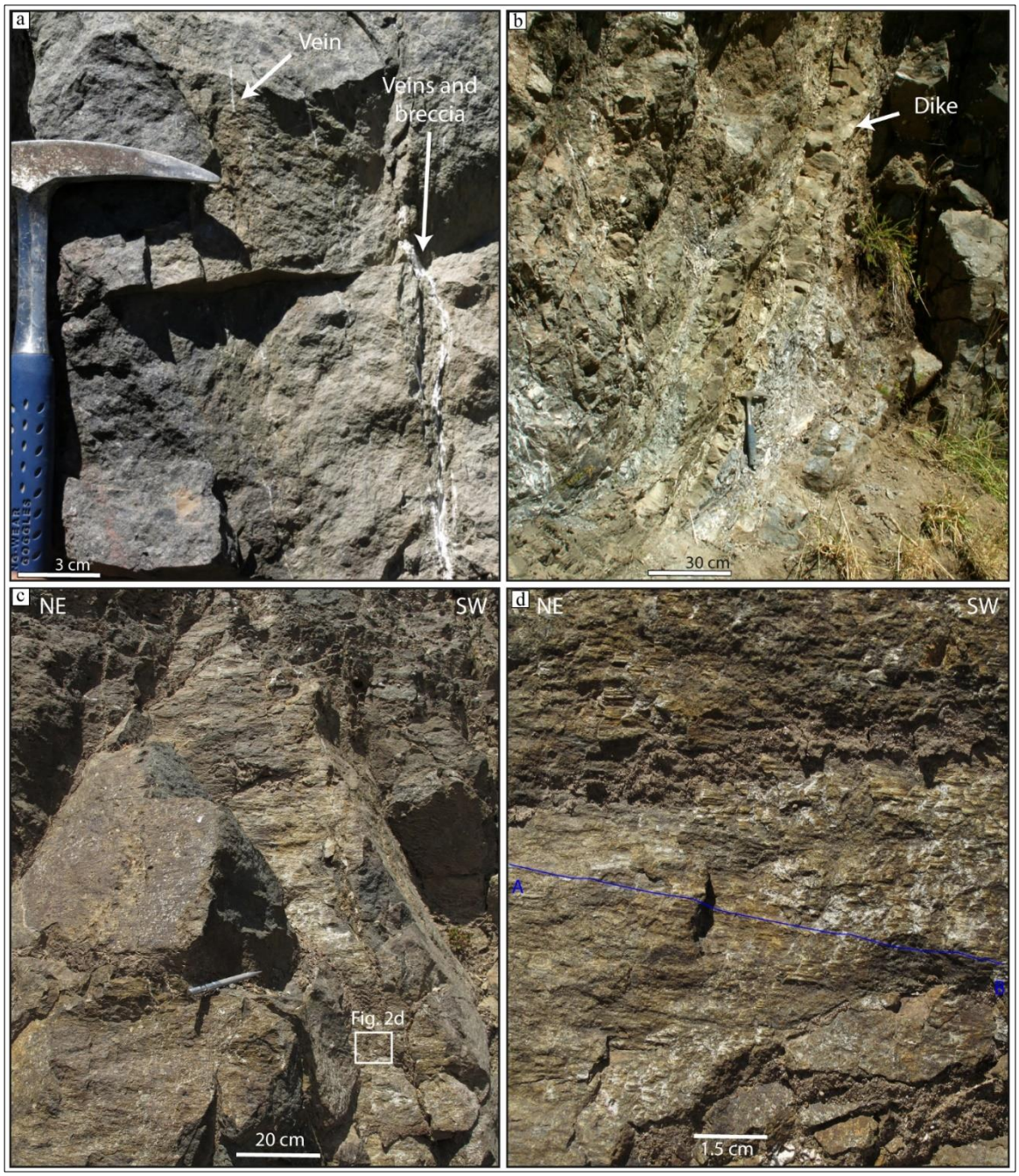

Figure 4-3. (a) Altered andesite crosscut by fractures and zeolite veins. (b) NE-striking fault zone-hosted andesitic dike, zeolite-calcite veins, and hydrothermal breccia. (c) NE-striking fault crosscut altered andesite. (d) Fault plane detail shows rough surface along the slip direction.

4.3 Materials and Methods

4.3.1 Sample materials

Permeability measurements were made on five lithologies. Four of these consist of representative rock types from the volcanic basement of the SVZ, which provides the host lithologies of the intra-arc LOFS and ATF (Fig. 4-2b): (1) crystalline tuff, (2) andesite dike, (3) altered andesite and (4) granodiorite (Fig. 4-4). For purposes of comparison and calibration, we also measured a complementary permeability on samples of Seljadalur the basalt (SB) from Iceland; a material that has been extensively studied previously (Benson et al., 2006b; Nara et al., 2011; Wang et al., 2016). The crystalline tuff has a pyroclastic fragmental texture comprising fragmented crystals of plagioclase and pyroxene, with lithic fragments and glass. This material has a moderate to highly developed clay alteration (Fig. 4-4a). The andesitic dike material has a porphyritic texture, and comprises primarily plagioclase and pyroxene, with a smaller quantity of hornblende phenocrysts, within a micro-crystalline matrix (Fig. 4-4b). The altered andesite is a porphyritic, amygdaloidal volcanic rock comprising plagioclase and pyroxene, within the same micro-crystalline matrix as the andesitic dike. Both crystallites and matrix have been subjected to moderate albitization, resulting in the presence of zeolites and clay minerals. The altered andesite exhibits narrow zeolite veins (< 1mm) and celadonite/smectite amygdales (Fig. 4-4c) (Vicencio, 2015). The granodiorite has a phaneritic texture, and comprises plagioclase feldspar, quartz, hornblende, K-feldspar, and sparse biotite. This material exhibits a low level of clay alteration and contains fine quartz veins (< 1 mm) (Fig. 4-4d). The Seljadalur basalt (SB) comprises plagioclase feldspar and pyroxene, with some accessory minerals, in a glassy matrix (Fig. 4-4e). SB is a compact, high-density rock with a porosity of 3-4% and a permeability in the range 10^{-20} – 10^{-19} m^2 (Eccles et al., 2005; Nara et al., 2011).

Cylindrical test samples were cored from a single block of each lithology, obtained from surface outcrops. The core samples were 38 mm in diameter and 38 mm long. Their end surfaces were ground flat and parallel within ±0.02mm using a surface grinder (Fig. 4-4).

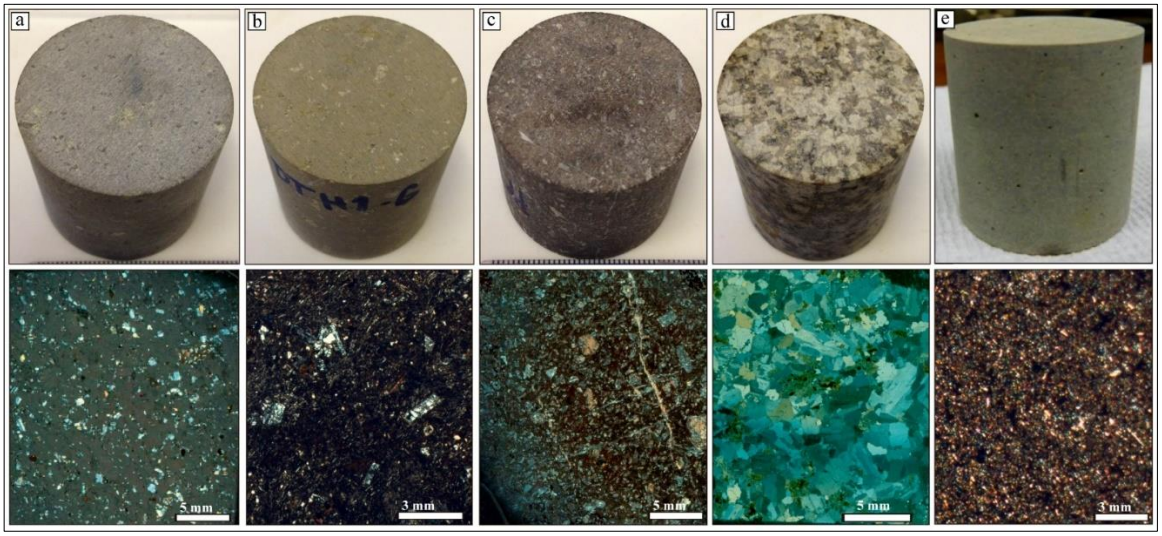

Figure 4-4. Cylindrical samples (38 mm in diameter) and thin section images (cross polarized light) of the five lithologies used in this study: (a) crystalline tuff, (b) andesite dike, (c) altered andesite, (d) granodiorite, and (e) Seljadalur basalt.

Table 4. Table of sample material properties.

Rock	*Composition*	*Grain size (mm)*
Granodiorite	61%Pl-20%Qz-9%Kfs-8%Hbl-2%Bt	3 - 6
Andesitic dike	90%Pl-8%Hbl-2%Px	< 1 – 3 phenocrysts
Altered andesite	85%Pl-10%Hlb-5%Px	< 1 – 4 phenocrysts
Crystalline tuff	45%Pl–25%Litics-10%Px – 10%Glass-10%Bt	<1
Seljadalur basalt	50%Pl-45%Px	<1

4.3.2 Permeameter and permeability measurement methodology

All permeability measurements were made in a servo-controlled permeameter using the steady-state flow method (e.g. Song et al., 2004). The apparatus (Fig. 4-5) and methodology are the same as those used by Nara et al. (2011). The permeameter consist of a 100 MPa hydrostatic pressure vessel equipped with dual 70 MPa servo-controlled pore fluid intensifiers. The samples are rubber-jacketed and positioned inside the pressure vessel between two stainless steel end-caps. The end-caps contain ports to allow pore fluid to be

introduced and distributed across one end of the sample, and to be received and expelled at the other end (Benson et al., 2006a; Nara et al., 2011).

The upstream and downstream pore fluid intensifiers are set to slightly different control pressures to maintain a small, constant pore pressure difference throughout the sample, thus inducing fluid flow. Once steady-state flow is established, the permeability is determined from the rate of fluid flow, the pressure gradient, and the sample dimensions via direct application of Darcy's Law. To minimize any potential temperature-induced pressure fluctuations, the equipment is located within a temperature-controlled laboratory. The temperature was kept constant at 20 °C during all experiments.

To analyze our data, we used the simple effective pressure law, $P_{eff} = P_c - \alpha P_p$, with $\alpha = 1$, where P_c is the applied confining pressure, P_p is the mean pore-fluid pressure and P_{eff} is the effective pressure. We varied the effective pressure, P_{eff}, during our experiments by holding the mean pore fluid pressure constant at 4 MPa, and increasing the confining pressure in a series of 5 or 10 MPa steps from 9 to 64 MPa.

4.3.3 Experimental protocol

In order to explore systematically the effect of fracture offset on permeability, we performed four sets of experiments; (1) baseline permeability measurements on intact samples (2) measurements on samples with mated (zero offset) macro-fractures, (3) measurements on macro-fractured samples with different fracture offsets, and (4) measurements on samples with macro-fractures filled with synthetic fault gouge. The baseline permeability measurements were made on intact samples of all five lithologies under an effective pressure (P_{eff}) of 5 MPa, obtained by applying a confining pressure of 9 MPa and a mean pore fluid pressure of 4 MPa. We then introduced axial macro-fractures into several initially intact samples by loading them across their diameter using a modified Brazil test apparatus at a displacement rate of 4×10^{-6} m s^{-1} (Fig. 4-6), using the same methodology as that described in Nara et al. (2011). The two halves of each macro-fractured sample were then placed together before being positioned in the permeameter, with great care being taken to ensure that the macro-fractures were fully mated with no shear offset (Nara et al., 2011). We then measured the permeability of the macro-fractured samples at effective pressures from 5 to 60 MPa.

For the third set of experiments, we manufactured samples with offset (i.e. unmated) macro-fractures. We first produced macro-fractured samples as described above (Fig. 4-6), and then ground the desired offset length (L_{off}) from the opposite ends of the two previously mated half samples (Fig. 4-7b, 4-7c). The two reduced sample halves were then placed together with their re-ground faces aligned to produce un-mated, macro-fractured samples with the desired offset (L_{off}) (Fig. 4-7d). We made samples with values of L_{off} ranging from 0.25 to 2.00 mm. We again measured the permeability of our offset samples over the same range of effective pressure conditions as for the samples with mated fractures.

Finally, for the fourth set of experiments, we manufactured a set of macro-fractured basalt samples and filled the fractures with synthetic fault gouge made from the same material. The gouge production and fracture filling technique was identical to that described in Wang et al. (2016). We then used the gouge-filled samples to measure changes in permeability as a function of fracture offset and gouge thickness, using the same methodology and over the same effective pressure range of 5 to 60 MPa.

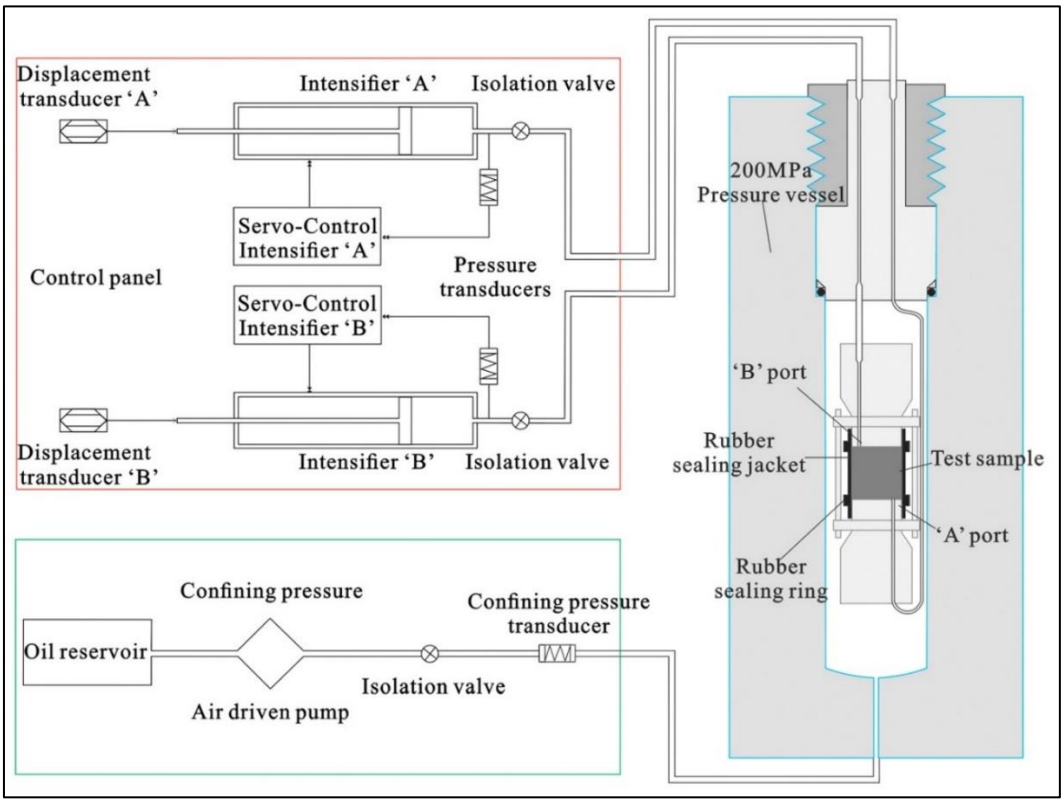

Figure 4-5. Schematic diagram of the permeameter used for all measurements (after Nara et al., 2011; Wang et al., 2016).

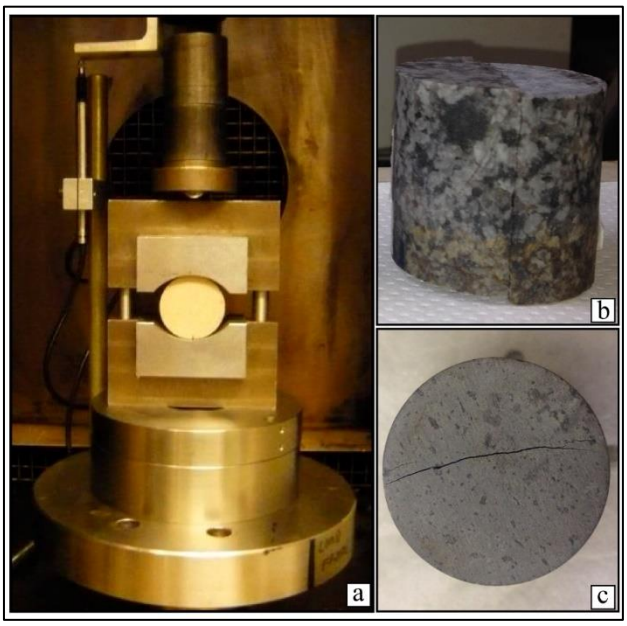

Figure 4-6. (a) Modified Brazil disk apparatus for producing macro-fractured samples, (b) macro-fractured sample of granodiorite, and (c) plan view of macro-fractured sample of crystalline tuff.

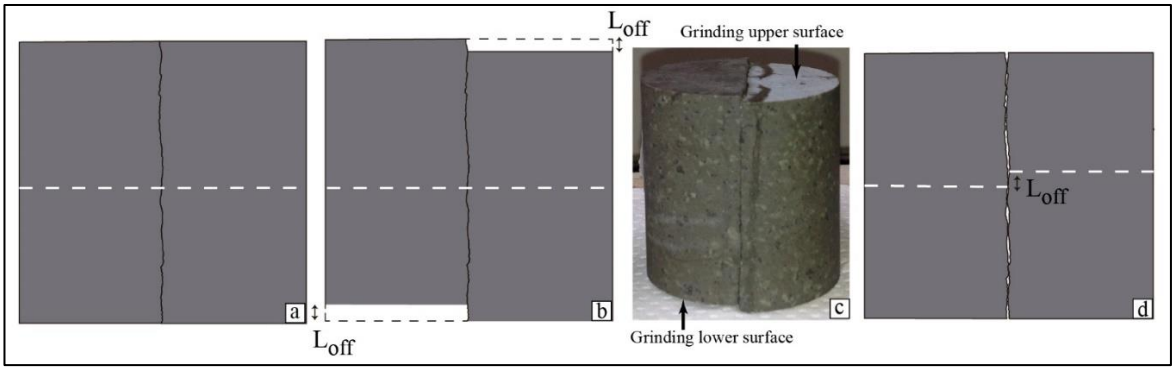

Figure 4-7. Schematic diagram illustrating the methodology used to prepare macro-fractured samples with controlled offsets. (a) Original mated macro-fractured sample; (b) and (c) show, respectively, a schematic and photograph of the mated sample with the offset dimension (L_{off}) ground off opposing sample halves; and (d) shows the final, unmated sample with a controlled offset produced by aligning the end faces of the ground halves.

4.4 Results

4.4.1 Permeability of intact and macro-fractured SVZ rocks.

The permeability of intact samples of all four lithologies from the SVZ are shown in Fig. 4-8, together with the change in permeability as a function of increasing effective pressure for samples of the same four rocks with mated macro-fractures. The permeability of intact SVZ samples are all low, and range from around 10^{-18} m^2 for the granodiorite to around 10^{-20} m^2

for the crystalline tuff and the andesitic dike. The presence of a macro-fracture increases the permeability by between about 5 and 7 orders of magnitude at the lowest effective pressure of 5 MPa. The largest increase is seen for the crystalline tuff, which had the lowest intact permeability, and the smallest increase is seen for the granodiorite, which had the highest intact permeability. For all four materials, the fracture permeability decreases markedly with increasing effective pressure; dropping about three orders of magnitude as effective pressure is increased from 5 to 60 MPa.

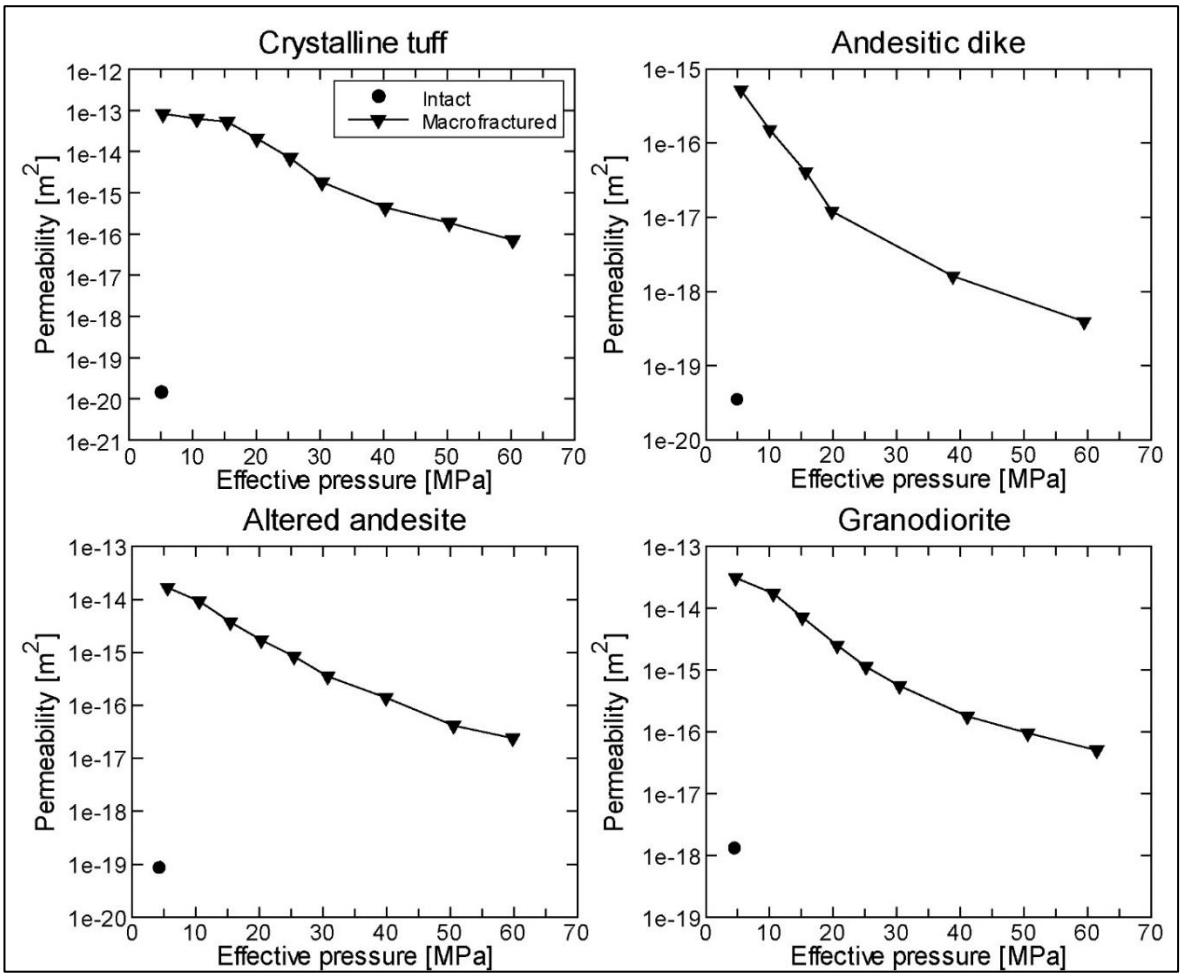

Figure 4-8. Permeability of intact samples of crystalline tuff, andesitic dike, altered andesite and granodiorite at an effective pressure of 5 MPa, and of macro-fractured but mated samples as a function of increasing effective pressure up to 60 MPa.

4.4.2 Permeability of macro-fractured SVZ rocks as a function of fracture offset.

Permeability of SVZ rock samples as functions of offset and effective pressure are shown in Fig. 4-9, plotted on both logarithmic and linear scales. Unsurprisingly, the permeability increases for all rock types and all effective pressures as offset is first increased from zero (mated fractures) and fractures become unmated. Again, unsurprisingly, this increase is most marked at the highest effective pressure where the permeability of mated fractures was lowest. However, the pattern of permeability change becomes more complicated with increasing offset. As for mated fractures, the permeability decreases as a function of effective pressure for all lithologies and all offsets. However, the decreases are much smaller than for mated fractures, being less than one order of magnitude for the crystalline tuff, altered andesite and granodiorite, and having a maximum decrease of around two orders of magnitude for the andesite dike.

The highest permeabilities are recorded at the smallest offset of 0.25 mm for all lithologies (Fig. 4-9), with permeability generally decreasing as offset is increased. However, the fluctuation in permeability as a function of offset is variable and appears to depend on lithology. Both the crystalline tuff (Fig. 4-9a) and the andesite dike (Fig. 4-9b) record two permeability peaks, at offsets of 0.25 and 1.0 mm. By contrast, permeability in the altered andesite and granodiorite generally decreases with offset after the initial peak at 0.25 mm (Fig. 4-9c and 4-9d). Overall there does not appear to be any systematic variation of permeability with increasing offset.

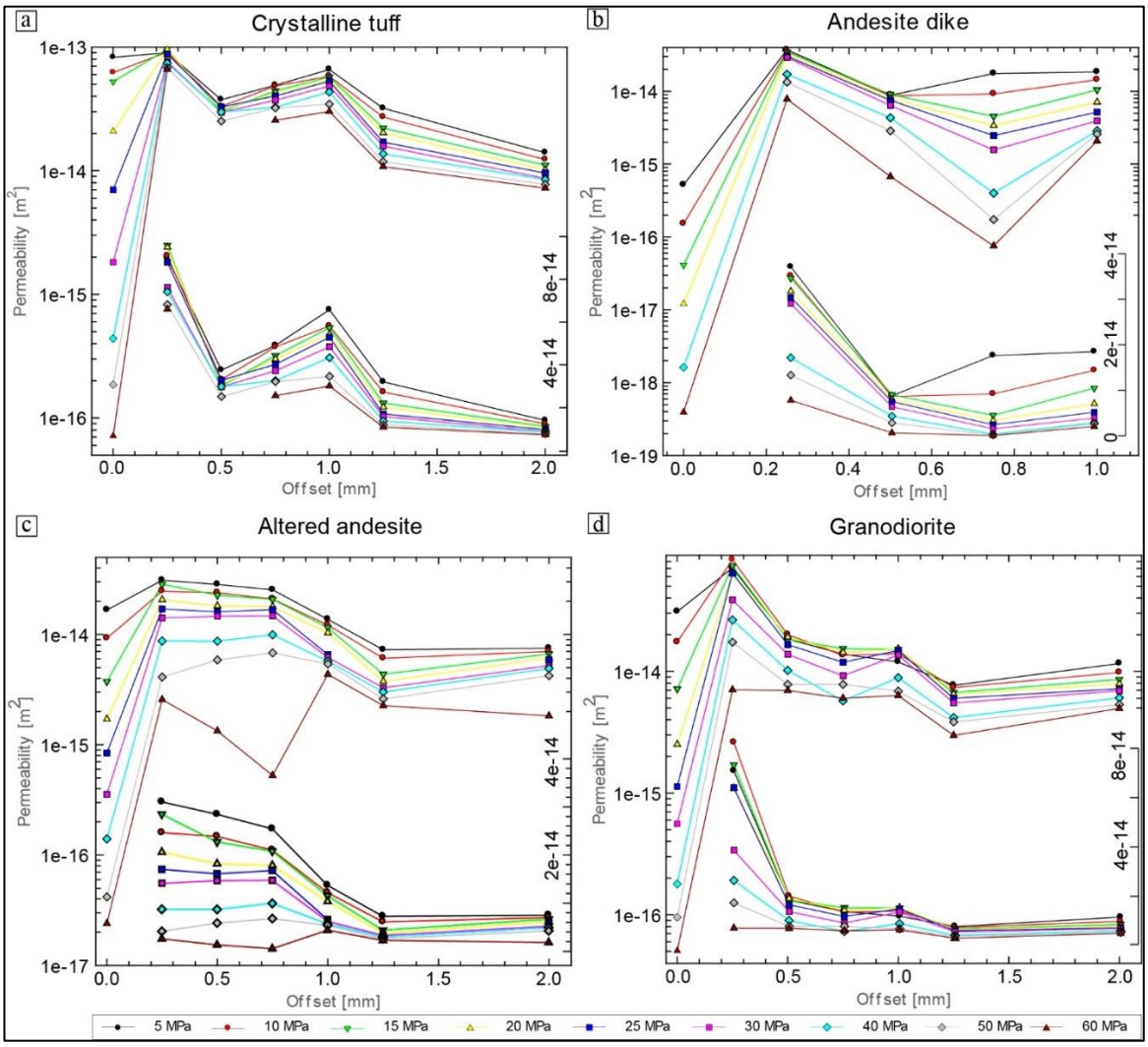

Figure 4-9. Change in permeability of SVZ rocks samples with increasing fracture offset and effective pressure of: (a) crystalline tuff, (b) andesite dike, (c) altered andesite and (d) granodiorite. Insets show the permeability on a linear scale (axis to the right).

4.4.3 Permeability of macro-fractured Seljadalur basalt as a function of fracture offset and gouge.

For comparison, the permeability of macro-fractured samples of Seljadalur basalt are shown as functions of offset and effective pressure in Fig. 4-10, again plotted on both logarithmic and linear scales. Here, the permeability increases dramatically between zero offset (mated fracture) and the first offset of 0.25 mm, by between two and three orders of magnitude. However, in contrast to all the SVZ rocks, the permeability also continues to increase somewhat with increasing offset up to a value of around 1.5 mm, but at a decreasing rate.

The permeability then decreases at higher offset values. As for the SVZ rocks, the permeability decreases with the increasing effective pressure for all values of offset. However, the decrease with increasing effective pressure is not uniform, with the pressure dependence exhibiting a remarkable peak at an offset of 1.5 mm where the permeability is also the highest, which is indistinct at effective pressure highest than 40 MPa.

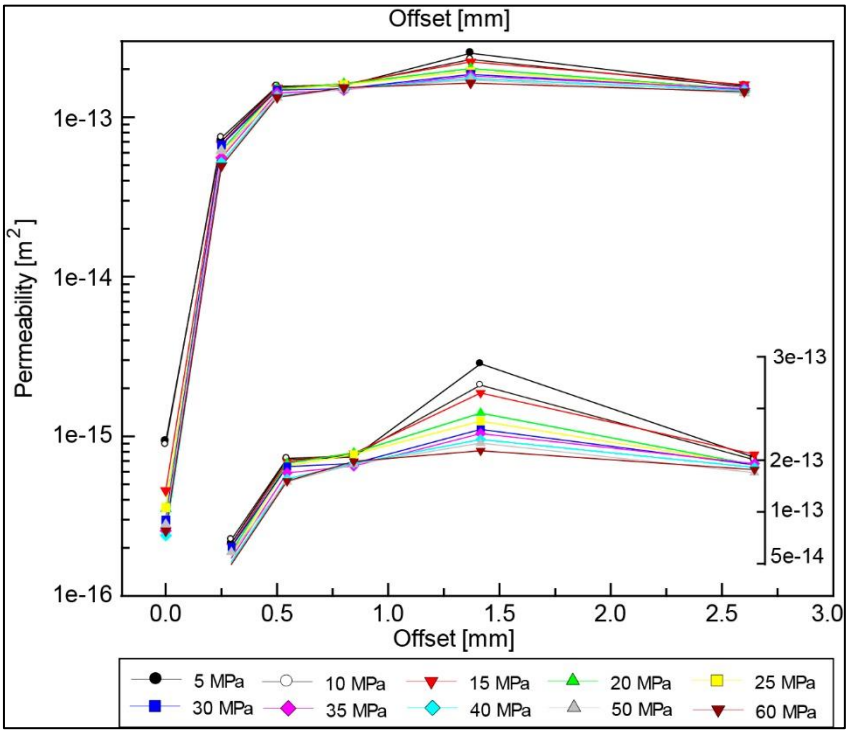

Figure 4-10. Change in permeability of Seljadalur basalt with increasing fracture offset. Inset shows the permeability on a linear scale (axis to the right).

We also made measurements of the permeability of macro-fractured samples of SB with an infilling layer of gouge. The methodology used for producing the gouge and filling the macro-fractures was identical to that reported in Wang et al., 2016. The results are shown in Fig. 1-11 as a function of both offset and gouge layer thickness. We observe that the sample with the mated (zero offset) macro-fracture has the highest permeability at low effective pressure, but there is a crossover region and the same sample has the lowest permeability at high effective pressure (Fig. 4-11a). This is consistent with the observations reported by Wang et al. (2016), and appears to occur because the gouge particles prop open the mated macro-fracture which would otherwise close up at elevated effective pressure and thus reduce the permeability significantly (as seen in the 'no gouge' curve of Fig. 4-11a). We also

note that the permeability crossover pressure decreases substantially with increasing gouge layer thickness; with the crossover pressure being about ~35 MPa for a gouge layer thickness of 0.3 mm and about 15 MPa for a gouge layer thickness of 1.0 mm.

By contrast, the presence of a gouge layer within unmated macro-fractures decreases permeability for all values of layer thickness, as illustrated in Figs. 4-11b and 4-11c. This is entirely as expected, because the main effect of a gouge layer within the unmated fractures is to fill the aperture space created by the displacement of the rough fracture surfaces. In this way, the presence of a gouge layer appears to be able to counteract the effect of fracture offset generally increasing permeability. But, the effect of the gouge layer on permeability is potentially complicated by the way it fills the aperture space. For example, the data of Fig. 4-11b show that the permeability increases with increasing gouge layer thickness. That is to be expected, since a thicker layer will provide more pathways for fluid flow. However, the data of Fig. 4-11c show that, for a larger fracture offset of 2 mm, the thinnest (0.3 mm) gouge layer gives the highest permeability; while thicker layers follow the previous trend. This is potentially because the thinnest gouge layer does not fully fill the larger fracture aperture at this larger offset, and a fracture that is only partially filled fracture will provide additional void space for fluid flow. This interpretation is supported by the data of Fig. 4-11d, which shows that the permeability in the fracture containing the 0.3 mm thick gouge layer increases for all offsets greater than 1.25 mm regardless of the effective pressure.

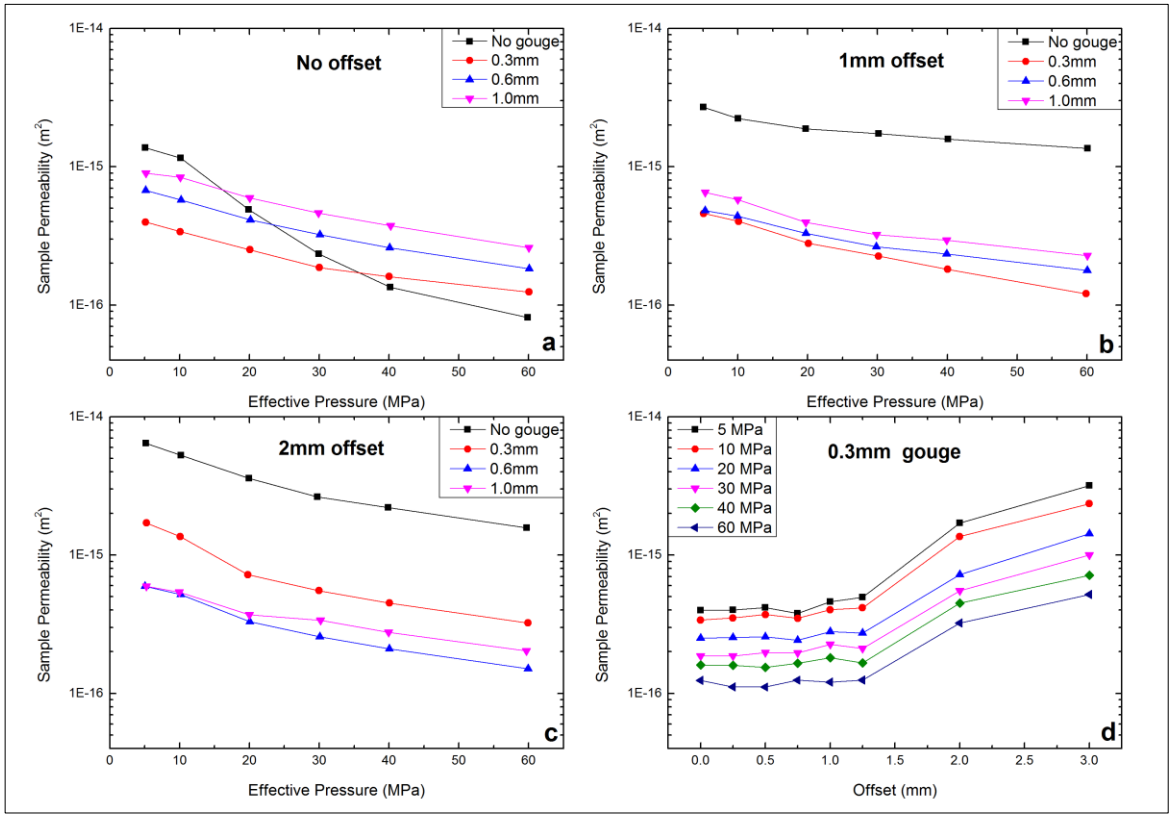

Figure 4-11. Effect of the presence and thickness of gouge (0, 0.3, 0.6 and 1.0 mm) on the permeability of mated (zero offset) and un-mated (offsets from 0.25 to 3.0 mm) samples of SB with as a function of increasing effective pressure.

4.4.4 Fracture trace analysis

4.4.4.1 Fracture characterization

In order to characterize the macro-fractures in our samples, we cut the cores axially in an orientation perpendicular to the fracture plane, thus producing a cross-section parallel to the fluid flow direction. These fracture traces were then digitized using Adobe Illustrator®, at a resolution of the 0.05 mm (Fig. 4-12). We quantify the traces by their roughness and their aperture. The power spectrum is a robust technique that is well-suited for characterizing fault and fracture roughness (Babadagli and Develi, 2003; Candela et al., 2012, 2009; Persson et al., 2005). We therefore calculate the power spectral density and spatial frequency from the fracture trace data using the Fast Fourier Transform (FFT) method (Cooley and Tukey, 1964) after correction for any linear alignment trend in the measured data (Fig. 4-13) (Kudo et al., 1992; Nara et al., 2006). From log-log plots of the power spectral density ($P(k) = Ck^{-1-2H}$)

against the spatial frequency (reciprocal wavelength), we characterize the roughness by the slope (-1-2*H)*, the Hurst, or roughness exponent (*H)* and its pre-factor (*C*). The slope describes how the roughness varies with the scale, while pre-factor describes the steepness of surface or the total profile variance, which is a quantitative measure of the amplitude at a specified wavelength (Candela et al., 2012, 2011; Mandelbrot, 1983; Power and Tullis, 1991; Turcotte, 1992). The mean roughness exponents (*H)* and pre-factors, (*C)* for each lithology are given in Table 5. Thus, from the pre-factor values, the fractures with higher amplitudes are those of andesitic dike and altered andesite, while the lower amplitudes are those of crystalline tuff and basalt (Fig. 4-13 and Table 5). The slope and H show that the roughness is dominated by high frequencies (shortest wavelength).

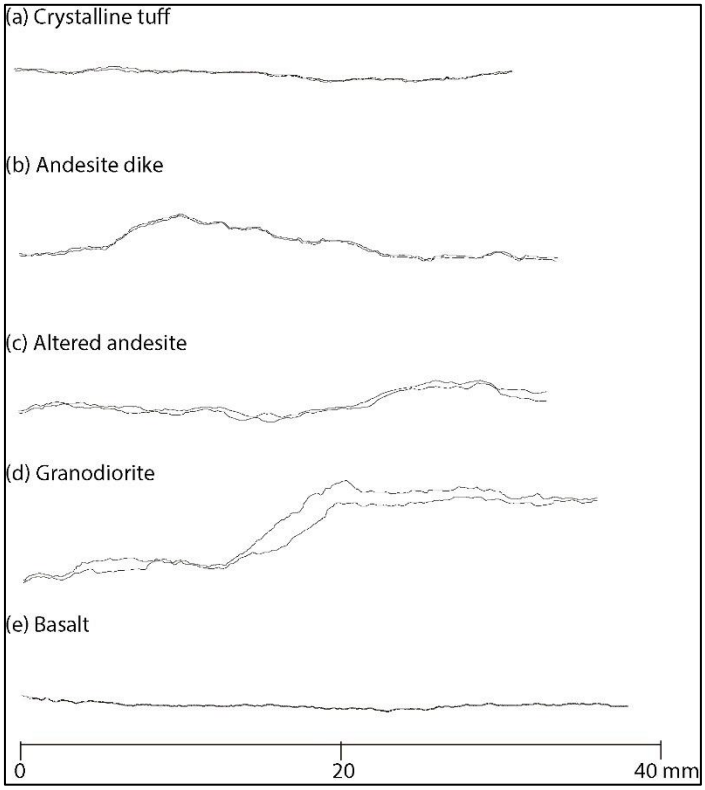

Figure 4-12. Examples of fracture traces from sectioned rock samples to show the fracture roughness parallel to the fluid flow direction. Both vertical and horizontal axes are on the same scale.

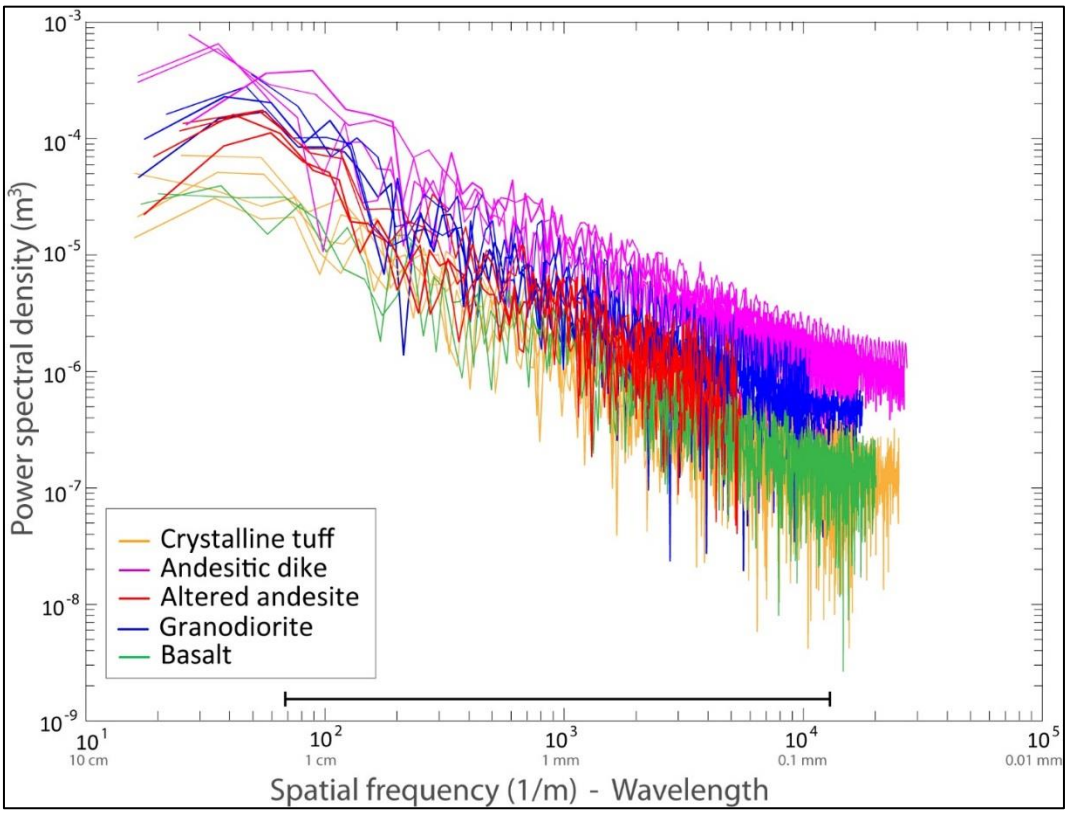

Figure 4-13. Fourier power spectral density $P(k)$ as a function of the spatial frequency for fracture traces of each lithology.

Table 5. Properties of the fracture traces for each lithology, showing the mean pre-factor, $\overline{C}$, the mean roughness exponent, $\overline{H}$, and their errors.

Lithology	$\overline{C}$	Error (±)	$\overline{H}$	Error (±)
Crystalline tuff	0.002	3.0×10^{-6}	0.665	0.021
Granodiorite	0.005	1.8×10^{-5}	0.523	0.014
Andesitic dike	0.007	3.7×10^{-5}	0.427	0.005
Altered Andesite	0.008	1.3×10^{-4}	0.597	0.111
Basalt	0.001	4.5×10^{-8}	0.487	0.002

The fracture aperture is defined as the separation between two opposing fracture surfaces (a_x), measured perpendicular to those surfaces (Lanaro, 2000). For each fracture trace (Fig. 4-12) we determined the mean aperture ($\bar{a}$) for each increment of offset, L_{off}, from the digitized traces after separating them by the minimum amount required to remove any

overlap (Fig. 4-14). In Fig. 4-15, we show the relation between aperture and offset length (L_{off}) determined from digitized fracture traces of each lithology. For all lithologies, aperture increases dramatically with increasing offset up to some characteristic value in the range 0.5 to 1.0 mm. Apertures then increase only marginally with greater offset, but exhibit small oscillations with increasing offset (Fig. 4-15).

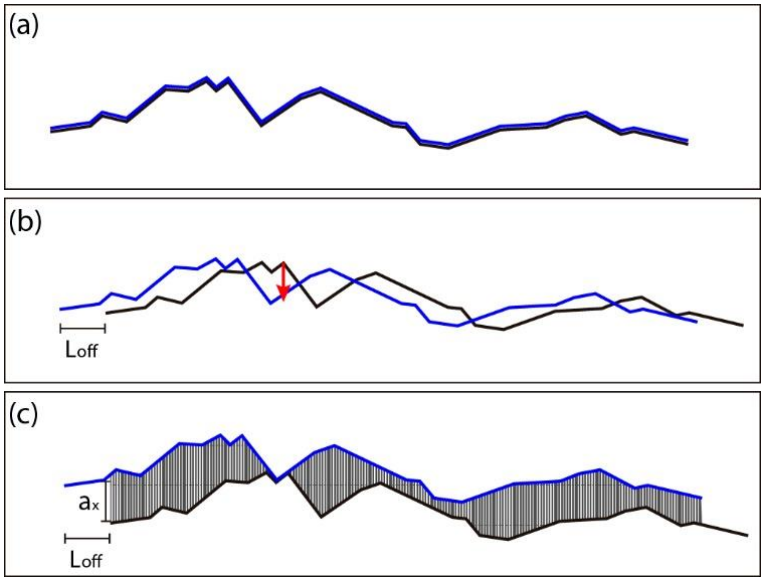

Figure 4-14. Schematic diagram illustrating the fracture aperture calculation method: (a) Mated traces of fracture, (b) opposite traces displaced by the offset distance, L_{off}, (c) displaced traces separated by the minimum amount required to remove any overlap (red arrow). The mean aperture ($\bar{a}$) is then the arithmetic mean of all a_x.

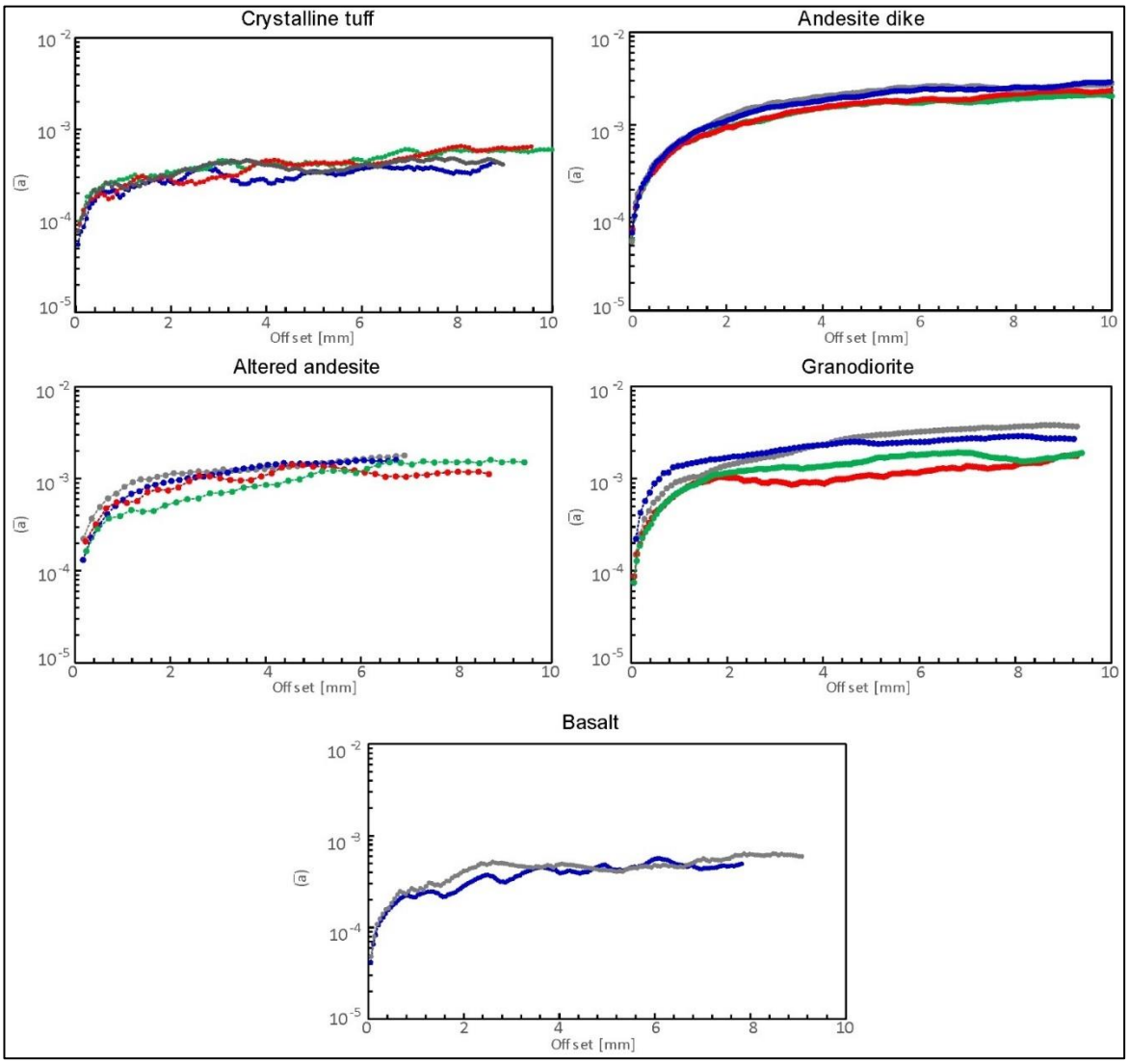

Figure 4-15. Mean aperture (ā) with increasing offset, calculated for several fracture traces of each lithology.

4.5 Discussion

Our results show that the intact granodiorite sample has a permeability of 10^{-18} m^2, which is about two orders of magnitude higher than both the SVZ volcanic rocks (10^{-20} m^2) (Fig. 4-9) and the basalt (Nara et al., 2011). As a first-order approximation, this could favor the existence of geothermal reservoirs in intrusive rocks, which is the main lithology making up the basement south of 39°S. The permeability of all rocks increases very significantly in samples containing mated macro-fractures (Fig. 4-8), similarly to results reported by Nara et al., (2011). The permeability of samples with unmated macro-fractures increases even

further, with respect to samples with mated macro-fractures, for all lithologies when the offset-length (L_{off}) is first increased (Fig. 4-9). At low effective pressure (P_{eff} = 5 MPa), this increase due to initial offset is around 2 orders of magnitude for the fresh volcanic rocks (andesitic dike and basalt) (Fig. 4-9 and Fig. 4-10) but less than one order of magnitude for the other rocks (Fig. 4-9). For all rocks, the permeability continues to increase with increasing offset until some characteristic value of L_{off} is reached; but the value is different for each different lithology. For higher values of offset, the permeability appears to change little, similar to the results obtained from shearing experiment reported by Esaki et al, (1999). However, we do observe some oscillation in the permeability values for given lithologies at higher offsets, and this may be a function of asperity contact, which will be different for each different lithology (e.g. Lanaro, 2000; Olsson and Barton, 2001). We observe a similar feature, as a function of increasing offset, in our fracture aperture analysis (Fig. 4-15).

A model that is widely applied in hydrogeology and related fields to relate fluid flow to fracture aperture is the *cubic law*, in which permeability is considered to be proportional to the cube of the mean aperture ($\bar{a}^3$) (e.g. Gudmundsson et al., 2012; Raven and Gale, 1985; Witherspoon et al., 1980; Zimmerman, 2012). The relation between permeability and mean aperture cubed, with increasing offset, is shown in Fig. 4-16. The general trend of the two sets of curves are similar, with both exhibiting a rapid initial increase with increasing offset. They then level off and exhibit little change with increasing offset above some characteristic offset value. However, the cubic law does not fully capture the very rapid transition from increasing values to steady values seen in the permeability data. Since the cubic law was derived for fluid flow between parallel plates, it is perhaps not surprising that it fails to capture all the details of fluid flow between two rough fracture surfaces. Furthermore, the aperture data in Fig. 4-16 were derived from single linear traces taken across the full fracture surface. This necessarily involves a loss of one dimension, and therefore likely also a loss of complexity. Nevertheless, the general trends are consistent.

The roughness index $\bar{H}$, derived from analysis of the fractures traces of Fig. 4-12 (Table 5), are shown in Fig. 4-17, plotted against the permeability of mated fractures (Fig. 4-17(a)) and against the difference in permeability between mated and un-mated fractures (Fig. 4-17(b)). For mated fractures, we see a general increase in permeability with increasing fracture

roughness across all lithologies tested. In contrast, figure 4-17b shows that the increase in permeability for a fixed offset of 0.25 mm is highest for the lithologies with the lowest fracture roughnesses (andesite dike, basalt, and granodiorite) and lowest for those with the highest fracture roughnesses (crystalline tuff and altered andesite). The variation in roughness is relatively well constrained for most of the lithologies tested, except for the altered andesite where the range is very wide. This may be due to the alteration and mineralogical changes that have occurred in this material.

The characteristic value of offset coincides with minimum contact area between fracture surfaces, which also corresponds to the point where the mean aperture reaches a plateau value and hence the capacity for the fluid flow is also maximized (Min et al., 2004; Watanabe et al., 2008). Furthermore, since this is the minimum contact area, it is the point with where the permeability is most pressure sensitive. The characteristic value of offset will therefore depend on the scale or the wavelength of fracture roughness, and hence on the aperture distribution. Although the permeability of un-mated fractures decreases with increasing P_{eff} for each increment of offset, it never drops below the permeability of samples with mated macro-fractures. Hence, permeability will always be dominated by un-mated fractures.

As each sample was subjected to multiple pressurizations for a range of offsets, it was necessary to ascertain whether our experimental procedure induced additional damage during experiments. Therefore, after pressurization and measurement at the maximum offset, we re-ground the basalt sample to remove the total offset so that we could re-mate the fractures and re-measure its permeability. The results are presented in Fig. 4-18 and show that the permeabilities of the re-mated fracture returns to values of the same order as the initial mated values. However, the permeability range is somewhat higher for the re-mated fracture, which indicates a higher-pressure sensitivity. This suggests that our experimental procedure causes only minimal additional damage, which was not great enough to significantly affect our overall results.

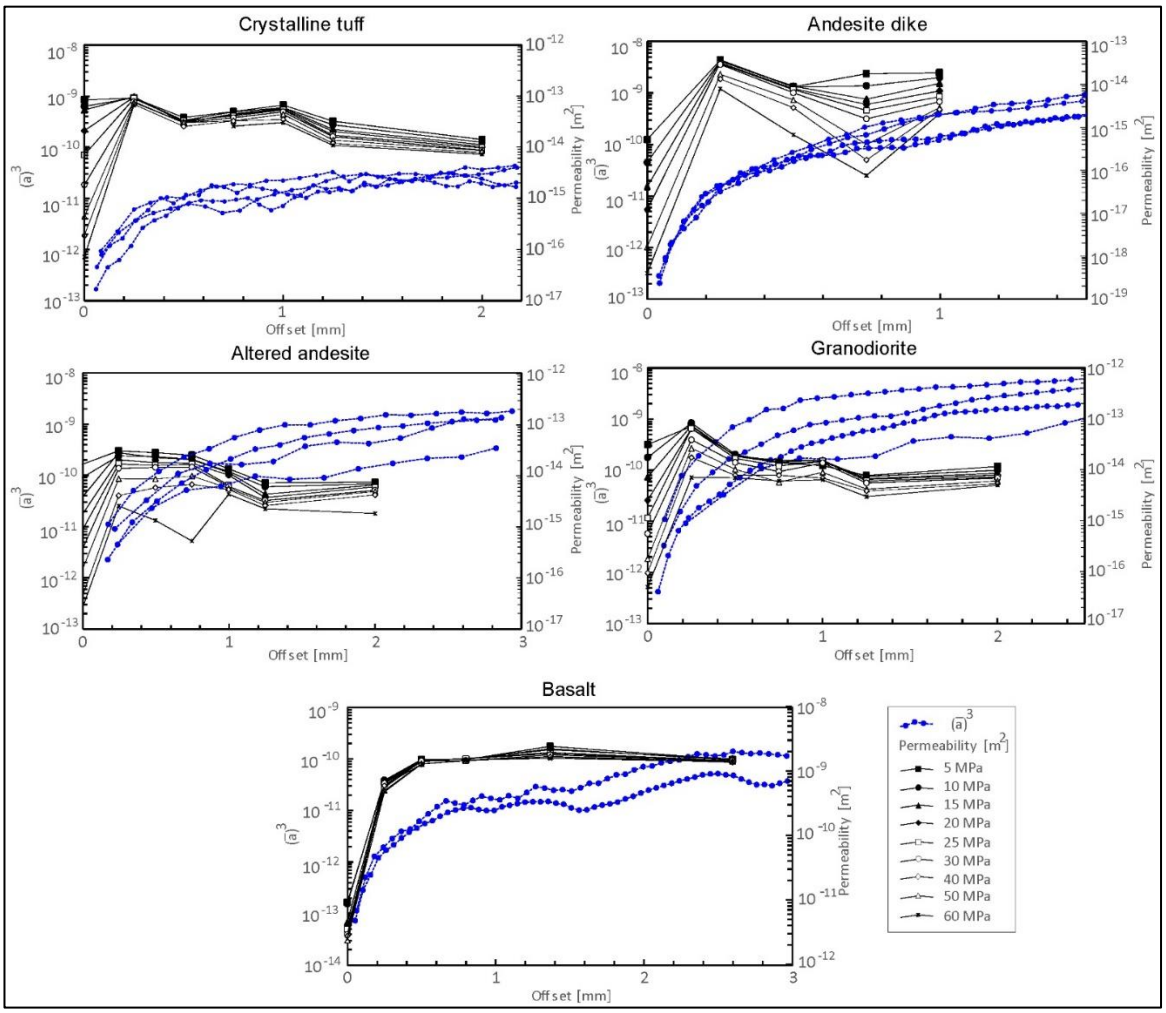

Figure 4-16. Graphics show the cubic aperture of the fracture traces with increase L_{off} (blue dot) and permeability of the un-mated macro-fractured sample with increase L_{off} (black square) for each lithology.

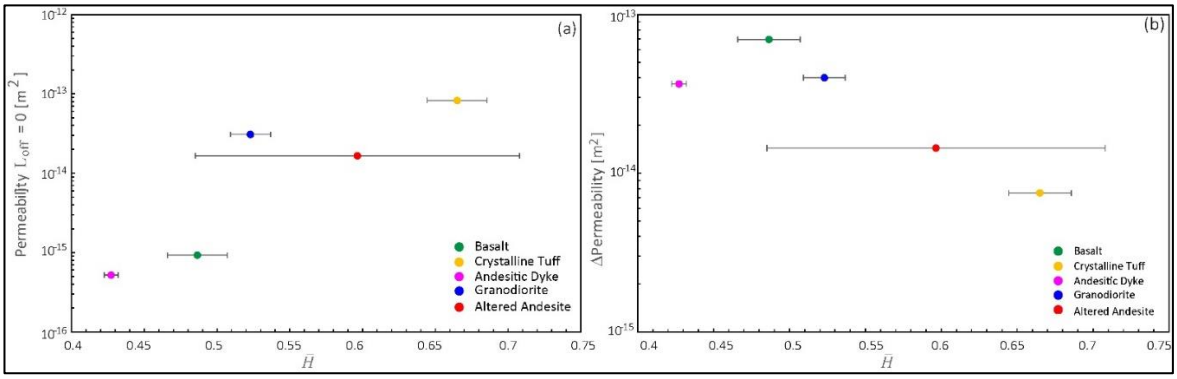

Figure 4-17. Mated macro-fractured samples permeability under 5 MPa effective pressure in relation with the average of roughness index $\bar{H}$ for each lithology. (b) The increment of permeability between unmated macro-fractured sample (L_{off} = 0) and unmated macro-fractured sample with L_{off} = 0.25 mm in relation with the average of roughness index $\bar{H}$ for each lithology. The bars show the roughness standard deviation.

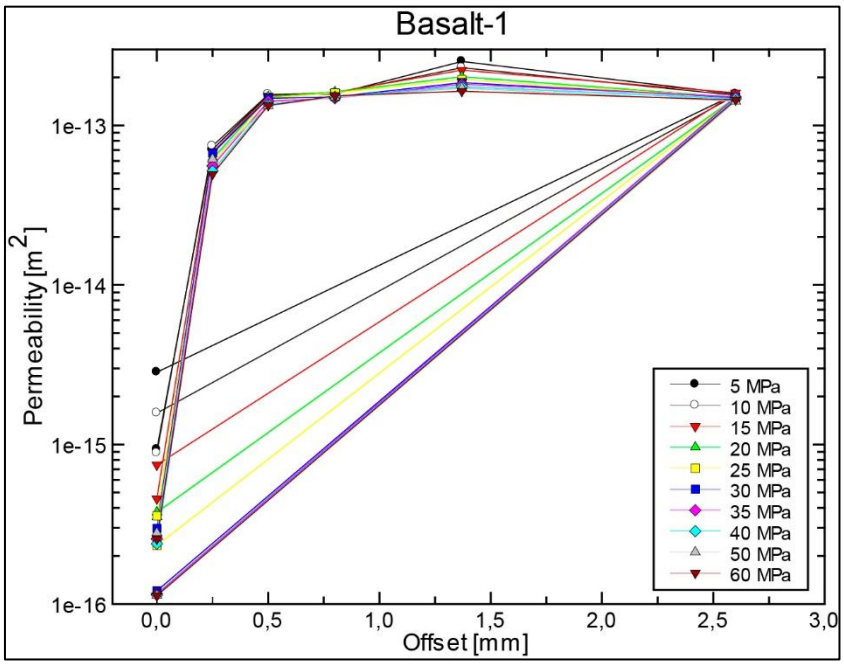

Figure 4-18. Permeability measurements with increasing offset and re-ground re-mated macro-fractured sample for increasing effective pressure (5 to 60 MPa) of basalt sample.

Our results show the change in permeability that results from discrete fracture offsets. In nature, this corresponds to situations where pore fluid pressure is higher than the least principal stress and fractures offset with minimal contact (e.g. hydrofractures) without generation of wear products (e.g. fault gouge or cataclastic material). Our study does not consider the situation where fractures are subjected to shear displacement under higher normal stress producing wear products that may partially fill fracture apertures.

Many field and laboratory studies demonstrate that damage zones have the highest permeability within a fault zone (Brogi, 2008; Caine et al., 1996; Caine and Forster, 1999; Evans et al., 1997; Mitchell and Faulkner, 2012; Walker et al., 2013). Our results indicate that while mated macro-fractures can maintain high permeability conditions (k 10^{-16}) up to P_{eff} = 40 MPa (Fig. 4-2), such conditions can only be reached with un-mated fractures – i.e. with finite offset - at higher effective pressures.

Our macro-fractured samples from the basement rocks of the SVZ record permeability values in the same range as those reported for geothermal reservoirs where advective/convective flow occur (Fig. 4-19) (Rowland and Sibson, 2004 and references therein). Permeability in crystalline tuff and granodiorite macro-fractured samples is higher

than 10^{-16} m^2, in the entire range of effective pressures measured, promoting the development of convention cells (Fig 4-19). This result shows that the damage zones developed in granodiorite and crystalline tuff are important permeable areas even at high effective pressure (60 MPa), especially in those described in the same area by Pérez-Flores et al. (2016) as NE-striking fault zones, which have an extensional component, and WNW-striking fault zones under fluid overpressure. The fracture filling and sealing would obstruct fluid flow through the fracture networks but the reactivation of faults may renew it. Small fault activations could be enhance by moderate interseismic fault slip rates, as has been described by Stanton-Yonge (2016) of 7.0 and 0.5 mm/yr of the LOFS and ATF, respectively.

An independent evidence of plutonic rocks being potential fractured fluid conducts/reservoirs along fault damage zones is described in a magnetotelluric (MT) work by Held et al. (2016). This research shows highly conductive domains along NNE-striking master faults of the LOFS and WNW-striking faults of the ATF in the vicinity and north of the Villarrica volcano (SVZ, Fig. 4-1). Held et al. (2016) also show a high conductivity anomaly in the lower crust apparently connected with the LOFS and ATF. The low permeable lithologies or alteration zones could act as a clay cap layer, which could increase the time span of reservoir conditions, as has been modeled by Sánchez-Alfaro et al. (2016) in the Tolhuaca volcano (Fig. 4-1b). This research shows a low permeability zone (< 10^{-18} m^2) acting as a clay cap, which has similar permeability values of intact volcanic rocks, especially Crystalline tuff. Finally, our results show that a geothermal reservoir architecture in the SVZ could consists in a combination of high-permeable plutonic-volcanic fractured rocks as a reservoir and low-permeable intact volcanic rock layers, enhanced by argillic alteration (Sanchez-Alfaro et al., 2016).

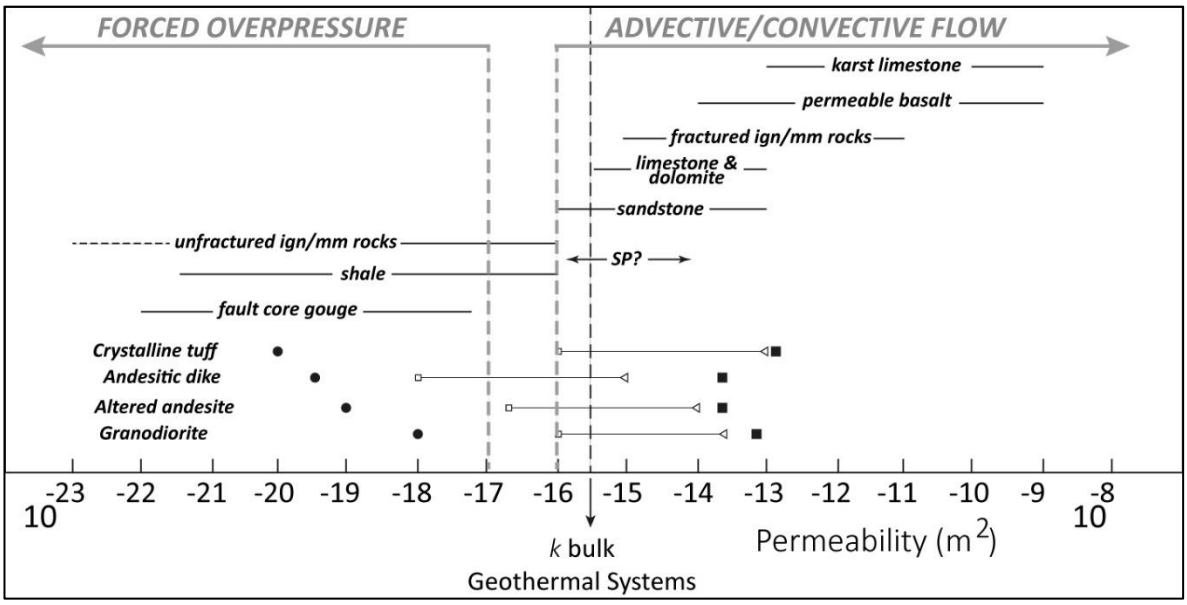

Figure 4-19. Permeability of intact (circle) sample, mated macro-fractured samples (triangle for 5 MPa and white square 60 MPa) and the highest value measured on unmated macro-fractured samples (black square) for each lithology from the SVZ. These permeability values are in context of a range of permeabilities for consolidated rocks, fault rock, seismogenic permeability (SP) estimated from migrating microseismicity of reservoirs in shallow crust, permeability bulk (*k*) for the Ohaaki-Broadlands & Wairakei geothermal systems, and the minimum permeability limits for the development of fluid convection (under hot/cold hydrostatic condition) and the condition for development of forced overpressures in areas of strong fluid release (Rowland and Sibson, 2004 and references therein).

4.6 Conclusions

This study records the first permeability results for the basement of the Andean Southern Volcanic zone, which provide us with a quantitative overview about the permeability variation within a fault zone under increasing effective pressure that mimics a fault zone behavior at different depth.

1. The granodiorite and crystalline tuff are the highest and least permeable intact rock, respectively. Macro-fracture increases permeability between 7 orders of magnitude in the crystalline tuff and 4 orders of magnitude for the granodiorite. Because granodioritic plutonic rocks dominate the SVZ basement, they may constitute both highly permeable pathways along faults and fractured geothermal reservoirs.
2. The unmated macro-fracture increases permeability between 2 to less than 1 order of magnitude with respect to mated macro-fractures depending on the lithology, being the highest and least increment the ones found for basalt and crystalline tuff, respectively.

3. The increment of permeability with offset records an oscillation and a characteristic value after which the permeability is maintained, similarly than the aperture. This increment depends on the lithology and the fracture roughness.
4. The increment of effective pressure decreases the permeability and its oscillation effect, especially in basalt lithology. Unmated macro-fractures with offset have an important role in the permeability maintenance under highest effective pressure (60 MPa).
5. Fractures filled with gouge decrease permeability and delete the oscillation with increases offset.

Acknowledgements

We are grateful to John Bowles, Steve Boon, and Neil Hughes for their essential support during laboratory experiments. Special thanks to the generous help of Jim Davy during rock samples preparation. Thanks to UCL Earth Science community especially to the Seismolab group for their collaboration and friendship during PPF internship. Special thanks to Gonzalo Yáñez for his continuous advises and help. Thanks to Pablo Iturrieta for his programing help and to Felipe Aron, Rodrigo Gomila and Gerd Sielfeld for their fruitful discussion and ideas. This paper is a contribution to the Andean Geothermal Center of Excellence (CEGA) FONDAP/CONICYT Project 15090013 and 1141139 (JC). Perez-Flores's PhD studies are funded by CONICYT-Beca Doctorado Nacional 21120519.

5 REFERENCES

Acocella, V., Funiciello, R., 2006. Transverse systems along the extensional Tyrrhenian margin of central Italy and their influence on volcanism. Tectonics 25. doi:10.1029/2005TC001845

Allmendinger, R.W., Cardozo, N.C., Fisher, D., 2012. Structural Geology Algorithms: Vectors & Tensors. Cambridge University Press, Cambridge, England.

Alstine, D.R. Van, Butterworth, J.E., 2002. Paleomagnetic core-orientation helps determine the sedimentological, paleostress, and fluid-migration history in the Maracaibo basin, Venezuela, in: Core Workshop for I Congreso de Sedimentología. Applied Paleomagnetics, Inc., pp. 1–29.

Angelier, J., 1984. Tectonic analysis of Fault Slip Data Sets. J. Geophys. Res. 89, 5835–5848.

Angermann, D., Klotz, J., Reigber, C., 1999. Space-geodetic estimation of the Nazca-South America Euler vector. Earth Planet. Sci. Lett. 171, 329–334. doi:10.1016/S0012-821X(99)00173-9

Arancibia, G., Cembrano, J., Lavenu, A., 1999. Transpresión dextral y partición de la deformación en la Zona de Falla Liquiñe-Ofqui, Aisén, Chile (44-45°S). Rev. geológica Chile 26. doi:10.4067/S0716-02081999000100001

Aravena, D., Mu??oz, M., Morata, D., Lahsen, A., Parada, M. ??ngel, Dobson, P., 2016. Assessment of high enthalpy geothermal resources and promising areas of Chile. Geothermics 59. doi:10.1016/j.geothermics.2015.09.001

Aron, F., Allmendinger, R.W., Cembrano, J., González, G., Yáñez, G., 2013. Permanent fore-arc extension and seismic segmentation: Insights from the 2010 Maule earthquake, Chile. J. Geophys. Res. Solid Earth 118, 724–739. doi:10.1029/2012JB009339

Aron, F., Cembrano, J., Astudillo, F., Allmendinger, R.W., Arancibia, G., 2014. Constructing forearc architecture over megathrust seismic cycles: Geological snapshots from the Maule earthquake region, Chile. Geol. Soc. Am. Bull. 127, 464–479. doi:10.1130/B31125.1

Babadagli, T., Develi, K., 2003. Fractal characteristics of rocks fractured under tension. Theor. Appl. Fract. Mech. 39, 73–88. doi:10.1016/S0167-8442(02)00139-8

Barnhoorn, A., Cox, S.F., Robinson, D.J., Senden, T., 2010. Stress- and fluid-driven failure during fracture array growth: Implications for coupled deformation and fluid flow in the crust. Geology 38, 779–782. doi:10.1130/G31010.1

Barrientos, S.E., Acevedo-Aránguiz, P.S., 1992. Seismological aspects of the 1988–1989 Lonquimay (Chile) volcanic eruption. J. Volcanol. Geotherm. Res. 53, 73–87. doi:http://dx.doi.org/10.1016/0377-0273(92)90075-O

Barton, C. a, Zoback, M.D., Moos, D., 1995. Fluid fow along potentially active faults in crystalline rock. Geology 23, 683–686. doi:Doi 10.1130/0091-7613(1995)023<0683:Ffapaf>2.3.Co;2

Beck, M.E., 1988. Analysis of late Jurassic-recent paleomagnetic data from active plate margins of South America. J. South Am. Earth Sci. 1, 39–52. doi:http://dx.doi.org/10.1016/0895-9811(88)90014-4

Bellier, O., Zoback, M. Lou, 1995. Recent state of stress change in the Walker Lane zone, western Basin and Range province, United States. Tectonics 14, 564–593. doi:10.1029/94TC00596

Benson, P.M., Meredith, P.G., Schubnel, A., 2006a. Role of void space geometry in permeability evolution in crustal rocks at elevated pressure. J. Geophys. Res. Solid Earth 111, 1–14. doi:10.1029/2006JB004309

Benson, P.M., Schubnel, A., Vinciguerra, S., Trovato, C., Meredith, P., Young, R.P., 2006b. Modeling the permeability evolution of microcracked rocks from elastic wave velocity inversion at elevated isostatic pressure. J. Geophys. Res. Solid Earth 111, 1–11. doi:10.1029/2005JB003710

Bertin, D., 2010. El complejo volcanico lonquimay y la zona de falla liquiñe-ofqui: estudio estructural, morfometrico y gravimetrico. Universidad de Chile.

Bistacchi, A., Ashley Griffith, W., Smith, S.A.F., di Toro, G., Jones, R., Nielsen, S., 2011. Fault Roughness at Seismogenic Depths from LIDAR and Photogrammetric Analysis. Pure Appl. Geophys. 168, 2345–2363. doi:10.1007/s00024-011-0301-7

Blanquat, M.D. Saint, Tikoff, B., Teyssier, C., Vigneresse, J.L., 1998. Transpressional kinematics and magmatic arcs. Geol. Soc. , London , Spec. Publ. 135, 327–340. doi:10.1144/GSL.SP.1998.135.01.21

Bons, P.D., Elburg, M. a., Gomez-Rivas, E., 2012. A review of the formation of tectonic veins and their microstructures. J. Struct. Geol. 43, 33–62. doi:10.1016/j.jsg.2012.07.005

Bouvet de Maisonneuve, C., Dungan, M. a., Bachmann, O., Burgisser, A., 2012. Insights into shallow magma storage and crystallization at Volcán Llaima (Andean Southern Volcanic Zone, Chile). J. Volcanol. Geotherm. Res. 211–212, 76–91. doi:10.1016/j.jvolgeores.2011.09.010

Brogi, A., 2011. Variation in fracture patterns in damage zones related to strike-slip faults interfering with pre-existing fractures in sandstone (Calcione area, southern Tuscany, Italy). J. Struct. Geol. 33, 644–661. doi:10.1016/j.jsg.2010.12.008

Brogi, A., 2008. Fault zone architecture and permeability features in siliceous sedimentary rocks: Insights from the Rapolano geothermal area (Northern Apennines, Italy). J. Struct. Geol. 30, 237–256. doi:10.1016/j.jsg.2007.10.004

Butler, R.F., 1998. PALEOMAGNETISM : Magnetic Domains to Geologic Terranes, University. ed. Tucson, Arizona.

Caine, J.S., Bruhn, R.L., Forster, C.B., 2010. Internal structure, fault rocks, and inferences regarding deformation, fluid flow, and mineralization in the seismogenic Stillwater normal fault, Dixie Valley, Nevada. J. Struct. Geol. 32, 1576–1589. doi:10.1016/j.jsg.2010.03.004

Caine, J.S., Evans, J.P., Forster, C.B., 1996. Fault zone architecture and permeability structure. Geology. doi:10.1130/0091-7613(1996)024<1025

Caine, J.S., Forster, C.B., 1999. Fault Zone Architecture and Fluid Flow : Insights From Field Data and Numerical Modeling.

Candela, T., Renard, F., Bouchon, M., Brouste, A., Marsan, D., Schmittbuhl, J., Voisin, C., 2009. Characterization of fault roughness at various scales: Implications of three-dimensional high resolution topography measurements. Pure Appl. Geophys. 166, 1817–1851. doi:10.1007/s00024-009-0521-2

Candela, T., Renard, F., Klinger, Y., Mair, K., Schmittbuhl, J., Brodsky, E.E., 2012. Roughness of fault surfaces over nine decades of length scales. J. Geophys. Res. Solid Earth 117, 1–30. doi:10.1029/2011JB009041

Candela, T., Schmittbuhl, J., Bouchon, M., Brodsky, E.E., 2011. Fault slip distribution and fault roughness 959–968. doi:10.1111/j.1365-246X.2011.05189.x

Cembrano, J., Garcia, A., Herve, F., 1992. Paleomagnetism of Lower Cretaceous rocks from east of the Liquine-Ofqui fault zone , southern Chile : evidence of small in-situ clockwise rotations. Earth Planet. Sci. Lett. 113, 539–551. doi:10.1016/0012-821X(92)90130-N

Cembrano, J., Herve, F., 1993. The Liquiñe-Ofqui Fault Zone: a major Cenozoic strike slip duplex in the Southern Andes, in: Second ISAG. Oxford, UK, pp. 175–178.

Cembrano, J., Herve, F., Lavenu, A., 1996. The Liquifie Ofqui fault zone: a long-lived intra-arc fault system in southern Chile. Tectonophysics 256, 55–56.

Cembrano, J., Lara, L., 2009. The link between volcanism and tectonics in the southern volcanic zone of the Chilean Andes: A review. Tectonophysics 471, 96–113. doi:10.1016/j.tecto.2009.02.038

Cembrano, J., Moreno, H., 1994. Geometria y naturaleza costrastante del volcanismo cuaternario entre los 38°y 46°S: Dominios compresionales y tensionales en un régimen transcurrente? 7. Congr. Geológico Chil.

Cembrano, J., Schermer, E., Lavenu, A., Sanhueza, A., 2000. Contrasting nature of deformation along an intra-arc shear zone , the Liquiñe – Ofqui fault zone , southern Chilean Andes. Tectonophysics 319, 129–149. doi:10.1016/S0040-1951(99)00321-2

Chernicoff, C.J., Richards, J.P., Zappettini, E.O., 2002. Crustal lineament control on magmatism and mineralization in northwestern Argentina : geological , geophysical , and remote sensing evidence. Ore Geol. Rev. 21, 127–155.

Cifuentes, I.L., 1989. The 1960 Chilean earthquakes. J. Geophys. Res. 94, 665. doi:10.1029/JB094iB01p00665

Connolly, P., Cosgrove, J., 1999. Prediction of fracture-induced permeability and fluid flow in the crust using experimental stress data. AAPG Bull. 83, 757–777.

Cooley, J.W., Tukey, J.W., 1964. An Algorithm for the Machine Calculation of Complex Fourier Series. Math. Comput. 19, 297–301.

Corazzato, C., Tibaldi, A., 2006. Fracture control on type , morphology and distribution of parasitic volcanic cones : An example from Mt . Etna , Italy. doi:10.1016/j.jvolgeores.2006.04.018

Cox, S.F., 2010. The application of failure mode diagrams for exploring the roles of fluid pressure and stress states in controlling styles of fracture-controlled permeability enhancement in faults and shear zones. Geofluids 217–233. doi:10.1111/j.1468-8123.2010.00281.x

Cox, S.F., 2007. Structural and isotopic constraints on fluid flow regimes and fluid pathways during upper crustal deformation : An

example from the Taemas area of the Lachlan Orogen , SE Australia 112, 1–23. doi:10.1029/2006JB004734

Cox, S.F., 1999. Deformational controls on the dynamics of fluid flow in mesothermal gold systems. Geol. Soc. London, Spec. Publ. 155, 123–140. doi:10.1144/GSL.SP.1999.155.01.10

Curewitz, D., Karson, J. a, 1997. Structural settings of hydrothermal outflow: Fracture permeability maintained by fault propagation and interaction. J. Volcanol. Geotherm. Res. 79, 149–168. doi:10.1016/S0377-0273(97)00027-9

Dewey, J.F., Holdsworth, R.E., Strachan, R.A., 1998. Transpression and transtension zones. Geol. Soc. , London , Spec. Publ. 135, 1–14. doi:10.1144/GSL.SP.1998.135.01.01

Didenko, A.N., 1996. Modification of the borehole core orientation method with the use of viscous magnetization. Phys. Solid Earth 31, 879–884.

Diraison, M., Cobbold, P.R., Gapais, D., Rossello, E. a., Le Corre, C., 2000. Cenozoic crustal thickening, wrenching and rifting in the foothills of the southernmost Andes. Tectonophysics 316, 91–119. doi:10.1016/S0040-1951(99)00255-3

Doblas, M., 1998. Slickenside kinematic indicators. Tectonophysics 295, 187–197. doi:10.1016/S0040-1951(98)00120-6

Dobson, P.F., Kneafsey, T.J., Hulen, J., Simmons, A., 2003. Porosity, permeability, and fluid flow in the Yellowstone geothermal system, Wyoming. J. Volcanol. Geotherm. Res. 123, 313–324. doi:10.1016/S0377-0273(03)00039-8

Dunlop, D.J., Ozdemir, O., 2000. Effect of grain size and domain state on thermal demagnetization tails. Geophys. Res. Lett. 27, 1311–1314. doi:10.1029/1999GL008461

Dziewonski, A.M., Ekström, G., Woodhouse, J.H., Zwart, G., 1990. Centroid-moment tensor solutions for January-- . March 1989 59, 233–242.

Eccles, D., Sammonds, P.R., Clint, O.C., 2005. Laboratory studies of electrical potential during rock failure. Int. J. Rock Mech. Min. Sci. 42, 933–949. doi:10.1016/j.ijrmms.2005.05.018

Esaki, T., Du, S., Mitani, Y., Ikusada, K., Jing, L., 1999. Development of a shear-flow test apparatus and determination of coupled properties for a single rock joint. Int. J. Rock Mech. Min. Sci. 36, 641–650. doi:10.1016/S0148-9062(99)00044-3

Evans, J.P., Forster, C.B., Goddard, J. V., 1997. Permeability of fault-related rocks, and implications for hydraulic structure of fault zones. J. Struct. Geol. 19, 1393–1404. doi:10.1016/S0191-8141(97)00057-6

Fagereng, Å., Remitti, F., Sibson, R.H., 2011. Tectonophysics Incrementally developed slicken fi bers — Geological record of repeating low stress-drop seismic events ? 510, 381–386. doi:10.1016/j.tecto.2011.08.015

Faulkner, D.R., Armitage, P.J., 2013. The effect of tectonic environment on permeability development around faults and in the brittle crust. Earth Planet. Sci. Lett. 375, 71–77. doi:10.1016/j.epsl.2013.05.006

Faulkner, D.R., Jackson, C. a. L., Lunn, R.J., Schlische, R.W., Shipton, Z.K., Wibberley, C. a. J., Withjack, M.O., 2010. A review of recent developments concerning the structure, mechanics and fluid flow properties of fault zones, Journal of Structural Geology. Elsevier Ltd. doi:10.1016/j.jsg.2010.06.009

Faulkner, D.R., Rutter, E.H., 1998. The gas permeability of clay-bearing fault gouge at 20°C. Geol. Soc. London, Spec. Publ. 147, 147–156. doi:10.1144/gsl.sp.1998.147.01.10

Federico, L., Crispini, L., Capponi, G., 2010. Fault-slip analysis and transpressional tectonics: A study of Paleozoic structures in northern Victoria Land, Antarctica. J. Struct. Geol. 32, 667–684. doi:10.1016/j.jsg.2010.04.001

Fitch, T.J., 1972. Plate Convergence, Transcurrent Fault, and Internal Deformation Adjacent to Southeast Asia and the Western Pacific. J. Geophys. Res. 77, 4432–4460.

Fossen, H., Tikoff, B., 1998. Geological Society , London , Special Publications Extended models of transpression and transtension , and application to tectonic settings Email alerting service Permission Extended models of transpression and transtension , and application to tectonic s 15–33. doi:10.1144/GSL.SP.1998.135.01.02

Fossen, H., Tikoff, B., Teyssier, C., 1994. Strain modeling of transpressional and transtensional deformation. Nor. Geol. Tidsskr.

Ganerød, G. V., Braathen, A., Willemoes-Wissing, B., 2008. Predictive permeability model of extensional faults in crystalline and metamorphic rocks; verification by pre-grouting in two sub-sea tunnels, Norway. J. Struct. Geol. 30, 993–1004. doi:10.1016/j.jsg.2008.04.001

Glodny, J., Echtler, H., Collao, S., Ardiles, M., Burón, P., Figueroa, O., 2008. Differential Late Paleozoic active margin evolution in South-

Central Chile (37°S–40°S) – the Lanalhue Fault Zone. J. South Am. Earth Sci. 26, 397–411. doi:10.1016/j.jsames.2008.06.001

Glodny, J., Gräfe, K., Echtler, H., Rosenau, M., 2007. Mesozoic to Quaternary continental margin dynamics in South-Central Chile (36–42°S): the apatite and zircon fission track perspective. Int. J. Earth Sci. 97, 1271–1291. doi:10.1007/s00531-007-0203-1

González, D., Pinto, L., Peña, M., Arriagada, C., 2012. 3D deformation in strike-slip systems: Analogue modelling and numerical restoration. Andean Geol. 39, 295–316. doi:10.5027/andgeoV39n2-a06

Griffith, W.A., Nielsen, S., Di Toro, G., Smith, S.A.F., 2010. Rough faults, distributed weakening, and off-fault deformation. J. Geophys. Res. Solid Earth 115. doi:10.1029/2009JB006925

Gudmundsson, A., Berg, S.S., Lyslo, K.B., Skurtveit, E., 2001. Fracture networks and fluid transport in active fault zones. J. Struct. Geol. 23, 343–353. doi:10.1016/S0191-8141(00)00100-0

Gudmundsson, A., Kusumoto, S., Simmenes, T.H., Philipp, S.L., Larsen, B., Lotveit, I.F., 2012. Effects of overpressure variations on fracture apertures and fluid transport. Tectonophysics 581, 220–230. doi:10.1016/j.tecto.2012.05.003

Gudmundsson, A., Simmenes, T.H., Larsen, B., Philipp, S.L., 2010. Effects of internal structure and local stresses on fracture propagation, deflection, and arrest in fault zones. J. Struct. Geol. 32, 1643–1655. doi:10.1016/j.jsg.2009.08.013

Haberland, C., Rietbrock, A., Lange, D., Bataille, K., Hofmann, S., 2006. Interaction between forearc and oceanic plate at the south-central Chilean margin as seen in local seismic data. Geophys. Res. Lett. 33, 1–5. doi:10.1029/2006GL028189

Hailwood, E. a, Ding, F., 1995. Palaeomagnetic re-orientation of cores and the magnetic fabric of hydrocarbon reservoir sands. Palaeomagnetic Appl. Hydrocarb. Explor. Prod. 98, 245–258. doi:10.1144/GSL.SP.1995.098.01.15

Held, S., Schill, E., Pavez, M., Díaz, D., Muñoz, G., Morata, D., Kohl, T., 2016. Resistivity distribution from mid-crustal conductor to near-surface across the 1200 km long Liquiñe-Ofqui Fault System, southern Chile. Geophys. J. Int. 207, 1387–1400. doi:10.1093/gji/ggw338

Herman, M.W., Herrmann, R.B., Benz, H.M., Furlong, K.P., 2014. Using regional moment tensors to constrain the kinematics and stress evolution of the 2010 – 2013 Canterbury earthquake sequence , South Island , New Zealand. Tectonophysics 633, 1–15.

Hernandez-Moreno, C., Speranza, F., Di Chiara, A., 2016. Paleomagnetic rotation pattern of the southern Chile fore-arc sliver (38°S–42°S): A new tool to evaluate plate locking along subduction zones. J. Geophys. Res. Solid Earth 121, 469–490. doi:10.1002/2015JB012382

Hernandez-Moreno, C., Speranza, F., Di Chiara, A., 2014. Understanding kinematics of intra-arc transcurrent deformation: Paleomagnetic evidence from the Liquiñe-Ofqui fault zone (Chile, 38-41°S). Tectonics 33, 1964–1988. doi:10.1002/2014TC003622

Hulton, N.R.J., Purves, R.S., McCulloch, R.D., Sugden, D.E., Bentley, M.J., 2002. The Last Glacial Maximum and deglaciation in southern South America. Quat. Sci. Rev. 21, 233–241. doi:10.1016/S0277-3791(01)00103-2

Jarrard, R.D., 1986. Terrane motion by strike-slip faulting of forearc slivers. Geology 14, 780–783. doi:10.1130/0091-7613(1986)14<780:TMBSFO>2.0.CO

Kaplan, M.R., Moreno, P.I., Rojas, M., 2008. Glacial dynamics in southernmost South America during Marine Isotope Stage 5e to the Younger Dryas chron: a brief review with a focus on cosmogenic nuclide measurements. J. Quat. Sci. 23(6-7), 649–658. doi:10.1002/jqs.1209

Karaoğlu, Ö., Karaoğlu, Ö., Karaoğlu, Ö., 2014. Tectonic controls on the Yamanlar volcano and Yuntdağı volcanic region , western Turkey : Implications for an incremental deformation. J. Volcanol. Geotherm. Res. 274, 16–33. doi:10.1016/j.jvolgeores.2014.01.013

Kim, Y.-S., Peacock, D.C.., Sanderson, D.J., 2004. Fault damage zones. J. Struct. Geol. 26, 503–517. doi:10.1016/j.jsg.2003.08.002

Kirschvink, J.L., 1980. The least-squares line and plane and the analysis of paleomagnetic data. Geophys. J. R. Astron. Soc. 62, 699–718. doi:10.1111/j.1365-246X.1980.tb02601.x

Kolb, J., Rogers, A., Meyer, F.M., Siemes, H., 2005. Dominant coaxial deformation of veins during the interseismic stage of the fault-valve cycle: microfabrics of laminated quartz veins of the Hutti gold mine, India. J. Struct. Geol. 27, 2043–2057. doi:10.1016/j.jsg.2005.06.005

Kudo, Y., Sano, O., Murashige, N., Mizuta, Y., Nakagawa, K., 1992. Stress-induced crack path in Aji granite under tensile stress. Pure Appl. Geophys. PAGEOPH 138, 641–656. doi:10.1007/BF00876342

Lahsen, A., Rojas, J., Morata, D., Aravena, D., 2015a. Geothermal Exploration in Chile: Country Update. World Geotherm. Congr. 2015 1–7.

Lahsen, A., Rojas, J., Morata, D., Aravena, D., 2015b. Exploration for High-Temperature Geothermal Resources in the Andean Countries of South America 1996, 19–25.

Lanaro, F., 2000. A random field model for surface roughness and aperture of rock fractures. Int. J. Rock Mech. Min. Sci. 37, 1195–1210. doi:10.1016/S1365-1609(00)00052-6

Lange, D., Cembrano, J., Rietbrock, a., Haberland, C., Dahm, T., Bataille, K., 2008. First seismic record for intra-arc strike-slip tectonics along the Liquiñe-Ofqui fault zone at the obliquely convergent plate margin of the southern Andes. Tectonophysics 455, 14–24. doi:10.1016/j.tecto.2008.04.014

Lara, L., Lavenu, A., Cembrano, J., Rodriguez, C., 2006. Structural controls of volcanism in transversal chains: Resheared faults and neotectonics in the Cordón Caulle–Puyehue area (40.5°S), Southern Andes. J. Volcanol. Geotherm. Res. 158, 70–86. doi:10.1016/j.jvolgeores.2006.04.017

Lara, L., Naranjo, J., Moreno, H., 2004. Rhyodacitic fissure eruption in Southern Andes (Cordón Caulle; 40.5°S) after the 1960 (Mw:9.5) Chilean earthquake: a structural interpretation. J. Volcanol. Geotherm. Res. 138, 127–138. doi:10.1016/j.jvolgeores.2004.06.009

Lara, L.E., Cembrano, J., Lavenu, A., 2008. Quaternary Vertical Displacement along the Liquiñe-Ofqui Fault Zone : Differential Uplift and Coeval Volcanism in the Southern Andes? Int. Geol. Rev. 50, 975–993. doi:10.2747/0020-6814.50.11.975

Lavenu, A., Cembrano, J., 1999. Compressional- and transpressional-stress pattern for Pliocene and Quaternary brittle deformation in fore arc and intra-arc zones (Andes of Central and Southern Chile). J. Struct. Geol. 21, 1669–1691. doi:10.1016/S0191-8141(99)00111-X

Legrand, D., Barrientos, S., Bataille, K., Cembrano, J., Pavez, a., 2011. The fluid-driven tectonic swarm of Aysen Fjord, Chile (2007) associated with two earthquakes (Mw=6.1 and Mw=6.2) within the Liquiñe-Ofqui Fault Zone. Cont. Shelf Res. 31, 154–161. doi:10.1016/j.csr.2010.05.008

Lin, Y.N., Sladen, A., Ortega-culaciati, F., Simons, M., Avouac, J., Fielding, E.J., Brooks, B.A., Bevis, M., Genrich, J., Rietbrock, A., Vigny, C., Smalley, R., Socquet, A., 2013. Coseismic and postseismic slip associated with the 2010 Maule Earthquake , Chile : Characterizing the Arauco Peninsula barrier effect 118, 3142–3159. doi:10.1002/jgrb.50207

Liou, J.G., Maruyama, S., Cho, M., 1987. Very low-grade metamorphism of volcanic and volcaniclastic rocks: mineral assemblages and mineral facies. In: Frey, M ed. Very low- grade metamorphism. Blackie, Glasgow and London, Glasgow and London.

Lizama, M., Reich, M., Sánchez-alfaro, P., Pérez-flores, P., Cembrano, J., Morata, D., Arancibia, G., 2015. Alteración hidrotermal en el pozo Tol-1 , Sistema Geotermal Tolhuaca , Chile : un nuevo modelo de capa sello en sistemas geotermales andinos. XIV Congr. Geológico Chil. 473–476.

Lohmar, S., Stimac, J., Colvin, A., González, A., Iriarte, S., Melosh, G., Wilmarth, M., 2012. Tolhuaca volcano (Southern Chile , 38.3°S): New learnings from surface mapping and geothermal exploration wells. Proc. Congr. Geológico Chil. 2012 Antofagasta, Chile, 5-9 August 2012 443–445.

López-Escobar, L., Cembrano, J., Moreno, H., 1995. Geochemistry and tectonics of the Chilean Southern Andes basaltic Quaternary volcanism. Andean Geol. 22, 219–234.

MacLeod, C.J., Parson, L.M., Sager, W., 1994. Reorientation of Cores Using the Formation Microscanner and Borehole Televiewer: Application To Structural and Paleomagnetic Studies With the Ocean Drilling Program. Proc. Ocean Drill. Progr. 135, 301–311. doi:10.2973/odp.proc.sr.135.160.1994

Mandelbrot, B.B., 1983. The Fractal Geometry of Nature, American Journal of Physics. W. H. Freeman and Company, New York. doi:10.1017/CBO9781107415324.004

Marrett, R., Allmendinger, R.W., 1990. Kinematic analysis of fault-slip data. J. Struct. Geol. 12, 973–986. doi:10.1016/0191-8141(90)90093-E

Martínez-Díaz, J.J., 2002. Stress field variation related to fault interaction in a reverse oblique-slip fault : the Alhama de Murcia fault , Betic Cordillera, Spain. Tectonophysics 356, 291–305.

Mas, G.R., Bengochea, L., Mas, L.C., 2005. Thermometric Study of Copahue Geothermal Field ; Argentina, in: World Geothermal

Congress 2005. Antalya, Turkey, Turkey.

Mas, L.C., 2005. Present Status of the Copahue Geothermal Project, in: World Geothermal Congress. Antalya, Turkey, Turkey.

Maurice, J., 2012. Geochemical and Structural Constraints on Magma Storage at Llaima Volcano , A Support for Shallow Dikes Reservoirs . Graduate School of State University of New York.

Mccaffrey, K.J.W., 1992. Igneous emplacement in a transpressive shear zone : Ox Mountains igneous complex 149, 221–235.

McCulloch, R.D., Bentley, M.J., Purves, R.S., Hulton, N.R.J., Sugden, D.E., Clapperton, C.M., 2000. Climatic inferences from glacial and palaeoecological evidence at the last glacial termination , southern South America. J. Quat. Sci. 15, 409–417. doi:10.1002/1099-1417(200005)15:4<409::AID-JQS539>3.0.CO;2-#

Meixner, J., Schill, E., Grimmer, J.C., Gaucher, E., Kohl, T., Klingler, P., 2016. Structural control of geothermal reservoirs in extensional tectonic settings: An example from the Upper Rhine Graben. J. Struct. Geol. 82, 1–15. doi:10.1016/j.jsg.2015.11.003

Melnick, D., Bookhagen, B., Strecker, M.R., Echtler, H.P., 2009. Segmentation of megathrust rupture zones from forearc deformation patterns over hundreds to millions of years , Arauco peninsula , Chile. J. Geophys. Res. 114, B01407. doi:10.1029/2008JB005788

Melnick, D., Folguera, A., Ramos, V., 2006a. Structural control on arc volcanism: The Caviahue–Copahue complex, Central to Patagonian Andes transition (38°S). J. South Am. Earth Sci. 22, 66–88. doi:10.1016/j.jsames.2006.08.008

Melnick, D., Rosenau, M., Folguera, A., Echtler, H., 2006b. Neogene tectonic evolution of the Neuquén Andes western flank (37-39°S). Geol. Soc. Spec. Pap. 407.

Melosh, B.L., Rowe, C.D., Smit, L., Groenewald, C., Lambert, C.W., Macey, P., 2014. Snap , Crackle , Pop : Dilational fault breccias record seismic slip below the brittle – plastic transition 403, 432–445.

Melosh, G., Cumming, W., Benoit, D., Wilmarth, M., Colvin, A., Winick, J., Soto-, E., Sussman, D., Urzúa-monsalve, L., Powell, T., Peretz, A., 2010. Exploration results and resource conceptual model of the Tolhuaca Gethermal Field, Chile, in: Proceedings World Geothermal Congress. Bali, Indonesia., pp. 25–29.

Melosh, G., Moore, J., Stacey, R., 2012. Natural reservoir evolution in the Tolhuaca geothermal field, southern Chile, in: Thirty-Sixth Workshop on Geothermal Reservoir Engineering. Stanford, California, United States.

Micklethwaite, S., Cox, S.F., 2004. Fault-segment rupture, aftershock-zone fluid flow, and mineralization. Geology 32, 813. doi:10.1130/G20559.1

Micklethwaite, S., Sheldon, H. a., Baker, T., 2010. Active fault and shear processes and their implications for mineral deposit formation and discovery. J. Struct. Geol. 32, 151–165. doi:10.1016/j.jsg.2009.10.009

Min, K.-B., Rutqvist, J., Tsang, C.-F., Jing, L., 2004. Stress-dependent permeability of fractured rock masses: a numerical study. Int. J. Rock Mech. Min. Sci. 41, 1191–1210. doi:10.1016/j.ijrmms.2004.05.005

Mitchell, T.M., Faulkner, D.R., 2012. Towards quantifying the matrix permeability of fault damage zones in low porosity rocks. Earth Planet. Sci. Lett. 339–340, 24–31. doi:10.1016/j.epsl.2012.05.014

Mitchell, T.M., Faulkner, D.R., 2009. The nature and origin of off-fault damage surrounding strike-slip fault zones with a wide range of displacements: A field study from the Atacama fault system, northern Chile. J. Struct. Geol. 31, 802–816. doi:10.1016/j.jsg.2009.05.002

Moeck, I., Kwiatek, G., Zimmermann, G., 2009. Slip tendency analysis , fault reactivation potential and induced seismicity in a deep geothermal reservoir. J. Struct. Geol. 31, 1174–1182. doi:10.1016/j.jsg.2009.06.012

Mohanty, S., Hsiung, S., 2011. An experimental investigation of single fracture behaviorunder normal and shear loads.

Moncada, D., Mutchler, S., Nieto, a., Reynolds, T.J., Rimstidt, J.D., Bodnar, R.J., 2012. Mineral textures and fluid inclusion petrography of the epithermal Ag–Au deposits at Guanajuato, Mexico: Application to exploration. J. Geochemical Explor. 114, 20–35. doi:10.1016/j.gexplo.2011.12.001

Moreno, H., Clavero, J., 2006. Geología del Volcán Villarrica. Carta geológica de Chile 1:50.000. SERNAGEOMIN, Chile.

Moreno, H., Naranjo, J., Polanco, E., 2012. Geología del complejo volcánico Lonquimay-Tolhuaca. Carta Geológica de Chile 1:50.000. SERNAGEOMIN, Chile.

Moreno, M., Melnick, D., Rosenau, M., Bolte, J., Klotz, J., Echtler, H., Baez, J., Bataille, K., Chen, J., Bevis, M., Hase, H., Oncken, O., 2011. Heterogeneous plate locking in the South-Central Chile subduction zone: Building up the next great earthquake. Earth Planet.

Sci. Lett. 305, 413–424. doi:10.1016/j.epsl.2011.03.025

Moreno, M.S., Bolte, J., Klotz, J., Melnick, D., 2009. Impact of megathrust geometry on inversion of coseismic slip from geodetic data: Application to the 1960 Chile earthquake. Geophys. Res. Lett. 36, 1–5. doi:10.1029/2009GL039276

Muñoz, J., Stern, C.R.R., Muñoz B., J., Stern, C.R.R., 1988. The quaternary volcanic belt of the southern continental margin of South America: Transverse structural and petrochemical variations across the segment between 38°S and 39°S. J. South Am. Earth Sci. 1, 147–161. doi:10.1016/0895-9811(88)90032-6

Nakamura, K., 1977. Volcanoes as possible indicators of tectonic stress orientation - principle and proposal. J. Volcanol. Geotherm. Res. 2, 1–16. doi:10.1007/BF01637099

Nara, Y., Koike, K., Yoneda, T., Kaneko, K., 2006. Relation between subcritical crack growth behavior and crack paths in granite. Int. J. Rock Mech. Min. Sci. 43, 1256–1261. doi:10.1016/j.ijrmms.2006.03.016

Nara, Y., Meredith, P., Mitchell, T., 2013. Influence of macro-fractures and fault gouge on permeability in basalt, in: EGU General Assembly 2013, Held 7-12 April, 2013 in Vienna, Austria, Id. EGU2013-1493. p. 2013.

Nara, Y., Meredith, P.G., Yoneda, T., Kaneko, K., 2011. Influence of macro-fractures and micro-fractures on permeability and elastic wave velocities in basalt at elevated pressure. Tectonophysics 503, 52–59. doi:10.1016/j.tecto.2010.09.027

Nasseri, M.H.B., Schubnel, A., Benson, P.M., Young, R.P., 2009. Common evolution of mechanical and transport properties in thermally cracked westerly granite at elevated hydrostatic pressure. Pure Appl. Geophys. 166, 927–948. doi:10.1007/s00024-009-0485-2

Nishiyama, S., Ohnishi, Y., Ito, H., Yano, T., 2014. Mechanical and hydraulic behavior of a rock fracture under shear deformation. Earth, Planets Sp. 66, 108. doi:10.1186/1880-5981-66-108

Nukman, M., Moeck, I., 2013. Structural controls on a geothermal system in the Tarutung Basin, north central Sumatra. J. Asian Earth Sci. 74, 86–96. doi:10.1016/j.jseaes.2013.06.012

Olsson, R., Barton, N., 2001. An improved model for hydromechanical coupling during shearing of rock joints. Int. J. Rock Mech. Min. Sci. 38, 317–329. doi:10.1016/S1365-1609(00)00079-4

Olsson, W.A., Brown, S.R., 1993. Hydromechanical response of a fracture undergoing compression and shear. Int. J. Rock Mech. Min. Sci. 30, 845–851. doi:10.1016/0148-9062(93)90034-B

Otsubo, M., Sato, K., Yamaji, A., 2006. Computerized identification of stress tensors determined from heterogeneous fault-slip data by combining the multiple inverse method and k-means clustering. J. Struct. Geol. 28, 991–997. doi:10.1016/j.jsg.2006.03.008

Ousadou, F., Dorbath, L., Ayadi, A., Dorbath, C., 2014. Stress field variations along the Maghreb region derived from inversion of major seismic crisis fault plane solutions. Tectonophysics 632, 261–280.

Pardo-Casas, F., Molnar, P., 1987. Relative Motion of The Nazca (Farellon) and South American Plates Since late Cretaceous Time 6, 233–248.

Parés, J.M., Schleicher, A.M., van der Pluijm, B.A., Hickman, S., 2008. Paleomagnetic reorientation of San Andreas Fault Observatory at Depth (SAFOD) core. Geophys. Res. Lett. 35, 1–6. doi:10.1029/2007GL030921

Pérez-Flores, P., Cembrano, J., Sanchez, P., Veloso, E., Arancibia, G., Roquer, T., 2016. Tectonics, magmatism and paleo-fluid distribution in a strike-slip setting: Insights from the northern termination of the Liquiñe-Ofqui fault System, Chile. Tectonophysics 680, 192–210. doi:10.1016/j.tecto.2016.05.016

Perez-Flores, P., Sanchez, P., Sielfeld, G., Cembrano, J., 2013. Tectonics, magmatism and fluid flow in a transtensional strike-slip setting: The northern termination of the dextral strike-slip Liquiñe-Ofqui fault System, Chile., in: AGU Meeting of the Americas. Mexico. doi:10.1080/00206814.2013.

Persson, B.N.J., Albohr, O., Tartaglino, U., Volokitin, a I., Tosatti, E., 2005. On the nature of surface roughness with application to contact mechanics, sealing, rubber friction and adhesion. J. Phys. Condens. Matter 17, R1–R62. doi:10.1088/0953-8984/17/1/R01

Petit, J.P., 1987. Criteria for the sense o f movement on fault surfaces in brittle rocks. J. Struct. Geol. 9, 597–608. doi:10.1016/0191-8141(87)90145-3

Plafker, G., Savage, J.C., 1970. Mechanism of the Chilean Earthquakes of May 21 and 22, 1960. Geol. Soc. Am. Bull. 81, 1001–1030.

Polanco, E., Moreno, H., Naranjo, J.A., Pérez de Arce, C., 2014. Nuevas edades Ar/Ar del Complejo Lonquimay-Tolhuaca y su contribución a la comprensión de su evolución geológica, in: Jornadas Geológicas, Sesión Temática 12. SERNAGEOMIN.

Santiago, Chile, pp. 139–142.

Power, W.L., Tullis, T.E., 1991. Euclidean and fractal models for the description of rock surface roughness. J. Geophys. Res. 96, 415. doi:10.1029/90JB02107

Power, W.L., Tullis, T.E., 1989. The relationship between slickenside surfaces in fine-grained quartz and the seismic cycle. J. Struct. Geol. 11, 879–893. doi:10.1016/0191-8141(89)90105-3

Pratt, H.R., Swolfs, H.S., Brace, W.F., Black, A.D., Handin, J.W., 1977. Elastic and transport properties of an in situ jointed granite. Int. J. Rock Mech. Min. Sci. 14, 35–45. doi:10.1016/0148-9062(77)90560-5

Radic, J.P., 2010. Las cuencas cenozoicas y su control en el volcanismo de los Complejos Nevados de Chillán y Copahue-Callaqui (Andes del Sur , 36-39 ° S). Andean Geol. 37, 220–246.

Raven, K.G., Gale, J.E., 1985. Water flow in a natural rock fracture as a function of stress and sample size. Int. J. Rock Mech. Min. Sci. 22, 251–261. doi:10.1016/0148-9062(85)92952-3

Reyes, A.G., 1990. Petrology of Philippine geothermal systems and the application of alteration mineralogy to their assessment. J. Volcanol. Geotherm. Res. 43, 279–309. doi:10.1016/0377-0273(90)90057-M

Ritz, J.-F., 1994. Determining the slip vector by graphical construction: use of a simplified representation of the stress tensor. J. Struct. Geol. 16, 737–741.

Roquer, T., Arancibia, G., Rowland, J., Iturrieta, P., Morata, D., Cembrano, J., 2017. Fault-controlled development of shallow hydrothermal systems: Structural and mineralogical insights from the Southern Andes. Geothermics 66, 156–173. doi:10.1016/j.geothermics.2016.12.003

Rosenau, M., Melnick, D., Echtler, H., 2006. Kinematic constraints on intra-arc shear and strain partitioning in the southern Andes between 38 ° S and 42 ° S latitude. Tectonics 25, 1–16. doi:10.1029/2005TC001943

Rowland, J. V., Sibson, R.H., 2004. Structural controls on hydrothermal flow in a segmented rift system, Taupo Volcanic Zone, New Zealand. Geofluids 4, 259–283. doi:10.1111/j.1468-8123.2004.00091.x

Rowland, J. V., Simmons, S.F., Zealand, N., Zealand, N., 2012. Hydrologic, Magmatic, and Tectonic Controls on Hydrothermal Flow, Taupo Volcanic Zone, New Zealand: Implications for the Formation of Epithermal Vein Deposits. Econ. Geol. 107, 427–457. doi:10.2113/econgeo.107.3.427

Russo, R., Mora-stock, C., Vandecar, J.C., Russo, R.M., Gallego, A., Comte, D., Mocanu, V.I., Murdie, R.E., Mora, C., Vandecar, J.C., 2011. Triggered seismic activity in the Liquiñe-Ofqui fault zone , southern Chile , during the 2007 Aysen seismic swarm Chile , during the 2007 Aysen seismic swarm. Geophys. J. Int 184, 1217–1326. doi:10.1111/j.1365-246X.2010.04908.x

Sagy, A., Brodsky, E.E., Axen, G.J., 2007. Evolution of fault-surface roughness with slip. Geology 35, 283–286. doi:10.1130/G23235A.1

Sanchez-Alfaro, P., Reich, M., Arancibia, G., Pérez-Flores, P., Cembrano, J., Driesner, T., Lizama, M., Rowland, J., Morata, D., Heinrich, C.. C.A., Tardani, D., Campos, E., 2016. Physical, chemical and mineralogical evolution of the Tolhuaca geothermal system, southern Andes, Chile: Insights into the interplay between hydrothermal alteration and brittle deformation. J. Volcanol. Geotherm. Res. 324, 88–104. doi:10.1016/j.jvolgeores.2016.05.009

Sánchez, P., Pérez-Flores, P., Reich, M., Arancibia, G., Cembrano, J., 2013. Crustal deformation effects on the chemical evolution of geothermal systems : the intra-arc Liquiñe–Ofqui Fault System , Southern Andes. Int. Geol. Rev. 55, 37–41. doi:10.1080/00206814.2013.775731

Sanderson, D.J., Marchini, W.R.D., 1984. Transpression. J. Struct. Geol. 6, 449–458. doi:10.1016/0191-8141(84)90058-0

Scholz, C.H., Gupta, A., 2000. Fault interactions and seismic hazard 29, 459–467.

Sepúlveda, F., Lahsen, A., Bonvalot, S., Cembrano, J., Alvarado, A., Letelier, P., 2005. Morpho-structural evolution of the Cordón Caulle geothermal region, Southern Volcanic Zone, Chile: Insights from gravity and 40Ar/39Ar dating. J. Volcanol. Geotherm. Res. 148, 165–189. doi:10.1016/j.jvolgeores.2005.03.020

Sheldon, H. a., Micklethwaite, S., 2007. Damage and permeability around faults: Implications for mineralization. Geology 35, 903. doi:10.1130/G23860A.1

Siame, L.L., Bellier, O., 2005. Deformation partitioning in flat subduction setting : Case of the Andean foreland of western Argentina (28 ° S – 24, 1–24. doi:10.1029/2005TC001787

Sibson, R.H., 2012. Reverse fault rupturing : competition between non-optimal and optimal fault orientations Reverse fault rupturing : competition between non-optimal and optimal fault orientations. Geol. Soc. , London , Spec. Publ. 367, 39–50. doi:10.1144/SP367.4

Sibson, R.H., 2004. Controls on maximum fluid overpressure defining conditions for mesozonal mineralisation. J. Struct. Geol. 26, 1127–1136. doi:10.1016/j.jsg.2003.11.003

Sibson, R.H., 2003. Brittle-failure controls on maximum sustainable overpressure in different tectonic regimes. Am. Assoc. Pet. Geol. Bull. 87, 901–908. doi:10.1306/01290300181

Sibson, R.H., 1996. Structural permeability of fluid-driven fault-fracture meshes. J. Struct. Geol. 18, 1031–1042. doi:10.1016/0191-8141(96)00032-6

Sibson, R.H., 1994. Crustal stress, faulting and fluid flow. Geol. Soc. Spec. Publ. 78, 69–84. doi:10.1144/GSL.SP.1994.078.01.07

Sibson, R.H., 1987. Earthquake rupturing as a mineralizing agent in hydrothermal systems. Geology 15, 701–704.

Sibson, R.H., 1985. A note on fault reactivation. J. Struct. Geol. 7, 751–754.

Sibson, R.H., Moore, J.M.M., Rankin, A.H., 1975. Seismic pumping a hydrothermal fluid transport mechanism 653–659. doi:10.1144/gsjgs.131.6.0653

Sielfeld, G., 2008. Condón Fisural Callaqui: Antecedentes tectónicos de la naturaleza y geometría del volcanismo fisural en el volcán Callaqui. Universidad de Concepción.

Sielfeld, G., Cembrano, J., Lara, L., 2016. Transtension driving volcano-edifice anatomy: Insights from Andean transverse-to-the-orogen tectonic domains. Quat. Int. 1–17. doi:10.1016/j.quaint.2016.01.002

Sielfeld, G., Cembrano, J., Lara, L., 2015. Transtension driving volcano-edifice anatomy: Insights from oblique-to-the-arc tectonic domains, in Interactions between Quaternary climatic forcing, tectonics and volcanism along some different tectonic settings of South America, Special volume of Quater. Quat. Int. Special Vo, XX.

Song, I., Elphick, S.C., Main, I.G., Ngwenya, B.T., Odling, N.W., Smyth, N.F., 2004. One-dimensional fluid diffusion induced by constant-rate flow injection: Theoretical analysis and application to the determination of fluid permeability and specific storage of a cored rock sample. J. Geophys. Res. Solid Earth 109, 1–13. doi:10.1029/2003JB002395

Stanton-Yonge, A., Griffith, W.A., Cembrano, J., St. Julien, R., Iturrieta, P., 2016. Tectonic role of margin-parallel and margin-transverse faults during oblique subduction in the Southern Volcanic Zone of the Andes: Insights from Boundary Element Modeling. Tectonics 1–24. doi:10.1002/2016TC004226

Stern, C.R., Moreno, H., López-Escobar, L., Clavero, J.E., Lara, L.E., Naranjo, J. a., Parada, M. a., Skewes, M.A., 2007. Chilean volcanoes, in: The Geology of Chile. The Geological Society, pp. 147–178.

Stimac, J., Goff, F., Goff, C.J., 2015. Intrusion-Related Geothermal Systems, Second Edi. ed, The Encyclopedia of Volcanoes. Dr Jim Stimac, Copyright © 2015. doi:10.1016/B978-0-12-385938-9.00046-8

Suárez, M., Emparan, C., 1997. Hoja Curacautín, región de la Araucanía y del Biobío. Carta geológica de Chile., Servicio N. ed, Carta Geológica de Chile, Servicio Nacional de Geología y Minería.

Suganuma, Y., Okada, M., Horie, K., Kaiden, H., Takehara, M., Senda, R., Kimura, J.I., Kawamura, K., Haneda, Y., Kazaoka, O., Head, M.J., 2015. Age of Matuyama-Brunhes boundary constrained by U-Pb zircon dating of a widespread tephra. Geology 43, 491–494. doi:10.1130/G36625.1

Tardani, D., Reich, M., Roulleau, E., Takahata, N., Sano, Y., Pérez-Flores, P., Sánchez, P., Cembrano, J., Arancibia, G., Sánchez-Alfaro, P., Cembrano, J., Arancibia, G., Sa, P., Sano, Y., Pe, P., Arancibia, G., 2016. Exploring the structural controls on helium, nitrogen and carbon isotope signatures in hydrothermal fluids along an intra-arc fault system . Geochim. Cosmochim. Acta 184, 193–211. doi:http://dx.doi.org/10.1016/j.gca.2016.04.031

Tauxe, L., 1998. Paleomagnetic principles and practice. Mod. approaches Geophys.

Teyssier, C., Tikoff, B., 1998. Strike-slip partitioned transpression of the San Andreas fault system : a lithospheric-scale approach. Geol. Soc. , London , Spec. Publ. 135, 143–158. doi:10.1144/GSL.SP.1998.135.01.10

Teyssier, C., Tikoff, B., Markley, M., 1995. Oblique plate motion and continental tectonics. Geology 23, 447–450. doi:10.1130/0091-7613(1995)023<0447:OPMACT>2.3.CO;2

Thiele, R., Lahsen, A., Moreno, H., Varela, J., Vergara, M., 1987. Estudios geológicos regionales a escala 1:100.000 de la hoya superior y curso medio del Biobío.

Tibaldi, A., Lagmay, A.M.F.A., Ponomareva, V. V, 2005. Effects of basement structural and stratigraphic heritages on volcano behaviour and implications for human activities (the UNESCO / IUGS / IGCP project 455). Episodes 28, 158–170.

Tikoff, B., Greene, D., 1997. Stretching lineations in transpressional shear zones: an example from the Sierra Nevada Batholith, California. J. Struct. Geol. 19, 29–39.

Turcotte, D.L., 1992. Fractals and chaos in geology and geophysics. Cambridge University Press.

Uehara, S. ichi, Shimamoto, T., 2004. Gas permeability evolution of cataclasite and fault gouge in triaxial compression and implications for changes in fault-zone permeability structure through the earthquake cycle. Tectonophysics 378, 183–195. doi:10.1016/j.tecto.2003.09.007

Ureel, S., Momayez, M., Oberling, Z., 2013. Rock Core Orientation for Mapping Discontinuities and. Int. J. Res. Eng. Technol. 2, 1–8.

Uysal, I.T., Feng, Y., Zhao, J., Bolhar, R., Işik, V., Baublys, K. a., Yago, A., Golding, S.D., 2011. Seismic cycles recorded in late Quaternary calcite veins: Geochronological, geochemical and microstructural evidence. Earth Planet. Sci. Lett. 303, 84–96. doi:10.1016/j.epsl.2010.12.039

Van Wyk De Vries, B., Merle, O., 1998. Extension induced by volcanic loading in regional strike-slip zones. Geology 26, 983–986. doi:10.1130/0091-7613(1998)026<0983:EIBVLI>2.3.CO;2

Veloso, E., Gomila, R., González, R., Cembrano, J., Jensen, E., Arancibia, G., 2015. Stress fields recorded on large-scale strike-slip fault systems: Effects on the tectonic evolution of crustal slivers during oblique subduction. Tectonophysics 664, 244–255. doi:10.1016/j.tecto.2015.09.022

Veloso, E.E., Anma, R., Yamaji, A., 2009. Ophiolite Emplacement and the Effects of the Subduction of the Active Chile Ridge System : Heterogeneous Paleostress Regimes Recorded in the Taitao Ophiolite (Southern Chile). Andean Geol. 36, 3–16. doi:10.5027/andgeoV36n1-a01

Vicencio, V., 2015. Geología y mineralogía de alteración en una sucesión volcano-sedimentaria en la Zona Volcánica Sur Central, Chile. Evidencias de un paleo-sistema volcánico y geotermal en la Formación Cura-Mallín. Universidad de Chile.

Vinciguerra, S., Trovato, C., Meredith, P.G., Benson, P.M., 2005. Relating seismic velocities, thermal cracking and permeability in Mt. Etna and Iceland basalts. Int. J. Rock Mech. Min. Sci. 42, 900–910. doi:10.1016/j.ijrmms.2005.05.022

Virgil, C., Ehmann, S., Hordt, A., Leven, M., Steveling, E., 2015. Reorientation of three-component borehole magnetic data. Geophys. Prospect. 63, 225–242. doi:10.1111/1365-2478.12175

Walker, R.J., Holdsworth, R.E., Armitage, P.J., Faulkner, D.R., 2013. Fault zone permeability structure evolution in basalts. Geology 41, 59–62. doi:10.1130/G33508.1

Walsh, J.B., Grosenbaugh, M.A., 1979. A New Model for Analyzing the Effect of Fractures on Compressibility. J. Geophys. Res. 84.

Wang, G., Mitchell, T.M., Meredith, P.G., Nara, Y., Wu, Z., 2016. Influence of gouge thickness and grain size on permeability of macro-fractured basalt. J. Geophys. Res. Solid Earth. doi:10.1002/2016JB013363

Wang, K., Hu, Y., Bevis, M., Kendrick, E., Robert, S., Vargas, R.B., Lauría, E., Smalley, R., Vargas, R.B., Lauría, E., 2007. Crustal motion in the zone of the 1960 Chile earthquake: Detangling earthquake-cycle deformation and forearc-silver translation. Geochemistry, Geophys. Geosystems 8, 1–14. doi:10.1029/2007GC001721

Watanabe, N., Hirano, N., Tsuchiya, N., 2008. Determination of aperture structure and fluid flow in a rock fracture by high-resolution numerical modeling on the basis of a flow-through experiment under confining pressure. Water Resour. Res. 44, 1–11. doi:10.1029/2006WR005411

Weatherley, D.K., Henley, R.W., 2013. Flash vaporization during earthquakes evidenced by gold deposits. Nat. Geosci. 6, 1–5. doi:10.1038/ngeo1759

Whitney, D.L., Evans, B.W., 2010. Abbreviations for names of rock-forming minerals. Am. Mineral. 95, 185–187. doi:10.2138/am.2010.3371

Wibberley, C. a. ., Shimamoto, T., 2003. Internal structure and permeability of major strike-slip fault zones: the Median Tectonic Line in Mie Prefecture, Southwest Japan. J. Struct. Geol. 25, 59–78. doi:10.1016/S0191-8141(02)00014-7

Winklhofer, M., Fabian, K., Heider, F., 1997. Magnetic blocking temperatures of magnetite calculated with a three-dimensional micromagnetic model. J. Geophys. Res. 102, 22695–22709. doi:10.1029/97JB01730

Witherspoon, P.A., Wang, J.S.Y., Iwai, K., Gale, J.E., 1980. Validity of Cubic Law for fluid flow in a deformable rock fracture. Water Resour. Res. 16, 1016–1024. doi:10.1029/WR016i006p01016

Yamaji, A., 2000. The multiple inverse method: a new technique to separate stresses from heterogeneous fault-slip data. J. Struct. Geol. 22, 441–452. doi:10.1016/S0191-8141(99)00163-7

Yáñez, G., Gana, P., Fernández, R., 1998. Origen y significado geológico de la Anomalía Melipilla, Chile central. Rev. geológica Chile.

Zang, A., Stephansson, O., Heidbach, O., Janouschkowetz, S., 2012. World stress map database as a resource for rock mechanics and rock engineering. Geotech. Geol. Eng. 30, 625–646. doi:10.1007/s10706-012-9505-6

Zhang, F.-Q., Song, J.-S., Shen, Z.-Y., Chen, H.-L., Dong, C.-W., Pang, Y.-M., Shu, P., 2007. A study on fracture orientation and characteristic of remnant magnetization of deep-burial volcanic rocks, north of the Songliao Basin. Chinese J. Geophys. 50, 1011–1017. doi:10.1002/cjg2.1118

Zhang, S., Tullis, T.E., 1998. The effect of fault slip on permeability and permeability anisotropy in quartz gouge. Tectonophysics 295, 41–52. doi:10.1016/S0040-1951(98)00114-0

Zhang, Y., Schaubs, P.M., Zhao, C., Ord, A., Hobbs, B.E., Barnicoat, A.C., 2008. Fault-related dilation, permeability enhancement, fluid flow and mineral precipitation patterns: numerical models. Geol. Soc. London, Spec. Publ. 299, 239–255. doi:10.1144/SP299.15

Zijderveld, J.D.A., 1967. A.C. Demagnetization of rocks: analysis of results, in Methods in Paleomagnetism (eds D. W. Collinson, K. M. Creer and S. K. Runcorn). Elsevier, Amsterdam.

Zimmerman, R.W., 2012. The history and role of the cubic law for fluid flow in fractured rocks. Agu 2012 Presentation.

6 APPENDIX

SM 1. Lolco and Ralco structural sites location and outcrop details showing structural elements analyzed.

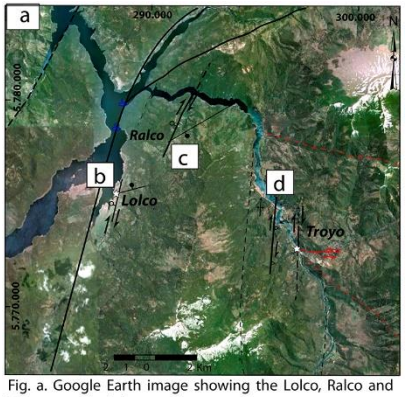

Fig. a. Google Earth image showing the Lolco, Ralco and Troyo structural sites

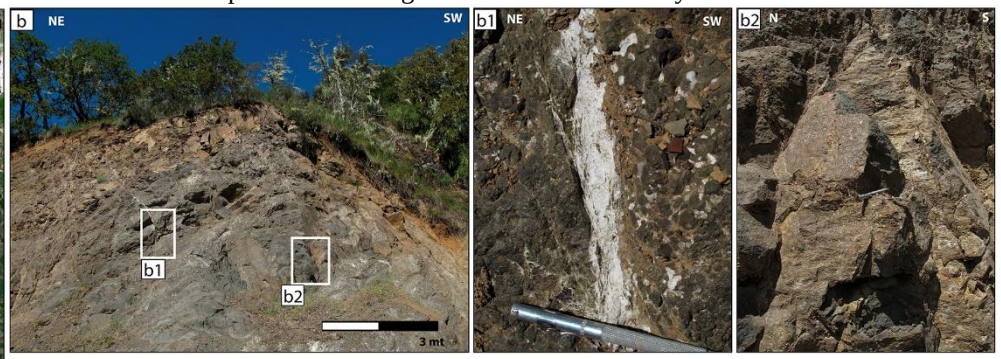

Fig. b. Field view looking SE at Lolco structural site. (b1) N65E/75W zeolite vein. (b2) N17E/70W, Right-lateral strike-slip faults with zeolite slickenfibers.

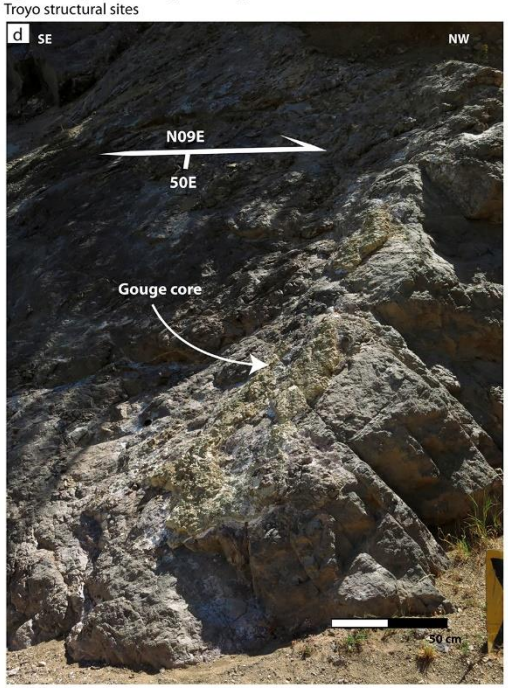

Fig. d. Field view looking west at Troyo structural site showing a N05E/50E, dextral-reverse fault zone with 20 cm thick gouge core.

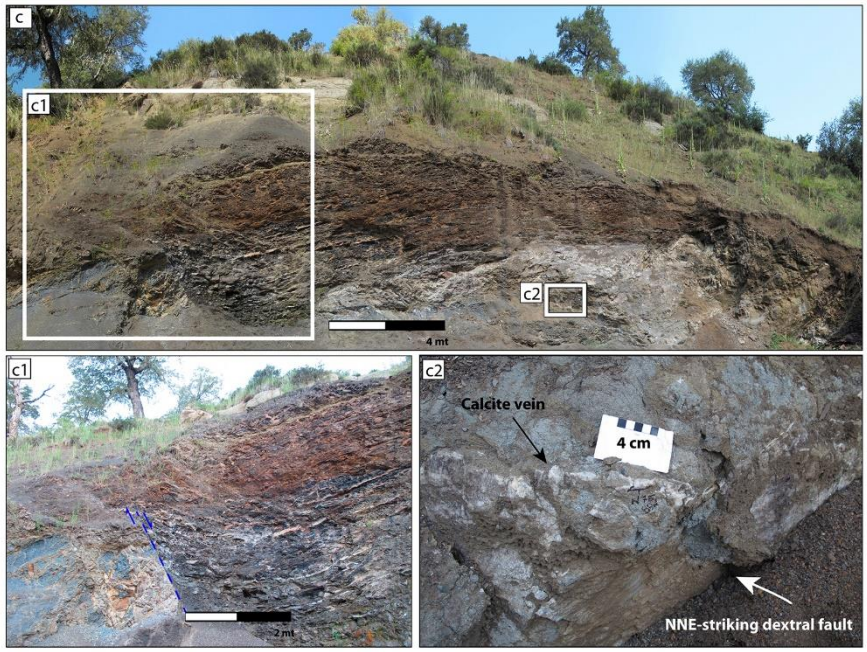

Fig. c. Field view looking east at Ralco structural site. (c1) N62E/61S calcite-zeolite dextral-normal oblique fault vein showing a ca. 1 m apparent offset and a fault propagated fold of the shale layers in the hanging wall. (b2) N70E/70S, calcite vein splayed off from NNE-striking dextral fault.

SM 2. Las Raices and Las Animas structural sites location and outcrop details showing structural elements analyzed.

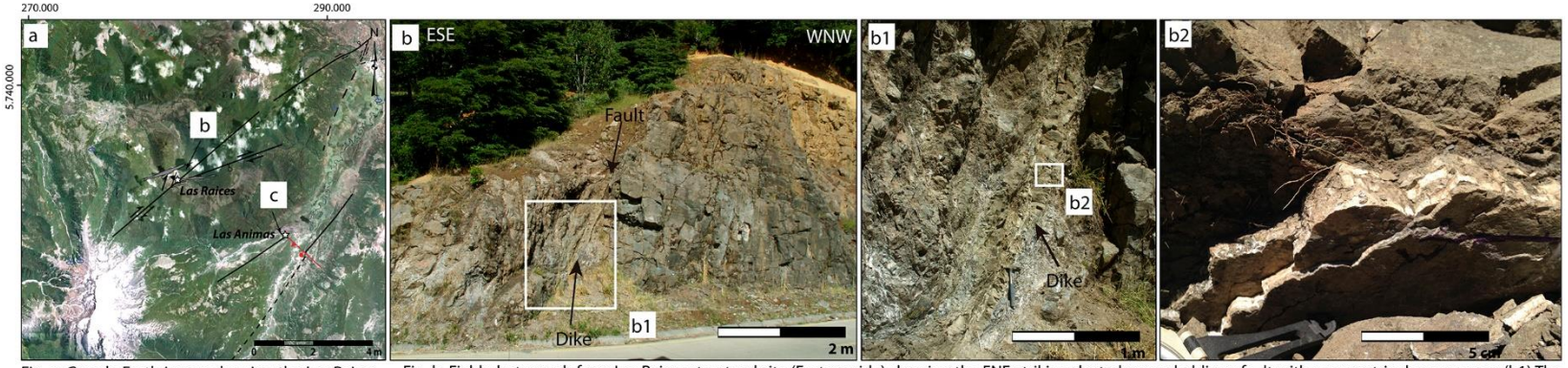

Fig. a. Google Earth image showing the Las Raices and Las Animas structural sites

Fig. b. Field photograph from Las Raices structural site (Eastern side) showing the ENE-striking dextral-normal oblique fault with asymmetric damage zone. (b1) The fault zone host a syntectonic dike, which is crosscut by ENE-striking zeolite-calcite veins-breccia (b2).

Fig. c. Field photograph showing one typical NW-striking fault belonging to ATF. The fault core consists of a calcite – zeolite – matrix breccia with rounded clast; the damage zone is characterized by vein network with the same infill. (c1) Fault-core breccia with evidence of at least two fracture episodes. (c2) Banded vein consisting of early zeolite veins and a late breccia with vein-clast.

SM 3. Structural sites fault-slip data.

La Poza Structural site			Coordinates	293158E	5743169N					
Fault strike	Fault dip	Striae trend	Striae plunge	Sense of Slip	T trend	T plunge	P trend	P plunge	Quality	Gouge thickness
262	43	57	21	TL	101	51	210	15	C	0.002
260	59	79	1	TL	120	22	219	21	D	0
270	63	84	11	TL	129	27	225	11	C	0
272	60	272	0	NL	133	21	231	21	B	0.002
252	58	257	8	NL	116	16	214	29	C	0
280	82	99	10	TL	144	13	54	1	C	0
248	64	252	7	NL	112	13	208	23	D	0
252	74	67	15	TL	115	22	205	0	F	0.001
200	80	8	49	NR	320	24	73	41	F	0.02
230	54	40	13	NR	185	15	84	35	C	0.001
241	49	43	19	NR	192	13	88	44	C	0.001
244	75	63	5	NR	199	7	107	14	F	0.001
238	74	57	2	TL	102	13	194	10	D	0.001
237	50	342	49	NR	334	5	94	81	C	0.001
195	66	199	9	TR	154	24	60	10	c	0.001
205	74	214	29	TR	161	32	257	8	C	0.001
184	72	197	34	TR	140	38	238	10	D	0
250	70	67	8	NR	205	9	112	20	D	0
288	74	101	24	TL	151	29	58	5	B	0.01
230	78	45	21	NR	1	6	94	24	A	0.15
48	80	57	41	TR	359	36	104	20	b	0
230	84	45	38	NR	357	21	100	30	D	0
235	85	53	21	NR	7	11	101	18	B	0.2

Lolco structural site			Coordinates	288609E	5775356N					
Fault strike	Fault dip	Striae trend	Striae plunge	Sense of Slip	T trend	T plunge	P trend	P plunge	Quality	Gouge thickness
232	44	13	31	NR	171	8	65	61	B	0
222	80	235	53	TR	167	43	284	26	D	0.02
65	84	67	15	TR	20	15	112	6	D	0.03
160	68	164	9	TR	119	22	25	9	C	0.001
319	46	129	10	NR	277	22	169	38	C	0.001
197	68	13	9	NR	152	9	58	22	A	0
194	70	8	15	NR	147	3	55	25	A	0
210	62	20	18	NR	162	7	68	33	A	0
214	66	29	11	NR	168	9	74	25	A	0
200	70	17	9	NR	155	7	62	21	A	0
26	78	26	0	TR	342	8	250	8	A	0
210	76	22	29	NR	338	10	74	31	A	0
205	76	22	12	NR	159	2	68	18	A	0
207	64	25	4	NR	164	15	68	21	B	0
192	68	7	12	NR	146	7	53	24	B	0
200	80	20	2	NR	155	6	64	8	A	0
25	87	27	30	TR	337	23	75	18	A	0
186	74	357	29	NR	314	8	50	32	B	0
206	80	22	24	NR	337	9	71	24	B	0
210	68	16	31	NR	336	6	71	39	B	0

Las Animas structural site			Coordinates	287737E	5730366N					
Fault strike	Fault dip	Striae trend	Striae plunge	Sense of Slip	T trend	T plunge	P trend	P plunge	Quality	Gouge thickness
263	90	263	46	TR	208	31	318	31	B	0.005
165	44	196	27	NL	41	11	148	56	C	0.05
180	58	185	8	NL	44	16	142	29	D	0.01
140	82	319	8	TL	4	11	94	0	D	0.002
192	78	198	25	NL	242	9	147	27	B	0.002
205	80	15	43	NR	328	21	75	37	C	0
205	87	23	38	NR	332	23	76	28	D	0.005
175	78	181	27	NL	226	10	130	28	D	0.002
180	68	355	11	NR	134	7	41	24	D	0
310	58	336	35	NL	8	2	276	51	D	0.01
334	80	347	53	NL	36	26	279	43	D	0.005
313	50	113	23	TL	160	46	262	11	D	0
305	80	319	55	NL	9	27	249	44	D	0.002
58	62	71	23	TR	21	37	288	3	B	0.002
104	86	278	56	NR	222	32	343	39	D	0.01
115	76	289	21	NR	246	5	338	25	D	0
295	58	342	50	NL	7	9	255	66	D	0.1
143	73	151	25	NL	193	5	100	30	D	0
180	66	352	18	NR	132	4	39	31	D	0.05
180	72	351	26	NR	309	5	42	32	D	0
330	64	146	7	TL	190	23	286	13	D	0
205	78	345	72	NR	307	32	98	55	D	0.02
70	84	249	6	NR	25	0	295	8	F	0
62	82	236	35	NR	189	18	290	30	F	0
45	78	220	23	TL	269	25	176	8	C	0.001
334	80	347	53	NL	36	26	279	43	D	0.5
120	84	122	20	NL	168	10	74	18	D	0.04
301	84	111	59	NR	56	32	182	43	D	0.04
90	78	100	38	NL	145	17	43	36	D	0.001
180	68	331	50	NR	294	16	48	54	C	0
217	79	32	25	NR	347	10	82	26	D	0.002
295	71	324	55	NL	3	20	242	54	C	0.01
317	60	355	47	NL	24	9	278	60	D	0.002
243	88	63	6	NR	18	3	108	6	C	0.01
295	86	300	54	NL	356	31	237	38	C	0.005
184	50	358	8	NR	142	21	38	33	D	0.015

Troyo structural site			Coordinates	297320E	5772812N					
Fault strike	Fault dip	Striae trend	Striae plunge	Sense of Slip	T trend	T plunge	P trend	P plunge	Quality	Gouge thickness
100	53	271	12	TL	314	35	55	16	B	5
95	55	263	16	TL	309	37	48	12	A	5
100	48	266	15	TL	309	41	54	17	A	0
100	50	268	14	TL	311	38	55	17	A	0
108	50	275	15	TL	318	40	62	16	A	0
125	50	285	23	TL	332	46	74	11	C	0
105	47	273	12	TL	314	39	61	19	C	0
353	72	356	10	TR	311	20	219	6	B	0
352	68	2	23	TR	312	33	42	1	C	0
350	70	42	65	TR	283	62	68	24	C	5
42	84	46	32	NL	93	17	354	27	C	0
173	72	350	10	NR	127	6	35	20	C	0
172	68	342	23	NR	302	1	32	33	C	0
180	74	355	17	NR	312	1	43	24	C	0
181	74	358	10	NR	135	4	44	18	C	0.02
200	84	202	20	TR	154	18	248	10	F	6
202	70	319	68	NR	300	24	96	64	C	0.03

Las Raices structural site			Coordenates	280556E	5733853N					
Fault strike	Fault dip	Striae trend	Striae plunge	Sense of Slip	T trend	T plunge	P trend	P plunge	Quality	Gouge thickness
270	74	85	17	TL	133	24	42	1	C	0
267	74	86	4	TL	130	14	222	8	C	0
249	83	65	30	NR	18	15	116	26		0.04
58	77	63	19	TR	14	23	106	4	D	0.02
60	80	64	20	TR	15	21	108	7	D	0.02
38	78	45	31	TR	352	31	90	13	D	0
220	55	6	39	NR	337	2	71	58	D	0.03
35	64	48	25	TR	357	37	266	1	A	0
250	66	47	41	NR	10	10	112	49	D	0.04
256	74	74	6	NR	211	7	119	15	D	0
78	87	80	36	NL	130	22	28	27	D	0.01
65	82	69	28	NL	115	13	19	25	C	0.01
90	86	92	24	NL	138	14	43	20	B	0.02
242	68	38	45	NR	360	14	107	50	C	0
180	70	341	42	NR	301	13	45	45	C	0.01
250	80	62	39	NR	15	19	119	35	A	0.07
242	84	58	34	NR	10	19	110	28	B	0.01
250	72	55	38	NR	14	12	114	41	B	0.001
250	82	55	61	NR	3	31	132	46	B	0.005
84	82	89	30	NL	135	15	37	27	B	0.003
92	80	96	22	NL	141	8	47	23	B	0.002
15	58	71	53	NL	91	11	329	70	B	0.003
35	40	63	22	TR	21	53	268	16	B	0.001
15	45	37	21	TR	353	49	246	14	B	0.001
20	38	68	30	NL	266	12	23	66	D	0
50	70	61	28	TR	8	35	102	5	C	0
30	44	81	37	TR	22	69	279	5	D	0
335	40	90	37	TL	142	76	259	7	B	0.1
355	30	110	28	TL	136	70	281	17	C	0.1
340	34	96	31	TL	131	72	266	13	C	0
45	78	52	29	TR	360	30	96	11	C	0.003
42	78	47	23	TR	358	25	91	8	D	0.004
35	54	189	31	NR	338	3	244	52	B	0
337	30	84	29	TL	105	73	258	16	D	0
355	30	91	30	TL	99	75	269	15	D	0
284	25	69	15	TL	94	56	233	27	D	0

Las Mentas structural site			Coordenates	293757E	5743624N					
Fault strike	Fault dip	Striae trend	Striae plunge	Sense of Slip	T trend	T plunge	P trend	P plunge	Quality	Gouge thickness
87	66	96	19	NL	316	3	48	31	D	0
216	26	280	24	NL	108	21	259	67	C	0.005
216	26	280	24	TR	259	67	108	21	C	0.005
153	46	283	39	TL	346	69	84	3	D	0
24	50	192	14	NR	339	17	235	38	C	0.001
90	38	123	23	TR	82	57	326	16	D	0
18	48	57	35	TR	358	61	261	4	D	0
46	86	49	37	TR	356	28	98	22	B	0
110	62	280	18	TL	328	33	62	7	A	0.001
105	56	267	24	TL	317	44	53	6	B	0
19	65	33	27	TR	340	38	71	1	B	0.1
95	83	125	76	NL	174	37	18	51	F	0
93	76	109	48	NL	154	21	42	44	D	0.2
120	78	262	71	NR	222	31	12	55	D	0
70	62	86	28	NL	303	0	33	42	A	0

Ralco structural site			Coordinates	291270E	5777731N					
Fault strike	**Fault dip**	**Striae trend**	**Striae plunge**	**Sense of Slip**	**T trend**	**T plunge**	**P trend**	**P plunge**	**Quality**	**Gouge thickness**
10	73	173	43	NR	131	16	237	44	A	0
10	73	143	67	NR	112	26	259	59	A	0
60	60	77	27	TR	25	42	293	2	D	0
75	50	200	44	TL	279	72	182	2	D	0
75	58	107	40	NL	138	5	41	56	A	0
270	56	287	24	NL	142	6	238	43	c	0
222	46	263	34	NL	106	5	206	63	B	0
220	50	298	49	NL	304	5	176	82	D	0
240	15	320	15	NL	142	30	316	60	C	0
75	84	82	50	NL	134	28	20	38	A	0
48	68	75	48	TR	1	52	112	15	B	0
72	80	83	47	TR	20	40	131	23	A	0
47	66	72	43	TR	4	50	108	11	A	0
190	66	351	36	NR	313	7	50	45	C	0
222	40	349	34	NR	153	9	40	69	C	0
195	74	2	38	NR	319	14	61	39	A	0
210	74	27	10	NR	164	4	73	19	B	0
200	88	13	75	NR	304	41	95	45	C	0
225	53	18	31	NR	168	3	73	52	B	0
230	45	327	45	NR	144	0	52	86	B	0
205	52	18	9	NR	162	19	59	33	B	0
215	30	22	7	NR	178	31	51	45	C	0
10	82	11	8	TR	326	11	56	0	C	0
195	56	354	28	NR	141	4	47	47	B	0
188	82	4	28	NR	318	14	54	25	A	0
185	85	3	20	NR	317	10	51	18	A	0
185	75	360	19	NR	317	3	48	24	A	0
206	21	328	18	NR	139	26	344	62	D	0
48	44	76	24	TR	30	53	282	13	D	0
225	80	44	5	NR	180	4	89	11	B	0
65	84	69	34	TR	16	28	117	19	B	0
30	83	42	60	TR	329	44	96	32	B	0
20	66	171	47	NR	135	13	245	54	B	0
330	68	348	37	TR	288	44	27	9	D	0
133	36	313	0	NR	103	35	343	35	D	0
262	73	264	6	TR	219	16	127	8	C	0
60	72	105	65	TR	354	59	137	25	D	0
244	61	11	55	NR	348	14	115	67	D	0
168	40	343	4	NR	132	29	17	36	C	0
160	62	160	0	TR	119	19	21	19	C	0

SM 4. Tol-1 drill core structural map scale 1:50.